Characterization of Mouse Lemur Brain by Anatomical, Functional and Glutamate MRI

Clément Garin

Thèse de doctorat

Characterization of mouse lemur brain by anatomical, functional and glutamate MRI

Thèse présentée et soutenue à Fontenay-aux-Roses, le 02/07/2019, par

Clément M. Garin

Composition du Jury :

Laura Adela HARSAN	Rapporteur
MCU-PH, Université de Strasbourg (– UMR 7357)	
Daniel Huber	Rapporteur
Professeur Assistant, Université de Genève (– CMU)	
Ben Hamed Suliann	Présidente
Directeur de Recherche, Université Lyon I (–UMR 5229)	
Luisa Ciobanu	Examinateur
Directeur de Recherche, Université PARIS-SACLAY (– CEA)	
Fabrizio De Vico Fallani	Examinateur
Chargé de Recherche, Sorbonne Universités (–Inria)	
Marc Dhenain	Directeur de thèse
Directeur de Recherche, Université PARIS-SACLAY (–UMR 9199)	

Si les animaux n'existaient pas, ne serions-nous pas encore plus incompréhensibles à nous-mêmes ?

Georges-Louis Leclerc de Buffon

Remerciements :

Je voudrais commencer par remercier mes parents qui m'ont soutenu pendant ces 11 années d'études mais pas seulement. Vous m'avez surtout apporté l'émerveillement devant l'inconnu, le plaisir de chercher à comprendre, apprendre et enfin à transmettre. Il n'y a pas de remerciement assez fort qui équivaudrait à ce merveilleux trésor que vous m'avez légué.

Chers papis et mamies, vous n'êtes plus tous là mais je mesure la chance que j'ai eu de vous avoir à mes côtés pendant toutes ces années. Merci infiniment à toi, papi jardinier, qui me contait des histoires de voleurs tout droit sorties de ton imagination débordante, de ta patience à me faire chanter les tables de multiplication associant pour toujours plaisir et apprentissage.

Merci à mon frère et ma sœur pour votre soutien inconditionnel et nos débats passionnés. Un grand merci à Baptiste sans qui cette thèse n'aurait jamais existé !

Merci Lyndsey pour ton amour, ton soutien en première ligne et de m'avoir fait réaliser que c'est avec les animaux que je souhaite continuer à chercher. Tu as combattu mes moments difficiles avec de l'amour, probablement la seule arme vraiment efficace.

Merci infiniment à Marc pour ces trois ans passés ensemble. La thèse peut parfois être une vraie descente aux enfers et j'ai eu beaucoup de chance de t'avoir comme « passeur » pour ma traversé du Styx. Ce serait long à résumer toutes les fois où j'ai pu compter sur ton soutien mais entre autres : la liberté et la confiance que tu as accordé à mes idées ou alors pour parler en ton nom dans les conférences. Merci pour la patience que tu as eu devant mes difficultés, parfois grandes. Ce qui est incroyable c'est que malgré mon retard dans certains domaines à mon arrivée, je ne me suis jamais senti jugé mais soutenu. Encore merci pour ta présence et ton aide, tout particulièrement pour la rédaction. Finalement, je ne pouvais pas espérer apprendre la recherche dans de meilleures conditions. J'espère sincèrement que nous continuerons à évoluer ensemble car c'est un bonheur de travailler avec quelqu'un d'aussi enrichissant et accessible.

Merci infiniment à Lyndsey, Lynda, Nathalie et Marc pour les corrections de cette thèse.

Contents

Figures

Table

List of abbreviations

ALFF   amplitude of low-frequency fluctuation

BOLD   blood-oxygen level dependent

CSF   cerebrospinal fluid

DMN   default mode network

EEG   electroencephalography

FC   functional connectivity

fMRI   functional magnetic resonance imaging

gluCEST   exchange saturation transfer imaging of glutamate

ICA   independent component analysis

MRI   magnetic resonance imaging

NHP   non-human primates

PET   positron emission tomography

RS   resting-state

rsfMRI   resting-state functional magnetic resonance imaging

SC   sparse component

Summary and aim of the thesis

Animal models are routinely used to mimic diseases in order to explore the impact of pathological processes on brain networks or to measure the effect of a new therapy. The mouse lemur (*Microcebus murinus*) is a primate that has attracted attention within neuroscience research. This small animal is a model for studying cerebral aging and various diseases such as diabetes-related encephalopathy, Parkinson's disease, or Alzheimer's disease. It has a key position on the phylogenetic tree of primates and is used to investigate primate brain evolution. Its cerebral anatomy is still poorly described and its cerebral networks have never been investigated.

The first objective of this study was to develop new tools to develop a 3D digital atlas of the brain of this model and to use this atlas to automatically follow-up brain characteristics in cohorts of animals. A common question for the study of cohorts of animals by MRI is the ability to register large series of images including images recorded with different protocols. We developed a Python package called sammba-MRI to generate specific cerebral templates and to coregister various images to this template. This package offers an efficient integration of existing coregistration methods (ANTS, AFNI). This package was used to create a template of mouse lemur brains to create a digital atlas of the mouse lemur brain. This atlas and several other available mammalian atlases have permitted to compare the regional brain volumes amongst species. Measures from MRI atlases indicate that white matter to cerebral volume index increased from rodents to small primates to macaques, reaching their highest values in humans.

Studies of cerebral connectivity have contributed to many breakthroughs in the understanding of brain function in normal as well as in pathological conditions such as Alzheimer's or Parkinson's diseases. The second objective of this work was to characterize cerebral connectivity in mouse lemurs. This study was based on the evaluation of mouse lemur brains after resting-state blood-oxygen level dependent (BOLD) functional magnetic resonance imaging (fMRI). Patterns of low-frequency signal oscillations recorded with this technique are similar in brain structures functionally connected. Dedicated MR protocols were developed and sammba-mri was used to coregister fMRI images. Then, we created a methodology to extract and

characterize, for the first time, cerebral networks in the mouse lemur. We showed that their brain is organised into local functional regions integrated into large scale functional networks. They were classified as default-mode-like, control-executive-like, motor, visual, basal ganglia and thalamic networks and compared to large scale networks in humans. We highlighted common organisation rules but also discrepancies between these two species.

The biological parameters associated to the organization of brain region into networks are still poorly understood. In a last part of the study, we characterized the relationship between resting-state fMRI and glutamate levels assessed by Chemical Exchange Saturation Transfer imaging of glutamate (gluCEST). We highlighted a relationship between the amplitude of low-frequency fluctuations (ALFF), a measure of cerebral activity issued from rsfMRI as well as hubness and glutamate level, which suggests that glutamate has a critical role on organization and regulation of brain function. A relationship between hubness, local neuronal activity and an index of glutamate level in the brain is consistent with the well-established role of glutamate as an excitatory neurotransmitter. More precisely we found that glutamate is strongly associated to ALFF in the cortical and subcortical brain regions. In the cortex, glutamate is also associated to functional connectivity (hubness). We also highlighted age-related changes for these parameters. They concern alterations of ALFF in the default mode network and reduction of glutamate in the globus pallidus. We also highlighted an age-related reorganization of the cortical/subcortical relationships between ALFF and functional connectivity.

I.   Introduction

I.1. Overview of the mouse lemur primate

The mouse lemur (*Microcebus murinus;* **Figure 1**) or gray mouse lemur is a prosimian non-human primate (NHP). It was first described in 1777 by the English illustrator John Frederick Miller. Phylogenetically the mouse lemur is classified in the Primate order, the Strepsirrhini sub-order, the infra order of the Lemuriforms and the family of the Cheirogaleidae. The Lemuriforms infra order is entirely endemic to Madagascar. The Cheirogaleidae are composed of 5 genera Microcebus, Mirza, Allocebus, Cheirogaleus, and Phaner weighing from 30g to 600g. They are all quadrupeds and mostly have an elongated body and short legs. They are **nocturnal species** and sleep in small nests or holes in a tree (Mittermeier et al., 2008). Although the mouse lemur is probably the most abundant mammalian species native to Madagascar, its trade for commercial purposes has been prohibited since 1975 by the Convention on International Trade of Endangered Species (CITES).

Figure 1 | Mouse lemur.

Morphologically the mouse lemur is characterized by its **small size**, around 25 to 28 centimetres including a tail length of 13 to 14.5 centimetres. Its body mass varies during the seasons (summer ≈ 75 grams, winter ≈ 120 grams). Seasonal variations can be reproduced in captivity by changing the photoperiod: long days (light >12h/day) correspond to summer *i.e.* the dry season and a short day (light <12h/day) correspond to winter i.e. the rainy season. These physiological variations are also characterized by torpor, a lower temperature and a hypometabolism in winter which facilitates the accumulation of fat reserves (Kobbe et al., 2014). These physiological modifications are uncommon in a primate species. The mouse lemur's diet in the wild is composed

of leaves, flowers, nectar, fruits and insects. In captivity it is composed of gingerbread, fruits (such as banana and apple), eggs and concentrated milk. Like many mammalian species, the mouse lemur has seasonal breeding (end of the dry season) with at most 3 estrus lasting 1 to 5 days for the females. The gestation latency (60 days) results in 1 to 4 progenies weighing around 5 grams. Young mouse lemurs reach maturity quickly (≈ 6 to 8 months).

The mouse lemur has a short lifespan in comparison to homologous primates, but has a remarkable longevity for a mammal of its size. The lifespan of the mouse lemur is around 4 years in the wild, due to high predation, but can reach 12 years in captivity (Perret, 1997). Interestingly, the mouse lemur is considered old at around 6 years and displays age-related alterations. As it ages, a decrease in its sensory function (hearing, olfaction, visual acuity) and motor activity are observed (Beltran et al., 2007) (Nemoz-Bertholet et Aujard, 2003) (Languille et al., 2012). MRI studies also described important **cerebral atrophies** linked to an increase of the cerebro-spinal fluid (CSF) surrounding the brain and within the ventricles (Dhenain et al., 2000)(**Figure 2**). This atrophy occurs in 60% of the aged lemurs (Kraska et al., 2011) with an important variability of atrophy patterns.
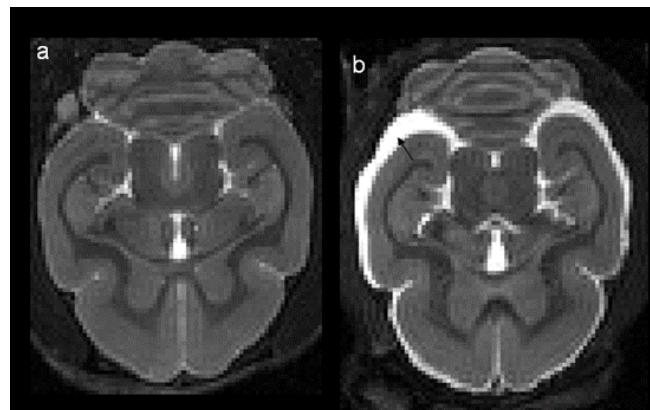
Figure 2 | Aged related atrophy in the mouse lemur brain. Anatomical MRI images of a non-atrophied (5.5 years, a) and atrophied (8.8 years, b) mouse lemur brain. The arrow shows CSF inclusion surrounding the cerebral cortex. Adapted from (Kraska et al., 2011).

Cognitive alterations related to the atrophy severity in the hippocampus and the entorhinal cortex are reported in the aged mouse lemur (Picq et al., 2012). Numerous studies have explored **Alzheimer-like pathology** (N. Bons et al., 2006; Kraska et al., 2011) while aging in the mouse lemur. The Alzheimer's disease-like pathological

changes were mainly defined by the accumulation of amyloid plaques occurring in about 20% of the aged lemurs (Noëlle Bons et al., 1992) and some rare tauopathy (Giannakopoulos et al., 1997). More recently, mouse lemurs were used to artificially induce **Parkinson's** (Mestre-Frances et al., 2018) or **Alzheimer's diseases** (Gary et al., 2015). Mouse lemurs were also used to evaluate different therapies. Pifferi et al. found that an Omega-3 fatty acid supplementation (Fish oil) enhances the resting-state glucose consumption of the lemur's brain (Pifferi et al., 2015). Another recent study found that caloric restriction increases lifespan of the lemurs but affects their brain integrity (Pifferi et al., 2018). Moreover, the key position of mouse lemurs on the phylogenetic trees of primates, makes this animal an important model to investigate primates' brain evolution (Montgomery et al., 2010).

Despite its use to evaluate physio-pathological changes, several improvements remain to be performed to characterize this animal. First, its brain was characterized using 2D anatomical atlas (N. Bons et al., 1998) (Zilles et al., 1979) (Le Gros Clark, 1931). New digital atlases are required to improve the possible use of this animal. Cerebral function is also poorly assessed in mouse lemurs. Here, we developed dedicated tools to create a 3D digital atlas of its brain. We also developed new protocols to characterize cerebral connectivity in mouse lemurs. We finally characterized glutamate-based mechanisms associated to the organization of their brains in neuronal networks and reported age-related changes modulating their cerebral function. Further presentation of the rationale leading to each study is presented before the presentation of an article focusing on each study.

I.2. Magnetic resonance imaging: from anatomy to brain networks

I.2.1. Magnetic resonance imaging: basics

Magnetic resonance imaging (MRI) is a non-invasive and non-ionizing technique that is used to create images of the body. It is routinely used in the clinic for diagnosis and in preclinical research to explore different tissue characteristics/contrasts. In addition to anatomy, MRI permits the detection of several physiological properties such as, spatial diffusion of water, metabolite concentration or blood flow and oxygenation.

Nuclear magnetic resonance was discovered by Bloch and Purcell in 1946 (Bloch, 1946) (Purcell et al., 1946). The theory is that most atomic nuclei such as hydrogen or

phosphorus have a property called "spin" or spin angular momentum. Spin can be oriented when absorbing the energy produced by a magnetic field. Thus, applying a magnetic field (B_0) upon nuclei polarize and align their spin parallel (low-energy state) or perpendicular (high-energy state) to this field (Grover et al., 2015). However, not all nuclei are aligned to B_0 and the proportion of the aligned nuclei results in a net magnetization (M). The higher the magnetic field of the MRI, the higher the net magnetization. The energy state of a nucleus can be changed by applying a radiofrequency field (B_1). These radiofrequencies are commonly applied in pulses lasting microseconds that cause energy transition of the nucleus from low to high. The absorbed energy is subsequently emitted by the nucleus, generating an oscillating current within a reception coil and this process is called "free-induction decay" (FID). The resonance frequency needed to induce a transition of energy can be calculated by the equation of Larmor. The Larmor frequency (ω_0) is dependent on a constant for each nucleus (γ_N) and the strength of the magnetic field (B_0).

$$\omega_0 = \gamma_N . B_0$$

Thus, the frequency required to resonate a nucleus in a given magnetic field can be established for each magnetic field. The localization of MR signal is performed using gradient to create B_0 field strength variations. The signal is encoded into two dimensions (frequency and phase) to create a 2D image or slice using the Fourier transform equation. The combination of this principle with the slice selective excitation pulse allows the spatial localization of the signal within a three-dimensional (3D) space.

Differentiating two tissues with anatomical MRI is often based on their relaxation properties that modify the signal intensity. The hydrogen nucleus (single proton) is the most studied nucleus because of its abundance in fat and water. A difference in relaxation properties between two tissues, changes the rate at which each nucleus returns to its thermal equilibrium. This process is called T_1 relaxation or longitudinal relaxation and measures the time until the magnetization returns to its thermal equilibrium. The transverse relaxation (T_2) is the disappearance of the transverse magnetization. It is due to the energy exchange between spins, which induces a loss of phase coherence in the transverse plane and therefore a progressive disappearance of the transverse magnetization. The T_2^* is referred to as T_2 but also considers local inhomogeneity of the magnetic field and the tissue susceptibility. Modifying several

parameters in a sequence such as the time between two excitatory radiofrequency pulses (repetition time) and time between the excitation pulse and the signal peak (echo time) "weights" the image toward a contrast T_1 or T_2. As an example, using T_1 contrast, brain tissues can be separated based on their distinctive contrasts producing low signal intensity within the brain ventricles (dark), medium intensity within the gray matter, and high intensity within the white matter (bright). This T1/T2 difference is one of the mechanisms that provide contrast by MRI.

Practically, acquisition of MR images reposes on the use of dedicated acquisition sequences that are particular setting of pulse sequences and pulsed field gradients that allow to record spins in a particular state. The two basic sequences are spin-echo and gradient echo sequences. The spin echo-sequence is based on the application of a 90° pulse followed up by a 180° pulse, prior to acquisition of the signal from an echo. This sequence can be adjusted to give T1-weighted, proton density, and T2-weighted images. Gradient echo sequences were initially based on a single pulse varying from 5 to 90 degrees followed-up by an echo that is recorded. This sequence provides T1-weighted, proton density, and T2*-weighted images. Larger flip angles give more T1 weighting to the image and the smaller flip angles give more T2* weighting to the images. These basic sequences have been largely complexified to provide new contrasts and faster imaging schemes.

I.2.2. BOLD signal

Blood oxygenation level dependent (BOLD) imaging is the standard technique used to generate images in functional MRI (fMRI) studies. It relies on the measure of cerebral blood flow and oxyhemoglobin/deoxyhemoglobin state of haemoglobin that evolve when neurons from a brain region are activated (Boniface, 2002). The reason fMRI is able to detect this change is due to a fundamental difference in the paramagnetic properties of oxyhemoglobin and deoxyhemoglobin. Deoxygenated hemoglobin is paramagnetic whereas oxygenated hemoglobin is not leading to different signal in images (**Figure 3**). Heavily T2* weighted sequences are used to detect this change, which is in the order of 1-5% (Gore, 2003).
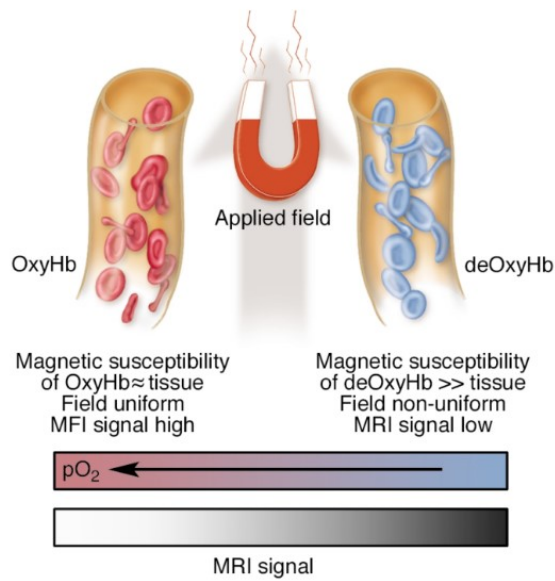
Figure 3 | BOLD signal: magnetic susceptibility to vascular oxygenation. The MRI signal within the deoxygenated tissue is lower because of the field inhomogeneity generated by the deoxyhemoglobin paramagnetic properties. The field inhomogeneity lead to a faster decay of the signal. From (Gore, 2003)

BOLD signal was discovered in 1990 by Ogawa et al. (Seiji Ogawa et al., 1990). They described tubular hypo-intensities in the rodent cortex that were visible with a T2*-weighted sequence but not with a T2-weighted (**Figure 4**)Erreur ! Source du renvoi introuvable.. They also highlighted for the first time, the paramagnetic effect of the deoxygenated blood on the MRI contrast (S. Ogawa et al., 1990).
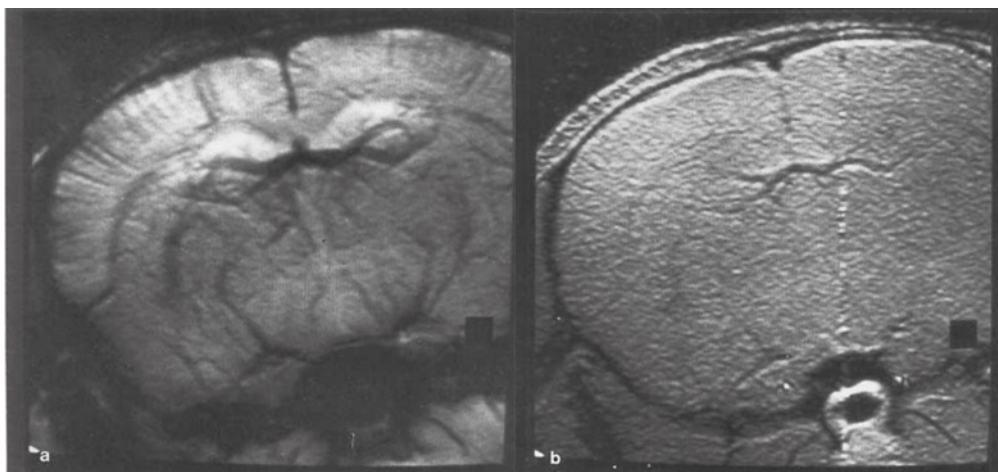
Figure 4 | Blood vessel detection with a gradient echo sequence in the rat brain. Gradient echo epi (a) and spin echo epi (b) image acquired in an anoxic mouse brain. Tubular intensities corresponding to blood vessels can be detected with gradient echo epi sequence. From (Seiji Ogawa et al., 1990)

Following the initial work by Ogawa et al., several groups characterized the relationships between neuronal activation by a task and evolution of the BOLD signal. They showed that following a stimulus, the BOLD signal show a small initial dip, followed by a tall peak, and then a variable post-stimulus undershoot (Barth et Poser, 2011) (**Figure 5**).
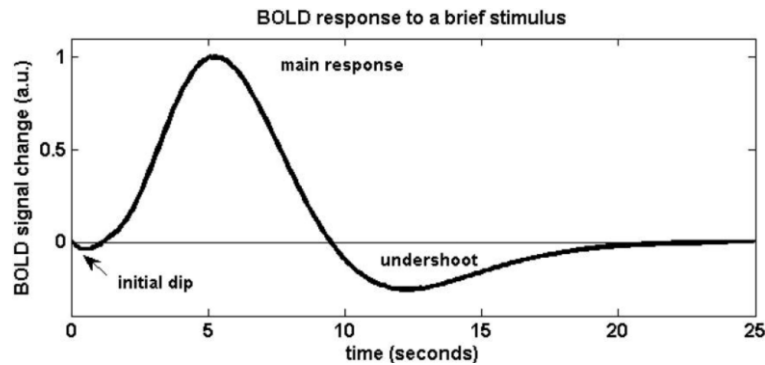
Figure 5 | BOLD hemodynamic response function following a single brief stimulus.
From (Barth et Poser, 2011).

The initial dip origin remains highly debated. It might reflect a quick extraction of the blood oxygen prior to any cerebral blood flow increase. The initial dip is found in many non-human species such as rats, cats and monkeys and is specific towards neuronal activity (K.-S. Hong et Zafar, 2018). The main response or peak is usually delayed by approximately 2 seconds. This interval could correspond to the time in which the blood travels from arteries to draining veins and capillaries (Logothetis, 2003). The bulk of the BOLD response is mediated by a variety of biological mechanisms contributing to the hemodynamic response such as: blood flow, blood volume, increases in deoxyhemoglobin concentration and oxygen metabolism. After the stimulus, a decrease of the BOLD signal is typically observed and called undershoot. The undershoot origin is also disputed and supposedly reflects an increase of the cerebral blood flow overcompensating for the oxygen increase (Logothetis, 2003).

Thus, the BOLD signal is assumed to indirectly measure the neuronal activity in a process called neurovascular coupling (Murakami et al., 2018).

I.2.3. From BOLD signal to evoked functional MRI

BOLD signal is largely used to characterize cerebral activity following activation with various stimuli (*i.e.* motor (Bandettini et al., 1994), speech (Hinke et al., 1993) or cognitive tasks (Buckner et al., 1996). The use of this technique to infer on brain function relies on block task paradigm. It corresponds to a series of trials (*i.e* resting and activity task) performed during a period of time. The signal acquired during these two blocks can be compared statistically. Blamire et al. was one of the first studies detecting a BOLD signal increase in the visual cortex in response to an external stimulus (flashing checkerboard) (Blamire et al., 1992) (**Figure** *6*).
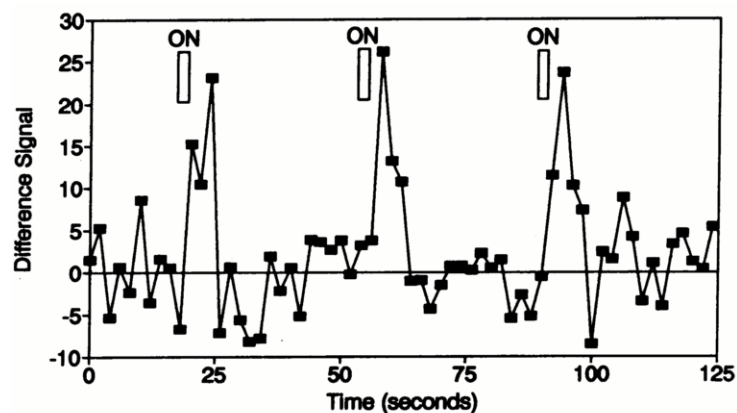
Figure 6 | BOLD response to stimuli in the visual cortex. BOLD signal total response from voxels extracted in the visual cortex. The BOLD signal peak exhibits a delay between the task (ON = 2 seconds) and its response. From (Blamire et al., 1992).

One of the major steps toward the wide use of BOLD fMRI was the development of fast imaging sequences permitting the acquisition of multiple images during a resolute period of time (Cohen et Weisskoff, 1991) in order to perform efficient blocked task paradigms.

I.2.4. From BOLD signal to resting-state functional MRI

Further analyses of BOLD-fMRI signal have also led to another major discovery, *i.e.* the existence of spontaneous and elaborated patterns of neuronal activity in the human brain at rest (B. Biswal et al., 1995). By exploring the correlated activity of the motor cortex for a finger-tapping experiment, Biswal et al. found during a baseline session that interhemispheric coordinated activity occurs even in the absence of stimuli (B.

Biswal et al., 1995)(**Figure 7**). Rapidly, this technique is coming to be used to describe a large set of brain areas connected by spontaneously coordinated activities at rest. These connected areas are defined as resting-state networks (Guye et al., 2008). The default-mode network, salience network, sensory motor network, visual networks are amongst the most widely described networks. We will focus on the description of cerebral networks characterized in humans ("I.4.1. Organization and function of cerebral networks in humans") and in animals ("I.4.2. Organization and function of cerebral networks in non-human primates"). The analysis of resting-state networks is based on image processing algorithms that will be described in the following paragraph
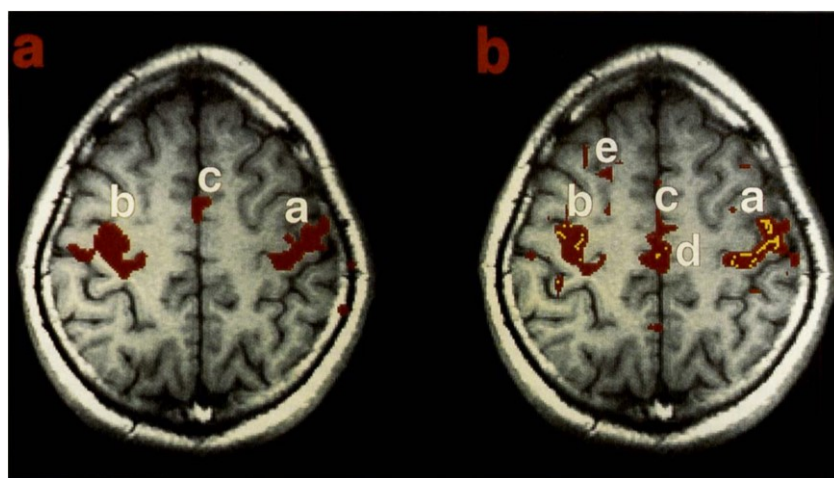
Figure 7 | BOLD correlation in the motor cortex under activation and at rest. This figure displays on the left (a) the correlated voxel corresponding to the activation paradigm (finger tapping). Coordinated activity is observed in the right and the left hemisphere of the motor cortex. Similar coordinated activity was observed at rest (b) and in similar areas. From (B. Biswal et al., 1995).

I.3. Overview of the methods used to characterize cerebral networks by resting-state fMRI

I.3.1. Overview of image acquisition schemes for rsfMRI

fMRI technique is based on the images acquisition at low spatial resolution. Thanks to this low spatial resolution, it is possible to obtain an excellent temporal resolution which produces images of the whole brain every 1 to 5 seconds. The total acquisition time of an fMRI scan can last a few minutes (usually between 5 and 15 minutes) resulting in hundreds of images covering the entire brain (or one 4D image with three spatial dimensions and one temporal dimension). The different slices of a single brain

image are not acquired at the same time. An interleaved acquisition (1, 3, 5…) is commonly used to reduce the "slice cross-talk artefacts". The intensity of the voxels of a 4D fMRI image varies by a low percentage over time. However, this small variation can be detected with the algorithms described in the following paragraphs.

I.3.2. From signal to functional connectivity analysis

Functional connectivity is the connectivity between brain regions that share functional properties. More specifically, it can be defined as the temporal correlation between spatially remote neurophysiological events, expressed as deviation from statistical independence across these events in distributed neuronal groups and areas (B. B. Biswal et al., 1997). Several algorithms have been implemented to analyze this connectivity. We will present the most widely used algorithms.

I.3.2.1. Seed-based correlation analysis

Seed-based correlation analysis is one of the most common methodologies for functional network characterization (Greicius et al., 2003) (**Figure 8**). This method was first adopted by Biswal et al. to explore Pearson's correlation coefficients between voxelwise signals and ROIs or "seeds" (B. Biswal et al., 1995). The seed is a small area, used to extract and average the BOLD signal. It can be defined by creating either a sphere corresponding to the coordinates of brain regions or by using regions predetermined by a brain atlas. The Pearson's correlation coefficients can be measured between the signal extracted within the seed and the voxelwise signals. The reconstruction of the Pearson's correlation coefficients corresponding to each voxel in the 3D space of the brain image highlights areas connected to the seed.
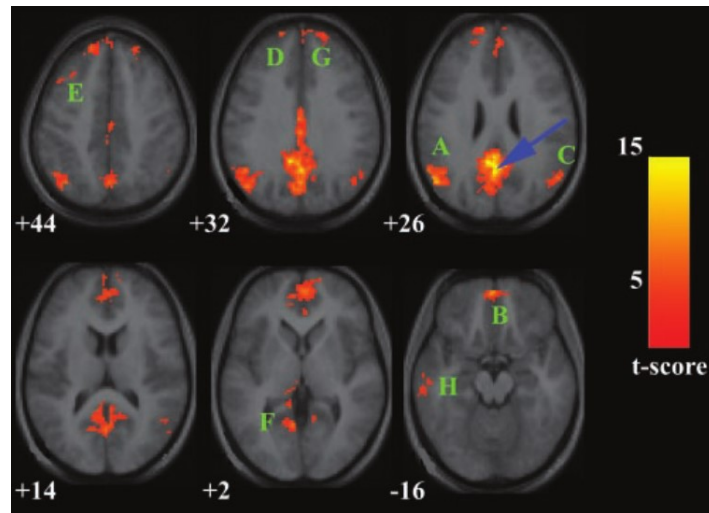
Figure 8 | Human default mode network characterized by seed-based correlation analysis.

Map of the resting-state default mode networks highlighted by the voxels connected to the posterior cingulate cortex (seed, blue arrow). Significant clusters are found in (A&C) inferior parietal cortex, (B) orbitofrontal cortex, ventral anterior cingulate cortex, (D&G) medial prefrontal cortex, (E) dorsolateral prefrontal cortex, (F) parahippocampal gyrus, (H) inferolateral temporal cortex. From (Greicius et al., 2003).

I.3.2.2. Analyses based on BOLD signal spatial decomposition

Network organization can also be explored by using spatial decomposition algorithms. Two main algorithms were developed in order to extract brain networks on raw images: (1) independent component analysis (ICA) and (2) dictionary learning. Both produce a set of activation 3D maps that permit the characterization of the cerebral networks. Although these algorithms are more complex than the seed based correlation analysis, the identification of co-activated areas remains based on the same basic principle.

(1) **ICA** was the first algorithm developed and adapted for fMRI images. This computational algorithm assumes that several areas of the brain can be separated into different spatially or temporally **independent** sources of signal called components. One of the assumptions of ICA is that the components display a non-Gaussian signal. The two broadest definitions of independence for ICA are the maximization of the non-Gaussianity and the minimization of mutual information.

(2) **The dictionary learning method** identifies a **sparse** representation (component) of an array that can form a linear combination. The array or 2D matrix is extracted using an fMRI image (column = brain voxels; rows = time points). One advantage to dictionary learning is that it allows repeated use of brain voxels, meaning that the same voxel could be included in different components. This property provides an improved flexibility of decomposition.

Both methods have succeeded in separating functional regions from rsfMRI datasets. Their limitation is that the number of components has to be estimated prior to the analysis and this assumption greatly affects the ICA or dictionary learning results (**Figure 9**). Clear segmentation differences between two similar components could appear. For example, the components of **Figure 9** (A; 24) and (B; 69) define the same network (executive) and are characterized by the anterior cingulate cortex. Their extraction using 27 (A) and 70 (B) components leads to the non-detection of several co-activated areas in (A; 24) compared to (B; 69). The other limitation specific to ICA, is that this algorithm struggles to reveal networks with partly neuro-anatomical overlaps (W. Zhang et al., 2019). This issue is a limitation for ICA since brain networks are not segregated in space but interact with each other. Indeed, the brain is a heterogeneous entity with intermixed neurons and various axonal projections within the same region.
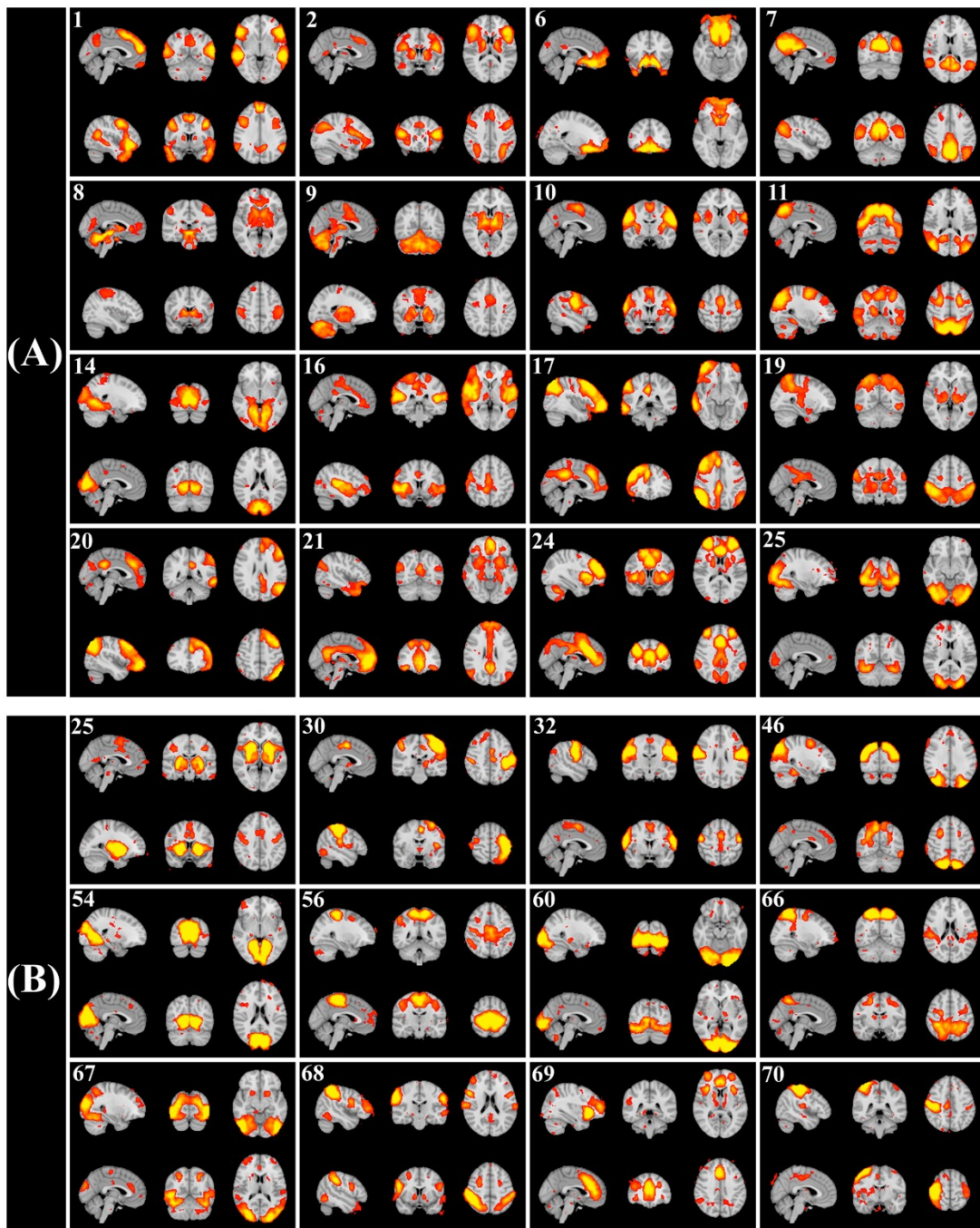
Figure 9 | Group-ICA analysis at rest: Assumption of the number of components.

Group-ICA in humans based on 27 components (A) where 16 were found non-artefactual and 70 components (B) where 12 were found non-artefactual. From (Tian et al., 2013).

I.3.2.3. Analyses based on graph analysis and hub identification

Graph theory is another technique to characterize local functional regions as well as large-scale networks. With graph theory, whole brain networks (graph) are defined as a set of nodes (basic elements of the system) and edges (allowing relationships between nodes). The correlations of the BOLD fMRI signal between the different nodes provides an index of functional connectivity (FC) (C. F. Beckmann et al., 2005; J. S. Damoiseaux et al., 2006) and are represented by the edges of the network.

In graph theory, large scale networks can be defined as **modules** or communities, which are groups of nodes densely connected by edges and sparsely connected with nodes from other modules. One of the most common methods to divide a network into communities is called **modularity maximization**. Modularity is a metric comparing the number of edges of a community and evaluating their differences with equivalent random communities (M. E. Newman, 2006). High modularity means dense connection within a module and sparse connection between nodes of different modules. Modularity maximization assigns a different community to each node and evaluates the gain of modularity if node A is removed from its community and placed in community X (D. B. Vincent et al., 2008). The community detection is useful for the automatic partition of a network into distinct communities that are relevant to the neurological organization of the brain (**Figure 10**). However, modularity maximization suffers from methodological limitations such as the existence of partitions that are equally optimal. Also, this algorithm cannot classify nodes in different modules (overlapping nodes) which is a problem for biological relevance (see chapter: I.3.2.2. Analyses based on BOLD signal spatial decomposition).
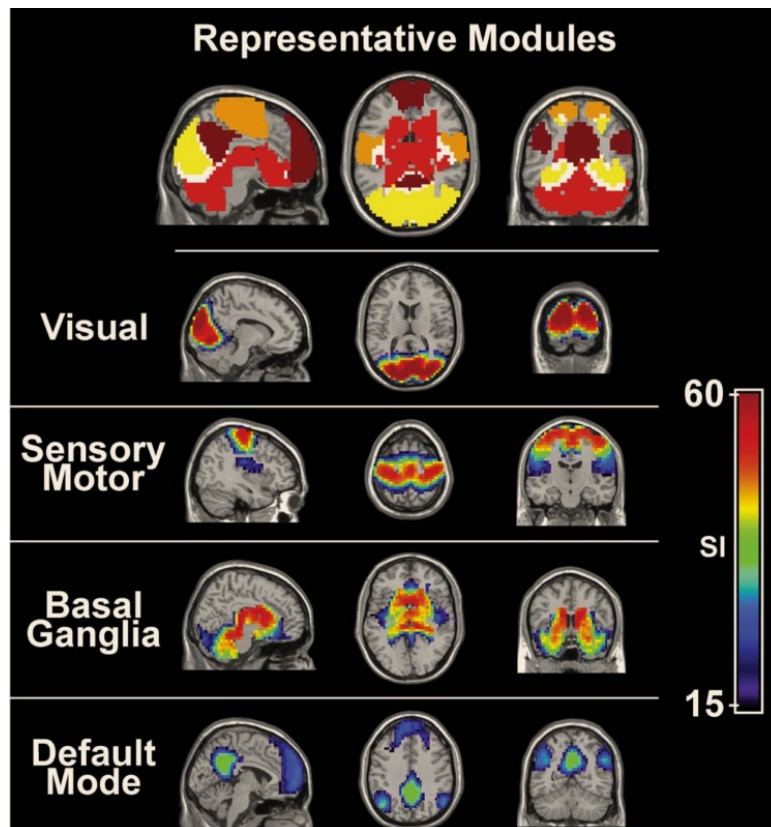
Figure 10 | Four modules detected in the human brain. The detected modules were based on a network in which each voxel represents a node. These four networks are consistent with the current knowledge of the human brain organization explored with other techniques. From (Moussa et al., 2012).

Whole brain networks can also be characterized using various descriptors of **topological properties**. For example, "**hubness**" describes the degree of node centrality or its influence in the network which is supposedly related to its importance for brain function. Eigenvector centrality was used as a hubness descriptor in our studies. However, a wide variety of descriptors exist, representing different hubness features in a given graph. Standard hubness metrics are:

- **Eigenvector centrality** that detects nodes highly connected to other highly connected nodes (Lohmann et al., 2010). Eigenvector centrality measures the centrality of a node according to the number of links it has with other nodes in the network. Eigenvector centrality also considers the connection quality of a node, the number of links it has, and so on for the whole network. Eigenvector centrality calculates the extended connections of a node, so it favors nodes that influence the entire network and is not limited to direct connections.

- **Degree centrality** simply represents the number of edges of a node (or the mean of their value on a weighted graph). Degree centrality find highly connected nodes that are likely to hold most of the information which can connect quickly with the larger network.

- **Closeness centrality** identifies the shortest path between two nodes and calculates the sum of its edges. It is estimated for a given node, by averaging the sum of the edges of the shortest path between the node and all other nodes in the graph (van den Heuvel et al., 2010).

- **Betweenness centrality** detects the amount of times a node appears on the shortest path along other nodes. It considers the influence of a node as its "bridges" property. To do this, it detects the shortest paths of the entire network and counts number of times a given node lie into it (van den Heuvel et al., 2010). This metric is probably the most commonly used to characterize hubness.

- **Current flow betweenness centrality** is a betweenness centrality measure that also considers the influence from all the paths across nodes. This algorithm provides more weight to the shortest path but also considers the other connections. Interestingly, the information is considered to spread as an electrical current (M. E. J. Newman, 2005).

To our knowledge, there is no consensus for the best hub metric to characterize brain networks.

Small-worldness is another index of **topological properties** of the network. It defines large scale specialization and global information transfer efficacy. It can be characterized using two small-world coefficients (σ and ω) (NetworkX (Hagberg et al., 2008))(**Figure 11**).

σ is defined as $\sigma = \frac{C/\text{Crand}}{L/\text{Lrand}}$ (Watts et Strogatz, 1998)

ω is defined as $\omega = \frac{L}{\text{Lrand}} - \frac{C}{\text{Crand}}$ (Telesford et al., 2011).

With C and L being, respectively, the average clustering coefficient (a measure of network segregation) and the average shortest path length (a measure of integration) of the network. Crand and Lrand are their equivalent derived random networks. Small-

world networks have σ values superior to 1 and ω values close to 0 (Telesford et al., 2011). The small-world coefficients are disrupted in several neuropathologies such as Alzheimer's disease (X. Zhao et al., 2012) or schizophrenia (Anderson et Cohen, 2013).
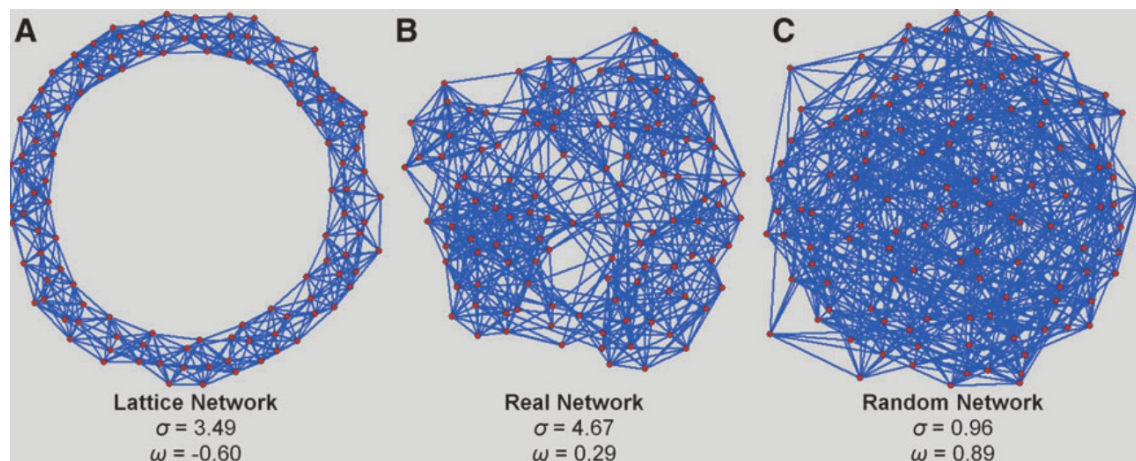
Figure 11 | Comparison of different networks based on their large scale topological properties.

Equivalent lattice (A), real (B), random (C) networks. The networks that are considered as small-world are the lattice (σ= 3.49) and the real world (σ= 4.67). From (Telesford et al., 2011).

I.4. Functional connectivity in mammalian species

I.4.1. Organization and function of cerebral networks in humans

Resting-state networks have been largely described in humans (**Figure 12**) (B. Biswal et al., 1995; B. B. Biswal et al., 2010; Fox et Raichle, 2007). Their study has contributed to many breakthroughs in understanding the relationship between human cognition and brain architecture (Mather et al., 2013).

The most studied resting-state network is the **DMN (Figure 12 ; Figure 26 ; Figure 8).** It was first described by Raichle et al. (Raichle et al., 2001) using positron emission tomography (PET). This network is particularly engaged during rest and is suspended/deactivativated during stimulated brain activity (Hampson et al., 2006; Tambini et al., 2010). The main regions implicated in the DMN are posterior cingulate cortex, medial prefrontal cortex, and medial, lateral, and inferior parietal cortices. The DMN is possibly involved in memory consolidation (Huo et al., 2018) or other cognitive functions such as mindfulness (Doll et al., 2015), self-referential and introspective state (Greicius et al., 2003). The DMN is often divided into two major networks (anterior and posterior DMN). The anterior DMN is more active during self-directed thoughts and the posterior DMN during passive rest (C. G. Davey et Harrison, 2018). Also, Davey et al. investigated the DMN during self-related processes and found that the posterior cingulate cortex is mainly implicated in the coordination of the mental representations. The medial prefrontal cortex is a regulator or 'gateway' function of self-representations (C. G. Davey et al., 2016). Furthermore, the DMN may prove to be implicated in and/or be an indicator of healthy and non-healthy brain aging including several pathological processes such as Alzheimer's or Parkinson's diseases (Buckner et al., 2005; Gao et Wu, 2016). Moreover, the pattern of deposition of one the major lesions in Alzheimer's disease (amyloid plaques), co-localizes with the DMN (Buckner et al., 2005).
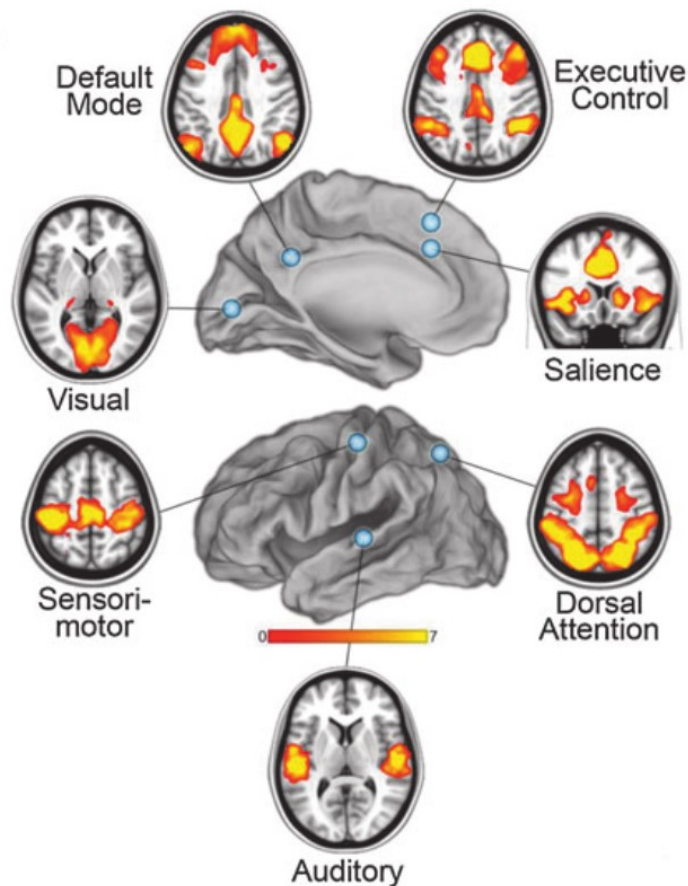
Figure 12 | Major resting-state networks of the human brain. Adapted from (Raichle, 2011)

The **executive-control** network (**Figure 12**) embeds regions from the superior and middle prefrontal cortex, anterior cingulate cortex, paracingulate gyri, ventrolateral prefrontal cortex and subcortical regions of the thalamus (Christian F. Beckmann et al., 2005; Mazoyer et al., 2001). The executive network is especially active during tasks involving target-directed, intellectual activities and participation in cognitive control. Anti-correlated activity is reported in this network at rest (Seeley et al., 2007a). Patients with attention-deficit/hyperactivity display a higher functional connectivity within the anterior cingulate cortex related to a decrease in their symptoms (Francx et al., 2015).

The **attention** network (**Figure 12**) is commonly divided into two separate fronto-parietal networks (dorsal and ventral) that both involve different areas of the frontal cortex (Vossel et al., 2014). The dorsal attention network embeds the intraparietal sulcus, as well as the frontal eye field. This network is implicated in attention processes such as the selection of stimuli (spatial cueing of color, shape, motion direction). Also,

this network is involved in the control of appropriate response, potentially mediated by a selection (top-down) of the cognitive stimuli and actions (Hopfinger et al., 2000). The ventral attention network involves the ventral frontal cortex and the temporo-parietal junction (Vossel et al., 2014). This network seems dedicated to the spatial attention of new stimuli (visual, sound and tactile) (Vossel et al., 2006). Therefore, the main function evoked for this network is the reorientation of the attention to relevant stimuli (Stevens et al., 2005).

The **salience** network (**Figure 12**) includes regions in the dorso-medial prefrontal cortex, anterior cingulate cortex, insula, and temporo-parietal junction. This network is associated with mindfulness and the regulation of the dynamic changes with other networks implicated in mindfulness (DMN or the control-executive) (Doll et al., 2015). The main function of the **salience** network is probably to regulate the switch between networks. It participates in answering to salient events by facilitating the access to working memory, attention or motor systems (Menon et Uddin, 2010). Other roles of this network are related to moral reasoning (Chiong et al., 2013), resistance to temptation (Steimke et al., 2017) and more global emotional and empathic functions (Seeley et al., 2007b). Dysfunctions of the network are associated with neuropsychiatric disorders such as autism, schizophrenia and frontotemporal dementia (Uddin, 2014).

The **visual** network (**Figure 12**) was divided into two main large- scale networks (J. S. Damoiseaux et al., 2006): (1) **medial visual cortical areas** composed of the primary visual area located in the calcarine sulcus, medial extrastriate nucleus and lingual gyrus (Christian F. Beckmann et al., 2005) as well as co-activated areas in the lateral geniculate nucleus precuneus regions. The thalamus is proposed as a "relay station" from the visual input to the primary visual cortex (Christian F. Beckmann et al., 2005). (2) **lateral visual cortical areas** including mainly non-primary visual areas such as the occipital pole and the occipito-temporal cortex as well as superior parietal regions. This set of regions is assumed to have a role in visuo-spatial attention or visual attention (Christian F. Beckmann et al., 2005). Some studies have demonstrated that lesions within the parietal regions can disturb spatial attention (Nachev et Husain, 2006).

The **sensory-motor network (Figure 12; Figure 7)** was the first rsfMRI found by Biswal et al. (B. Biswal et al., 1995) using seed-based analysis. This network is mainly

composed of regions from the pre and postcentral gyri (Brodmann areas 1, 2 and 3) and the supplementary motor area. The sensory-motor network display high interhemispheric correlations (Bharat B. Biswal, 2012). The primary sensory cortex and the primary motor cortex can be subdivided into areas responsible for the processing of sensory and motor information dedicated to specific areas of the body such as the nose, eyes, toes, etc. (Grodd et al., 2001).

The **auditory** network (**Figure 12**) involves the primary and secondary auditory cortices and is dedicated to the process of auditory stimuli. An asymmetry of this network is highly debated (Andoh et al., 2015).

The **basal ganglia** network is mainly composed of the caudate nucleus, putamen, pallidum, substantia nigra and subthalamic nucleus (Afifi, 2003). This network is associated with a variety of functions such as motivational, emotional, motor and cognitive processes (Bednark et al., 2015). This network is highly damaged in Parkinson's disease and Huntington's disease (Wen et al., 2012) and the functional connectivity matrix of this network was used to classify Parkinson's disease patients versus healthy controls with 81% accuracy (Rolinski et al., 2015).

This list of networks is not exclusive and other major networks have been described in humans. We cannot describe all these networks here.

I.4.2. Organization and function of cerebral networks in non-human primates

Cerebral networks have been described in non-human primates as in humans. The first characterization of cerebral networks in anesthetized non-human primates at rest found four large scale networks (J. L. Vincent et al., 2007) classified as the DMN, oculomotor, somatomotor and visual. They were anatomically close to those previously described in humans. This major discovery highlighted that the brain functional organization transcends the consciousness and reflects an evolutionarily conserved property of the primate brain.
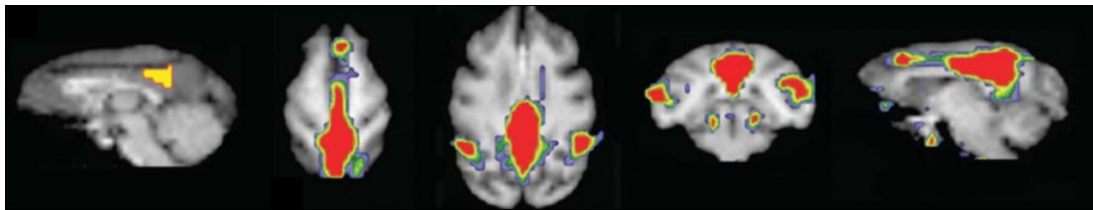
Figure 13 | Default mode network discovered for the first time in the macaque brain.

Significant voxels correlated to the posterior cingulate cortex (seed-based analysis) in anesthetized macaque using BOLD fMRI. Adapted from (J. L. Vincent et al., 2007).

These results were quickly confirmed by Rilling et al. using [18F]-fluorodeoxyglucose PET on awake chimpanzees at rest (Rilling et al., 2007) and later with [15O]H_2O PET in macaques (Kojima et al., 2009). In 2009, the posterior cingulate cortex activity measured by electrophysiology was found to be suppressed during task performance and returned to a higher resting baseline at rest in macaques (Hayden et al., 2009). Hutchison et al. was the first to analyze fMRI images with ICA (20 components) on the macaque (*Macaca fascicularis*) cortex and found 11 relevant components ((R. M. Hutchison et al., 2011); **Figure 14**)
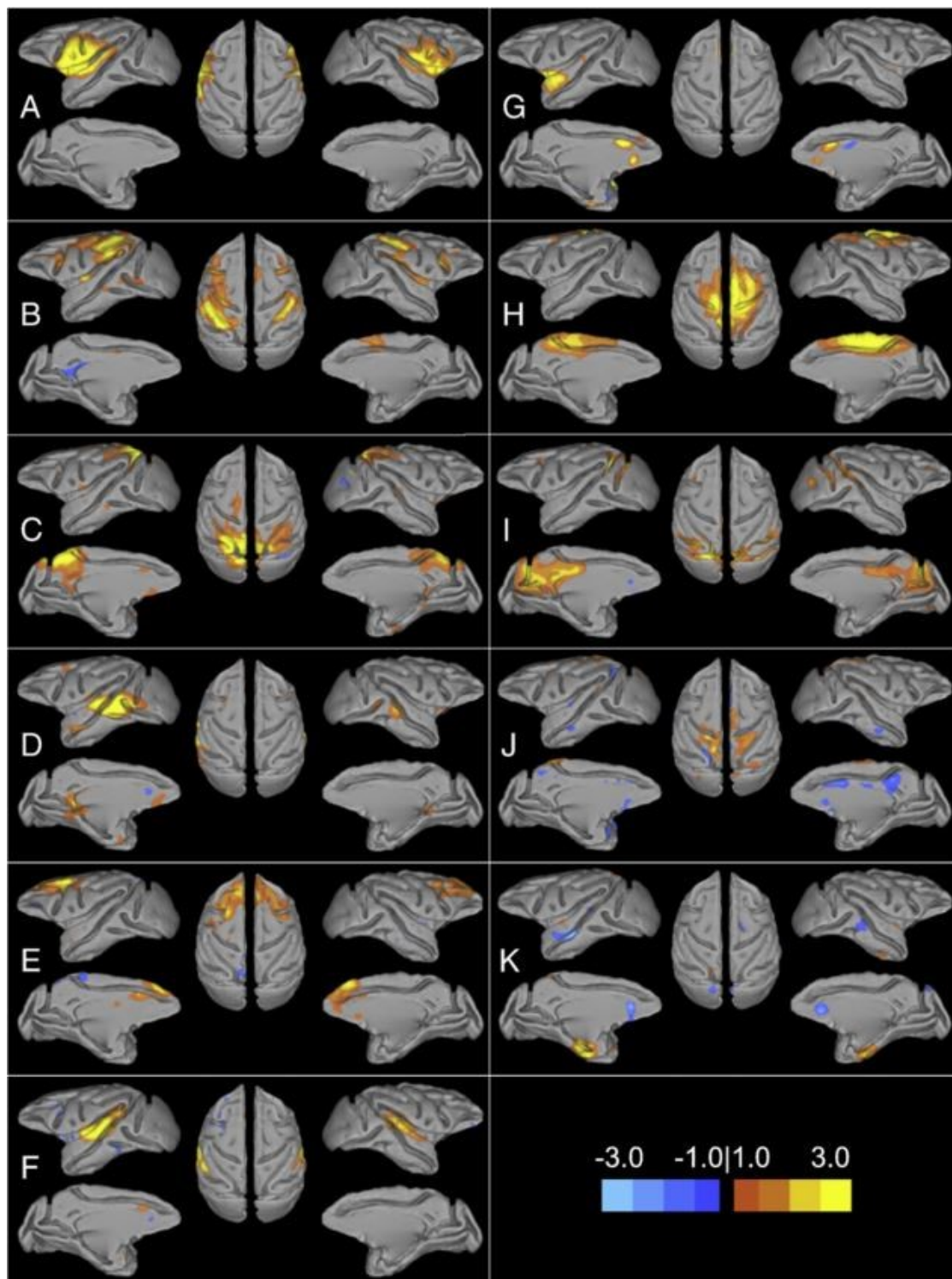
Figure 14 | Eleven independent components extracted from fMRI images of the macaque brain.

The ICA was performed using 20 components, 11 were selected as relevant and named as follows: A: precentral–temporal; B: fronto-parietal; C: posterior-parietal; D: occipito-temporal; E: frontal; F: superior-temporal; G: cingulo-insular; H: paracentral; I: parieto-occipital; J: postcentral; K: hippocampal. From (R. M. Hutchison et al., 2011)

A meta-analysis of macaque fMRI images has allowed a comparison of the reduction of activity during goal-directed behavior within the **DMN** rather than the functional connectivity analysis at rest or under anaesthesia (D. Mantini et al., 2011). This publication was followed by a meta-analysis synthesizing all the DMN organization descriptions of macaques published before 2012 (R. M. Hutchison et Everling, 2012). This article found a diversity of anatomical clusters included in this network (*Figure 15*).
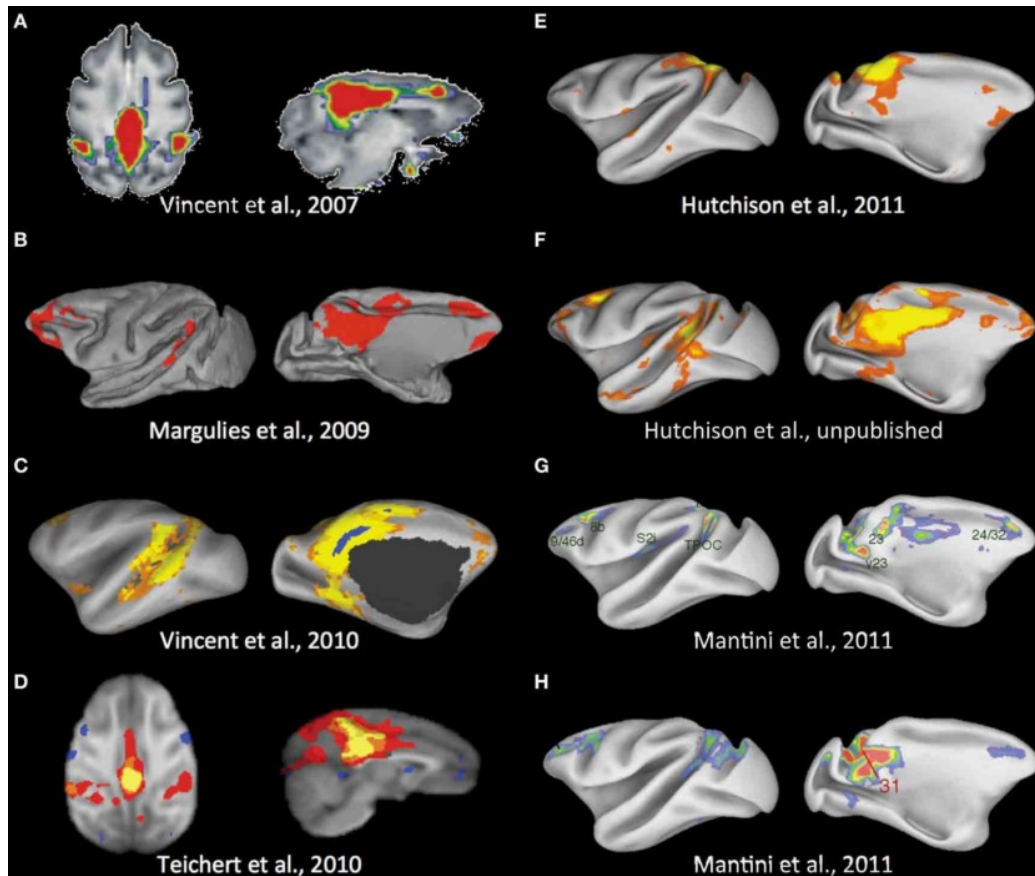
Figure 15 | Synthesis of the macaque DMNs observed in rsfMRI literature.

(A) (J. L. Vincent et al., 2007), (B) (Margulies et al., 2009), (C) (J. L. Vincent et al., 2010), (D) (Teichert et al., 2010), (E, F) (R. M. Hutchison et al., 2011), (G, H) (D. Mantini et al., 2011). From (R. M. Hutchison et Everling, 2012).

Different articles reported common features as well as discrepancies between the macaque DMN. (J. L. Vincent et al., 2007) and (Margulies et al., 2009) found similar correlated activity (seed-based analysis) in the lateral temporoparietal cortex, the posterior parahippocampal cortex, the dorsal medial prefrontal cortex and the anterior cingulate cortex; (D. Mantini et al., 2011) and (J. L. Vincent et al., 2010) found similar correlated activity in the dorsal medial prefrontal cortex and in the inferior parietal lobule. However, the lateral temporoparietal cortex and the posterior parahippocampal cortex were absent; (Teichert et al., 2010) and (R. M. Hutchison et al., 2011) did not find medial and dorsal frontal and hippocampal regions. Differences features of the macaque DMN were explained by the limitations of seed-based analyses and by the use of different seeds in various studies. Indeed, different seeds locations or sizes could potentially impact the reproducibility of the features (R. M. Hutchison et Everling, 2012). The use of ICA was proposed as a solution to provide more reproducible results.

In chimpanzees, DMN regions similar to those reported in humans were proposed (medial prefrontal cortex, posterior cingulate cortex and precuneus) (Barks et al., 2015). The DMN is also found in awake marmosets, recruiting the retrosplenial and posterior cingulate cortices, medial parietal area, premotor and posterior parietal areas and areas surrounding the intraparietal sulcus (Belcher et al., 2013).

Other large scale networks similar to those detected in humans are observed in the non-human primates at rest. For example, using different seeds in the cingulate cortex Hutchison et al. identified four large scale networks (somatomotor, executive, attention-orienting and limbic) ((R. M. Hutchison et al., 2012); **Figure 16**).
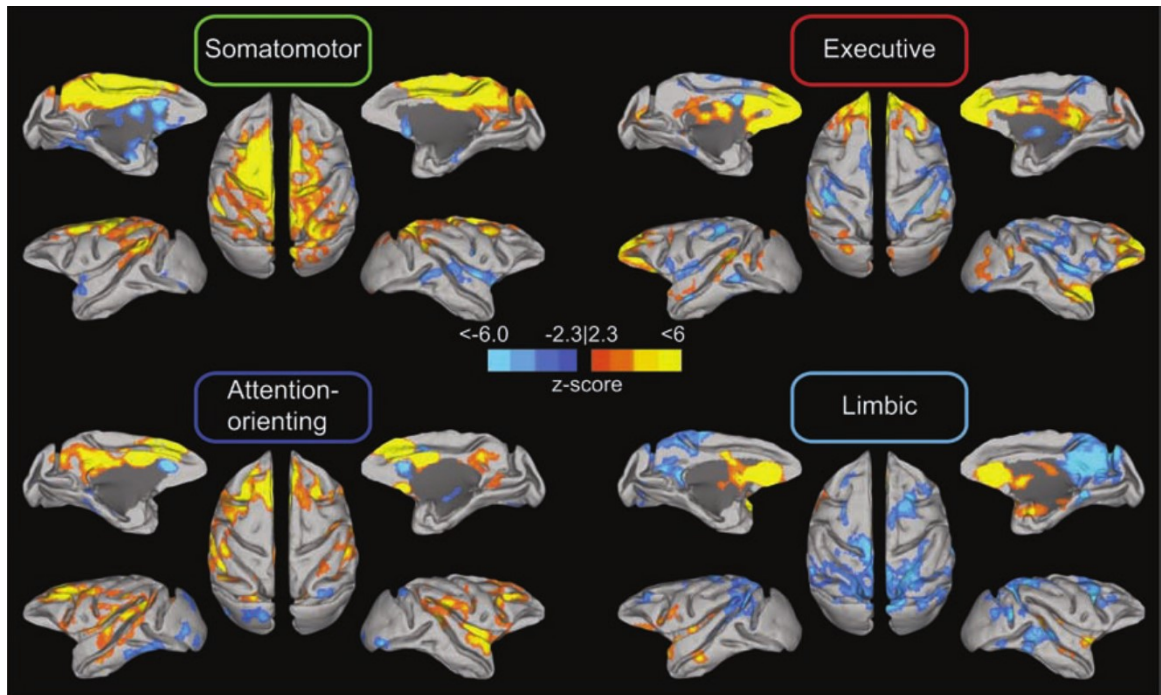
Figure 16 | Four large scale networks extracted from the macaque brain using various seeds in the cingulate cortex. From (R. M. Hutchison et al., 2012)

The salience network has also been described in the macaque brain but its identification is not justified on a behavioral/functional basis (Touroutoglou et al., 2016).

In the awake marmoset, the diversity and the number of networks extracted with ICA (eleven) was exceptionally high (higher-order visual, basal ganglia, primary visual, dorsal (medial) somatomotor, higher-order visual, higher-order midline visual, default mode, salience, orbitofrontal, cerebellar, ventral (lateral) somatomotor, frontal pole). The frontal-parietal network was recently described in the marmoset brain and is characterized as a major network (high hubness score) (Ghahremani et al., 2016).

As evoked for the DMN and other networks, difficulties occurred in describing the spatial limits between distinct networks and in identifying their functions. These difficulties generated different conclusions concerning the identifications of several large scale networks. A standardized methodology will be necessary in order to obtain reproducible results across laboratories.

I.4.3. Organization and function of cerebral networks in rats

As in non-human primates, rat cerebral networks were first discovered under anaesthesia. One of the first studies to observe correlated areas with fMRI signals in rats was performed with a 9.4T MRI. It found two networks corresponding to the sensorimotor and visual networks (Pawela et al., 2008). One year after this discovery, Zhao discovered a caudate/putamen network in rats (F. Zhao et al., 2008). Later, a large list of reproducible networks that were extracted with ICA was proposed by Hutchiston et al. under two types of anaesthesia ((R. M. Hutchison et al., 2010); **Figure 17**).
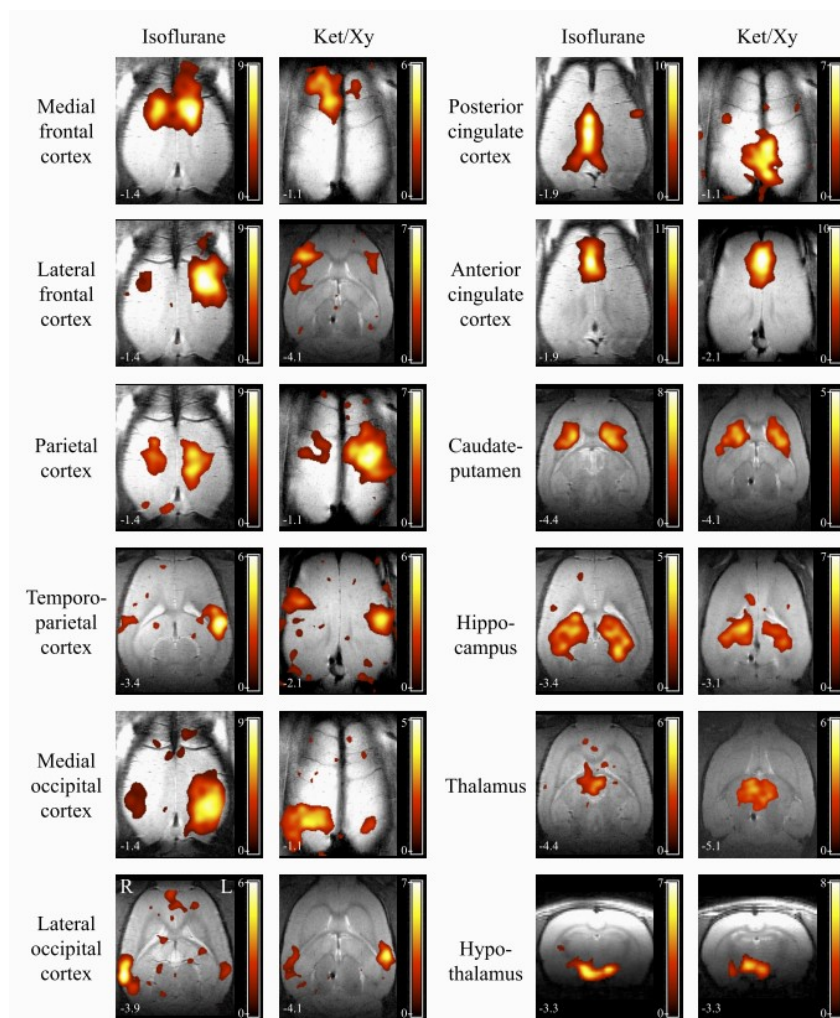
Figure 17 | Reproducible cerebral networks in rats under two types of anaesthesia. Rat networks were extracted from rsfMRI images using an ICA with 40 components. From (R. M. Hutchison et al., 2010).

Modularity algorithms have also been used to describe the rat cerebral network organization. Using partial correlations, with 36 anatomical regions D'Souza et al. found two pure cortical (frontal, somato-motor) and four mixed large scale networks (hippocampal and perihippocampal cortices, basal ganglia, thalamic nuclei and pons, Q=0.39) (D'Souza et al., 2014).

A similar organization was found in awake rats (N. Zhang et al., 2010) (Becerra et al., 2011) including a network analogous to the human DMN. The rat DMN was described in several publications (Upadhyay et al., 2011) (Lu et al., 2012). According to Lu et al., the co-activated clusters of the rat DMN are the orbital cortex, prelimbic cortex, cingulate cortex, auditory/temporal association cortex, posterior parietal cortex, retrosplenial cortex (corresponding to the posterior cingulate cortex in humans) and the hippocampus (Lu et al., 2012). As in non-human primates, rsfMRI networks have been compared to humans. Sierakowiak et al. (Sierakowiak et al., 2015) found four remarkable similarities between rat rsfMRI networks and human networks (DMN, motor, dorsal basal ganglia and ventral basal ganglia). These results are particularly interesting for the development of translational experiments to validate animal models of brain disorders. However, the DMN regions extracted from this study were different when compared to the study of Lu et al. This difficulty to identify a reproducible pattern of network organization is probably due to the multiple levels of systems and subsystems that may support distinct functions, as suggested by Hsu et al. and Smith et al. (Hsu et al., 2016) (Smith et al., 2009).

The advantage of using rats is that numerous pathological models of brain disorders have been developed. As a consequence, alterations of the rat functional connectivity or of network organization are studied in various neuropathological models such as Alzheimer's disease (Sanganahalli et al., 2013), Parkinson's disease (Westphal et al., 2017), stress (Henckens et al., 2015) and aging (Ash et al., 2016).

I.4.4. Organization and function of cerebral networks in mice

One of the first publications describing and comparing rat and mouse rsfMRI network organization highlighted the difficulties of cross-species comparison. The extracted maps remain highly dependent on the ICA components number that can skew the results (Jonckers et al., 2011). However, comparing two species with the same number of components remains potentially more accurate than using seed based-analysis. As for primates ((R. M. Hutchison et al., 2012); **Figure 16**) the localization of a seed within the same region could totally change the type of network detected. As a consequence, in order to accurately compare two equivalent networks across species, the anatomical correspondence of the seeds has to be known prior to the analysis. To our knowledge, these criteria are rarely met. The methodological strength of the study by Jonckers et al. was the use of two ICA component numbers which allowed them to evaluate the stability of the extracted maps across the two species and to identify that the components of the mouse brain are more unilateral than rats (Jonckers et al., 2011)(**Figure 18**).

	Rat		Mouse	
	15	40	15	40
motorcortex	1 component	1 component	1 component	1 component
Somatosensory cortex (SSC)	1 component	1 component	2 unilateral components (left + right) covering SSC, AC and VC	2 components (left + right)
auditory cortex (AC)	1 component	1 component	2 unilateral components (left + right) covering SSC, AC and VC	2 components (left + right)
Retrosplenial (dys)granular cortex (RC)	1 component	1 component	1 component covering RC and CC	1 component
hippocampus	1 component	1 component	1 component	2 components (dorsal + ventral)
striatum	1 component	2 components	/	/
cingulate cortex (CC)	1 component	3 components	1 component covering RC and CC	1 component
visual cortex	1 component	2 components	2 unilateral components covering SSC, AC and VC	2 components (left + right)
inferior colliculus	1 component	6 components	/	/
piriform cortex	/	1 component	1 component	1component
entorhinal cortex	/	/	entorhinal cortex 1 component (right)	4 component left medial and lateral + Right medial and lateral)

Figure 18 | Similar components are extracted in rats and mice. ICA applied to rat and mouse rsfMRI with 15 and 40 components. The components in the mouse brain seem to be more unilateral than in rats. From (Jonckers et al., 2011).

These two levels of ICA (low and high number of components) have also been studied in several studies in humans (Smith et al., 2009), and mice (F. Sforazzini et al., 2014). Sforazzini et al. explored the functional brain of mice by varying the number at a high level (20 components; **Figure 19**) and low level (5 components; **Figure 20**) (F.

Sforazzini et al., 2014). The ICA using 20 components resulted in maps encompassing several established neuro-anatomical systems of the mouse brain (**Figure 19**).
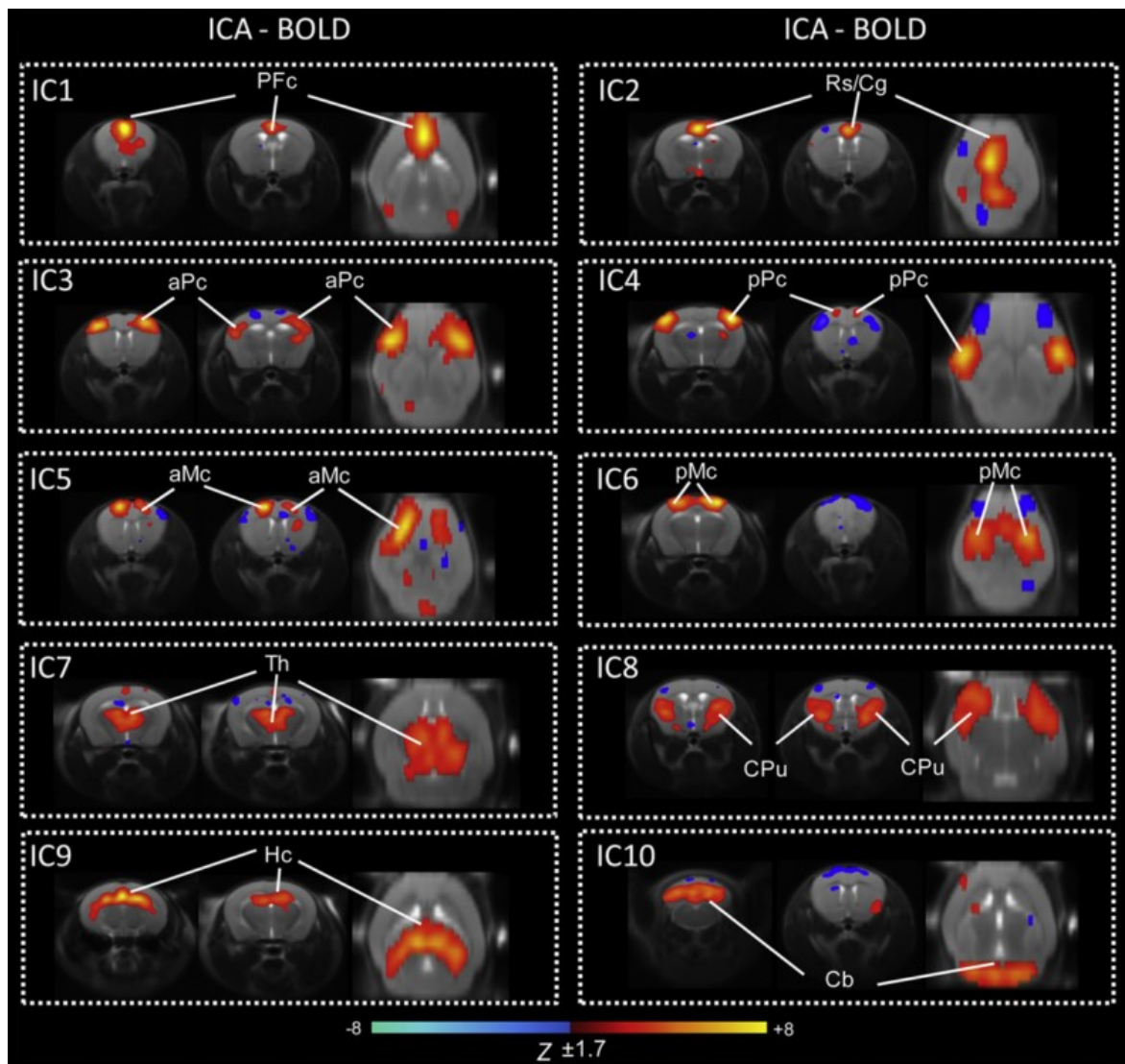
Figure 19 | Functional regions identified via ICA in the mouse brain using twenty components.

The ICA was performed on BOLD images. IC1: pre-frontal cortex, IC2, cingulate/retrosplenial cortex, IC3 and IC4, anterior and posterior parietal (somatosensory) cortex; IC5, anterior motor cortex, IC6, posterior motor cortex, IC7, thalamus, IC8, caudate putamen, IC9, dorsal hippocampus, IC10, cerebellum and brain stem. Abbreviations: aMc, anterior motor cortex; aPc, anterior parietal cortex; Cb, cerebellum; Cg, cingulate cortex; CPu, caudate-putamen; Hc, dorsal hippocampus; PFc, prefrontal cortex; pMc, posteriormotor cortex; pPc, posterior parietal cortex; Rs, retrosplenial cortex; Th, thalamus. From (F. Sforazzini et al., 2014).

Interestingly, the low level ICA applied to BOLD images (**Figure 20**; left) highlighted a putative DMN in mice that was very similar to the DMN-like network observed in the same study with a seed-based approach and CBV weighted images (**Figure 20**; right)
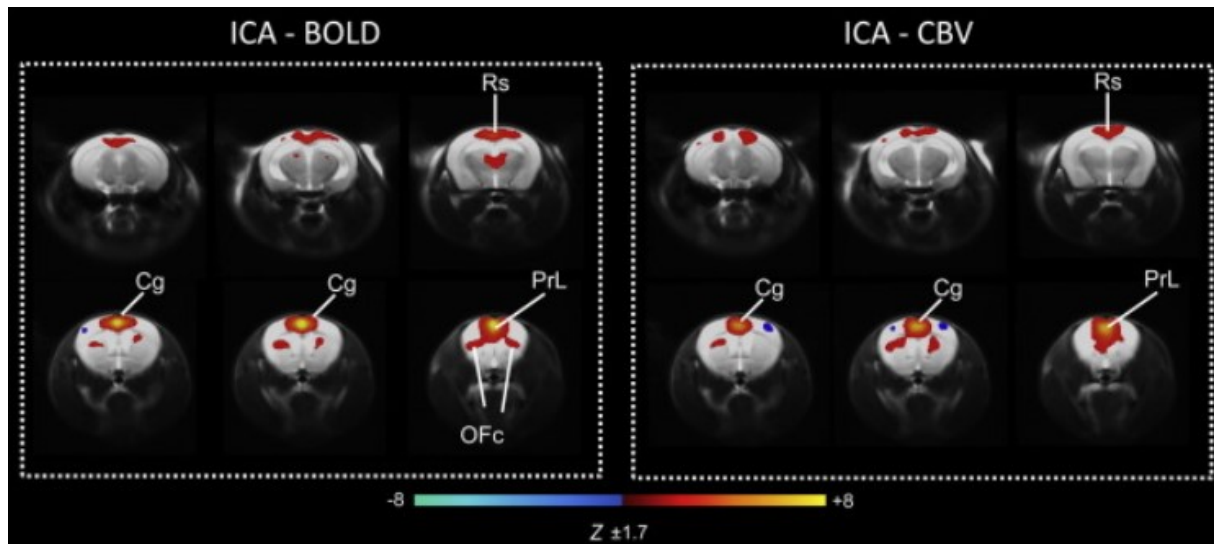
Figure 20 | DMN identified with ICA in the mouse brain using five components.

The ICA was performed on BOLD and CBV weighted images. Abbreviations: Acb, nucleus accumbens; Cg, cingulate cortex; OFc, orbitofrontal cortex; Pc, parietal cortex; Prl, prelimbic cortex; Rs, retrosplenial cortex. From (F. Sforazzini et al., 2014).

This study also observed anti-correlations between the mouse DMN and the neighboring fronto-parietal regions which is consistent with literature based on human studies. However, as in rat and non-human primates, the regions thought to be involved in the DMN are highly debated. Sforazzini et al. found that the DMN includes the nucleus accumbens, cingulate cortex, orbitofrontal cortex, parietal cortex, prelimbic cortex and the retrosplenial cortex (F. Sforazzini et al., 2014). Stafford et al. found a DMN encompassing the parietal cortex, the lateral/medial orbital cortex and the cingulate area (Stafford et al., 2014). For Zerbi et al. this network covers the caudomedial entothinal cortex, cingulate cortex area, caudate putamen, medial entorhinal cortex, medial orbital cortex, parasubiculum, prelimbic cortex, retrosplenial dysgranular and granular cortex and the thalamus (Zerbi et al., 2015).

As previously discussed for other species, these studies have clearly highlighed the difficulty in identifying reproducible cerebral networks. Morever, this difficulty is accentuated by the extremely small size of the mouse brain (around 400 mm^3). Other

techniques such as the mesoscale structural connectome (*i.e., an anterograde tracer mapping axonal projections*) provides evidence towards the existence of a DMN in mice (Stafford et al., 2014). However, not all networks have been validated using tracers. In a similar study, Grandjean et al. found that interhemispheric homotopic cortical, hippocampal and cortico-striatal networks displayed direct neuronal connections. However, interhemispheric striatum functional connectivity exhibited indirect neuronal connections. In contrast, limited functional connectivity involved in the cortico-thalamic pathways was observed when direct anatomical connection was identified (probably due to anaesthesia) (J. Grandjean, Zerbi, et al., 2017).

The small world property of the mouse brain has been added to the list of the similarities of brain organization with humans and other mammals (Mechling et al., 2014). As in humans, the dynamic organization of intrinsic functional networks in the mouse brain was demonstrated in healthy animals and fluctuates to different degrees, depending the anaesthesia duration (J. Grandjean, Preti, et al., 2017). Moreover, the dynamic functional states of the networks were affected in animal models of chronic psychosocial stress (J. Grandjean, Preti, et al., 2017).

The study of pathological models is probably one of the major applications for the study of the mouse fMRI networks. Several studies have already proved that alterations of functional connectivity can be measured in Alzheimer's disease-like models (J. Grandjean, Schroeter, He, et al., 2014) (D. Shah et al., 2018) or in models of Huntington's disease (Q. Li et al., 2017).

I.4.5. Organization and function of cerebral networks in other mammalian species

Individually, resting-state network organization is characterized in several other mammalian species including ferrets (Zhou et al., 2016), rabbits (Schroeder et al., 2016), dogs (Kyathanahally et al., 2015) and the prairie vole (Ortiz et al., 2018). It seems that all the mammalian species studied so far, possess a brain that can be spatially organized by their spontaneous neuronal activity.

I.4.6. Comparison of the resting-state organization between mammals

I.4.6.1. Homologous resting-state organization in mammals

Throughout evolution, brain regions could have been duplicated, fused, reorganized or expanded (R. M. Hutchison et Everling, 2012). Improving the accuracy of resting-state network identification and comparison of networks between species is critical to assess their evolution during species evolution. The description of functional architecture of each species is based on a variety of acquisitions, analyses, and anaesthesia (or awake) protocols. This lack of standardization is justified by the variety of brain sizes and anatomical organizations observed within mammals. For these reasons only, a few studies have compared the connectivity between different species and with similar approaches.

To compare human and macaque resting-state networks, Mantani et al. developed a projection of the macaque brain to human space (Dante Mantini et al., 2013). Based on this technique, they described common and specific resting-state networks to each species. They suggested that **resting-state networks common to macaques and humans** concern ventral somatomotor, dorsal somatomotor, parafoveal visual, peripheral visual, early auditory, ventral attention, medial prefrontal, dorsal attention, default mode, lateral prefrontal and language regions. **Resting-state networks specific to humans** concern the left fronto-parietal, right fronto-parietal and cingulo-insular. **Resting-state networks specific to monkeys** concern the caudate/putamen. However, the caudate/putamen has been found numerous times in humans (Afifi, 2003).

The identification of similar large scale networks between species has also been carried out in a large number primate species (Wey et al., 2014). This study identified **five common networks** in the capuchin, baboon, chimpanzee, and human: visual, sensory-motor, auditory, cerebellum and DMN. This study also quantified the strength of the interhemispheric connectivity in the fronto-parietal network of these four species. They highlighted that the intra-hemispheric connectivity is much higher in humans than in non-human primates. This result was supported by a measure of the inter-hemispheric response of the fronto-parietal network during a working-memory oculomotor task which was more pronounced in macaques than in humans (Kagan et al., 2010). A strong interhemispheric functional connectivity between homologous

regions is always present in humans and primates suggesting a phylogenetically preserved mammalian characteristic (R. Matthew Hutchison et al., 2012). However, lateralized networks (*i.e.* fronto-parietal resting-state network) have only been demonstrated in humans.

According to the few studies on functional organization in mammals, humans seem to display the largest variety of functional networks. The complexity and diversity of the behaviors is probably related to this large repertoire of networks. This complexity is also reflected by the volume of the white matter fiber tracts network (Nadkarni et al., 2018). Moreover, direct evidence is in favor of a close relationship between the structural and functional organization in humans (Jessica S. Damoiseaux et Greicius, 2009), in primates (Miranda-Dominguez et al., 2014) and in mice (J. Grandjean, Zerbi, et al., 2017).

Determining the topologies, the critical regions or the network organizations that are conserved across species throughout evolution could indicate patterns that have essential, basic and/or developmental functions. Despite the lack of consensus concerning a standardized methodology in mammal fMRI, cross-species studies could provide essential clues towards understanding brain physiology.

Studies performed during this thesis

Overview and objectives

i. Develop a pipeline to register large series of images including images recorded with different protocols and species

ii. Develop a robust methodology to extract and characterise cerebral networks in the mouse lemur that can be adapted for other species

iii. Evaluate the ability of the fMRI to differentiate young and aged lemurs

iv. Evaluate a possible association between highly connected regions, local neuronal activity and an excitatory neurotransmitter

II.1. **Study 1: 3D digital atlas of mouse lemur brain: Tool development and applications**

A first objective of this thesis was to develop a 3D digital atlas of the brain of mouse lemurs. This atlas was based on the use of MR images from a cohort of 34 mouse lemurs. A common question for the study of cohorts of animals by MRI is the ability to register large series of images including images recorded with different protocols. In clinical research, image coregistration to a standardize space is commonly performed by using tools such has SPM (K.J. Friston et al., 2007), FSL (Jenkinson et al., 2012), AFNI (Cox, 1996), ANTS (Tustison et al., 2014). Most of the fMRI studies in animals use in-house pipelines that are often adapted from humans. Here, we developed a Python package called sammba-MRI designed to generate specific cerebral templates and to coregister various images to this template. My work was dedicated to test the co-registration robustness of sammba-mri on various anatomical MR images, on various species and to develop its use. Here, we present the tools that we developed to create and use the atlas and then present the article that has been published in NeuroImage.

II.1.1. Atlas of the mouse lemur brain

The brain of the mouse lemur was first described in 1931 by Le Gros Clark (**Figure 21**) (Le Gros Clark, 1931).
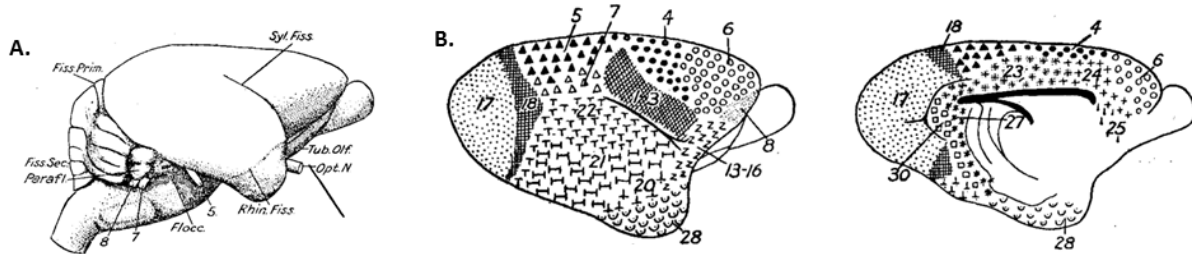
Figure 21 | The mouse lemur brain

Lateral view of the mouse lemur brain (A). Segmentation of the cortex of the mouse lemur based on its histological features (B). From (Le Gros Clark, 1931).

Le Gros Clark segmented 19 cortical structures and found that the mouse lemur brain is characterized by a marked and deep Sylvian fissure. Le Gros Clark also observed that the differentiation of cortical structures was more pronounced than in non-primate species. However, the segmentation of the temporal cortex by Le Gros Clark was disapproved by Zilles (Zilles et al., 1979). Zilles produced a detailed description and another segmentation of the mouse lemur brain based on cytoarchitectonics. More recently, the first stereotaxic atlas of the mouse lemur brain was produced by Bons (N. Bons et al., 1998). This atlas provided more detail of the different anatomical structures and specified landmarks for stereotaxic injections.

The main disadvantage of histological atlases is that they only offer two-dimensions which limits the spectrum of analysis. The method commonly used to extract a signal from 3D MRI or histology image is manual segmentation guided by an atlas paper. This method is based on drawing regions of interest upon each slice of a 3D image. It requires an expertise in biology to identify and extract relevant information. This work is also fastidious and limits the amount of data extracted as well as the number of anatomical regions segmented. It leaves a large amount of information untapped. Moreover, the manual extraction is dependent upon the operator, leading to an increase in variability of the extracted results. To overcome these disadvantages,

an automatic extraction of the signal of interest based on a 3D digital atlas can be performed. In humans, several atlases registered on standardized template spaces already exists such as MNI (Fan et al., 2016) and Talairach (Brett et al., 2002). MR images recorded during biological studies can be registered on the standardized templates, which allows to indirectly register them to an abundant repertoire of 3D MRI brain atlases already available within these spaces. Note that the diversity of the human 3D digital brain atlases is important and is dependent on which method is used to segment the brain. The manual segmentation of atlases is often based on a paper atlas and is carried out by expert on an anatomical image template. Automatic segmentations can also be performed on various 3D images (anatomical, diffusion tensor imaging (connectome), fMRI, etc.) by different algorithms. As an example, if we reviewed several cortical atlas parcellations in MNI space (downloadable at http://www.lead-dbs.org/helpsupport/knowledge-base/atlasesresources/cortical-atlas-parcellations-mni-space/), the number of structures varies from about ten to several thousand. This diversity calls for caution concerning the use of these different atlases. Two main questions before starting any study would be 1) what is the biological significance of the segmented regions? and 2) at what level of detail they are defined by?

In mammals, atlases were also created for various purposes such as the segmentation and the quantification of stained tissue originating from 2D or 3D histology (Lebenberg et al., 2011) (Vandenberghe et al., 2016). MRI digital brain atlases of primates (Balbastre et al., 2017) or rodents (Dorr et al., 2008) in standardized space (templates) can also be downloaded easily on specific websites. MRI atlases can further be used to extract any signal as well as quantify the volume of different brain regions. However, such an atlas did not exist for the mouse lemur. For this purpose, an anatomical atlas of the mouse lemur brain was created in our first publication (Nadkarni et al., 2018).

II.1.2. Overview of the developed methodology

Aligning MR images together or to a standardized space is an important step for many studies in humans or animals. This alignment is used to correct subject motion in the scanner, to compare data from longitudinal studies and data from different scanners. Also, this step is necessary to use digital atlases and to extract information of interest. The methodology developed here, is an adaptation for small mammals of different tools and algorithms commonly used to coregister human MR images. Our methodology was mainly based on AFNI algorithms (Cox, 1996).

Image coregistration is based on the geometrical alignment of different images. The purpose is to superpose two voxels that correspond to the same anatomical structure. As an example, if we considered image A(x) and the target image (template) B(x), aligning voxels is finding a geometrical transformation T[x] so that A(T[x]) ≈ B(x). Note that all the transformations are registered and saved in the image header. The different geometrical transformations or movements can be classified based on their degrees of freedom (**Figure 22**). The rigid-body is a transformation comprising of translations and rotations (6 degrees of freedom). A coregistration based only on this transformation, assumes that the source and the target images display the same volumes and shapes. The diversity of the brain volumes and shapes forces an increase in the number of degrees of freedom. **Affine is a transformation** (12 degrees of freedom) that can distort voxels (scale, skew) and realign brain images with different sizes and shapes. **Nonlinear transformation** allows voxels to move in any direction (elastic transformations). However, if important transformations have to be made for the coregistration, the use of an excessive amount of the degrees of freedom maximizes the risk of errors. The common way to fix this issue is to apply the different movement parameters from low to high degrees of freedom.
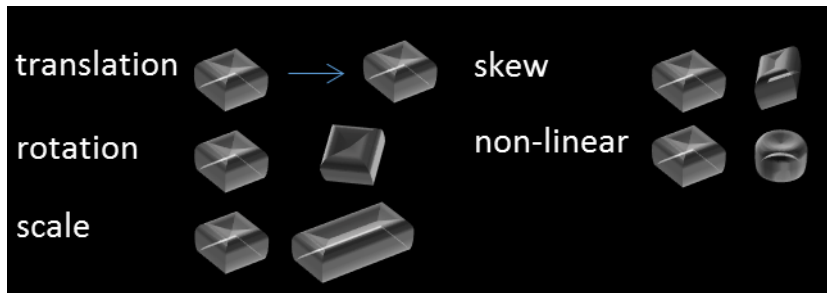
Figure 22 | Voxel movement parameters

Restraining the coregistration space in the brain (in comparison to the head) is another standard way to increase the accuracy of the coregistration. It limits the voxel movements in a more homogenous and within a smaller space that decreases the amount of coregistration errors. For this purpose, we use a mask that is an image composed of 0 (outside of the structure of interest) and 1 (inside the structure of interest). **Skull-stripping** is the technique used to extract a brain mask from a brain anatomical image (**Figure 23**). The brain is a relatively easy structure to extract with a good contrast to the surrounding tissue that can be extracted from the rodent's head using RATS (Oguz et al., 2014) or the human's head with AFNI (Cox, 1996). The skull was used to identify the brain and proxy its position in space.
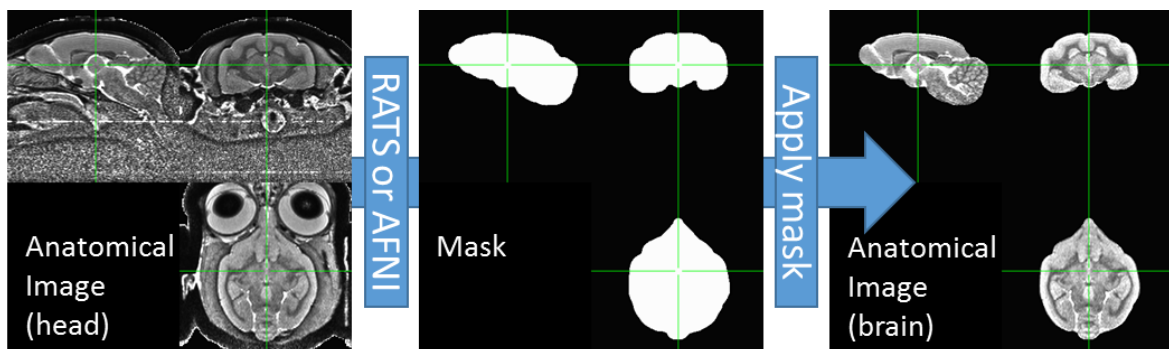
Figure 23 | Extracting the brain from anatomical images. As a first step a mask of the brain is produced using AFNI or RATS. Then, by using only the voxels within the mask, the brain can also be extracted from the first anatomical image.

Voxels of a head image that overlap the brain mask can be extracted to create an anatomical brain image. Then, the brain anatomical image can be coregistered to a brain template by applying the different movement parameters in the correct order. The

complete process to which one might create a study template will be explained in this first publication. The creation of a template based on the anatomical images of our cohort presents the advantage to increase the quality of the coregistration. This can be explained by the contrast similarity between the study template and the anatomical images. The application of the whole process was developed to be scalable to many other mammalian species.

II.1.3. Published article: Nadkarni, N. A., Bougacha, S., Garin, C., Dhenain, M., & Picq, J. L. (2019). A 3D population-based brain atlas of the mouse lemur primate with examples of applications in aging studies and comparative anatomy. Neuroimage, 185, 85-95.

A 3D population-based brain atlas of the mouse lemur primate with examples of applications in aging studies and comparative anatomy

Nachiket A. Nadkarni[1,2], Salma Bougacha[1,2,3,4], Clément Garin[1,2], Marc Dhenain[1,2], Jean-Luc Picq[1,2,5]

[1] Centre National de la Recherche Scientifique (CNRS), Université Paris-Sud, Université Paris-Saclay, UMR 9199, Neurodegenerative Diseases Laboratory, 18 Route du Panorama, F-92265 Fontenay-aux-Roses, France

[2] Commissariat à l'Énergie Atomique et aux Énergies Alternatives (CEA), Direction de la Recherche Fondamentale (DRF), Institut François Jacob, MIRCen, 18 Route du Panorama, F-92265 Fontenay-aux-Roses, France

[3] Inserm, Inserm UMR-S U1237, Normandie Univ, UNICAEN, GIP Cyceron, Caen, France

[4] Normandie University, UNICAEN, EPHE, INSERM, U1077, CHU de Caen, Neuropsychologie et Imagerie de la Mémoire Humaine, 14000 Caen, France

[5] Laboratoire de Psychopathologie et de Neuropsychologie, EA 2027, Université Paris 8, 2 Rue de la

Liberté, 93000 St Denis, France.

Corresponding author: Marc Dhenain

MIRCen, UMR CEA-CNRS 9199

18 Route du Panorama

92 265 Fontenay-aux-Roses CEDEX

France

Tel: +33 1 46 54 81 92; Fax: +33 1 46 54 84 51

email: Marc.Dhenain@cea.fr

Abstract

The gray mouse lemur (*Microcebus murinus*) is a small prosimian of growing interest for studies of primate biology and evolution, and notably as a model organism of brain aging. As brain atlases are essential tools for brain investigation, the objective of the current work was to create the first 3D digital atlas of the mouse lemur brain. For this, a template image was constructed from *in vivo* magnetic resonance imaging (MRI) data of 34 animals. This template was then manually segmented into 40 cortical, 74 subcortical and 6 cerebro-spinal fluid regions. Additionally, we generated probability maps of gray matter, white matter and CSF. The template, manual segmentation and probability maps, as well as imaging tools used to create and manipulate the template, can all be freely downloaded. The atlas was first used to automatically assess regional age-associated cerebral atrophy in a cohort of mouse lemurs previously studied by voxel based morphometry (VBM). Results based on the atlas were in good agreement with the VBM ones, showing age-associated atrophy in the same brain regions such as the insular, parietal or occipital cortices as well as the thalamus or hypothalamus. The atlas was also used as a tool for comparative neuroanatomy. To begin with, we compared measurements of brain regions in our MRI data with histology-based measures from a reference article largely used in previous comparative neuroanatomy studies. We found large discrepancies between our MRI-based data and those of the reference histology-based article. Next, regional brain volumes were compared amongst the mouse lemur and several other mammalian species where high quality volumetric MRI brain atlases were available, including rodents (mouse, rat) and primates (marmoset, macaque, and human). Unlike those based on histological atlases, measures from MRI atlases indicated similar cortical to cerebral volume indices in all primates, including in mouse lemurs, and lower values in mice. On the other hand, white matter to cerebral volume index increased from rodents to small primates (mouse lemurs and marmosets) to macaque, reaching their highest values in humans.

Graphical abstract

34 mouse lemurs → template

120 structures delineated
Whole brain 3D atlas

Examples of applications:
Age-related atrophy

Comparative anatomy
Mouse   Mouse lemur   Macaque
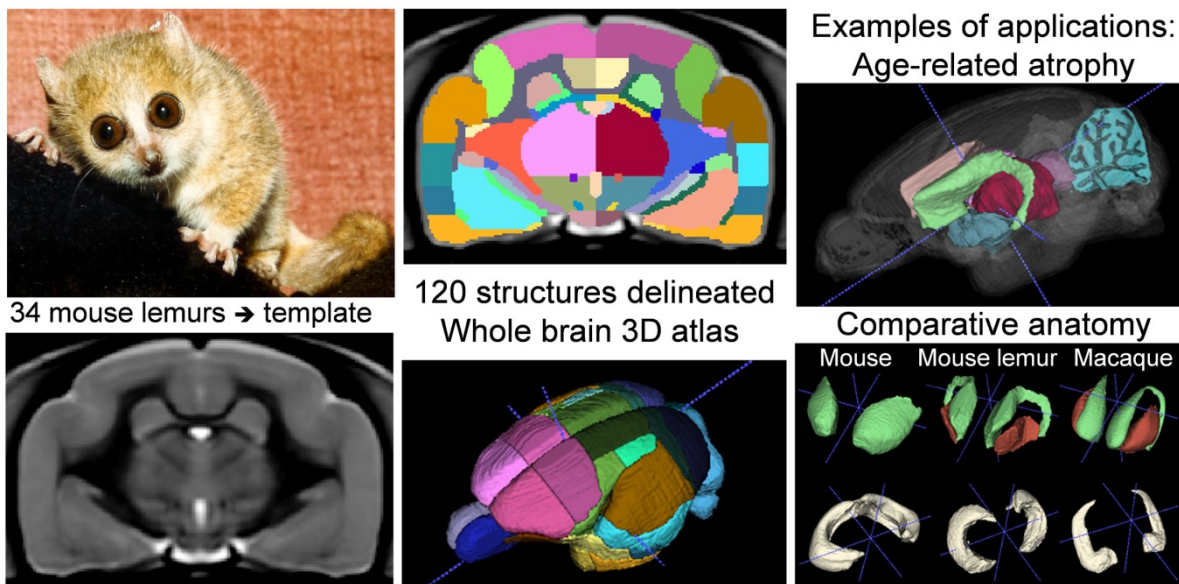
Highlights

• The mouse lemur primate is an original model for neuroscience studies and comparative anatomy.

• We present an anatomical brain template, constructed from *in vivo* MRI scans of 34 mouse lemurs.

• We created the first high resolution 3D atlas of the mouse lemur brain by delineating 120 regions encompassing each voxel of the template.

• The template, code developed to create and manipulate the template as well as segmentation maps are freely available.

• The atlas was used to characterize age-related atrophy and to compare the mouse lemur brain with brains from other mammals.

Keywords

Atlas, Cerebral atrophy, Comparative anatomy, MRI, Mouse lemur, Template.

1. Introduction

The gray mouse lemur (*Microcebus murinus*) is one of the smallest non-human primates (NHPs). Its small size (typical length 12cm, 60-120g weight) and rapid maturity (puberty at 6-8 months) bring rodent-like practicality to primate experimentation. As a result, the mouse lemur is used as an NHP model organism for primate and human biology (Ezran et al., 2017). It has a life span of approximately 12 years, which is short for a primate, and displays age-associated cerebral atrophy that is correlated with cognitive alterations (Picq et al., 2012) as well as various neuropathological lesions (Kraska et al., 2011). As a consequence, it is used as a model of aging and age-related diseases in the brain (Languille et al., 2012). In particular it has been used to evaluate how cerebral aging is modulated by various biological factors or diseases, such as chronic caloric restriction (Pifferi et al., 2018) or diabetes (Djelti et al., 2016).

Mouse lemurs can also be used to shed light on primate brain evolution (Montgomery et al., 2010). Surprisingly, most studies of this (Barton and Harvey, 2000; Finlay and Darlington, 1995) rely on the analysis of the same set of volumetric measurements made on a large variety of mammalian species by a single research group using perfused brains processed by histology (Stephan et al., 1981). Because of the tediousness of the evaluation of brain region volumes by histology, the experiments were not reproduced by other research groups, leaving scientists with a single lone source of data to provide reference measures.

Given the importance of the mouse lemur for biomedical research and as a key species for studying primate brain evolution, it is critical to have a 3D digital brain atlas and associated template (standard image reflecting the population's brain anatomy) for this species. However, today, reference atlases available to study mouse lemurs are based on histological sections (Le Gros Clark, 1931; Bons et al., 1998). Such atlases suffer from distortions caused by histological processing and do not cover the whole brain. Also, they are very unsuited to use with non-invasive imaging data from live individuals. A first MRI-based description of the mouse lemur brain was developed in the 1990s, but it is mainly a partial annotation of MR images of one *post mortem* brain sample (Ghosh et al., 1994). More recently, a population image based on 30 mouse lemur brains including probabilistic gray matter (GM), white matter (WM) and cerebro-spinal fluid (CSF) maps was developed, but it did not include annotated labels (Sawiak et al., 2014). Here we present the first 3D digital brain atlas and associated template of the mouse lemur. We used MR acquisitions from 34 young to middle-aged adult mouse lemurs to create the template: scans were iteratively mutually registered and meaned through linear then increasingly refined non-linear stages, a standard process that does not favor any one

individual, but rather produces an unbiased average of the population used to create it (Guimond et al., 1998; Guimond et al., 2000). The template was then segmented manually into 120 structures based on a previous histological atlas (Bons et al., 1998) and other previous characterizations of mouse lemur brain anatomy (Le Gros Clark, 1931; Zilles et al., 1979). The template was also used to create probability maps of mouse lemur GM, WM and CSF. The template, atlas and probability maps are available for download in NIfTI-1 format at https://www.nitrc.org/projects/mouselemuratlas. The code developed to create and manipulate the template has been refined into general procedures for registering small mammal brain MR images, available within a python module sammba-mri (SmAll-maMMals BrAin MRI; https://sammba-mri.github.io).

Two applications of the atlas are presented in this article. The first is an evaluation of age-related regional cerebral atrophy in a mouse lemur cohort that was previously studied by voxel based morphometry (VBM) (Sawiak et al., 2014). We show that atlas-based registration detects age-related atrophy in regions very similar to those identified by VBM. The second application is a comparative anatomy study. Initially, we highlight that reference published histological reports of brain region volumes are very different to those found with our atlas. More interestingly, using morphometric analysis and comparison of measures of the ratios between various brain regions, we show that, despite its rodent-like size, the mouse lemur's cortex/cerebrum index does not differ from those of other primates, and that major differences amongst primates concern more the WM/cerebrum indices.

2. Materials and Methods

2.1. Animals

This study was carried out in accordance with the recommendations of the European Communities Council directive (2010/63/EU). The protocol was approved by the local ethics committees CEtEA-CEA DSV IdF (authorizations 201506051 736524 VI (APAFIS#778)). 34 mouse lemurs (22 males and 12 females) were used for template creation. Age range was 15-58 months, mean ± standard deviation 36.8 ± 9.2 months, so all were young to middle-aged adults at scan time (Languille et al., 2012). All mouse lemurs were born in a laboratory breeding colony (Brunoy, France, authorization n°E91-114-1), and maintained at steady ambient temperature (24–26°C) and relative humidity (55%). Full demographic information is provided in Table 1 in (Nadkarni et al, Submitted).

2.2. MR acquisition

One T2-weighted *in vivo* MRI scan was recorded for each animal. After an overnight fast, animals were immobilized for MRI by isoflurane anaesthesia (4% induction, 1-1.5% maintenance). Breathing rate was monitored to ensure animal stability until the end of the experiment. Body temperature was maintained by an air-heating system. Images were acquired using a 7 Tesla (T) Agilent system using a four channel phased-array surface coil (Rapid Biomedical, Rimpar, Germany) actively decoupled from the transmitting birdcage probe (Rapid Biomedical, Rimpar, Germany). The sequence was a 2D T2-weighted fast spin echo with a resolution of 230x230x230 µm: TR/TE = 10000/17.4 msec, RARE factor = 4, field of view (FOV) = 29.44 × 29.44 mm with a matrix (Mtx) = 128 × 128, 128 slices, number of averages (NA) = 6, acquisition duration 32 mins.

2.3. Template creation and validation

Raw k-space slice data from the 34 mouse lemurs were zero-filled to 256 × 256 and reconstructed to 3D NIfTI-1 format using custom python code. Images were then up-sampled in the through-slice direction as well to 256 slices, thus giving a final matrix of 256^3, 115 µm isotropic resolution.

The template generation pipeline is diagrammed in Fig. 1, and has been developed into the function anats_to_common available within the sammba-mri python module (https://sammba-mri.github.io/generated/sammba.registration.anats_to_common.html#sammba.registration.anats_to_common). All steps used tools from freely available AFNI software (https://afni.nimh.nih.gov/ (Cox, 1996)), except for brain extraction, which was done with RATS (Oguz et al., 2014; Yin et al., 2010). Head images were bias corrected (Fig. 1b), brain extracted (Fig. 1c), and individual brain extracted image centers were shifted to the brain center of mass (Fig. 1d). Brains were then all rigid body aligned to a digitized version of a previous histological atlas (Bons et al., 1998) (Fig. 1e) and the transform was then applied to the original heads. The aligned heads were meaned to produce a first brain template (Fig. 1f). The previous rigid body registration step was performed a second time to align the 34 centered brains to the first template leading to a template 2 (Fig. 1g). Then, the 34 centered brains were affine aligned to template 2 leading to a template 3 (Fig. 1h). Finally, four cycles of non-linear registration were executed, the first to affine template 3, the rest to templates of heads from the previous non-linear cycle, including initialization using the concatenated transforms of the previous cycles, and an adjustment after each cycle to correct for systematic biases in the non-linear transforms (Fig. 1i) leading to the final template. Note that non-linear registration used the AFNI tool

3dQwarp, which repeatedly composes incremental warps defined by Hermite cubic basis functions, first over the entire volume, then over steadily shrinking and overlapping patches, with the resulting final warp being a grid representation of a diffeomorphism between source and target images. In the non-linear cycles above, final patch size was relatively large in the first cycle and was reduced substantially with each subsequent cycle. The intermediate and final templates were all means in intensity space of transformed images.

The contrast to noise ratio (CNR) was measured in the template and in raw images by evaluating the difference between the mean intensity of GM (in the caudate nucleus, 1920 voxels, 1.45 mm^3) minus mean intensity of WM (splenium of the corpus callosum, 500 voxels, 0.38 mm^3) divided by the standard deviation of the intensities in the tympanic bulla (1280 voxels, 0.96mm^3).

Finally, adopting procedures of template validation from previous studies, landmark distance measures were used to validate the mouse lemur template (Black et al., 2001a; Black et al., 2001b; Ella and Keller, 2015; Hikishima et al., 2011; McLaren et al., 2009; Quallo et al., 2010). Landmarks were identified at the level of the middle of the anterior (AC) and posterior (PC) commissures in the template, raw images and images normalized to the mouse lemur template (Anatomist freeware; http://brainvisa.info/index_f.html). The 3D Euclidean distances (AC-PC) between each of these landmarks and the equivalent landmarks in the mouse lemur template were calculated.

Figure 1. Template generation pipeline. T2-weighted MRI scans of the brain were collected from 34 mouse lemurs. (a) Head images were bias corrected (AFNI-3dUnifize), (b) brain extracted (RATS), and (c) each individual head (and brain extracted images) center was shifted to the brain center of mass (AFNI-3dCM). (d) Brains were then all rigid body aligned to a digitized version of a previous histological template (Bons et al., 1998)(AFNI-3dAllineate) and the 6 degrees of freedom (DOF) transforms were then applied to the centered heads. (e) The aligned heads were averaged to produce a first template and similarly for the aligned brains. (f) The rigid body registration was performed a second time to align the 34 centered heads to the first created template leading to a template 2. (g) Then, the 34 centered brains were affine aligned to brain template 2 and the 12 DOF transforms were applied to the centered heads leading to template 3. (h) Finally, four cycles of non-linear registration were carried out, the first to affine template 3, then subsequently to match templates of heads from the previous cycle (AFNI-3dQwarp), including initialization by the concatenation of previous transforms, and an adjustment after each cycle to correct for systematic biases in the non-linear transforms

(AFNI-3dNwarpAdjust). These steps used a weight, created by using a mask of brain template 3 dilated by 5 voxels (AFNI-3dmask_tool).
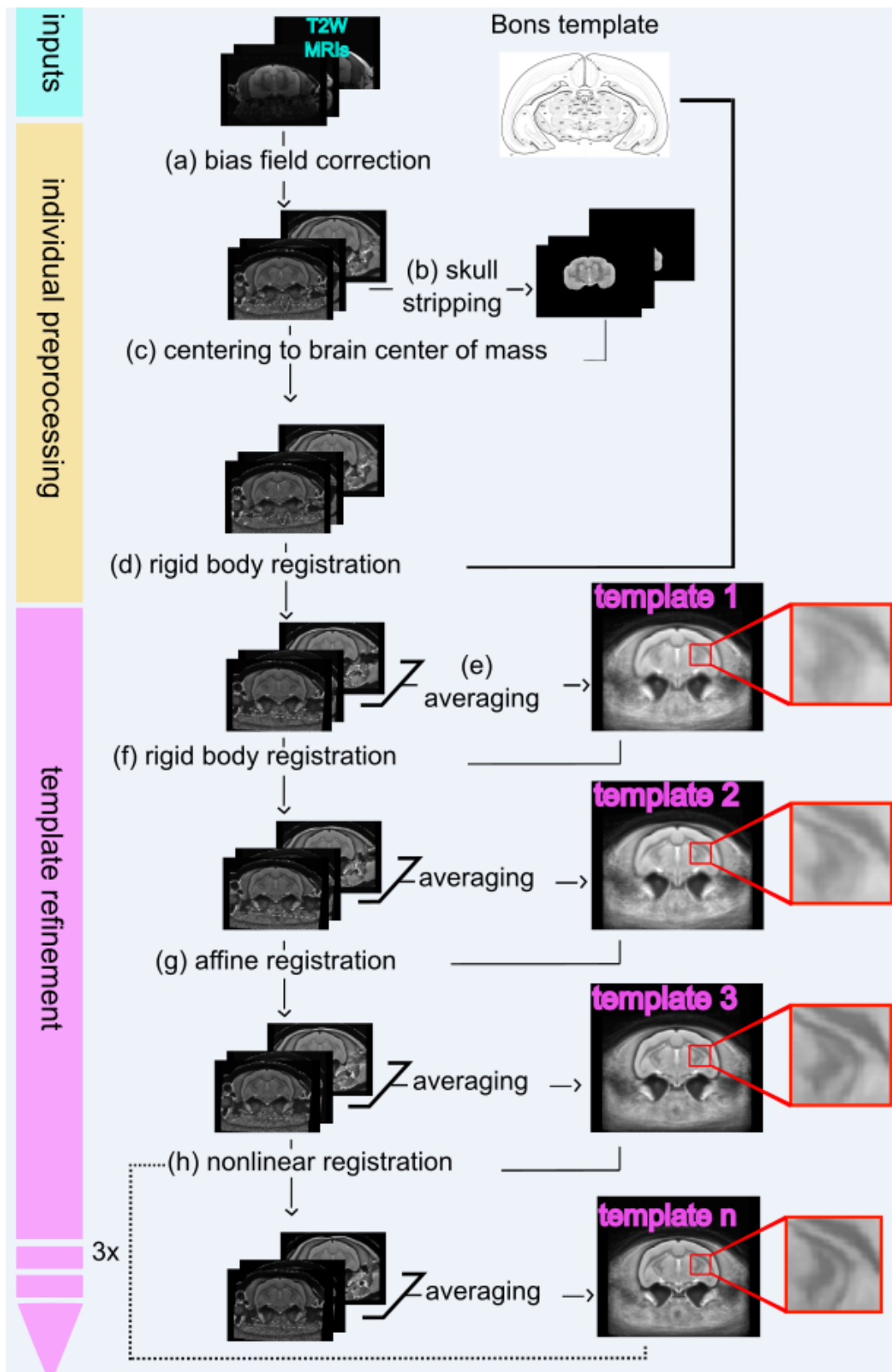
2.4. Segmentation of the MRI-based atlas

The template image was up-sampled to 91 μm isotropic resolution, then segmented manually by a single person (JLP) using ITK-SNAP software (http://www.itksnap.org; (Yushkevich et al., 2006)). Brain structures, except cortical areas, were defined according to the histological atlas of Bons (Bons et al., 1998) on the basis of the contrast in the anatomical images. Each structure was segmented slice by slice along either the coronal, axial or sagittal orientations depending on which orientation offered the best contrast for the structure. The boundaries of each structure were then checked, corrected using all three orientations and continuously updated until, after several iterations in each direction, the three-dimensional representation of the labelled structure was found to be smooth and non-jagged. Due to insufficient contrast within the cortex of the template image, the boundaries of cortical areas were approximated from the histological atlas of Le Gros Clark (Le Gros Clark, 1931), and even then only on coronal slices of the template because this histological atlas only contains some coronal sections and a rough lateral view of the mouse lemur cortex parcellation. After the delineation of the cortical areas on the coronal orientation was completed, the boundaries were carefully adjusted using the axial and sagittal orientations until achieving internal coherence among the three views. The study of the cytoarchitectonic structure of the mouse lemur cortex by Zilles et al. (Zilles et al., 1979) was used to make three small changes to the Le Gros Clark-based cortical parcellation: 1) the more rostral parts of the temporal pole were occupied by the prepyriform and periamygdalar areas instead of area 28 (entorhinal cortex), 2) areas 26 and 29 were merged to form the retrosplenial area, 3) area 22 was identified as the whole auditory cortex corresponding to areas 41, 42 and 22 of Brodmann (Brodmann, 1999 (original in 1909)). In total, 120 regions were drawn. They included 40 cortical, 74 subcortical and 6 CSF regions. Each structure was outlined bilaterally. The names of the structures were based on the NeuroName ontology (http://www.braininfo.org; (Bowden et al., 2012)). Labels of all brain regions are provided in Table 2 in (Nadkarni et al, Submitted).

Table 1. List of brain structures and volumes (mm^3, mean ± standard deviation) determined by transformation of atlas labels back to individual mouse lemurs. Animals' age range was 15-58 months. Sex, age and identifier of individual animals is given in Suppl. Table 1.

Region	Structure	All animals (n=34)		Male (n=22)		Females (n=12)	
		Left	Right	Left	Right	Left	Right
Cortical gray	cerebral cortex 1-3	18.9±1.8	18.8±1.9	19.2±1.8	19.0±1.9	18.4±1.5	18.4±2.1
	cerebral cortex 4	26±2.7	27.0±3	26.1±2.8	27.0±3.4	25.7±2.5	26.9±2.1
	cerebral cortex 5	23.8±3.6	24.9±2.9	24.5±3.5	25.3±2.9	22.3±3.7	23.9±2.8
	cerebral cortex 6	34.5±3	35.9±3	34.7±3.2	34.2±2.6	36.0±3.1	35.5±2.8
	cerebral cortex 7	5.8±1.1	5.7±1	6.1±1.1	5.9±1.1	5.2±1.1	5.3±0.8
	cerebral cortex 8	7.9±0.9	7.8±0.9	8.0±0.9	7.8±0.9	7.8±1	7.7±1
	cerebral cortex 13-16	10.9±1.2	9.9±1.1	11.0±1.2	10.1±1.2	10.9±1.1	9.7±0.8
	cerebral cortex 17	46.2±5	47.1±5.1	46.6±5.3	47.7±5	45.5±4.6	46.0±5.5
	cerebral cortex 18	17.9±2.8	18.6±3.2	18.2±2.9	18.6±3.3	17.3±2.3	18.6±3.2
	cerebral cortex 20	2.6±0.6	2.6±0.5	2.5±0.4	2.5±0.4	2.9±0.9	2.9±0.5
	cerebral cortex 21	28.8±3.4	28.1±2.9	28.5±2.8	27.9±2.6	29.5±4.5	28.5±3.5
	cerebral cortex 22 (40-42)	32.8±3.7	34.5±3.6	33.1±3.5	34.5±3.9	32.2±4.3	34.5±3.2
	cerebral cortex 23	7.8±1.1	7.7±0.9	7.7±0.7	7.6±0.9	8.0±1.7	7.8±1.1
	cerebral cortex 24	6.9±0.9	6.4±0.9	6.9±1	6.4±0.9	6.8±0.7	6.5±0.7
	cerebral cortex 25	0.8±0.3	0.8±0.2	0.8±0.3	0.8±0.2	0.7±0.2	0.8±0.2
	cerebral cortex 26-29	8.7±1.2	8.9±1.2	8.8±1.3	9.1±1.3	8.4±0.8	8.6±0.9
	cerebral cortex 27	2.1±0.5	2.0±0.4	2.1±0.4	2.0±0.4	2.2±0.6	1.9±0.4
	cerebral cortex 28	19.1±2.1	18.5±1.8	19.4±2	18.8±1.7	18.4±2.1	17.8±2
	cerebral cortex 30	2.5±0.5	2.4±0.4	2.5±0.5	2.4±0.4	2.5±0.6	2.3±0.5
	cerebral cortex prepyriform and periamygdalar	6.3±0.7	5.7±0.6	6.3±0.5	5.8±0.6	6.2±0.9	5.5±0.9
Central gray	Amygdala	12.6±1.1	13.5±1.2	12.7±1.1	13.6±1.2	12.5±1.1	13.2±1.1
	basal forebrain	3.6±0.6	3.7±0.6	3.6±0.5	3.7±0.6	3.5±0.6	3.6±0.6
	basal forebrain nucleus	0.3±0.1	0.3±0.1	0.3±0.1	0.3±0.1	0.2±0.1	0.3±0.2
	caudate nucleus	18.1±1.8	18.3±1.8	18.4±1.5	18.6±1.5	17.5±2.1	17.6±2.3
	claustrum	5.0±0.5	4.4±0.6	5.0±0.5	4.5±0.6	4.8±0.5	4.2±0.5
	globus pallidus	8.9±1.1	8.4±2.2	9.3±0.9	8.8±0.9	8.2±1.2	7.5±1.1
	habenula	0.5±0.2	0.5±0.1	0.5±0.2	0.5±0.1	0.5±0.2	0.5±0.1
	hippocampal formation	36.6±3.3	36.1±3.4	36.7±3.2	35.9±3.3	36.4±3.7	36.6±3.7
	hypothalamus	12.4±0.7	12.7±0.9	12.4±0.6	12.7±0.8	12.2±0.9	12.6±1.2
	mammillary body	0.4±0.1	0.4±0.1	0.4±0.1	0.4±0.05	0.4±0.1	0.4±0.03

	nucleus accumbens	4.0±0.7	3.9±0.6	3.9±07	3.8±0.6	4.1±0.6	4.0±0.7
	putamen	18.0±2.7	18.3±2.3	18.1±2.6	18.5±2.2	17.7±3.0	18.0±2.6
	thalamus	45.4±3.5	44.1±3.3	46.0±3.	44.6±3.4	44.1±3.1	43.0±3.1
	septum	6.3±0.6	6.2±0.6	6.3±0.6	6.2±0.6	6.3±0.6	6.2±0.6
	subthalamic nucleus	0.1±0.03	0.1±0.03	0.1±0.3	0.1±0.4	0.1±0.3	0.1±0.4
Cerebral white	Anterior commissure	4.0±1.1		4.3±0.9		3.4±1.3	
	corpus callosum	139.4±25		148.5±17.3		120.4±28.5	
	fasciculus retroflexus	0.6±0.2	0.5±0.1	0.6±0.1	0.6±0.1	0.5±0.2	0.5±0.1
	fornix	4.6±0.5	4.8±0.5	4.7±0.5	4.9±0.5	4.5±0.5	4.7±0.6
	internal capsule	12.7±2.5	12.6±2.4	13.6±1.5	13.2±1.6	11.0±3.2	11.2±3.1
	mamillo-thalamic tract	0.4±0.2	0.4±0.1	0.4±0.1	0.5±0.1	0.3±0.2	0.4±0.1
	optic chiasm	2.1±0.3		2.1±0.3		2.2±0.3	
	optic tract	4.2±0.6	4.3±0.5	4.3±0.5	4.4±0.6	3.9±0.5	4.1±0.6
	stria medullaris of the thalamus	0.9±0.1	1.1±0.2	1.0±0.1	1.1±0.2	0.9±0.2	1.0±0.1
	stria terminalis	1.8±0.2	1.7±0.2	1.8±0.2	1.8±0.2	1.7±0.2	1.7±0.2
Olfactory	olfactory bulb	28.2±2.5	28.3±2.8	28.6±2.3	29±2.7	27.3±2.7	26.9±2.6
	olfactory tract	2.6±0.4	2.7±0.3	2.7±0.4	2.7±0.3	2.5±0.4	2.6±0.3
	olfactory tubercle	2.9±0.4	3.1±0.4	2.9±0.4	3.0±0.4	2.8±0.4	3.1±0.3
Cerebellum	arbor vitae of cerebellum	33.8±5.1	34.1±5.4	34.8±4.5	35.1±4.5	31.6±5.8	32.0±6.7
	cerebellum	68.1±6.3	70.3±6.5	68.1±7.1	70.4±7.2	68.0±4.7	70.2±5.1
CSF and ventricles	CSF (peri-brain)	327.6±16.4		330.8±13.9		320.8±19.7	
	lateral ventricle	12±1.3	11.8±1.1	12.1±1.4	11.6±1.1	11.8±1.1	12.0±1.0
	third ventricle	9.4±1.7		9.5±1.6		9.2±2.0	
	cerebral aqueduct	2.3±0.4		2.3±0.4		2.3±0.5	
	fourth ventricle	2.9±0.6		2.9±0.6		3.0±0.7	
Brain stem	central gray of the midbrain	8.4±1.0		8.6±1.1		8.0±0.8	
	cerebral peduncle	3.0±0.6	3.2±0.6	3.1±0.4	3.3±0.7	2.6±0.5	3.0±0.7
	substantia nigra	1.5±0.3	1.7±0.2	1.5±0.2	1.7±0.2	1.3±0.3	1.6±0.2
	superior colliculus	8.3±1.1	8.8±1	8.4±1.0	9.0±1.0	7.9±1.4	8.4±0.9
	inferior colliculus	11.6±1.2	11.4±1.1	11.8±1.1	11.5±1.0	11.3±1.4	11.1±1.3
	posterior commissure	0.4±0.1		0.4±0.1		0.3±0.1	
	commissure of the inferior colliculus	0.5±0.1		0.5±0.1		0.4±0.1	
	medulla	26.7±2.8		27.7±1.7		24.7±3.5	
	midbrain	24.0±2.3	24.6±2.3	24.1±2.3	24.9±2.3	23.9±2.2	23.8±2.2
	pons	47.5±4	49.5±3.9	48.0±3.8	49.9±3.9	46.5±4.5	48.7±4.2

2.5. Tissue probability maps

Tissue probability maps were created using SPM8 (Wellcome Trust Institute of Neurology, University College London, UK, www.fil.ion.ucl.ac.uk/spm) with the SPMMouse toolbox (http://spmmouse.org) for animal brain morphometry as previously described (Sawiak et al., 2014; Sawiak et al., 2013). Briefly, MR images from the 34 animals involved in the study were registered to a previously published SPM template of the mouse lemur brain (Sawiak et al., 2014). Affine registration adjusted the images to control for different head positions and scanner geometry as well as overall brain size. Then unified segmentation iteratively warped the data whilst correcting for signal inhomogeneity due to the receiver coil. The images of the rigidly-aligned brains of each animal were then segmented using a k-means algorithm (MacKay, 2003) with 4 segments: background, GM, WM, and CSF. These maps were then averaged across individuals separately for each tissue type to produce mean GM, WM and CSF tissue probability maps. These maps were manually edited, particularly around the edges of the brain where partial volume effects lead to mislabeling of CSF as GM or WM voxels. The templates were also masked using masks derived from the segmented atlas, to conserve only brain and CSF structures.

2.6. Evaluations and applications

2.6.1. Quality of registration to other images

Using sammba-mri (anats_to_template, https://sammba-mri.github.io/generated/sammba.registration.anats_to_template.html#sammba.registration.anats_to_template), our MRI atlas was non-linearly registered to different MR images, including *in vivo* MRI recorded at different field strengths (4.7 and 11.7 T), and *ex vivo* high-resolution gadolinium-stained MRI. These images were collected from mouse lemurs unrelated to the atlas. Images at 4.7 T were recorded according to previously published protocols on a Bruker Biospec 47/30 system by using a surface coil (diameter = 30 mm) actively decoupled from the transmitting birdcage probe (Bruker GmbH) and a three-dimensional inversion-recovery fast spin-echo sequence of 234x234x234 μm nominal resolution (TR/TE = 2500/6 msec, TEw = 45 msec, TI = 200 msec, RARE factor = 16, Mtx = 128 x 128 x 128, NA = 1). MR images were zero-filled to reach an apparent resolution of 117x117x117 μm. Images at 11.7 T were recorded on a Bruker Biospec 117/16 system (Bruker, Ettlingen, Germany) using a two-dimensional multi-slice multi-echo sequence of 200x200x200 μm nominal resolution (TR/TE =

5000/5 msec, TEw = 17.5 msec, 6 echos, Mtx = 160 x 160, 75 slices, NA = 1). For each field, we present images from young non-atrophied animals (1.9 and 2.4 years at 4.7 and 11.7 T, respectively) and old atrophied animals (10.9 and 10.4 years at 4.7 and 11.7 T, respectively). *Ex vivo* gadolinium-stained MRI were recorded on a 7 T clinical magnet (Siemens, Syngo MR VB15) using a 2D gradient echo T2*-weighted sequence with a spatial resolution of 31 x 31 x 120 µm (TR/TE = 200/20.8 msec, flip angle = 80°, Mtx = 768 x 648, 144 slices, NA = 1). Animal brains came from an in-house mouse lemur brain collection. The brains were extracted and formalin-fixed for at least 6 months after the death of the animals. They were then stained by a one-week soaking in a solution of Gadolinium (Dotarem, Guerbet, France) in PBS at 2.5 mmol/l. This protocol enhances the signal- and contrast-to-noise ratios on MR images of fixed brains (Bertrand et al., 2013).

2.6.2. Evaluation of cerebral atrophy

The MRI brain atlas was then used to measure the volumes of individuals' brain structures and evaluate age-related cerebral atrophy in a cohort of 30 mouse lemurs that had previously been evaluated by voxel-based morphometry (Sawiak et al., 2014). Animals from this cohort had ages ranging from 1.9 to 11.3 years old (7 "young" animals (2.2 ± 0.2 years), 11 "middle-aged" (4.8 ± 1.0 years) and 12 "old" (8.3 ± 1.7 years) animals). Compared to those used for atlas creation, images for these animals were recorded by MRI at a different field strength (4.7 T) with a 3D inversion-recovery fast spin-echo sequence using the same parameters as described in the previous section though without zero-filling (Dhenain et al., 2003; Kraska et al., 2011).

A study template representative of the 30 animals was created by registering individuals' images using the same procedure described earlier for template creation. The study template was then non-linearly registered to the earlier-created mouse lemur template. The mouse lemur atlas was then transformed to each individual's original image by applying the concatenated inverted study-template-to-mouse-lemur-template and animal-to-study template transforms. CSF accumulations and infiltrations were identified by simple thresholding and used to correct the animal-specific atlases, which were then used to measure the volumes of different brain structures. These volumes were analyzed by linear regression in R (function lm, https://www.R-project.org) using the following model:

$$V_{ij} = \beta_0 + \beta_{1j}\, age_i + \beta_{2j}\, IV_i + \varepsilon_{ij}$$

where the dependent variable V_{ij} is the estimated volume (in mm^3) of region j for animal i, the independent variables being age_i the age (in years) and IV_i the intracranial volume (total volume of the individually-transformed mouse lemur atlas, which marks brain plus surrounding CSF, so total intracranial volume, in mm^3) of animal i, and ε_{ij} is the error term.

2.6.3. Comparative anatomy

Cerebral anatomy in the mouse lemur was compared to that of other mammals using available downloadable 3D digital MRI-based brain atlases of the mouse (Dorr et al., 2008), rat (Papp et al., 2014), marmoset (Woodward et al., 2018), macaque (Reveley et al., 2017), and compared to human data from MRI-based morphometric analysis (Filipek et al., 1994). The volumes of the hippocampal formation, striatum (caudate nucleus + putamen), cortex and cerebral WM (see list of structures in Table 1) were measured and expressed as a proportion of total cerebrum (cortical GM + central GM + cerebral WM, see Suppl. Table 2).

3. Results

3.1. Mouse lemur template and probability maps

An MRI template of mouse lemur brains was generated from 34 animals aged 15-60 months old scanned at 7 T using a T2-weighted sequence with a final isotropic resolution of 115 µm (Fig. 2A, C, E, Fig 3A). The orientation of the template roughly corresponded to that of the reference Bons atlas (Bons et al., 1998). The image grid mid-plane coincided with the anatomical midsagittal plane, and the image grid horizontal plane passed through the centers of the AC and PC, corresponding to a standard anatomical coordinate system similar to Talairach space (Talairach and Tournoux, 1988).

This template was used to create tissue probability maps for GM, WM and CSF (See Fig. 2 in Nadkarni et al, Submitted). The template and tissue probability maps are available from https://www.nitrc.org/projects/mouselemuratlas. Contrast to noise in the template reached 58 between GM and WM. The quality of the template was improved as compared to individual images that had a GM/WM CNR of 13.2±2.6 (See Fig. 2 in Nadkarni et al, Submitted). The Euclidian AC-PC distance was 4740 µm in the template and in each of the individual images registered to the template. It was 4678±163 µm in the original images, which represents a 1.3% difference between raw and template images.

The usability of an atlas for imaging studies relies on the accuracy of registration to its template. Here, we tested the performance of our MRI-based atlas on non-linear registration with imaging

data obtained from *in vivo* T2-weighted MRI at different field strengths (4.7 T (Fig. 3E, F) and 11.7 T (Fig. 3G, H)), as well as with *ex vivo* MRI recorded at 7 T (Fig 3D). Visual inspection of the registered images suggested good accuracy of registration to the template (Fig. 3A).

3.2. Mouse lemur atlas

The template was manually labelled (https://www.nitrc.org/projects/mouselemuratlas). A two-dimensional representation of the atlas in three orientations is shown in Fig. 2B, D, F and 3B; a three-dimensional representation from the superior lateral view is shown in Fig. 2G. 74 subcortical structures could be identified (See Table 2 in Nadkarni et al, Submitted). 40 cortical structures were outlined by interpreting borders defined in the Le Gros Clark atlas (Le Gros Clark, 1931) with some adjustments on the basis of updates in more recent atlases (Zilles et al., 1979). The volumes of each structure and their variation across the 34 animals used for template creation, including measures of cerebral asymmetry and sex difference, are shown in Table 1.

3.3. Application to evaluating regional atrophy from atlas-based defined regions

We assessed atrophied brain regions in a cohort of 30 mouse lemurs aged from 1.9 to 11.3 years old that had previously been evaluated with other methods such as voxel-based analysis (Sawiak et al., 2014). Regions presenting with a significant atrophy are presented in Fig. 4 and Table 2. Nearly all of the changes were symmetric with both sides of the brain affected. Most cortical regions displayed some atrophy with age, with the most prominent including the insular (areas 13-16, Fig. 4C), frontal (area 6), parietal (areas 5 (Fig. 4D) and 7), occipital (areas 17, 18), inferior temporal (areas 21, 28) and cingulate cortices (areas 23, 24, 25) (Table 2). With the exception of the visual cortex, the primary motor and sensory cortices were spared. Subcortical regions such as the thalamus (Fig. 4E), hypothalamus, caudate nucleus, and central gray of the midbrain were also particularly affected by aging. Interestingly, with some minor exceptions, the regions that were reported atrophied here are the same as those declared atrophied in a previous article focusing on this cohort (Table 2, (Sawiak et al., 2014)). These data confirm that in mouse lemurs 1) the cortex as a whole is more vulnerable to age-related atrophy than subcortical regions, 2) the magnitude of age-related cortical shrinkage varies greatly among cortical regions, 3) atrophy of association cortices is prominent whereas motor and primary sensory (except the visual area) cortices are relatively spared, 4) multimodal association cortices such as areas 13-16 and the cingulate cortex -which are viewed as equivalent of prefrontal regions subserving executive functions (Le Gros Clark, 1931)- are also especially vulnerable to aging.

Figure 2. Labeling of the mouse lemur atlas. Brain structure delineations are shown in coronal, sagittal and axial views (B, D, F) together with corresponding template images (A, C, E). Panel G displays a three-dimensional representation of the atlas from a superior lateral view. Scale bars equal 1 cm. For clarity, the label marking surrounding CSF is not displayed.
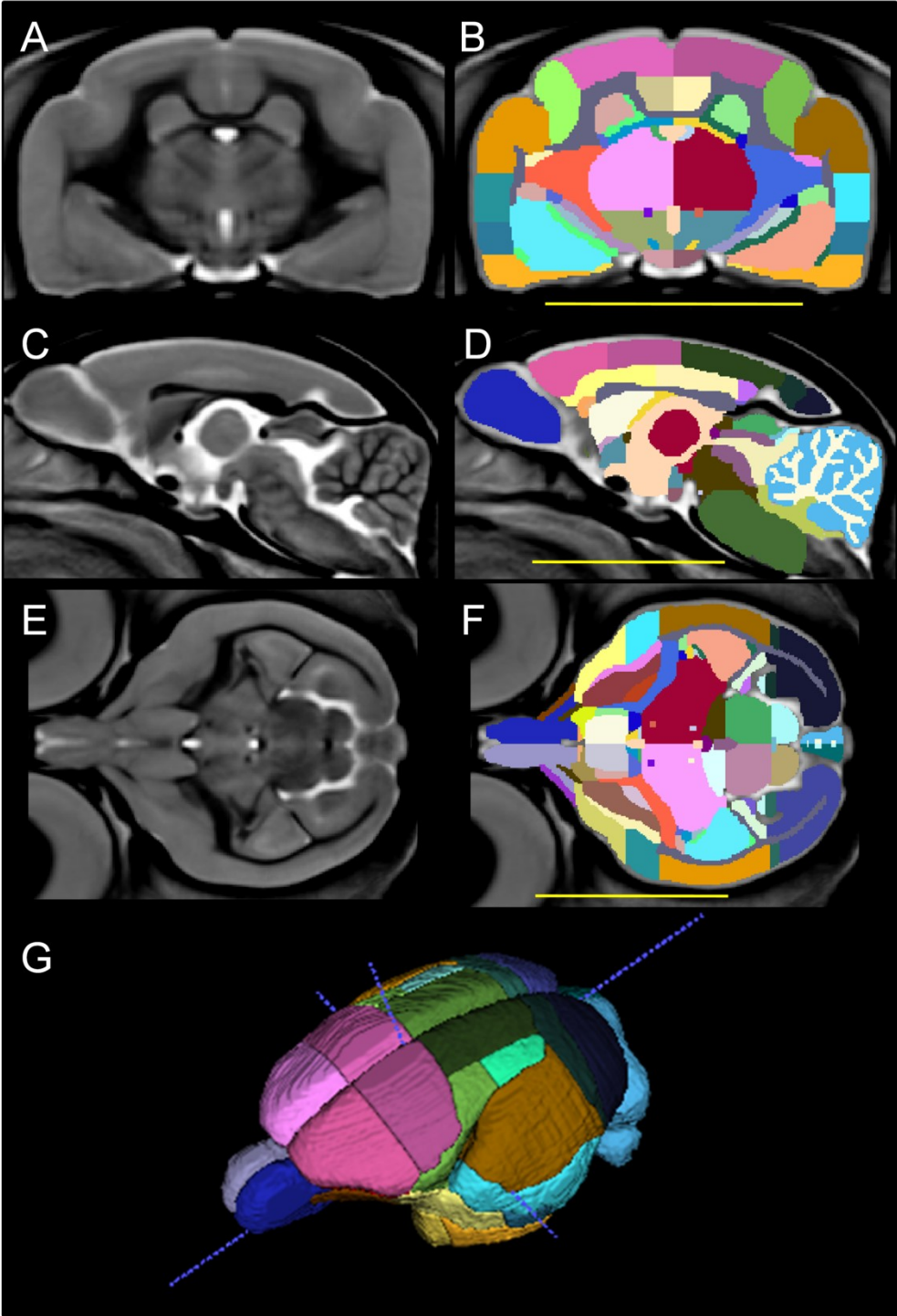
Figure 3. Registration of various *in vivo* and *ex vivo* MR images to the mouse lemur template. A-B. Coronal section of the mouse lemur MRI template (level of the anterior commissure, A) and associated section in the atlas (B). C displays an MR image from one of the 34 animals used to create this template. D displays 7 T gradient echo T2*-weighted, gadolinium stained images from an *ex vivo* brain registered on the template. E-F highlight 4.7 T fast-spin echo T2-weighted MR images from 1.9 year-old (E) and 10.9 year-old (F) animals, registered on the template. G-H display 11.7 T-T2-weighted multi-slice multi-echo MR images from 2.3 year-old (G) and 10.4 year-old (H) animals, registered on the template. Scale bar: 5 mm.
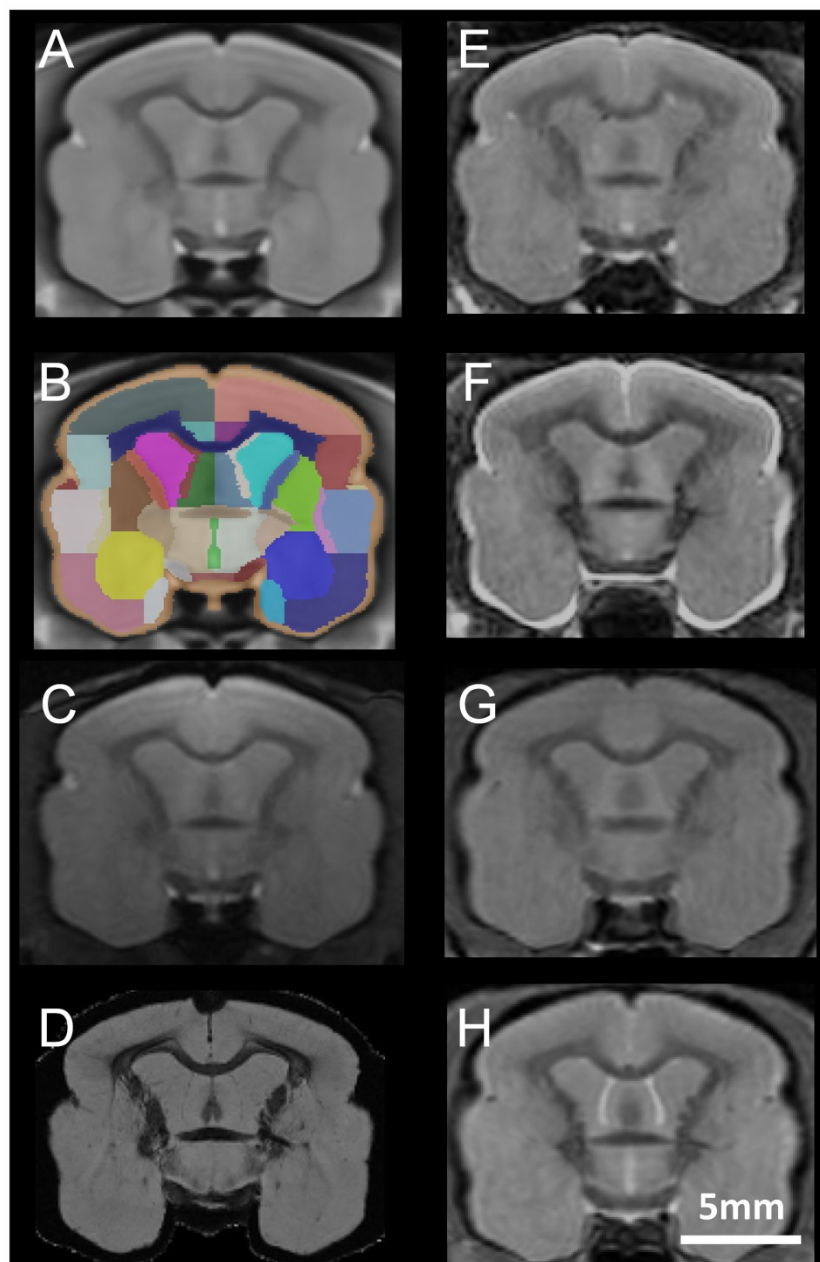
Figure 4. Age-related evolution of cerebral atrophy in various brain regions. (A). Dorsal (left), ventral (middle) and lateral (right) views of the cortex showing regions presenting with a significant age-related atrophy (colored labels) and spared cortical areas (white). (B) Dorsal (left), ventral (middle) and lateral (right) views of atrophied subcortical brain structures. (C-E) Age-related evolution of the volume of area 13-16 (insular cortex, C), area 5 (D) and thalamus (E). Statistical modeling was performed as described in Section 2.6.2, with numerical results given in Table 2. Annotations: ca = caudate nucleus, ce = cerebellum, g = central gray of the midbrain, h = hypothalamus, Prp-pa = prepyriform and periamygdalar area, t = thalamus.
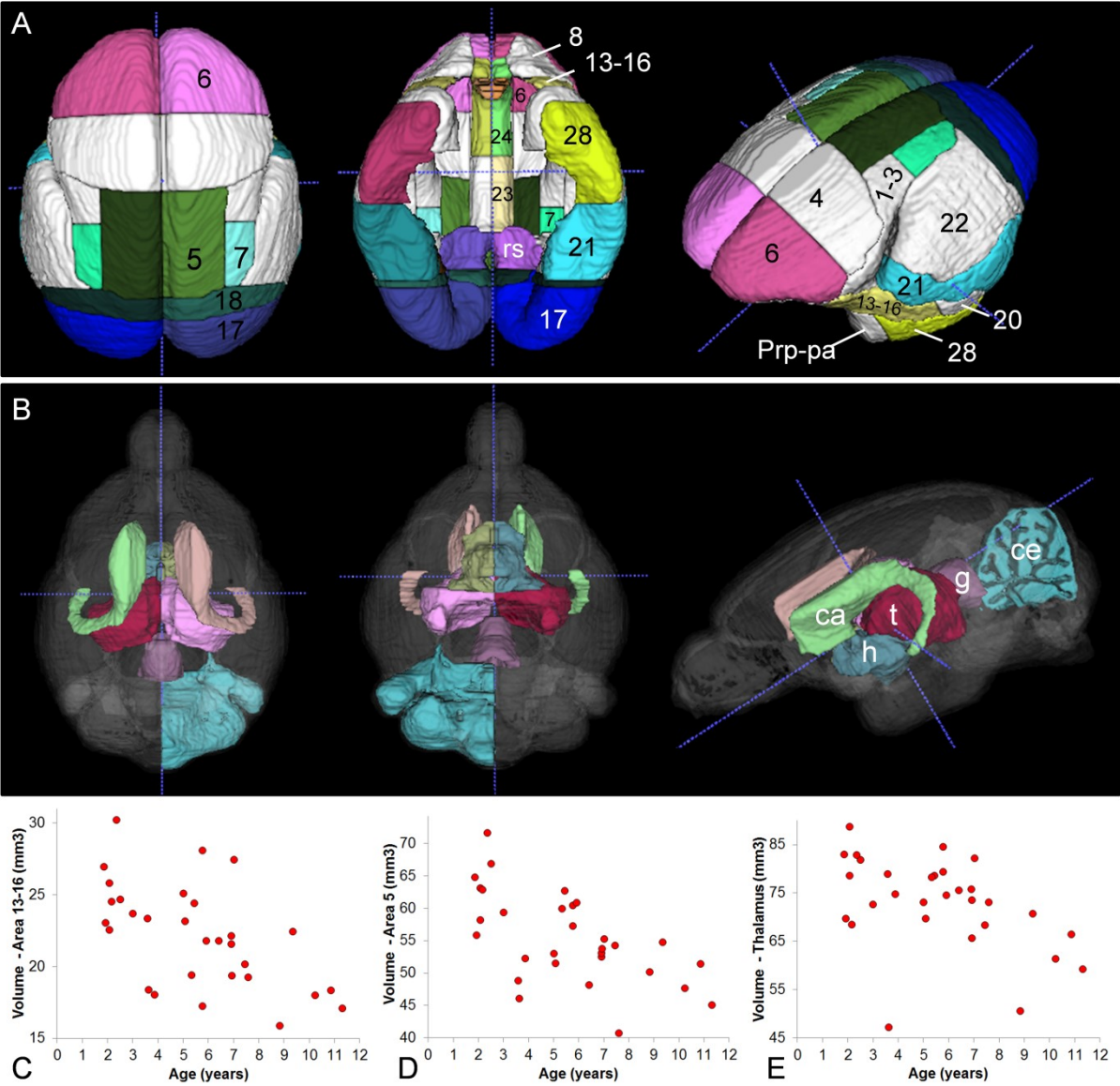
Table 2. Brain structures presenting with age-related atrophy. Analysis was carried out as detailed in Section 2.6.2. Slope is the co-efficient estimated for the parameter age (β_{1j} effectively in mm³ per year) and p-value is its associated p-value (p-value for the hypothesis test H_o: $\beta_{1j} = 0$ versus H1: $\beta_{1j} \neq 0$, reflecting the significance of the regression coefficient associated to the age). NS: $p > 0.05$. 30 animals were used for this study Animals' age range was 1.9 to 11.3 years old.

name of structure	slope	p-value	Structures detected as atrophied by VBM analysis in (Sawiak et al., 2014)
Insular cortex (13-16)	-1.01	0.000039	+
Frontal cortex			
Area 6	-1.36	0.0019	+
Parietal cortex			
Area 5	-2.22	0.00000027	+
Area 7	-0.70	0.000000016	+
Occipital cortex			
Area 17	-3.55	0.00000370	+
Area 18	-0.69	0.011	+
Retrosplenial cortex	-0.63	0.000013	+
Cingulate cortex			
Area 23 left	-0.24	0.0086	+
Area 24	-0.27	0.00058	+
Area 25	-0.10	0.00014	+
Temporal cortex			
Area 21	-1.20	0.0030	+
Area 28	-0.75	0.015	-
Area 20	NA	NS	+
Area 22	NA	NS	+
Total cortex	-14.46	0.00000030	NA
Thalamus	-2.50	0.000072	+
Hypothalamus	-0.90	0.00000001	+
Caudate	-0.75	0.0016	+
Central gray of the midbrain	-0.48	0.00000052	+
Putamen	-0.30	0.057	+
Septum right	-0.20	0.020	+
Cerebellum right	-1.53	0.035	-

3.4. Application to comparative neuroanatomy

Most studies on brain evolution rely on the analysis of the same set of volumetric measurements made on a large variety of mammalian species by a single research group using histology-based measures (Stephan et al., 1981). Our 3D MRI-based brain atlas offered the opportunity to compare the volumes of brain regions assessed in this histology-based reference article to *in vivo* MRI-based data. This revealed large discrepancies between the two methods (Suppl. Table 1). For example, the size of the hippocampus is overestimated by about 38% with histology-based measures whereas the size of the pallidum is under-estimated by about 38%. For the whole cortex, it is difficult to compare cortical prominence between the two methods since the histology-based dataset has the limitation of including the underlying WM and corpus callosum within the volume of the neocortex.

In addition to measures of volumes within a single species, digital atlases offer new opportunities to compare cerebral volumes across different species (Suppl. Table 2). As a proof of principle, we found that, in our population of adult mouse lemurs, the cortex contributes 54% of cerebral volume (Fig. 5). This value is close to that given by Filipek and al. for the human brain (Filipek et al., 1994). By using freely downloadable 3D MRI-based brain atlases of the mouse (Dorr et al., 2008), rat (Papp et al., 2014), marmoset (Woodward et al., 2018), and macaque (Reveley et al., 2017), it can be determined that the cortex is around 56±3% of cerebral volume in the four primate species as in the rat but only 51% in the mouse (Fig. 5, Suppl. Table 2). Fig. 5 also shows that overall, the mouse lemur brain is very close to that of the marmoset in terms of relative volumes of brain components and that primate brains differ from those of rodents in the relatively smaller volumes of the hippocampus and striatum, and relatively larger volumes of WM. These trends are especially marked in the human brain, in particular the large volume of WM. In addition to measures of brain volumes, another advantage of 3D digital brain atlases is that they allow an easy visualization of the 3D shape of each brain structure. As an illustration, Fig. 6A shows that the shape of the striatum is very different between rodents and primates. Also, within the primate group, it is very similar between the mouse lemur and the marmoset. In particular it can be noted that the putamen is flat and bent in these two primate species whereas it is rounded and domed in the macaque as well as in human. Likewise, it can be seen in Fig. 6B that the hippocampus is much thinner with a dorsal part that is much less developed in the macaque than in the mouse lemur, the shape being intermediate in the marmoset.

Figure 5. Volume fractions of hippocampus, cortex, WM and striatum plotted against total cerebrum volume in mouse, rat, mouse lemur, marmoset, macaque and human.
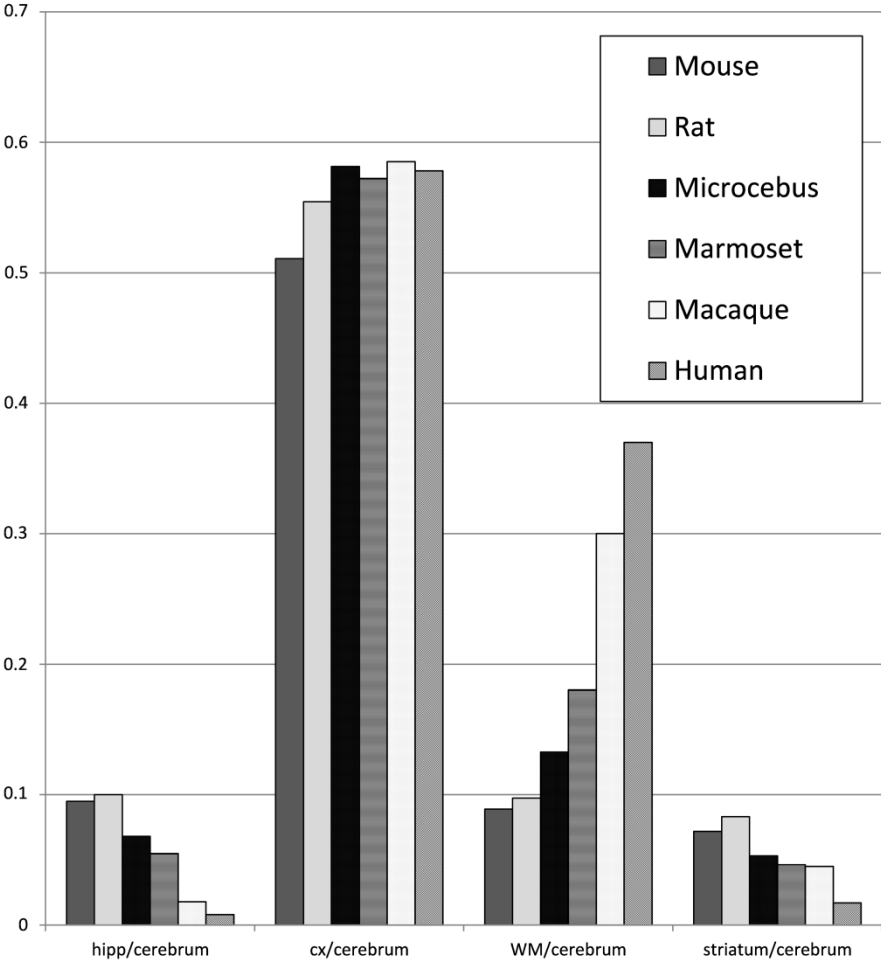
Figure 6. 3D shape comparison of the striatum and hippocampal formation in rodent and primate species. A: 3D visualizations of the striatum in mouse, rat, mouse lemur, marmoset and macaque as seen from a left anterior-superior view (green: caudate in primates, striatum in rodents, brown: putamen). B: 3D visualizations of the C-shaped hippocampal formation in mouse, rat, mouse lemur, marmoset and macaque as seen from a right anterior-superior view.
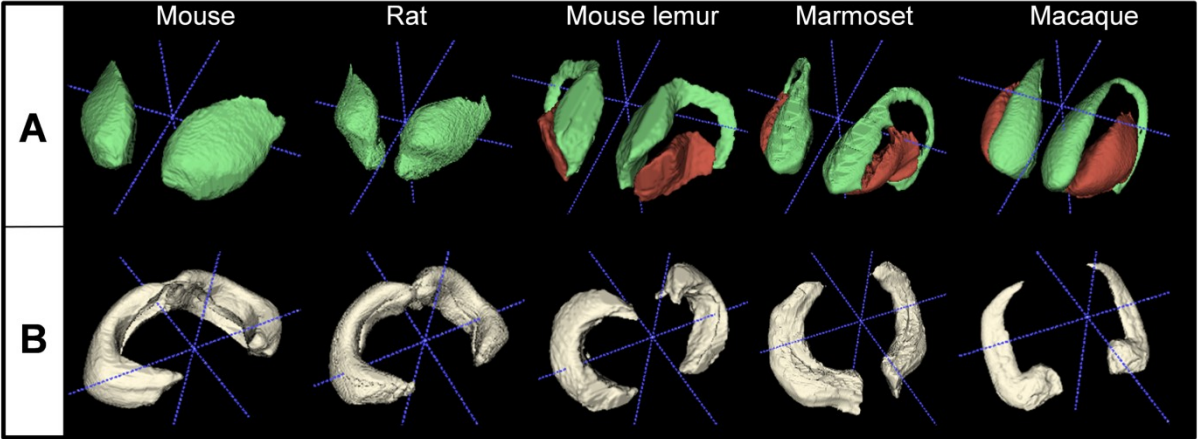
4. Discussion

Mouse lemurs are generating more and more interest as models of neurodegenerative disease and references for comparative anatomy. The use of these animals in biological research depends on the development of tools for high throughput and automatic analysis as well as for standardization. We presented here one such tool: the first 3D digital brain atlas of the mouse lemur primate, consisting of an MRI template and labels for the whole brain. We also presented two potential applications of this atlas to assess age-related cerebral atrophy and for comparative neuroanatomy.

Compared to previous traditional 2D histology-based atlases of the mouse lemur brain, our MRI-based atlas has three main advantages: 1) a high resolution MRI template is provided for accurate registration to different imaging modalities and we showed that it can be used to register images recorded in various conditions (MRI recorded on 3 different scanners, from 4.7 to 11.7 T, *in vivo* and *ex vivo*), 2) brain regions are directly delineated onto 3D MR images, 3) all the voxels from the brain were labeled, including WM areas, subcortical nuclei and cortical regions.

In other species, including primates, several atlases have been based on *ex vivo* samples. Here, we developed an atlas based on *in vivo* images that do not suffer from the deformation of *post mortem* tissue processing. We also averaged data from several animals to reduce bias linked to individual differences.

4.1. Accuracy of cerebral label attribution

After the seminal work of Brodmann (Brodmann, 1999 (original in 1909)), cytoarchitectural and other histology-based labeling techniques were the standard methods used for brain parcellation. This strategy was used to annotate cortical region atlases (Le Gros Clark, 1931; Zilles et al., 1979) and non-cortical structures (Bons et al., 1998) in mouse lemurs. For our atlas, delineation of WM and subcortical structures was relatively accurate because of the strong contrast in the brain template. Delineation of cortical regions, however, was mainly based on the transfer of structures found in histological atlases (Le Gros Clark, 1931; Zilles et al., 1979). New techniques of brain parcellation such as registration of MRI to 3D histological sections or measures of anatomical or functional connectivity (Glasser et al., 2016) will allow future refinements of atlas labels.

4.2. Application of the mouse lemur atlas to automatically annotate brain regions

Previous studies of cerebral atrophy in mouse lemurs were based on time-consuming manual segmentations (Kraska et al., 2011) or on VBM that can highlight atrophied structures, but that does not provide individual measures of the volume of atrophied structures (Sawiak et al., 2014). Here we showed that using atlas-based registration, individual scans can be annotated automatically, eliminating the time consuming step of manual tissue segmentation, and enabling rapid and objective quantification of individual subjects' brain region volumes. Using this method, a reanalysis of past data processed by VBM (Sawiak et al., 2014) produced similar results. The interest of this method is that, unlike VBM measures of atrophy, it provided individual measures of the volumes of each brain region and allowed a quantitative assessment of the atrophy. Caution should, however, be recommended after automatic annotation of brain regions, and in particular for small regions or for regions close to CSF, and it is always recommended to perform a visual assessment of the quality of the annotation.

4.3. Application of the mouse lemur atlas for comparative neuroanatomy

Comparative anatomy should be performed on reliable measures of brain structures to provide reliable interpretations. One of the obstacles when evaluating many different rare animals is to have access to anatomical data that are often difficult to record. For this reason, many studies (Barton and Harvey, 2000; Finlay and Darlington, 1995) have used measures from a histological study published in the 1980s (Stephan et al., 1981). The study was based on perfused brains, extracted out of the skull, embedded in paraffin and sectioned serially. The borders of brain structures were delineated from the stained histological sections. Calculations were performed to take into account distances between the sections and corrections applied for shrinkage resulting from fixation and embedding. Although it has been acknowledged that the different components of the brain may have sustained different degrees of shrinkage, these differences were considered negligible and not accounted for. We found substantial differences between the measures we made and the data reported in this reference article. One likely explanation is the *post mortem* artefacts associated with brain sampling and shrinkage resulting from fixation and embedding during histological preparation. An additional explanation may be differences in delineation of brain structures. It is impossible to evaluate how delineation was done in the reference article as technologies at the time did not allow digitization of large datasets. Delineation of an MRI template is expected to be less accurate than that of histological sections, but one of the advantages of MRI-based digital atlases is that the whole set of data is publicly available and can thus be corrected by other researchers.

Published datasets suggest that the ratio of the cortical to cerebral volume is highly different between humans (92%) and mouse lemurs (61%) (Stephan et al., 1981). Also, they report intermediate values for the marmoset, macaque and chimpanzee (76%, 85%, and 89%, respectively). These reference data support the theory of the corticalization of the human brain. Unexpectedly, our own analyses based on MRI-based atlases show similar cortical indices (56±3%) in four primates (mouse lemurs, marmosets, macaques and humans) while lower values were found in mice. Our results are not consistent with a corticalization theory of brain evolution. This is a good demonstration of the interest in revisiting previous comparative anatomy studies but using MRI-based atlases. Also, contrary to some previous assertions (see (Passingham, 1981) for example), we showed that mouse lemurs do not differ from other primates in the proportion of their cortex and must not be considered, in this respect, as "lower primates". Major differences between primates were found for the WM/cerebrum indices. These are bigger in macaques and humans, suggesting that WM increase, a marker for reinforced intracerebral connectivity, is a critical event for primate brain evolution, as already proposed by several authors (Schenker et al., 2005; Schoenemann et al., 2005). Hippocampus/cerebrum indices also decreased for the different primates. Our atlas of the mouse lemur is thus a key tool for future collaborative studies of primate brain evolution.

5. Conclusion

We constructed the first 3D digital atlas of the mouse lemur brain. It consists of a template constructed from *in vivo* MRI of 34 animals and labelled maps including all brain regions. It is freely distributed at https://www.nitrc.org/projects/mouselemuratlas and also includes GM, WM and CSF probability maps. The imaging tools used to create and manipulate the template are also available (https://sammba-mri.github.io). The labelled atlas itself has room for improvement. For example, future cortex parcellation could be based on the registration of our atlas to histological data. Newer brain imaging modalities such as structural or functional connectivity could also be included in future versions to improve understanding of primate brains. This atlas is an important tool for current and future automatic evaluation of pathologies in mouse lemur brains and for comparative anatomy.

6. Acknowledgements

7. References

Barton, R.A., Harvey, P.H., 2000. Mosaic evolution of brain structure in mammals. Nature 405, 1055-1058.

Bertrand, A., Pasquier, A., Petiet, A., Wiggins, C., Kraska, A., Joseph-Mathurin, N., Aujard, F., Mestre-Francés, N., Dhenain, M., 2013. Micro-MRI study of cerebral aging: Detection of hippocampal subfield reorganization, microhemorrhages, and amyloid plaques in mouse lemur primates. PlosOne 8, e56593. doi:56510.51371/journal.pone.0056593.

Black, K.J., Koller, J.M., Snyder, A.Z., Perlmutter, J.S., 2001a. Template images for nonhuman primate neuroimaging: 2. Macaque. Neuroimage 14, 744-748.

Black, K.J., Snyder, A.Z., Koller, J.M., Gado, M.H., Perlmutter, J.S., 2001b. Template images for nonhuman primate neuroimaging: 1. Baboon. Neuroimage 14, 736-743.

Bons, N., Sihol, S., Barbier, V., Mestre-Frances, N., Albe-Fessard, D., 1998. A stereotaxic atlas of the grey lesser mouse lemur brain (Microcebus murinus). Brain Res. Bull. 46, 1-173.

Bowden, D.M., Song, E., Kosheleva, J., Dubach, M.F., 2012. NeuroNames: an ontology for the BrainInfo portal to neuroscience on the web. Neuroinformatics 10, 97-114.

Brodmann, K., 1999 (original in 1909). Brodmann's 'Localisation in the cerebral cortex' {Vergleichende Lokalisationslehre der Grosshirnrinde in ihren Orinzipien dargestellt auf Grund des Zellenbaus}, Garey, Laurence J. ed. Imperial College Press, London.

Cox, R.W., 1996. AFNI: software for analysis and visualization of functional magnetic resonance neuroimages. Comput. Biomed. Res. 29, 162-173.

Dhenain, M., Chenu, E., Hisley, C.K., Aujard, F., Volk, A., 2003. Regional atrophy in the brain of lissencephalic mouse lemur primates: measurement by automatic histogram-based segmentation of MR images. Magn. Reson. Med. 50, 984-992.

Djelti, F., Dhenain, M., Terrien, J., Picq, J.L., Hardy, I., Champeval, D., Perret, M., Schenker, E., Epelbaum, J., Aujard, F., 2016. Impaired fasting blood glucose is associated to cognitive impairment and cerebral atrophy in middle-aged non-human primates. Aging (Albany NY) 9, 173-186.

Dorr, A.E., Lerch, J.P., Spring, S., Kabani, N., Henkelman, R.M., 2008. High resolution three-dimensional brain atlas using an average magnetic resonance image of 40 adult C57Bl/6J mice. Neuroimage 42, 60-69.

Ella, A., Keller, M., 2015. Construction of an MRI 3D high resolution sheep brain template. Magn. Reson. Imaging 33, 1329-1337.

Ezran, C., Karanewsky, C.J., Pendleton, J.L., Sholtz, A., Krasnow, M.R., Willick, J., Razafindrakoto, A., Zohdy, S., Albertelli, M.A., Krasnow, M.A., 2017. The mouse lemur, a genetic model organism for primate biology, behavior, and health. Genetics 206, 651-664.

Filipek, P.A., Richelme, C., Kennedy, D.N., Caviness, V.S., Jr., 1994. The young adult human brain: an MRI-based morphometric analysis. Cereb. Cortex 4, 344-360.

Finlay, B.L., Darlington, R.B., 1995. Linked regularities in the development and evolution of mammalian brains. Science 268, 1578-1584.

Ghosh, P., O'Dell, M., Narasimhan, P.T., Fraser, S.E., Jacobs, R.E., 1994. Mouse lemur microscopic MRI brain atlas. Neuroimage 1, 345-349.

Glasser, M.F., Coalson, T.S., Robinson, E.C., Hacker, C.D., Harwell, J., Yacoub, E., Ugurbil, K., Andersson, J., Beckmann, C.F., Jenkinson, M., Smith, S.M., Van Essen, D.C., 2016. A multi-modal parcellation of human cerebral cortex. Nature 536, 171-178.

Guimond, A., Meunier, J., Thirion, J.-P., 1998. Automatic computation of average brain models. Medical image computing and computer-assisted intervention. In: Wells W.M., C.A., Delp S. (eds) (Ed.), Medical Image Computing and Computer-Assisted Intervention — MICCAI 98. Springer, Berlin, Heidelberg, pp. 631-640.

Guimond, A., Meunier, J., Thirion, J.-P., 2000. Average brain models: a convergence study. Comput. Vis. Image. Underst. 77, 192-210.

Hikishima, K., Quallo, M.M., Komaki, Y., Yamada, M., Kawai, K., Momoshima, S., Okano, H.J., Sasaki, E., Tamaoki, N., Lemon, R.N., Iriki, A., Okano, H., 2011. Population-averaged standard template brain atlas for the common marmoset (Callithrix jacchus). Neuroimage 54, 2741-2749.

Kraska, A., Dorieux, O., Picq, J.-L., Petit, F., Bourrin, E., Chenu, E., Volk, A., Perret, M., Hantraye, P., Mestre-Frances, N., Aujard, F., Dhenain, M., 2011. Age associated cerebral atrophy in mouse lemur Primates. Neurobiol. Aging 32, 894–906.

Languille, S., Blanc, S., Blin, O., Canale, C.I., Dal-Pan, A., Devau, G., Dhenain, M., Dorieux, O., Epelbaum, J., Gomez, D., Hardy, I., Henry, P.Y., Irving, E.A., Marchal, J., Mestre-Frances, N., Perret, M., Picq, J.L., Pifferi, F., Rahman, A., Schenker, E.I., Terrien, J., Thery, M., Verdier, J.M., Aujard, F., 2012. The grey mouse lemur: A non-human primate model for ageing studies. Ageing Res. Rev. 11, 150-162.

Le Gros Clark, W.E., 1931. The brain of *Microcebus murinus*. Proc. Zool. Soc. London 101, 463-486.

MacKay, D.J.C., 2003. Information theory, inference and learning algorithms. Cambridge University Press, Cambridge.

McLaren, D.G., Kosmatka, K.J., Oakes, T.R., Kroenke, C.D., Kohama, S.G., Matochik, J.A., Ingram, D.K., Johnson, S.C., 2009. A population-average MRI-based atlas collection of the rhesus macaque. Neuroimage 45, 52-59.

Montgomery, S.H., Capellini, I., Barton, R.A., Mundy, N.I., 2010. Reconstructing the ups and downs of primate brain evolution: implications for adaptive hypotheses and Homo floresiensis. BMC biology 8, 9.

Nadkarni, N. A., Bougacha, S., Garin C., Dhenain M., Picq J.L. Digital templates and brain atlas of the mouse lemur primate. Data Brief. Submitted.

Oguz, I., Zhang, H., Rumple, A., Sonka, M., 2014. RATS: Rapid Automatic Tissue Segmentation in rodent brain MRI. J Neurosci Methods 221, 175-182.

Papp, E.A., Leergaard, T.B., Calabrese, E., Johnson, G.A., Bjaalie, J.G., 2014. Waxholm Space atlas of the Sprague Dawley rat brain. Neuroimage 97, 374-386.

Passingham, R.E., 1981. Primate specialization in brain and intelligence. Symposia of the Zoological Society of London 46, 361-388.

Picq, J.L., Aujard, F., Volk, A., Dhenain, M., 2012. Age-related cerebral atrophy in nonhuman primates predicts cognitive impairments. Neurobiol. Aging 33, 1096–1109.

Pifferi, F., Terrien, J., Marchal, J., Dal-Pan, A., Djelti, F., Hardy, I., Chahory, S., Cordonnier, N., Desquilbet, L., Hurion, M., Zahariev, A., Chery, I., Zizzari, P., Perret, M., Epelbaum, J., Blanc, S., Picq, J.-L., Dhenain, M., Aujard, F., 2018. Caloric restriction increases lifespan but affects brain integrity in grey mouse lemur primates. Comm. Biol. 1, 30.

Quallo, M.M., Price, C.J., Ueno, K., Asamizuya, T., Cheng, K., Lemon, R.N., Iriki, A., 2010. Creating a population-averaged standard brain template for Japanese macaques (M. fuscata). Neuroimage 52, 1328-1333.

Reveley, C., Gruslys, A., Ye, F.Q., Glen, D., Samaha, J., B, E.R., Saad, Z., A, K.S., Leopold, D.A., Saleem, K.S., 2017. Three-Dimensional Digital Template Atlas of the Macaque Brain. Cereb. Cortex 27, 4463-4477.

Sawiak, S.J., Picq, J.L., Dhenain, M., 2014. Voxel-based morphometry analyses of in vivo MRI in the aging mouse lemur primate. Front. Aging Neurosci. 6, 82.

Sawiak, S.J., Wood, N.I., Williams, G.B., Morton, A.J., Carpenter, T.A., 2013. Voxel-based morphometry with templates and validation in a mouse model of Huntington's disease. Magn. Reson. Imaging 31, 1522-1531.

Schenker, N.M., Desgouttes, A.M., Semendeferi, K., 2005. Neural connectivity and cortical substrates of cognition in hominoids. J. Hum. Evol. 49, 547-569.

Schoenemann, P.T., Sheehan, M.J., Glotzer, L.D., 2005. Prefrontal white matter volume is disproportionately larger in humans than in other primates. Nat. Neurosci. 8, 242-252.

Stephan, H., Frahm, H., Baron, G., 1981. New and revised data on volumes of brain structures in insectivores and primates. Folia Primatol. (Basel) 35, 1-29.

Talairach, J., Tournoux, P., 1988. Co-planar stereotaxic atlas of the human brain.

Woodward, A., Hashikawa, T., Maeda, M., Kaneko, T., Hikishima, K., Iriki, A., Okano, H., Yamaguchi, Y., 2018. The Brain/MINDS 3D digital marmoset brain atlas. Scientific data 5, 180009.

Yin, Y., Zhang, X., Williams, R., Wu, X., Anderson, D.D., Sonka, M., 2010. LOGISMOS-- layered optimal graph image segmentation of multiple objects and surfaces: cartilage segmentation in the knee joint. IEEE Trans. Med. Imaging 29, 2023-2037.

Yushkevich, P.A., Piven, J., Hazlett, H.C., Smith, R.G., Ho, S., Gee, J.C., Gerig, G., 2006. User-guided 3D active contour segmentation of anatomical structures: significantly improved efficiency and reliability. Neuroimage 31, 1116-1128.

Zilles, K., Rehkamper, G., Schleicher, A., 1979. A quantitative approach to cytoarchitectonics. V. The areal pattern of the cortex of *Microcebus murinus* (E. Geoffroy 1828), (Lemuridae, primates). Anat. Embryol. 157, 269-289.

Supplementary Table 1. Comparison of the volumes (mm³) of various cerebral structures according to our 3D atlas and that of the reference histological evaluation (Stephan et al., 1981).

	Current 3D atlas	Reference histological-based evaluation	Difference between histology-based measures and 3D atlas
Total brain	1668	1680	+0.7%
Telencephalon	1180	1129	-4%
Diencephalon	120	134	+12%
Striatum	72.7	85.7	+18%
Pallidum	17.3	10.7	-38%
Amygdala	26.1	36.4	+39%
Cerebellum	206.3	234.0	+13%
Septum	12.5	15.3	+21%
Hippocampus	72.7	100.0	+38%
Thalamus	89.5	78.3	-12%
Hypothalamus	25.1	29.8	+19%
Olfactory bulb	56.5	43.0	-23%

Supplementary Table 2. Total brain volume and volume fractions of hippocampus, cortex, WM and striatum against total cerebrum volume in mouse, rat, mouse lemur, marmoset, macaque and human.

	brain volume (mm³)	hippocampus/ cerebrum	cortex/ cerebrum	WM/ cerebrum	striatum/ cerebrum
Mouse	426	0.095	0.51	0.09	0.072
Rat	2314	0.100	0.55	0.10	0.083
Mouse lemur	1668	0.063	0.54	0.17	0.063
Marmoset	7678	0.055	0.57	0.18	0.046
Macaque	74324	0.018	0.59	0.30	0.045
Human	1380000	0.008	0.58	0.37	0.017

References

Stephan, H., Frahm, H., Baron, G., 1981. New and revised data on volumes of brain structures in insectivores and primates. Folia Primatol. (Basel) 35, 1-29.

II.2. Study 2: Resting state cerebral networks in mouse lemur primates: from multilevel validation to comparison with humans

Studies of cerebral connectivity have contributed to many breakthroughs in the understanding of brain function in normal as well as in pathological conditions such as Alzheimer's or Parkinson's diseases. One of the objectives of this thesis was to characterize cerebral connectivity in mouse lemurs. This study was based on evaluation of mouse lemur brains after resting-state blood-oxygen level dependent (BOLD) functional magnetic resonance imaging (fMRI). Patterns of low-frequency signal oscillations recorded with this technique are similar in brain structures functionally connected. Dedicated MR protocols were developed and sammba-mri was used to coregister fMRI images. This article was posted on bioRxiv (Garin, C. M., Nadkarni, N. A., Landeau, B., Chételat, G., Picq, J-L, Bougacha, S., & Dhenain, M. (2019). Resting state cerebral networks in mouse lemur primates: from multilevel validation to comparison with humans. I acquired the fMRI and anatomical images of the lemurs at 11.7T and coregistered them. I designed the multilevel validation methodology for the exploration and the analysis of the neuronal networks in lemurs and humans. I created, named and compared the functional atlas of these two species.

BioRxiv https://www.biorxiv.org/content/10.1101/599423v1

doi: https://doi.org/10.1101/599423) submitted to E-life.

II.2.1. Introduction to the methodology: Animal preparation for fMRI acquisition

fMRI connectivity relies on the analysis of correlations of BOLD fMRI signal evolution in different brain regions. This signal assesses neuronal activity through the evaluation of the hemodynamic response *i.e.* the ability of blood to release oxygen to active neurons at a greater rate than to inactive neurons. This measure is dependent on the relative levels of oxyhemoglobin and deoxyhemoglobin (oxygenated or deoxygenated blood) and is modulated by local blood volumes. For these reasons, controlling the physiological parameters during fMRI acquisition in animals has proven to be one of the crucial aspects to access reliable BOLD acquisition. In addition, fMRI

acquisitions are highly sensitive to the subject's movement. As a consequence, the first question that arises prior to any fMRI study in animals is: How to prepare an animal to monitor and control the physiological parameters during the image acquisition?

II.2.1.1. Controlling for motion: trade-off between awake and anaesthesia-based connectivity

In humans, several studies showed that small head motions can produce spurious but spatially structured patterns in functional connectivity (Jonathan D. Power et al., 2014). In animals as well, it is critical to control for head motion. As animals are non-compliant species, the most widely used method to control for head stability is to anesthetize them and to stabilize the head with bitebar and earbars. However, training for awake restraint techniques has been developed in rodents and primates. Briefly, these procedures are based on progressive acclimation to the scanner environment. Atraumatic devices such as head cylindrical head-holder or flat earbars can be used to fix the head (Liang et al., 2011). In primates, individualized plastic helmets have been constructed based on 3D anatomical images for a better stabilization of the head (Belcher et al., 2013). The quality of the mechanical set-up to fix the head is critical and according to Kalthoff et al. (Kalthoff et al., 2011), even with carefully fixed heads, motion remains the main source of noise in rats fMRI and it contributes to 30% of the non-neuronal signal variance (60% being attributed to residual noise). This residual motion is related to respiration that represents 5% of the total variance of rsfMRI signal (Kalthoff et al., 2011). It can be minimized by artificially-ventilating and paralyzing the animals, a process that results in excellent control of the motion artefacts (Ferrari et al., 2012), but that remains invasive and technically challenging. Cardiac motion induces low-frequency BOLD fluctuations and is another source of noise for rsfMRI signal interpretation (Murphy et al., 2013).

II.2.1.2. Anaesthetics: mechanisms of action

Because of the difficulties related to awake rsfMRI, anaesthesia remains the method of choice to control for head stability. Several options are available regarding the anaesthetic to be used. Anaesthetics have been classified into several classes

according to their targets: GABA$_A$ receptors, NMDA receptors, two-pore-domain K$^+$ channels, and other modes of actions.

GABA$_A$ receptors are the most widely used targets for anaesthetic. They are chloride channels that hyperpolarize neurons, making them less excitable and thus inhibiting the possibility of an action potential. Widely used anaesthetics such as isoflurane, propofol and barbiturates belong to GABA$_A$ receptors agonists (Franks, 2008; Garcia et al., 2010). Each drug within this category displays a subtly unique pharmacological characteristic. For example, isoflurane and sevoflurane have opposite metabolic activities on cerebral blood flow and glucose consumption in various brain regions (Lenz et al., 1998). Alpha-chloralose is a drug that is widely used in the context of BOLD-fMRI because it provides robust metabolic and hemodynamic responses to functional stimulation and is also expected to act on GABA$_A$ receptors (Garrett et Gan, 1998).

NMDA receptors are also targets commonly used. The use of antagonists for these receptors, such as ketamine, is supposed to block excitatory synaptic activity and potentially lead to anaesthesia. The latter is probably related to the fact that ketamine binds preferentially to the NMDA receptors on GABAergic interneurons. Ketamine however, leads to a "dissociative anaesthesia" during which the perception of pain is dissociated from the perception of a noxious stimuli. It also has psychotomimetic effects at low concentrations leading to auditory and visual hallucinations (Franks, 2008). Interestingly, ketamine increases regional brain activity, mainly in the anterior cingulate, the thalamus, the putamen, and the frontal cortex (Bonhomme et al., 2012; Långsjö et al., 2003).

Two-pore-domain K$^+$ channels are targeted by volatile anaesthetics (isoflurane, halothane, nitrous oxide) which have different affinities for subfamilies (TREK-1 or TASK) of these receptors (Patel et al., 1999). These channels modulate the potassium conductance that contributes to the resting membrane potential in neurons. The opening of this channels therefore facilitates a hyperpolarizing current, which reduces neuronal excitability leading to anaesthesia.

Among other targets, **alpha2 adrenergic receptor agonists** are targeted by xylazine, medetomidine, dexmedetomidine (Sinclair, 2003). The effect of these drugs is related to their action upon the receptors located in locus coeruleus. At this level they prevent the release of norepinephrine, a neurotransmitter that is necessary for arousal. The anaesthesia induced by these compounds resembles a state of non-REM sleep, i.e. the first four of the five stages of the sleep cycle (Franks, 2008). All of these drugs can be reversed by atipamezole (Sinclair, 2003).

II.2.1.3.   Impact of anaesthesia on global BOLD signal

BOLD signal can be affected by heart rate, arterial CO_2 concentration and body temperature. Different anaesthetics modulate various targets in the brain and have different impacts on peripheral receptors acting on respiration or cardiac regulation. Thus, they have different impacts on BOLD signal. For example, in mechanically ventilated animals under various anaesthetic conditions and for which arterial blood gases (PaCO2, PaO2) and pH were maintained constant, there was a higher BOLD signal in rats anesthetized with medetomidine or ketamine-xylazine in comparison to isoflurane (2%). This was explained by lower CBF, CMRO2, PtO2, vasodilatation in animals under isoflurane (Ciobanu et al., 2012). The use of mechanical ventilation has the advantage of avoiding hypercapnia (controlled with $paCO_2$ monitoring) which has an impact on fMRI reproducibility (B. Biswal et al., 1997 ; Ramos-Cabrer et al., 2005). In spontaneously breathing animals, isoflurane causes dose-dependent respiratory depression leading to hypercapnia (increased $paCO_2$) (Wren-Dail et al., 2017), that significantly decreases the BOLD signal and the variation of this signal induced by stimuli (Sicard et Duong, 2005). The hypercapnia also leads to vasodilatation and increases cerebral blood flow (Xu et al., 2011). The modulation of the cerebral blood flow could explain the decrease of the BOLD signal specificity to neuronal activity induced by stimuli (L. Uhrig et al., 2014). Interestingly, Uhrig et al. showed the different impacts of various anaesthetics on blood oxygenation in different brain regions. For example, ketamine leads to higher oxygenation in the cortex in comparison to the thalamus while the opposite occurs for propofol (Lynn Uhrig et al., 2014). This variability probably impacts the ability to detect networks connecting these regions. Thus, it seems that anaesthesia limits the ability to detect local BOLD signal variations.

However, resting-state BOLD connectivity was found not to be dependent on $paCO_2$ or paO_2 in rats (Fatima A. Nasrallah et al., 2015). Despite this result, the use of a 1:(4 or 5) oxygen and air mixture (D'Souza et al., 2014; J. Grandjean, Zerbi, et al., 2017; Kundu et al., 2014; Sierakowiak et al., 2015) in anesthetized animals was commonly observed. The use of oxygen in the mixture is probably useful to renew arterial blood gases and support normocapnic conditions.

The impact of anaesthesia on other physiological parameters, such as temperature or the auto-regulatory range of the cardiovascular parameters (contributing to 1% of the variability) can modulate the quality of the measured connectivity. These parameters must be monitored to assure normal physiological conditions during image acquisition. The body temperature can easily be controlled with a heating cradle, pad or any additional heating system.

However, few laboratories can afford all of these monitoring instruments. Controlling the temperature, the paCO2 and the movement parameters (before and after the acquisition) remains essential in assuring the animal's physiological stability and the quality of the data.

II.2.1.4. Impact of anaesthetics on neuronal network organization

What is the impact of anaesthesia on brain network evaluations? In a recent study, Barttfeld et al. compared connectivity measures in awake and anesthetized conditions (Barttfeld et al., 2015). They showed that under anaesthesia, functional connectivity patterns inherit the structure of anatomical connectivity, exhibit fewer small-world properties, and lack negative correlations. Conversely, wakefulness is characterized by the sequential exploration of a richer repertoire of functional configurations, often dissimilar to anatomical structure and exhibiting positive and negative correlations among brain regions. In another study, the same authors showed that some regions such as the posterior cingulate cortex are disconnected following anaesthesia. Some large scale networks (DMN, frontoparietal network) also show decreased functional connectivity (Hudetz, 2012). Some other studies found that the functional connectivity is preserved in lower order sensory networks, with an increase of the functional connectivity in sensori-motor networks (L. Uhrig et al., 2014).

II.2.1.5. Anaesthetics used in rodents and primate for resting-state fMRI studies

In rodents, isoflurane and medetomidine are the most commonly used anaesthetics. In addition to their different mechanisms of action (GABA$_A$ receptors agonist for isoflurane and alpha2 adrenergic receptor agonists for medetomidine), they have opposite vasoproperties (vasodilatation for isoflurane and vasoconstriction for medetomidine) which could impact neurovascular coupling differently. In rodents, isoflurane seems to preserve the interhemispheric and cortico-cortical functional connectivity but only at low doses (~1%) (Bukhari et al., 2017; J. Grandjean, Schroeter, Batata, et al., 2014). Medetomidine seems to present opposite effects such as a cortico-cortical FC disruption and a pronounced striatal FC (Bukhari et al., 2017; J. Grandjean, Schroeter, Batata, et al., 2014; Paasonen et al., 2018). The effect of isoflurane and medetomidine on the thalamo-cortical FC is still debated. Several studies suggested that a combination of isoflurane and medetomidine (med/iso) at low doses is the best compromise (Table 1, med/iso) to preserve the functional connectivity and to replicate the awake state (J. Grandjean, Schroeter, Batata, et al., 2014). Other anaesthetics used in rodents (propofol, urethane, chloralose) are presented in **Table 1**. They presented ambiguous effects on the functional connectivity and are not recommended any more.

In primates, isoflurane is the most used anaesthetic (Grayson et al., 2016; R. Matthew Hutchison et al., 2013; Miranda-Dominguez et al., 2014; J. L. Vincent et al., 2007). As in rodents, lower dose and anaesthesia duration are associated to increased ability to detect functional connectivity (**Table 2**) (Barttfeld et al., 2015; Uhrig et al., 2018). Also, one should keep in mind that direct comparison of the impact of anaesthetics on cerebral networks is difficult because anaesthesia depth also modulates networks and can lead to misinterpretation of the results.

Anesthetics	Doses	Comparison	Effects	Studies	Species
isoflurane	1%	vs the awake state	preserve interhemispheric FC	(Jonckers et al., 2014)	Mice
		vs anesthetics	cortical and thalamo-cortical FC preserved but disruption of striatal FC	(J. Grandjean, Schroeter, Batata, et al., 2014)	
			cortico-cortical FC preserved but disruption of thalamo-cortical FC	(Bukhari et al., 2017)	
	1% to 2%	increasing doses	disruption of interhemispheric FC with increasing doses	(Bukhari et al., 2018)	
	1.3%	vs the awake state	cortico-cortical and striatal FC increase	(Paasonen et al., 2018)	Rats
medetomidine	0.1 mg/kg	vs anesthetics	disruption of thalamo-cortical FC but pronounced striatal FC	(J. Grandjean, Schroeter, Batata, et al., 2014)	Mice
			thalamo-cortical FC preserved but disruption cortico-cortical FC	(Bukhari et al., 2017)	Mice
		vs the awake state	cortico-cortical FC decreased	(Paasonen et al., 2018)	Rats
med/iso	0.05 mg/kg; 0.5%	vs anesthetics	preserved FC	(J. Grandjean, Schroeter, Batata, et al., 2014)	Mice
				(Bukhari et al., 2017)	
	0.06 mg/kg; 0.5%	vs the awake state	thalamo-cortical annd intra-subcortical FC deacrease	(Paasonen et al., 2018)	Rats
urethane	2.5 g/kg	vs the awake state	disruption of interhemispheric FC	(Jonckers et al., 2014)	Mice
	1.5 g/kg	vs anesthetics	cortical and thalamo-cortical FC preserved but disruption of striatal FC	(J. Grandjean, Schroeter, Batata, et al., 2014)	
	1.25 g/kg	vs the awake state	replication of the awake state	(Paasonen et al., 2018)	Rats
α-chloralose	120 mg/kg	vs the awake state	disruption of interhemispheric FC	(Jonckers et al., 2014)	Mice
	60 mg/kg	vs the awake state	cortico-cortical FC suppression	(Paasonen et al., 2018)	Rats

Table 1 | Anaesthetic effects on the functional connectivity in rodents.
Review of five studies between 2014 and 2018.

Anesthetics	Doses	Comparison	Effects	Studies	Species
isoflurane	1% to 2.75%	increasing doses	disruption of interhemispheric FC after 1.5%	(R. M. Hutchison et al., 2014)	Macaca fascicularis
	0.89% to 1.19%	duration effect	reduction of the DMN FC with a prolonged administration	(C. X. Li et Zhang, 2018)	Macaca mulatta

Anesthetics	Doses	Comparison	Effects	Studies	Species
ketamine	20 mg/kg	vs the awake state	preservation of positive FC but average positive FC reduced	(Uhrig et al., 2018)	Macaca mulatta

Anesthetics	Doses	Comparison	Effects	Studies	Species
sevoflurane	2.2 to 4.4 vol%	vs the awake state	average positive FC reduced	(Uhrig et al., 2018)	Macaca mulatta

Table 2 | Anaesthetic effects on the functional connectivity in primates. Review of five studies between 2014 and 2018.

II.2.2. Introduction to the methodology: MRI sequences

MRI sequences are the second critical parameter to perform rsfMRI studies in animals. In a preliminary part of the study (see article Common functional networks in the mouse brain revealed by multi-centre resting-state fMRI analysis in annex), we developed rsfMRI protocols for mice. In the context of this study, we evaluated the diversity of the fMRI sequences used in this animal (**Table 3**). Most of rsfMRI studies in rodents use high field MRI (>7T), cryocoil and gradient EPI sequences. According to our study, high field and cryocoil can improve the fMRI acquisition and lead to reproducible patterns of functional connections (Joanes Grandjean et al., 2019). The observed resolution varied between 0.15 x 0.15 and 0.263 x 0.233. The averages, the repetition and echo times varied respectively between 150 and 500, 1000 and 2500, 9.2 and 20.

Mice	field / echo	readout / reception	Resolution / FOV (mm)	matrice / Averages	TR/TE	slice number / thickness	anaesthesia
(Mechling et al., 2014)	7 / gradient	EPI / cryocoil	0.15 x 0.15 / 19.2 x 12	128x80 / NI	1700/10	12 / 0.7	medetomidine
(J. Grandjean, Schroeter, Batata, et al., 2014)	9.4 / gradient	EPI / cryocoil	0.263×0.233 / 23.7 × 14	90×60 / NI	1000/10	/ NI	iso, med, propofol, urethane, iso/med
(J. Grandjean, Schroeter, He, et al., 2014)	9.4 / gradient	EPI / cryocoil	0.25x0.22 / NI	90x70 / 500	1500/9.3	12 / 0.5	isoflurane
(Stafford et al., 2014)	11.7 / gradient	EPI / surface	0.2×0.2 / 25.6×18	128×90 / 450	2000/10	30 / 0.5	isoflurane
(D. Shah et al., 2015)	9.4 / gradient	EPI / surface	0.156 × 0.312 / 20 × 20	128 × 64 / 150	2000/15	16 / 0.4	medetomidine
(Liska et al., 2015)	7 / gradient	EPI / surface	NI / 20 x 20	100 x 100 / 300	1200/15	24 / 0.5	halothane
(Zerbi et al., 2015)	9.4 / gradient	EPI / cryocoil	0.263 x 0.233 / 23.7 x 14	90 x60 / NI	1000/10	NI / NI	iso/med
(D. Shah, Deleye, et al., 2016)	9.4 / gradient	EPI / surface	0.156 x 0.312 / 20 x 20	128 x 64 / 150	2000/15	16 / 0.4	iso/med
(J. Grandjean et al., 2016)	9.4 / gradient	EPI / cryocoil	0.22 x 0.25 / 20 x 17.5	90 x 70 / 360	1000/9.2	12 / 0.5	iso/med
(Gass et al., 2016)	9.4 / gradient	EPI / cryocoil	NI / 17.28 x 11.52	93 x 64 / 400	1300/18	21 / 0.4	medetomidine
(D. Shah, Praet, et al., 2016)	9.4 / gradient	EPI / surface	0.156 × 0.312 / 20 x 20	128 x 64 / 150	2000/15	16 / 0.4	iso/med
(Mechling et al., 2016)	7 / gradient	EPI / cryocoil	0.15 x 0.15 / 19.2 × 12	128 × 80 / 200	1700/10	12 / 0.7	medetomidine
(Bergmann et al., 2016)	9.4 / spin	EPI / surface	0.15 x 0.15 / 14.4 × 9.6	128 x 128 / 200x4	2500/18.3	30 / 0.45	awake
(Takata, 2016)	7 / gradient	EPI / cryocoil	0.2 x 0.2 / 19.2 × 19.2	96 × 96 / 200	1500/20	18 / 0.5	awake and medetomidine
(Latif-Hernandez et al., 2016)	9.4 / gradient	EPI / surface	0.2 x 0.2 / 0.16 × 0.31	128 × 64 / 150	2000/15	16 / 0.4	iso/med
(Okano, 2016)	7 / gradient	EPI / cryocoil	0.2 x 0.2 / NI	NI / NI	1000/20	16 / 0.5	medetomidine
(DeSimone et al., 2017)	11.1 / NI	EPI / surface	NI / 19.2 x 19.2	64 x 64 / NI	1000/20	12 / 0.75	isoflurane
(Hubner et al., 2017)	7 / gradient	EPI / cryocoil	0.15×0.15 / 19.2×12.0	128×80 / 200	1700/10	12 / 0.7	medetomidine

Table 3 | MRI sequence parameters of mouse fMRI studies published between 2014 and 2017.

Due to the rat-like size of the mouse lemur primate brain, we then evaluated the diversity of the sequence used in rat fMRI (**Table 4**). In rats, all the studies use high field MRI (>4.7T) and surface coil. The observed resolution varied between 0.3 x 0.3 and 0.5 ×0.5. The averages, repetition and echo times varies respectively between 100 and 450, 1000 and 3000, 12 and 45.

Rats	field / echo	readout / reception	Resolution / FOV (mm)	Matrice / Averages	TR/TE	slice number / thickness	anaesthesia
(Kalthoff et al., 2011)	11.7 / gradient	EPI / surface	0.3 x 0.3 / NI	96×96 / 100	2840/ 17.5	NI / NI	medetomidine
(Sanganahalli et al., 2013)	9.4 / gradient	EPI / surface	0.4 x 0.4 / 2 x 2.56	64×64 / NI	1000/16	NI / 2	α-chloralose
(Wehrl et al., 2013)	7 / gradient	EPI / surface	0.5×0.5 / NI	64×64 / 300	2000/18	NI / 1	iso / med / chlor
(Shim et al., 2013)	9.4 / gradient	EPI / surface	NI / 25 x 25	64×64 / 600	1000/12.8	9 / 1	chlor / panc
(F. A. Nasrallah et al., 2014)	9.4 / spin	EPI / surface	NI / 25.6 × 25.6	64×64 / 300	2000/45	NI / 1	iso et med
(Liang et al., 2014)	4.7 / gradient	EPI / surface	NI / 32 × 32	64×64 / NI	1000/30	18 / 1	awake
(C. Li et al., 2014)	9.4 / gradient	EPI / surface	NI / 35 × 35	64×64 / 110	2000/19.4	10 / 1	dexdomitor + pancuronium bromide
(Song et al., 2015)	9.4 / gradient	EPI / surface	0.39x0.39 / 25.6 × 25.6	64×64 / 450	2000/17	10 / 1	dexdomitor
(Sierakowiak et al., 2015)	10.4 / gradient	EPI / surface	NI / NI	64×64 / 300	1000/16.3	11 / 1	medetomidine
(Huang et al., 2016)	7 / gradient	EPI / surface	NI / 30 × 30	64×64 / 300	1000/20	11 / 1	isoflurane
(Becerra et al., 2017)	4.7 / gradient	EPI / surface	NI / 30 × 30	64×64 / 90	3000/12	15 / 1.5	awake

Table 4 | MRI sequence parameters of rat fMRI studies published between 2011 and 2017.

II.2.3. Coregistration of EPI images

When images (anatomical and EPI) come from different subjects, standard coregistration transformations such as the different brain shapes and sizes have to be corrected. However, **EPI images** display a poor contrast complicating their coregistration. So, in addition to the standard anatomical coregistration, additional corrections have to be made.

The usual coregistration strategy is based on four major steps illustrated in **Figure 24**:

(1) EPI images from one sequence are realigned together using an **affine transformation** (translation, rotation, scale, skew). The average of these EPI images is also calculated to create an EPI reference ("refEPI"). The generated transformation parameters are further used as confounds (motion during the fMRI acquisition) in subsequent analyses. The affine transformation is followed by a **nonlinear registration** to the EPI reference.

EPI distortion is an inhomogeneity of the B0 field that produces distortion which vary according to the subject's orientation. The correction of EPI distortion is optional but highly advised, especially at high field. Moreover, susceptibility artefacts are even more severe in animals with small brain sizes (X. Hong et al., 2015).

Slice timing correction has to be performed because usually the 3D volumes of an EPI sequence are not acquired at once but within a sequence of 2D slices obtained at different times. The purpose of this correction is to interpolate all the slices by knowing the time of repetition and the slice order acquisition.

(2) EPI brain images (skull striped) of a given subject are registered using a **non-linear transformation** to their anatomical image (acquired in the same space).

(3) The anatomical brain images (skull striped) of a cohort are coregistrated to an anatomical template using an **affine transformation** followed by a **nonlinear transformation**. This step spatially normalizes the different anatomical images and generate transformations that will be used in step (4).

(4) Coregistration to the anatomical template space is performed by applying the transformation parameters from (2) and (3) to the EPI images produced by (1).
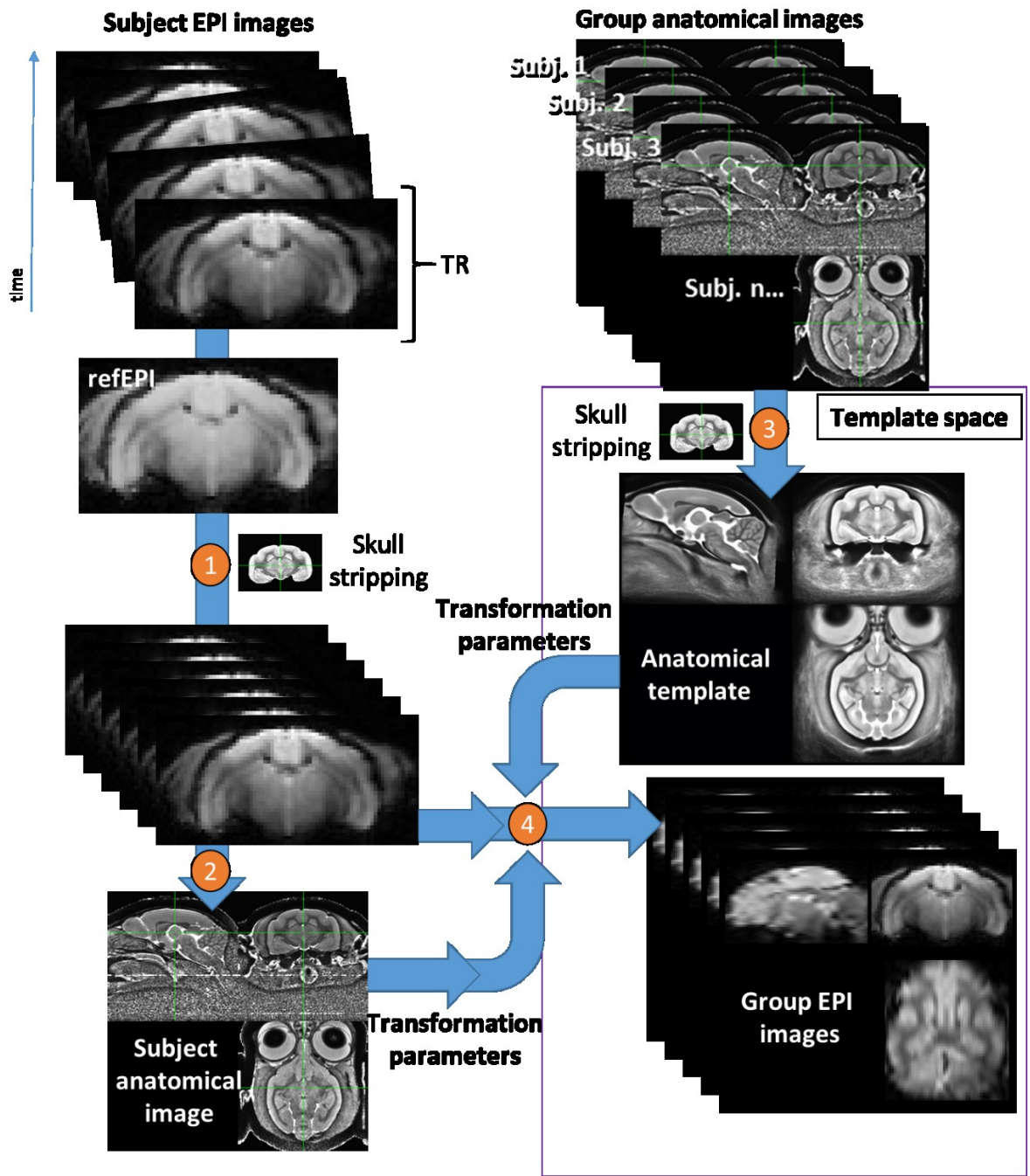
Figure 24 | Four major steps for the fMRI image coregistration to an anatomical template.
The images used to illustrate this are taken from our mouse lemur study. The different numbers correspond to the text above this figure.

II.2.4. Signal pre-treatment for resting-state fMRI

Pre-treatment of the BOLD signal is an important step towards the control of the non-neuronal signal. The selection of the confounds and the techniques used to remove them remains a major question in the rsfMRI field due its impact on the reproducibility of the results. To our knowledge, no consensus exists concerning the fMRI confounds and their clean-up. The major challenge of the BOLD pre-treatment is to remove confounds with a minimum loss of the signal of interest.

Controlling the motion during an acquisition has been exposed in a previous Chapter (II.2.1.1 Controlling for motion: trade-off between awake and anaesthesia-based connectivity). However, because motion systematically alters the BOLD signal it remains one of the main confounds to regress. The standard method is to use a regressor based on the **realignment parameters** produced by the transformation of the EPI images to EPI reference (see II.2.3. Coregistration of EPI images (1)). The 6 motion parameters are commonly regressed as well as their derivatives, squares and these of the preceding volume (K. J. Friston et al., 1994).

Signal regressions using BOLD signal from various tissues are one of the most standard ways to clean up the fMRI signal. This method used the BOLD signal extracted and averaged within specific masks such as white matter, cerebrospinal fluid (CSF) or the whole brain (global signal regression). The regression of the global signal and its derivative is very effective toward motion confounds (Jonathan D. Power et al., 2014). However, the global signal regression is very controversial these last ten years and has led to contradictory conclusions, especially concerning the appearance of anti-correlations, distance dependent effect of motion, or the removal of the signal of interest (Murphy et Fox, 2017) (Lydon-Staley et al., 2019). Using the tissue based signal (CSF, ventricles) as a regressor it is also expected that confounds will be removed such as physiological signal, scanner artefacts, and motion. The latter is more common but displayed moderate results for motion control (Ciric et al., 2017).

Time series regressions of physiological recordings are rarely performed in both human and animal fMRI studies despite that the correlation between BOLD signal and heart beat or respiration has been proven. However, cardiac and respiratory regression have demonstrated opposed results. Jo et al. found that physiological regressors account for a small amount of the variance (Jo et al., 2010) while Vogt et

al. found a significant contribution (Vogt et al., 2011). Many studies have highlighted networks that were coherent with the current literature without any physiological regression. These results suggest that the signal regression using BOLD signal from various tissues can be potentially adequate.

Censoring methods are used to reduce the impact of motion or MRI artefacts. **Despiking** identifies outlier time points based on their abnormal intensity and interpolates over them. **Scrubbing** identifies the time points to censor/delete them based on a prior threshold. These methods are only used in specific cases.

Principal component analysis is a method used to (1) isolate noisy signals extracted from CSF or white matter signal and that can be further used in the nuisance regressors or (2) identify highly noisy regions by their temporal standard deviation. **Independent component analysis**, this method also allowed the identification of artefactual structures. Note that the principal component analysis method is more effective than the tissue mean regression (Muschelli et al., 2014).

The use of **spatial smoothing** is also very controversial. Theoretically, bigger voxels provide a better signal to noise ratio but the separation of the different types of tissues is less precise. According to some studies, spatial smoothing has an important impact on graph-theoretical features (Alakorkko et al., 2017) probably due to an overestimation of functional correlation (Liu et al., 2017). However, other studies claim that spatial smoothing has a limited impact on fMRI analyses (Op de Beeck, 2010). Nevertheless, estimating the optimal spatial smoothing seems to be necessary to extract meaningful regions with independent component analysis (Z. Chen et Calhoun, 2018).

The use of **frequency filters** at rest is justified since high frequencies are related to physiological noise (J. D. Power et al., 2014). The current rsfMRI studies commonly use filters between 0.01 and 0.1 Hz at rest. However, several publications claimed that artificially induced correlations were related to bandpass filters (C. E. Davey et al., 2013).

In conclusion for this introduction to BOLD pre-treatment, different approaches can be tested to maximize the removal of general noise but there is no unique correct way to pre-process fMRI data, each one being specific to the dataset and the further analyses.

Resting state cerebral networks in mouse lemur primates: from multilevel validation to comparison with humans

Clément M. Garin [1,2], Nachiket A. Nadkarni[1,2], Brigitte Landeau[3,4], Gaël Chételat[3,4], Jean-Luc Picq[1,2,5], Salma Bougacha[1,2,3,4], Marc Dhenain[1,2,*]

[1] Centre National de la Recherche Scientifique (CNRS), Université Paris-Sud, Université Paris-Saclay UMR 9199, Neurodegenerative Diseases Laboratory, 18 Route du Panorama, F-92265 Fontenay-aux-Roses, France

[2] Commissariat à l'Energie Atomique et aux Energies Alternatives (CEA), Direction de la Recherche Fondamentale (DRF), Institut François Jacob, MIRCen, 18 Route du Panorama, F-92265 Fontenay-aux-Roses, France

[3] Inserm, Inserm UMR-S U1237, Normandie Univ, UNICAEN, GIP Cyceron, Caen, France

[4] Normandie University, UNICAEN, EPHE, INSERM, U1077, CHU de Caen, Neuropsychologie et Imagerie de la Mémoire Humaine, 14000 Caen, France

[5] Laboratoire de Psychopathologie et de Neuropsychologie, EA 2027, Université Paris 8, 2 Rue de la Liberté, 93000 St Denis, France.

Correspondance

Marc Dhenain
MIRCen, UMR CEA-CNRS 9199
18 Route du Panorama
92 265 Fontenay-aux-Roses CEDEX
France
Tel: +33 1 46 54 81 92; Fax: +33 1 46 54 84 51
email: Marc.Dhenain@cea.fr

Abstract

Measures of resting-state functional connectivity allow the description of neuronal networks in humans and provide a window on brain function in normal and pathological conditions. Animal models are critical to further address experimentally the function of brain networks and their roles in pathologies. Here we describe for the first time brain network organization in the mouse lemur (*Microcebus murinus*), a small primate attracting increased attention as a model for neuroscience. Resting-state functional MR images were recorded at 11.7 Tesla. Forty-eight functional regions were identified and used to identify networks using graph theory, dictionary learning and seed-based analyses. Comparison of results issued from these three complementary methods allowed the description of the most robust networks from mouse lemurs. Large scale networks were then identified from resting-state functional MR images of humans using the same method as for lemurs. Strong homologies were outlined between cerebral networks in mouse lemurs and humans.

Keywords

1. Introduction

Blood-oxygen level dependent (BOLD) functional magnetic resonance imaging (fMRI) is largely used to investigate brain function in response to specific tasks. In the absence of explicit tasks (*i.e.* in resting state conditions) patterns of oscillations of the fMRI signal are similar in functionally connected brain structures (Biswal et al., 1995). The detection of the synchronicity of BOLD signal in various brain regions in resting state conditions can thus be used to describe cerebral network organization. In particular this allows the characterization of *i.* local regions in which highly coordinated neuronal activity occurs and *ii.* large scale networks composed of widespread functional regions connected together (Biswal et al., 1995; Power et al., 2014).

Studies of brain networks have contributed to many breakthroughs in the understanding of brain function in normal as well as in pathological conditions such as Alzheimer's or Parkinson's diseases (Buckner et al., 2005; Gao and Wu, 2016). However, many questions remain concerning both the technique and interpretation of resting state fMRI. For example, both the role of resting state networks in cerebral function, and the biological mechanisms underlying their activity, are still partly unknown. Also, how their modulations impact behavior and cognition in pathological conditions is still debated (Mohan et al., 2016).

Using animal models is critical to further address these questions. Indeed, in animals it is possible to artificially stimulate neuronal activity to characterize biological mechanisms underlying network function (Gerits et al., 2012). Another interest of studying neuronal networks in animals is to evaluate how evolution has driven network architecture and to assess to what extent animal behaviors and ecology (Burkart et al., 2016) have impacted this architecture. Finally, animals can be used to model diseases and explore the impact of pathological processes on brain networks.

Various analysis pipelines have been proposed to investigate neuronal networks in humans and animals. For example, large scale networks were identified using data-driven methods relying on spatial map decomposition (dictionary learning (Varoquaux et al., 2011), independent component analysis (Damoiseaux et al., 2006)) or on graph theory (modularity analysis (Grayson et al., 2016)), as well as hypothesis-driven methods (seed-based analysis (Hutchison et al., 2014)). These methods are based on different algorithms and each one has its own inherent advantages and disadvantages (Lee et al., 2013). They can provide complementary approaches for identifying

networks in unexplored animals.

The mouse lemur (*Microcebus murinus*) is a primate attracting increased attention in neuroscience research. This small animal (typical length 12cm, 60-120g weight) is arboreal and nocturnal. It has a decade-long lifespan and is a model for studying cerebral aging (Sawiak et al., 2014) and various diseases such as diabetes-related encephalopathy (Djelti et al., 2016), Parkinson's disease (Mestre-Frances et al., 2018), or Alzheimer's disease (Kraska et al., 2011). It has a key position on phylogenetic trees of primates and is used to investigate primate brain evolution (Montgomery et al., 2010). Characterizing its cerebral networks is thus useful in the context of comparative biology as well as for further use of this animal to model various pathologies. Thus, the first aim of this study was to characterize neuronal networks in mouse lemurs. Our second objective was to implement a protocol that could define functional regions directly from resting-state fMR images and to compare large scale networks identified with data-driven and hypothesis-driven methods to assess the robustness of the identified networks. Our third objective was to compare resting state networks identified in lemurs with those identified in humans using the same procedure.

Resting state functional MR images were recorded from 14 mouse lemurs at 11.7 Tesla. These images enabled the identification of 48 functional regions using dictionary learning (Varoquaux et al., 2011). These regions were concatenated into a 3D functional atlas covering most of the brain and were used as nodes for whole brain network characterization. Large scale networks were identified using several methods based on graph theory, dictionary learning and seed-based analysis. They included default-mode-like, visual, fronto-temporal, somato-motor, basal ganglia and thalamic networks. These networks were then compared to large scale networks in humans. We found a strong homology between cerebral networks in mouse lemurs and humans.

2. Results

2.1 Identification of local functional regions and concatenation in a 3D functional atlas

Resting state fMR images were recorded from 14 anaesthetised (isoflurane 1.25-1.5%) mouse lemurs at 11.7 Tesla (Suppl. Table 1). Images were recorded using a gradient-echo echo planar imaging (EPI) sequence. Each animal was scanned twice with an interval of 6 months.

Organisation of whole brain networks can be modelled using graph theory. During this modelling, whole brain networks are defined as a set of nodes (basic elements of the system) and edges (allowing relationships between nodes). The identification of nodes can be based on the use of anatomical atlases (Ghahremani et al., 2016) or on the use of study-specific functional atlases that identify local functional regions (Ma et al., 2018).

Here, we identified local functional regions by performing a dictionary learning based on a large number of sparse components (SCs). This method extracts maps of cerebral networks from fMRI data and relies on sparsity-based decomposition of the signal. Multi-animal dictionary learning analyses of resting state fMR images were performed in mouse lemurs using 35 components (Fig. 1). Each component was manually classified using anatomical (Bons et al., 1998; Nadkarni et al., 2018) and Brodmann atlases (Brodmann, 1999 (original in 1909); Le Gros Clark, 1931). First, brain regions were classified based on their locations within the frontal, parietal, temporal and occipital lobes as well as subcortical and midbrain regions. The 35 components were used to create a 3D functional atlas of the brain (Fig. 2). Some single components were associated to bilateral structures as shown, for example, for the precentral cortex in Fig. 1. These bilateral regions were classified as two different regions (*i.e.* one in each hemisphere). Thus, 48 local functional regions (27 cortical, 21 subcortical) could be extracted from the 35 component dictionary analysis (Table 1). They can be downloaded from https://www.nitrc.org/projects/fmri_mouselemur/.
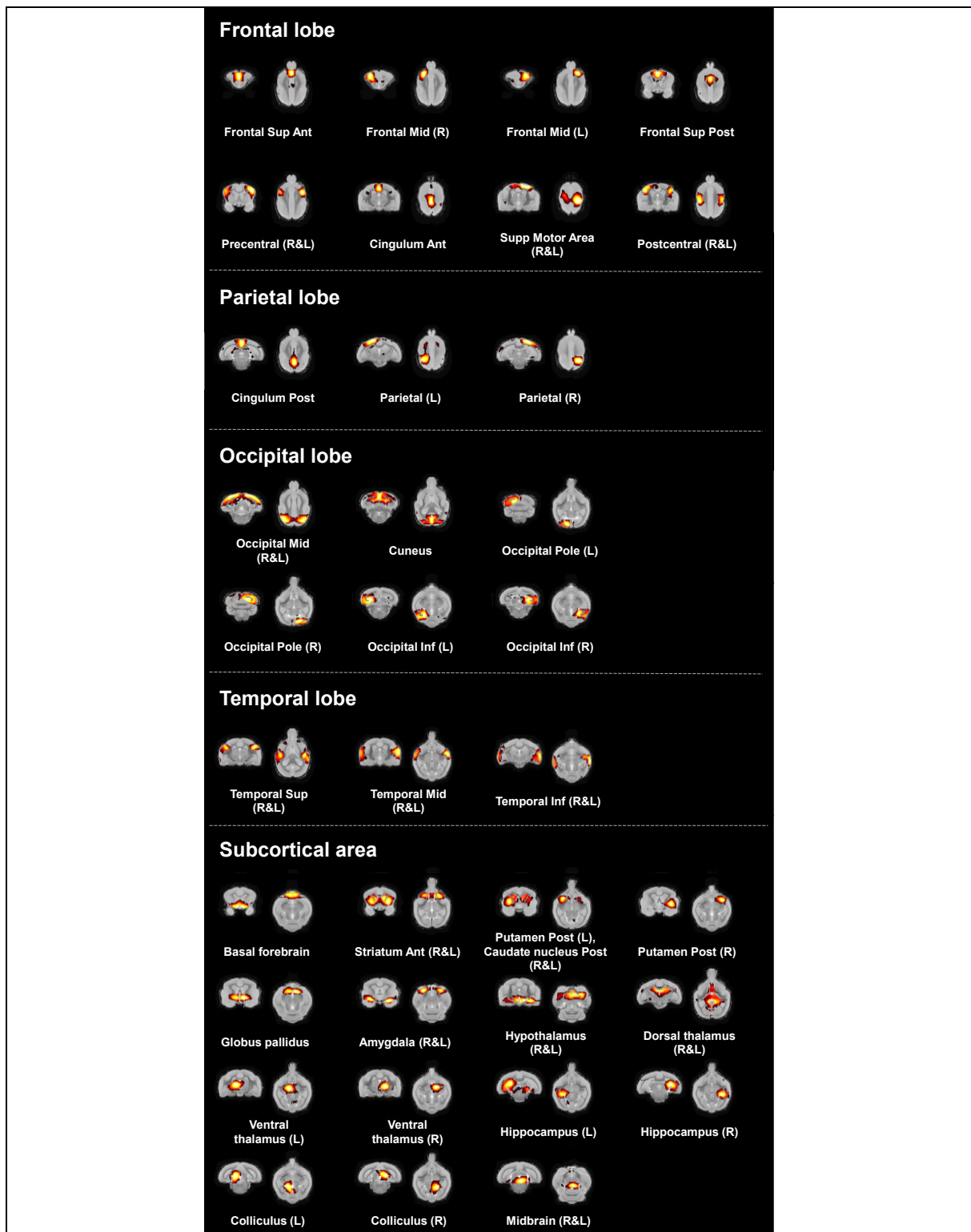
Figure 1. Regions of functional activity identified in mouse lemurs.

Regions of functional activity were identified following dictionary learning analyses of resting state fMR images using 35 components. They are shown on coronal and axial anatomical templates with an automatic slice selection based on the center of mass of each component. All components were organized within five anatomical areas: frontal, parietal, occipital, temporal, and subcortical regions.
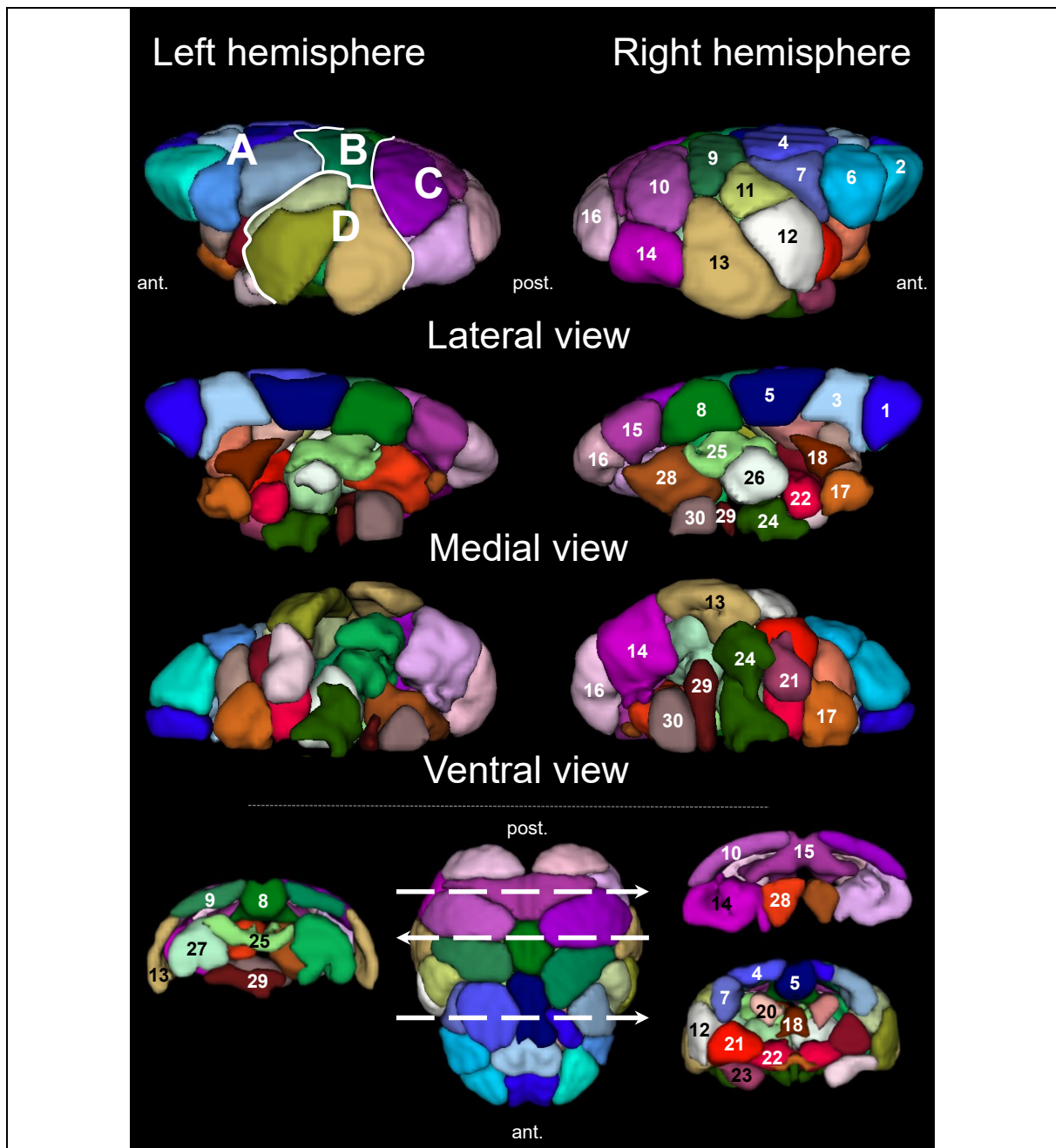
Figure 2. Mouse lemur 3D functional atlas based on dictionary learning.
Forty eight local functional regions were identified following dictionary learning analyses of resting state fMR images using 35 components. Brain regions were classified based on their locations within the frontal (A), parietal (B), occipital (C), and temporal (D) lobes. We display three different views and three slices extracted from the functional atlas. 1. Frontal Superior Anterior, 2. Frontal Middle, 3. Frontal Superior Posterior, 4. Supplementary Motor Area, 5. Cingulum Anterior, 6. Precentral, 7. Postcentral, 8. Cingulum Posterior, 9. Parietal, 10. Occipital Middle, 11. Temporal Superior, 12. Temporal Middle, 13. Temporal Inferior, 14. Occipital Inferior, 15. Cuneus, 16. Occipital Pole, 17. Basal forebrain, 18. Septal nuclei, 19. Striatum Anterior, 20. Caudate nucleus Posterior, 21. Putamen Posterior, 22. Globus pallidus, 23. Amygdala, 24. Hypothalamus, 25. Dorsal thalamus, 26. Ventral thalamus, 27. Hippocampus, 28. Colliculus, 29. Pons, 30. Midbrain.

	Label name	Area	Function
Frontal lobe	Frontal Sup Ant (1)	10/46	task coordination
	Frontal Mid (2)	45/12	visual, auditory processing
	Frontal Sup Post (3)	8	coordinated movements
	Supp Motor Area (4)	4	primary motor
	Cingulum Ant (5)	24	multimodal
	Precentral (6)	6	secondary motor area
	Postcentral (7)	1-3	primary somatosensory
Parietal lobe	Cingulum Post (8)	23	multimodal
	Parietal (9)	5	secondary somatosensory
		7	somatosensory association
Temporal lobe	Temporal Sup (11)	22	secondary auditory area
	Temporal Mid (12)	38/21	auditory processing
	Temporal Inf (13)	20	secondary visual
Occipital lobe	Cuneus (15)	18	visual processing
	Occipital Mid (10)	18	secondary visual area
	Occipital Inf (14)	37	visual processing
	Occipital Pole (16)	17	primary visual
Subcortical regions	Basal forebrain (17)		
	Septal nuclei (18)		
	Striatum Ant (19)		
	Caudate nucleus Post (20)		
	Putamen Post (21)		
	Globus pallidus (22)		
	Amygdala (23)		
	Hypothalamus (24)		
	Dorsal thalamus (25)		
	Ventral thalamus (26)		
	Hippocampus (27)		
	Colliculus (28)		
	Pons (29)		
	Midbrain (30)		

Table 1. Identification of functional regions of the mouse lemur brain.
Brain regions were classified based on their locations within the frontal, parietal, temporal, or occipital lobes as well as subcortical regions. Each labelled region was compared to cytoarchitectonic (Brodmann, 1999 (original in 1909); Le Gros Clark, 1931) and anatomical atlases of the mouse lemur (Bons et al., 1998; Nadkarni et al., 2018) and of the human "AAL for SPM12" atlas (Tzourio-Mazoyer et al., 2002) to evaluate the Brodmann areas that were the closest to the identified regions. A function is also proposed for each region following expectations from Brodmann classification.

2.2 Large scale brain networks in mouse lemurs

The quantification of correlations of temporal evolution of BOLD fMRI signal between two regions (or nodes) provides an index of the "functional connectivity" between these nodes. Here, the 48 functional regions identified with the dictionary learning analysis were used as nodes for graph analysis of the mouse lemur brain. A 3D-view of the mouse lemur network based on these 48 functional regions is presented in Suppl. Fig. 1. Partial correlation matrices were created using fully preprocessed MR images by calculating the partial correlation coefficients between temporal evolutions of BOLD MR signals within each region of this 3D functional network.

2.2.1 Modularity and large scale network identification based on graph analysis

In graph theory, large scale networks are defined as community structure (or modules), which are groups of nodes connected densely and sparsely with nodes from other modules. The modularity of a partition (Q) is the degree to which a network can be subdivided into non-overlapping groups of nodes with maximum within-group connections and minimum number of between-group connections (D. B. Vincent et al., 2008). Here, the average partial correlation matrix was used to evaluate the modular structure of the mouse lemur brain by graph theory. Q was calculated to assess the ability of this weighted undirected matrix to be segregated into non-overlapping groups of nodes. A high modularity value (Q = 0.43) was obtained which suggests a prominent modular structure of mouse lemur brain networks. This modularity index was associated with the classification of the matrix into 6 modules (large scale networks) (Fig. 3, Suppl Table 2). Each functional region was associated with one and only one network. These networks were identified as:

$M-1_6$ – Default mode network-like (DMN-like). This module involved posterior and anterior cingulum, superior posterior frontal and parietal cortices. In other species, these regions are reported to be part of the DMN (Belcher et al., 2013; Hutchison et al., 2010; J. L. Vincent et al., 2007). This module also embedded nodes from the superior motor area and postcentral cortices.

$M-2_6$ – Visual. This module involved the cuneus, the occipital pole, the middle, the inferior occipital and the inferior temporal cortices. Those clusters correspond to visual areas and regions involved in integration of visual information.

M-3$_6$ – Frontal. This module involved nodes from frontal and precentral cortices.

M-4$_6$ – Temporal. This module embedded temporal structures usually implicated in response to auditory stimuli as well as the right posterior putamen.

M-5$_6$ – Basal ganglia. This module embedded the anterior striatum, the posterior striatum (posterior caudate nucleus and posterior putamen), the amygdala, basal forebrain, septal nuclei, as well as the hypothalamus and globus pallidus.

M-6$_6$ – Thalamic. This network involved a large number of subcortical regions including and surrounding the thalamus, the hippocampus, the colliculi and the midbrain.
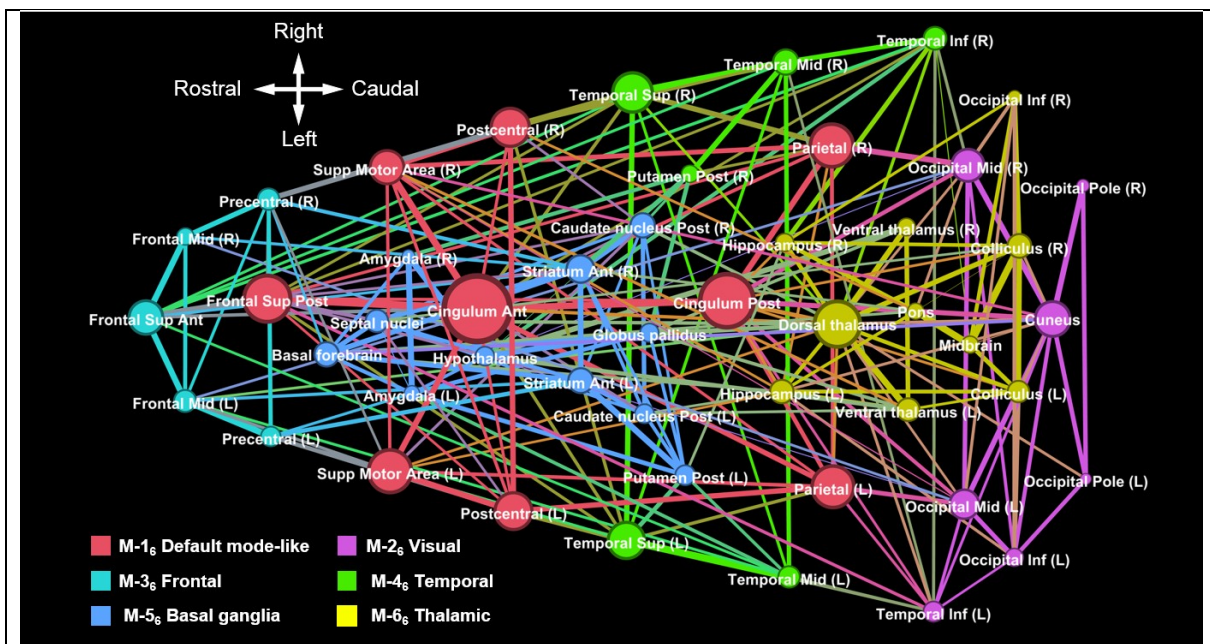
Figure 3. Mouse lemur networks identified using graph analysis based on 48 functional regions.

Using graph analysis, we partitioned the mouse lemur brain into six cortical and subcortical modules. A color and a name were assigned to each module. Colors highlight interactions between different nodes, *i.e.* they outline large scale networks. Eigenvector centrality, a measure of node influence, is represented by the node size.

2.2.2 Identification of large scale networks based on dictionary learning

We then wondered whether the six previously identified modules could be identified with dictionary learning analysis, another data-driven method. A six-component analysis revealed bilateral networks spread over the whole brain (Fig. 4, Suppl. Table 2). Four networks (the DMN, visual, basal ganglia and thalamic) were very similar to those identified with the module analysis. One network (fronto-temporal) was a concatenation of two networks identified by module analysis. The last network (somato-motor) was not identified with module analysis. Unlike for the graph analysis some functional regions (*e.g.* the anterior cingulate cortex) could be attributed to different networks (*e.g.* the DMN, fronto-temporal and somato-motor networks). More precisely, the networks were identified as:

SC-1_6 – DMN. This network involved structures identified with graph analysis (posterior and anterior cingulum cortices, superior posterior frontal and parietal cortices). Some nodes (superior motor area and postcentral cortices) identified as part of the DMN by graph analysis were not detected with dictionary learning.

SC-2_6 – Visual. This network involved the same nodes as those detected with module analysis (occipital pole, middle, inferior occipital and inferior temporal cortices), except the inferior temporal cortex.

SC-3_6 – Fronto-temporal. This network involved several regions that were identified as frontal or temporal network with graph analysis. It also included the anterior cingulum cortex.

SC-4_6 – Somato-motor. This network embedded frontal and parietal regions located above the Sylvian fissure (corresponding to Brodmann 1-3 (primary region involved in body sensation), 4 (primary motor region) and 6 (secondary motor region)) and temporal regions surrounding the Sylvian fissure. This network could thus be involved in somato-motor activities.

SC-5_6 – Basal ganglia. This network involved the same regions as those identified for this network with module analysis except for the hypothalamus and globus pallidus.

SC-6_6 – Thalamic. This last network involved mostly the same regions as the ones identified with graph analysis. In addition, it included the basal forebrain, septal nuclei and globus pallidus.
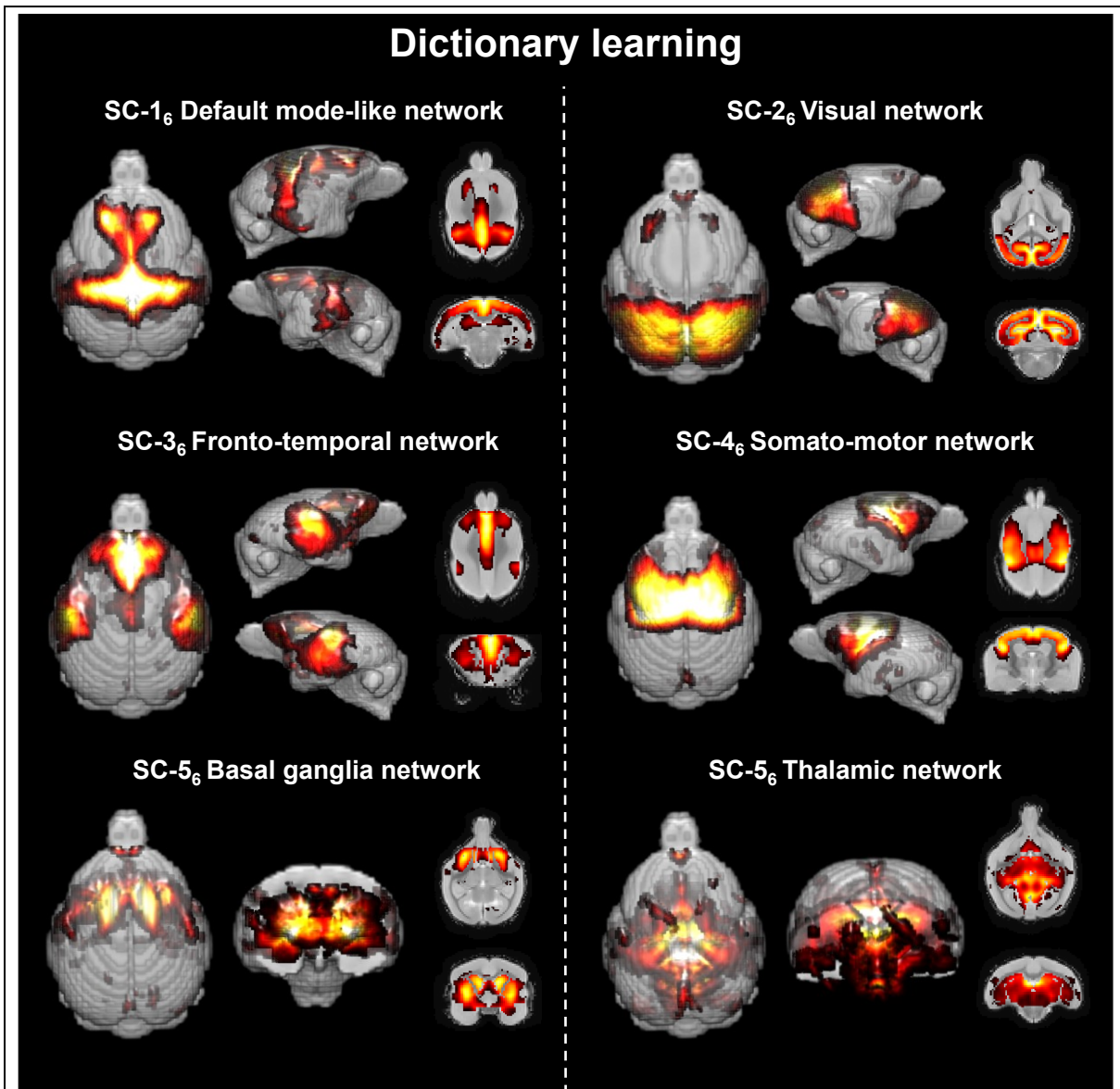
Figure 4. Cerebral networks identified following six component dictionary learning in mouse lemurs.

This analysis revealed bilateral networks that included several regions spread over the whole brain classified as default mode-like, visual, fronto-temporal, somato-motor, basal ganglia and thalamic networks.

2.2.3 Identification of large scale networks based on seed-based analysis

Another way to analyse cerebral networks is to perform seed-based studies. This method evaluates the relationships between mean BOLD signal in a brain region (seed) and BOLD signal in any voxel of the brain. Here, the seeds corresponded to the 48 previously identified functional regions. Some seeds were only connected with voxels from the same brain region and were not further explored (*i.e.* the visual and thalamic networks, SB-2_6 and SB-6_6 in Fig. 5). Four seeds were connected with voxels localized in brain networks previously described with the graph analysis and dictionary learning methods (*i.e.* the DMN, fronto-temporal, somato-motor and basal ganglia networks, Fig. 5). Two networks identified with other methods were not identified by seed-based analysis (the visual and thalamic networks). As for dictionary learning, some structures (*i.e.* the anterior cingulum cortex) could be attributed to different networks (Suppl. Table 2). More precisely, the networks highlighted by seed-based analysis are described as follows.

SB-1_6 – DMN. The seed from the posterior cingulum cortex (PCC) is usually used to define the DMN. Here, using this seed we highlighted highly connected voxels in the regions identified as DMN with graph analysis and dictionary learning methods (posterior and anterior cingulum cortices, superior posterior frontal and parietal cortices). Additional parts of this network were also identified (middle frontal cortex and dorsal thalamus).

SB-3_6 – Fronto-temporal. The seed from the left middle temporal cortex was connected with the right middle and superior temporal cortices, superior anterior frontal cortex, superior posterior frontal cortex and anterior cingulum cortex.

SB-4_6 – Somato-motor. Using a seed in the left superior motor area, we highlighted a network englobing several regions included in the somato-motor network identified by dictionary learning (fronto and parietal cortices, superior temporal regions, anterior cingulum cortex). Voxels from the middle frontal, superior posterior frontal cortex, posterior cingulum cortices as well as the posterior caudate nucleus and dorsal thalamus were also associated with this network.

SB-5_6 – Basal ganglia. Using the posterior caudate nucleus (left) as a seed, we highlighted a basal ganglia network that involved the striatum. It was already identified for this network with graph analysis and dictionary learning. Voxels from the superior posterior frontal cortex and anterior cingulum cortices were also associated with this
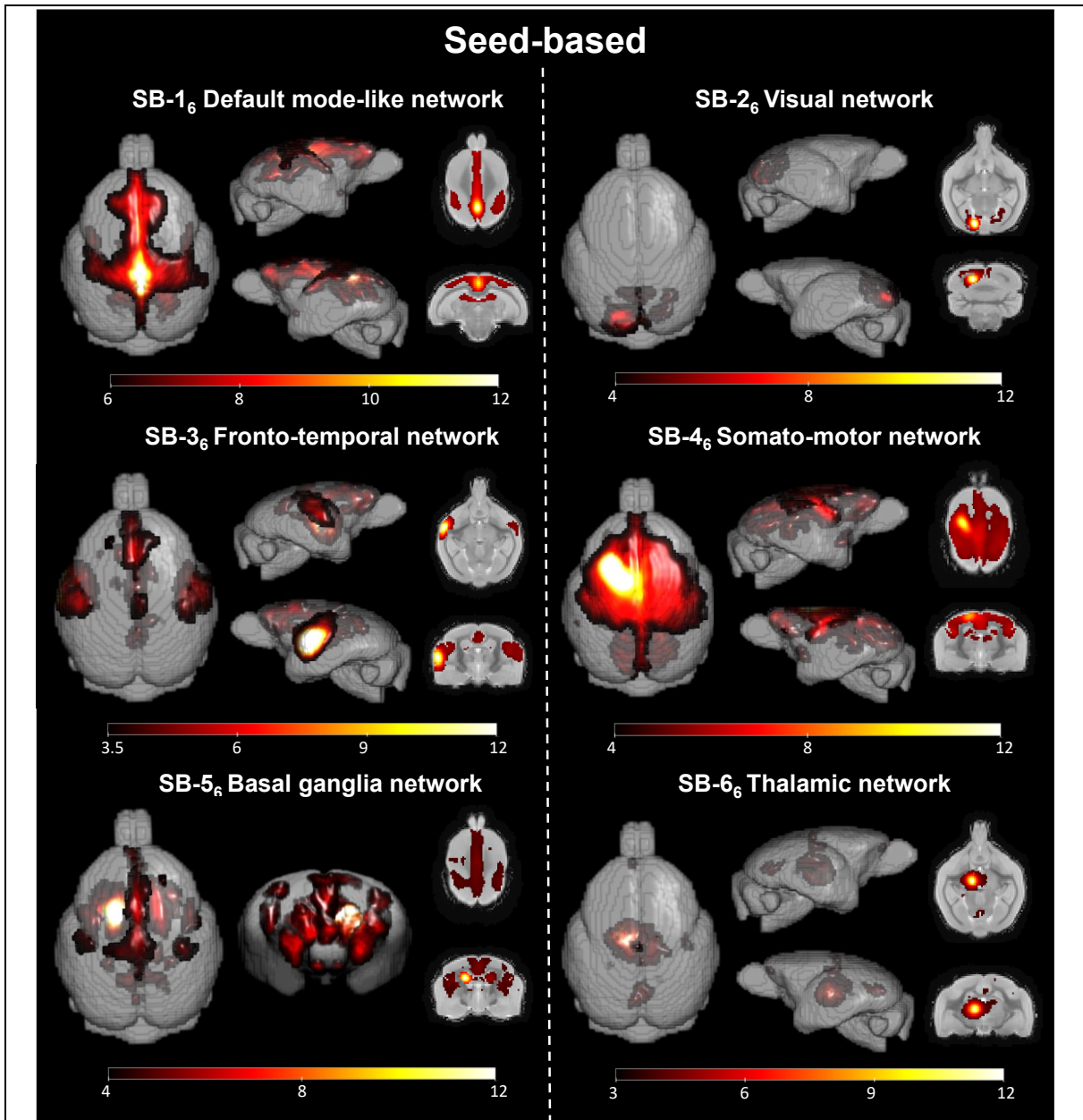
network.

Figure 5. Mouse lemur resting-state networks characterized with seed-based analysis.
Each image highlights mean *z*-statistic maps of regions connected to a cerebral seed. Seed-based analysis detected four of the six previous large scale networks identified with dictionary learning: default mode-like, fronto-temporal, somato-motor, and basal ganglia (seeds positioned in the posterior cingulate cortex, the left medial temporal cortex, the left superior frontal cortex and the left posterior caudate nucleus, respectively). Visual and thalamic networks that were detected with dictionary learning were not detected with seed-based analysis: SB-2_6 and SB-6_6 display lack of large network detection using seeds in the left occipital cortex and the left ventral thalamus. Color bars represent *z*-statistic values.

2.3 Functional hubs and small-worldness features of mouse lemur brains

2.3.1 Brain hubs in mouse lemurs

Whole brain networks can also be characterized using various descriptors. One of these descriptors, "hubness", describes the centrality of nodes in the network. This is a measure of node influence within the whole brain network. It can be measured by eigenvector centrality. For each node, this index is mainly calculated based on its partial correlation values (edges) with all regions of the 3D functional atlas, weighted by the eigenvector scores of its neighbourhood nodes. In other words, nodes which display high eigenvector centrality scores are strongly linked to other nodes and/or to strongly connected nodes. Here, eigenvectors were presented as histograms (Fig. 6) or as the size of the nodes in the graphical representation of the networks (Fig. 3). The 3 nodes presenting the highest eigenvector centrality were the anterior cingulum cortex, the posterior cingulum cortex, and the superior posterior frontal cortex. These three regions belong to the DMN. The dorsal thalamus was the next region showing highest hubness properties. Then the following hubs involved the parietal cortex, superior motor area, as well as the superior temporal and postcentral cortices (Fig. 6).

2.3.2 Small-worldness of mouse lemur brain networks

Network topology describes properties of regional specialization and global information transfer efficacy. It can be classified into three main classes: random, lattice and small-world networks (Telesford et al., 2011). Network topology can be characterized using two small-world coefficients (σ and ω) (NetworkX (Hagberg et al., 2008)). Small-world networks have σ values superior to 1 and ω values close to 0 (Telesford et al., 2011). In mouse lemurs these coefficients (σ = 1.47 and ω = 0.39) indicated small-world properties. Usually, mammal brains have small-worldness topology (Mechling et al., 2014).
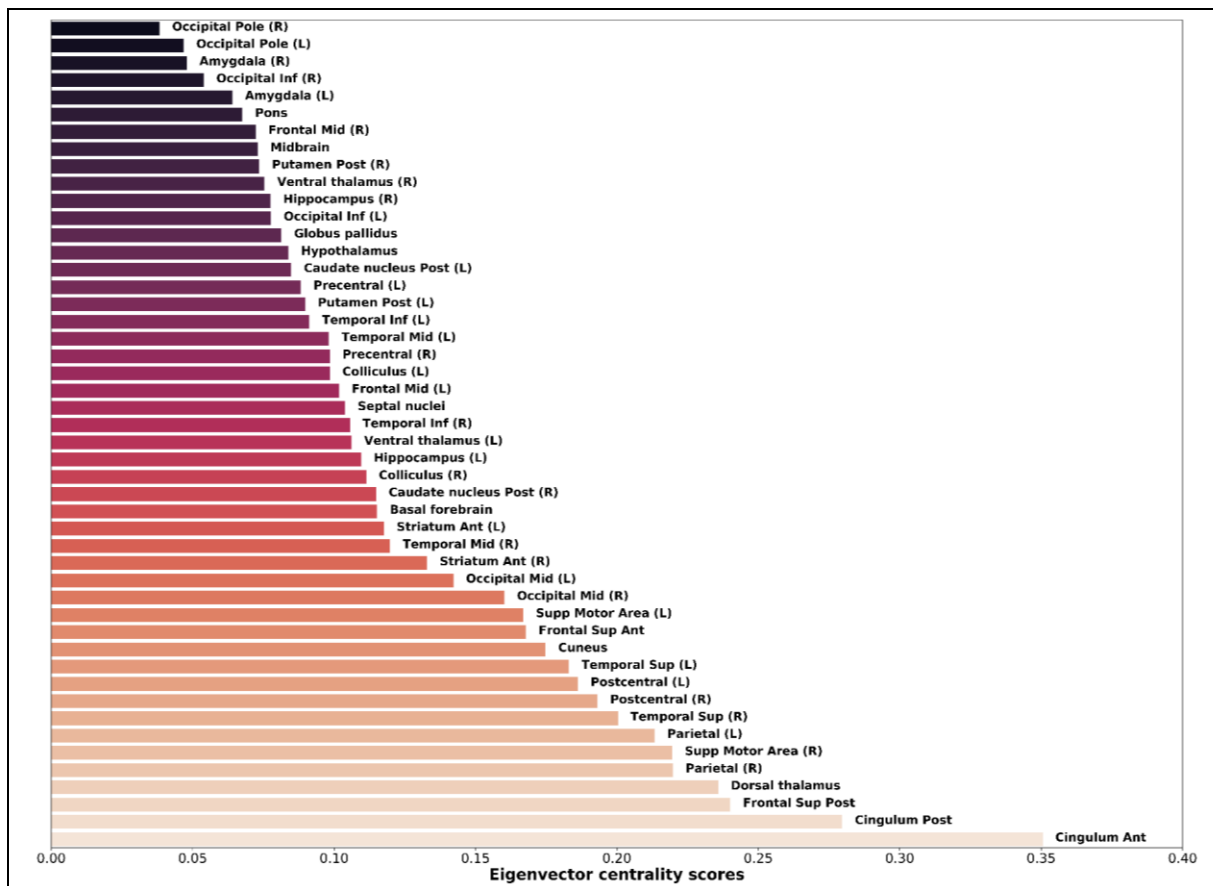
Figure 6. Eigenvalue centrality scores, reflecting "hubness", in mouse lemur brain regions.

The three regions displaying the highest scores were the anterior cingulate cortex, the posterior cingulate cortex and the central frontal cortex. The dorsal thalamus was the next region showing highest hubness properties. Then the following hubs involved the parietal cortex, superior motor area, as well as the superior temporal and postcentral cortices.

2.4 Cerebral networks in humans

We then wondered how comparable mouse lemur and human brain networks are. To answer to this question, resting state fMRI data were recorded from 42 healthy humans ranging from 41 to 60 years old at 3.0 Tesla using an interleaved 2D T2* SENSE EPI. Participants were asked to keep their eyes closed and relax without falling asleep during image acquisition. Human images were then processed with the same graph analysis and dictionary learning algorithms as mouse lemur images.

Local functional regions were identified using a dictionary learning based on 35 components. Single components spread on bilateral structures were dissociated into two different regions (*i.e.* one in each hemisphere). Ultimately, the brain was partitioned into 56 local functional regions (55 cortical, 1 subcortical). They were named based on the "AAL for SPM12" atlas (Tzourio-Mazoyer et al., 2002) (Suppl. Fig. 2)

As for mouse lemurs, the 56 functional regions identified with the dictionary learning analysis were used as nodes for large scale network analysis. First, we calculated partial correlation coefficients between temporal evolutions of BOLD MR signals within each region of the 3D functional atlas. The obtained correlation matrix was used to calculate the matrix modularity value (Q = 0.56). This index was associated with the segregation of the matrix into 6 modules that were classified as default mode, visual, frontal, temporal somato-motor, and temporo-insular networks (Suppl. Fig. 3).

Then large scale networks were further characterized in humans using a dictionary learning analysis with 6 components (Fig. 7, Table 2). The 6 networks identified could be classified as the default mode, visual, fronto-supramarginal (classified as control-executive network in (Solé-Padullés et al., 2016)), somato-motor, temporal, and a fronto-parietal network (classified as attention network in (Raichle, 2011)).
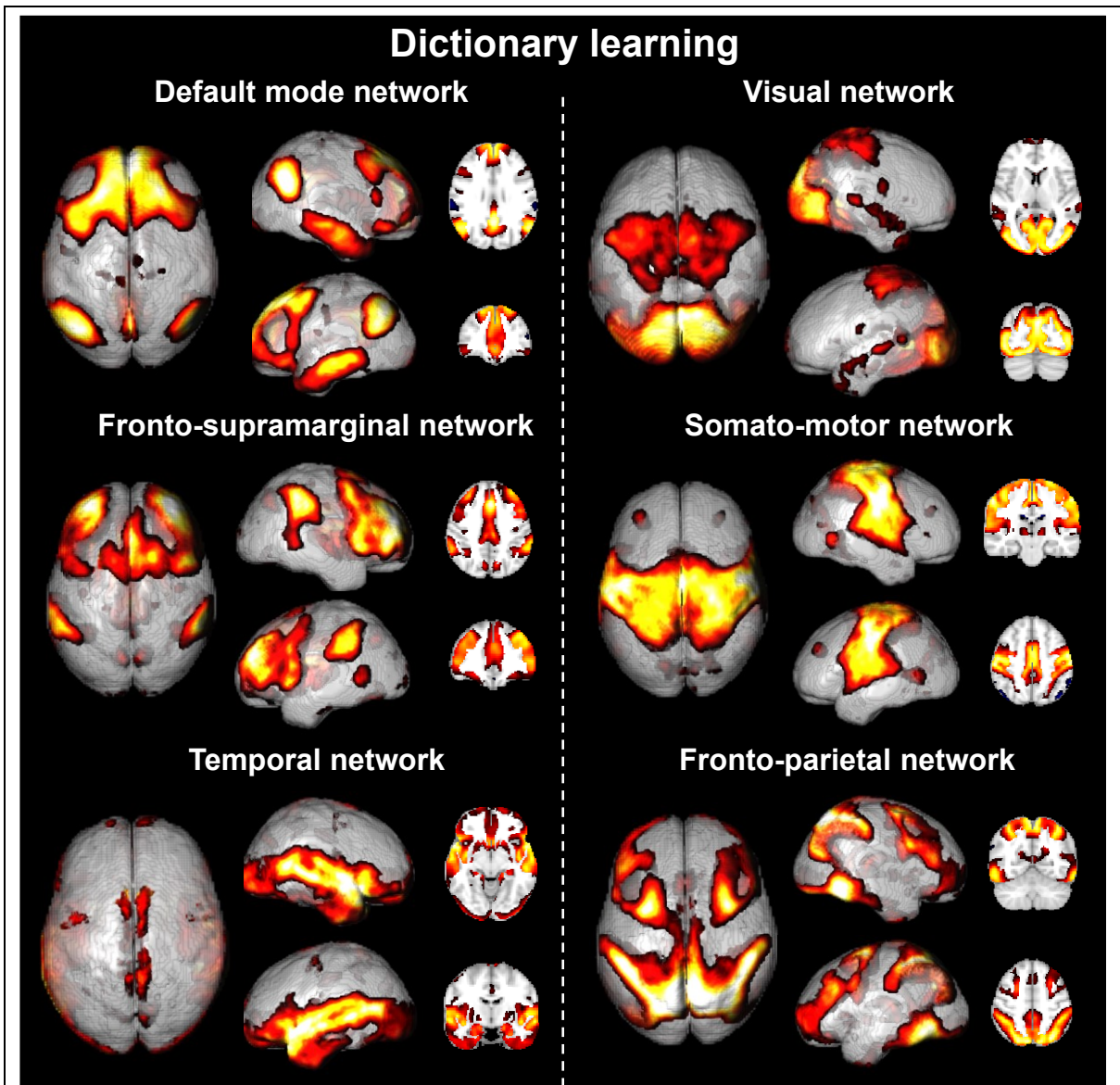
Figure 7. Human cerebral networks identified following six component dictionary learning.

The spatial map decomposition extracted 6 cortical networks commonly observed in the literature (DMN, visual, fronto-supramarginal, somato-motor, temporal, fronto-parietal). This analysis was performed with similar pretreatments as for the mouse lemurs.

2.5 Functional hubs and small-worldness features of human brains

Eigenvector centrality and network topology were evaluated in humans using the same procedures as for mouse lemurs. Eigenvector centrality was presented as histograms (Fig. 8) or as the size of the nodes in the graphical representation of the networks (Suppl. Fig. 3). The 3 nodes presenting the highest eigenvector centrality were the parietal inferior (right and left) and the precuneus posterior. Then the next hubs were located in the middle frontal cortex (left), the angular region (left) and the posterior cingulum cortex. All these regions except the middle frontal cortex belong to the DMN. Regarding network topology, as expected we found small-world properties in the human brain (σ = 1.1 and ω = 0.08).
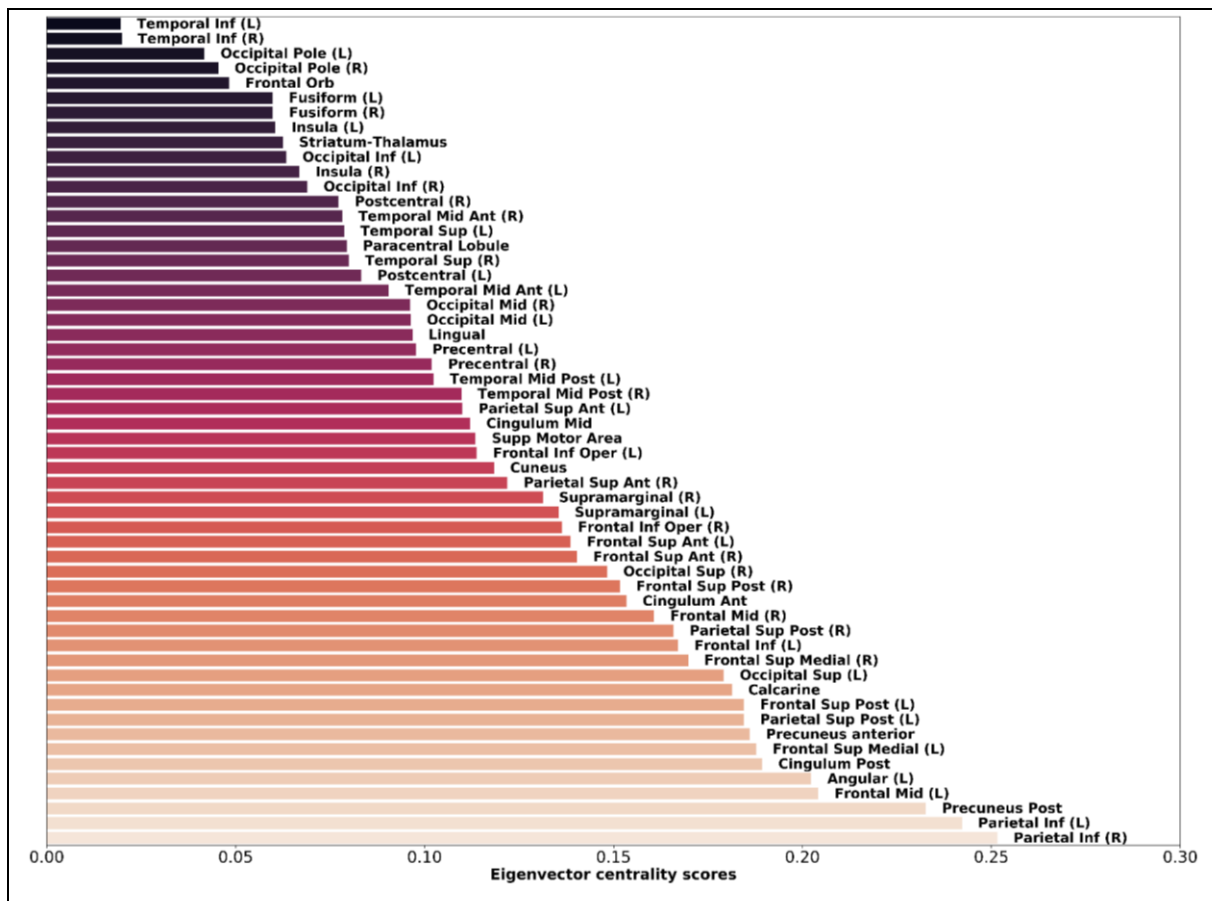
Figure 8. Eigenvalue centrality scores, reflecting "hubness", in human brain regions.
The 3 nodes presenting the highest eigenvector centrality were the parietal inferior (right and left) and the precuneus posterior. Then the next hubs were located in the middle frontal cortex (left), the angular region (left) and the posterior cingulum cortex.

3. Discussion

This study provides a detailed characterisation of the organisation of functional networks in mouse lemur primates under isoflurane sedation. Complementary analyses based on dictionary learning, seed-based studies and graph analysis highlighted 48 local functional regions that could be grouped into several large scale networks. We also identified the main hubs and small-world characteristics of mouse lemur brains. Human brain networks were also analysed with algorithms similar to those used in lemurs in order to compare networks in both species.

3.1 Parcellation of functional regions within mouse lemur brains

Up to now, description of mouse lemur functional organisation was based on cytoarchitectonic atlases (Bons et al., 1998; Le Gros Clark, 1931; Nadkarni et al., 2018). Here, using dictionary learning with a large number of components, we created a 3D map of 48 local functional regions. The quality of this functional atlas was supported by the bilateralism of the extracted regions. One of the strengths of this functional map is that it can be used to create a whole brain graph that relies on brain function rather than on anatomical boundaries. Studies of animal resting state networks often used regions of interest based on anatomical atlases (Li and Zhang, 2018), as opposed to functional atlases. The latter approach is preferable since anatomical boundaries do not necessarily correspond to underlying brain function. Therefore, regions of interest based on anatomical atlases display less signal homogeneity and so increase non-specific signal (Craddock et al., 2012). The second advantage of functional atlases is that no predetermined anatomical atlas is required during the analysis. Consequently, the independence of our pipeline provides the capacity to build brain networks in species that have not been fully investigated.

3.2 Modular organisation of mouse lemur brains

High modularity is an important principle of brain organisation (Bullmore and Sporns, 2009). It can be measured with modularity of a partition (Q). Here we found Q=0.43 in mouse lemurs. This value is consistent with Q values reported in rats (Q=0.39 (D'Souza et al., 2014)), other non-human primates (0.33 < Q < 0.54 (Shen et al., 2012)) or humans in our study (Q = 0.56) and indicates that the mouse lemur brain can be partitioned into modules. Using graph analysis, we identified six cortical and subcortical modules that corresponded to large scale networks. This organisation into six modules is consistent with the number of modules reported in rats (n=6 (D'Souza et al., 2014)), other non-human primates (for example n=4 (Shen et al., 2012) or n=7 (Grayson et al., 2016) in *Macaca fascicularis*), or humans in our study (n=6).

3.3 Characterisation of large scale networks in mouse lemur brains

3.3.1 Multi-method approach of resting state analysis in animals

Whole brain networks can be decomposed into large scale networks. However, there are no absolute frontiers between these large scale networks due to the gradualness of the interactions between the different regions of the brain. Several methods, such as dictionary learning, graph analysis and seed-based studies can be used to identify these large scale networks in mammal brains. They rely on various mathematical bases associated with various sensitivities to image artefacts (Power et al., 2014). Also, these methods have diverse abilities to classify brain regions into networks. For example, graph analysis attributes each region to one and only one network while dictionary learning and seed-based analysis can attribute a region to several networks. In most resting state fMRI studies in animals, neuronal networks are identified on the basis of a single method. Here we showed that different methods do not detect exactly the same networks. However, networks identified with each method display a strong overlap. Functional regions included in a network by several methods represent the more robust parts of the network. Thus, we propose a first classification of the mouse lemur networks that takes into account only regions identified by two or three methods (Fig. 9, Suppl. Table 3). An overview of each network is presented in the following paragraphs.
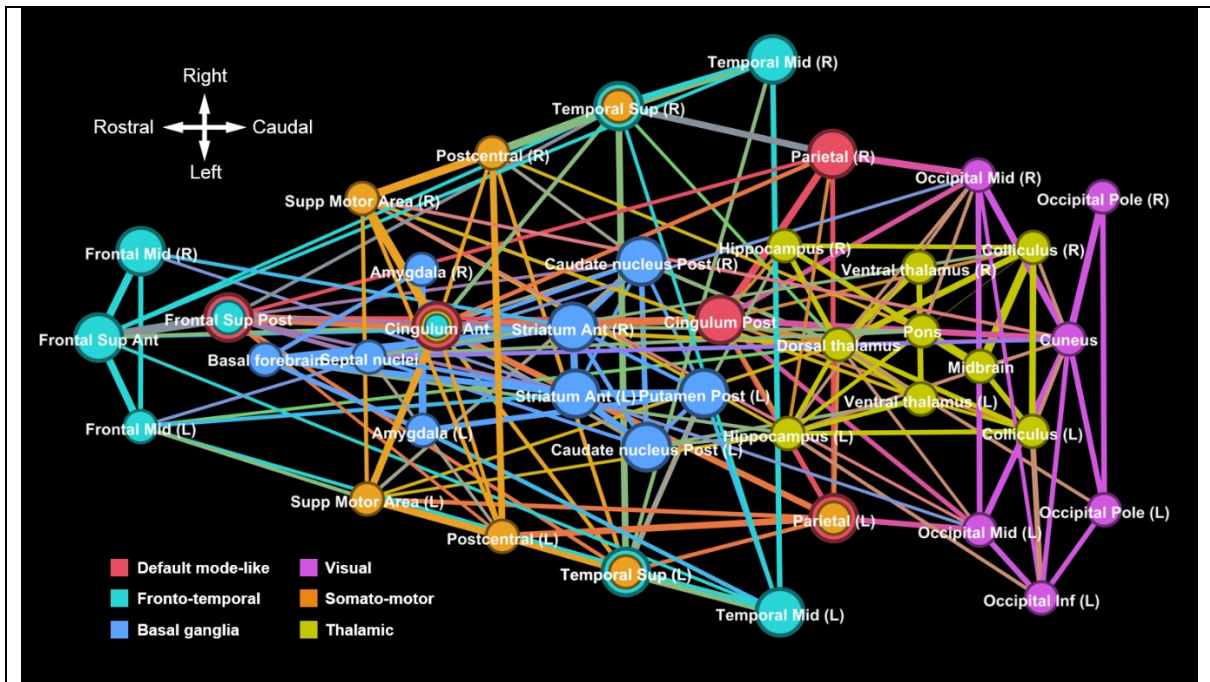
Figure 9. Most robust functional networks identified in mouse lemurs using two or three network identification methods.
Regions from the DMN, visual, fronto-temporal, somato-motor, basal ganglia and thalamic networks that could be identified by two or three network identification methods are considered as robustly associated to a network and are displayed on this figure. For each network, edges were reported from those identified with graph analysis.

3.3.2 Default-mode-like network

The DMN is one of the most studied networks in humans (Hampson et al., 2006) and other mammals including rodents (Lu et al., 2012) and non-human primates (J. L. Vincent et al., 2007). It plays a critical role in several physiological and pathological processes such as Alzheimer's or Parkinson's diseases (Buckner et al., 2005; Gao and Wu, 2016). In mouse lemurs, four regions of this network were detected with network identification methods: anterior and posterior cingulum cortices, superior posterior frontal cortex and parietal cortex. In several species, these regions are reported to be part of the default mode network (Belcher et al., 2013; J. L. Vincent et al., 2007).

In humans and other mammals, the DMN contains highly connected hub nodes. In the mouse lemur brain, we also found that it contained the most connected nodes. Given the importance of this network it was critical to characterize it in the mouse lemur, which is widely used as a model of neurodegenerative diseases (Kraska et al., 2011; Mestre-Frances et al., 2018).

3.3.3 Fronto-temporal network

The fronto-temporal network was found in mouse lemurs with dictionary learning and seed-based analysis, but was split into two networks (frontal and temporal) with graph analysis. One of its components, the superior temporal cortex, was a strong hub in the mouse lemur brain. In primates, these regions are reported to be part of the executive network (Hutchison et al., 2012)

3.3.4 Networks specialized in sensory and motor information processing

We also identified networks that could be classified as externally-driven. The first one is the visual network. It involved mainly occipital areas. This network has been described in numerous primates under task and rest conditions (Belcher et al., 2013). The second externally-driven network is the somato-motor network. It has also been widely defined in humans (Beckmann et al., 2005), primates (Nelissen and Vanduffel, 2011), and many other mammals (Sierakowiak et al., 2015). It integrates sensory input and motor commands. In mouse lemurs, we found that this network contains several hubs such as the anterior cingulum cortex, the superior motor area and the postcentral cortices.

3.3.5 Subcortical networks

Finally, two networks were identified in subcortical areas. The first one involved the basal ganglia. Similar networks are described in primates (Belcher et al., 2013), and other mammals (Sierakowiak et al., 2015) and are involved in emotional, motivational, associative and cognitive functions (Herrero et al., 2002).

The second subcortical network involved several regions such as the ventral thalamus (a strong hub in mouse lemurs), dorsal thalamus, hippocampus, colliculus, pons and midbrain. It was called "thalamic network".

3.4 Small-worldness features of mouse lemur brains

We finally evaluated the small-worldness properties of the mouse lemur functional networks by calculating small-world coefficients σ and ω. Our results attested that mouse lemur networks have small-world properties (ω = 0.39). Interestingly, ω was much smaller in the human brain (ω = 0.08) than in the lemur brain suggesting stronger small-world properties in humans. The small-world configuration is considered as optimal for local information processing and for its global transfer. Indeed, small-world networks have the unique ability to have specialized regions while simultaneously exhibiting shared or distributed processing across all of the communicating regions of a network (Telesford et al., 2011).

3.5 Cross species comparison: homologies and divergence between humans and mouse lemur networks

In a last part of the study, cerebral networks were analyzed in humans with the same graph analysis and dictionary learning algorithms as the ones used in mouse lemurs. Two major differences were reported between the two species. First, large scale networks were only cortical in humans while they involved two subcortical networks in lemurs. Second, in humans, large scale networks involved more functional regions than in lemurs. This latter result is consistent with the stronger small-world organization in humans than in lemurs suggesting a better efficacy of whole brain networks in humans. These differences between the two species may be related to a better efficacy of neuronal networks in humans, but they could also be associated to different awareness levels as lemurs were anesthetized while humans were awake during image acquisition. Indeed, Barttfeld et al. compared connectivity measures in awake and anesthetized conditions in primates. They showed that under anaesthesia, the more frequent functional connectivity patterns inherit the structure of anatomical connectivity and exhibit fewer small-world properties (Barttfeld et al., 2015).

Graph analysis revealed four similar modules (default mode-like, visual, frontal, and temporal networks) in mouse lemurs and humans, although their regional organization was not strictly identical. Two other modules detected in humans (somato-motor and temporo-insular) corresponded to networks that were not detected in lemurs. On the contrary, the two subcortical modules detected in lemurs (basal ganglia and thalamic networks) were not detected in humans. Because of the multiple regions involved in

module description by graph analysis and because of the possibility to attribute a region to only one network with this method, it was difficult to further compare human and lemur networks with this technique.

Dictionary learning also revealed four similar networks (DMN, visual, fronto-temporal/supramarginal and somato-motor networks) in lemurs and humans (Table 2; Suppl. Fig. 4). In both species, the DMN network involved the cingulum, frontal, and parietal cortices. In mouse lemurs, it involved the superior posterior frontal cortex that was probably subdivided in two functional regions (frontal superior medial and frontal superior posterior cortices) in humans. Other regions such as the temporal cortex were included in the human DMN but not in the mouse lemur DMN. Interestingly, in both species, this network was the one in which highest hubness coefficients (eigenvectors) were detected. This reinforces the importance of this network for brain functional organization. In humans, the default mode network has been largely linked to self-referential thought, internal-oriented cognition and monitoring of the environment (Buckner et al., 2008). The strength and stability of this network in mouse lemurs under anaesthesia is consistent with the discovery of this network in many other anesthetized animals (J. L. Vincent et al., 2007). This suggests that it is an essential element of brain functional organization and that it may be dedicated to other tasks too.

In the visual network, occipital cortex was detected in both species. Additional more anterior-parietal regions such as the paracentral lobule and the postcentral were highlighted in humans. We cannot rule out that this wider extension in human dataset is not related to the wakefulness state as it induces a richer repertoire of functional configurations (Barttfeld et al., 2015).

In mouse lemurs, a network involving the anterior cingulum, frontal and temporal regions was classified as the fronto-temporal network. In humans, one network involving mostly the anterior cingulum and frontal regions could be homologous to this network. Interestingly, in lemurs, this networks also involved temporal (superior and medial temporal regions) while it involved parietal regions (supramarginal anterior and parietal inferior cortices) as well as additional regions (supplementary motor, cingulum median and opercular regions) in humans. This network could correspond to the control-executive network (Solé-Padullés et al., 2016). If the fronto-temporal network of mouse lemur is equivalent to the fronto-supramarginal human network, then this would suggest a shift of the functional region localized in the superior temporal area in lemurs towards a supramarginal location in humans.

The last comparable network was the somato-motor network. In humans it involved regions surrounding the central sulcus (precentral and postcentral regions) as well as the supplementary motor region. In lemurs, there is no central sulcus, but this network involved similar regions (precentral and postcentral regions) as well as the supplementary motor region. Interestingly, this part of the network seemed to have a more anterior position in the brain of lemurs than in humans. This is consistent with the more anterior part of the motor regions reported in lemurs by Le Gros Clark (Le Gros Clark, 1931) and Brodmann (Brodmann, 1999 (original in 1909)). This pattern is linked to the smaller size of the frontal region in lemurs as compared to humans. Finally, in humans, this region involved the paracentral and the precuneus anterior cortices while it involved the region classified as anterior cingulate cortex in the mouse lemur. These two regions are localized in the same area and we cannot rule out that the functional region classified as anterior cingulate cortex in lemur indeed involved the pre and post central lobule in addition to the anterior cingulate cortex.

3.6 Anaesthesia-related limitations

One of the objectives of this study was to describe for the first time neuronal networks in mouse lemurs. It was conducted on sedated animals using isoflurane with the lowest non-awakening isoflurane level possible for mouse lemurs (1.25%). Isoflurane is expected to decrease the functional connectivity but at high doses (superior to 1.5%) or after a long exposure (Hutchison et al., 2014; Li and Zhang, 2018). Evaluating resting state networks in anesthetised and not in awake animals is an obvious limitation of the study (Schroeter et al., 2014). However, several animal studies showed that the major functional networks are preserved under anaesthesia (J. L. Vincent et al., 2007). Here, we confirm this assumption by describing several networks, including a DMN-like in anesthetised mouse lemurs. In the future, one may also focus on resting state fMRI in awake mouse lemurs to possibly evaluate more physiological brain states and increase the number of nodes associated with each identified network. Such an approach is challenging but has already been performed in marmosets (Belcher et al., 2013) and macaques (Goense et al., 2008).

Network	Mouse lemur Label	Mouse lemur	Human	Human Label
Default mode	(8)	Cingulum Post		(20)
	(5)	Cingulum Ant		(7)
	(3)	Frontal Sup Post	Frontal Sup Post (R&L)	(2)
			Frontal Sup medial (R&L)	(3)
			Frontal Inf (L)	(35)
	(9)	Parietal (R&L)	Parietal Inf (R&L)	(14)
			Angular (L)	(15)
			Temporal Mid Ant(R&L)	(23)
			Occipital Sup (R&L)	(27)
			Precuneus Post	(18)
			Calcarine	(30)
Visual	(16)	Occipital Pole (R&L)		(33)
	(10)	Occipital Mid (R&L)		(28)
	(14)	Occipital Inf (R&L)		(29)
	(15)	Cuneus		(26)
			Calcarine	(30)
			Lingual	(31)
			Fusiform (R&L)	(32)
			Paracentral lobule	(19)
			Postcentral (R&L)	(11)
Fronto-temporal / Fronto-supra-marginal	(5)	Cingulum Ant		(7)
	(1)	Frontal Sup Ant (R&L)		(1)
	(3)	Frontal Sup Post	Frontal Sup Post (R)	(2)
			Frontal Sup medial (R)	(3)
	(2)	Frontal Mid (R&L)	Frontal Mid (R&L)	(4)
			Frontal Inf operc (R&L)	(5)
			Frontal Inf (L)	(35)
			Supp motor area	(12)
			Cingulum Mid	(8)
	(11)	Temporal Sup (R&L)	Supramarginal (R&L)	(21)
			Parietal Inf (R)	(14)
			Striatum-thalamus	(34)
	(12)	Temporal Mid (R&L)		
Somato-motor	(6)	Precentral (R&L)		(10)
	(7)	Postcentral (R&L)		(11)
	(4)	Supp motor area (R&L)		(12)
	(9)	Parietal (L)	Parietal Sup Ant (R&L)	(13)
	(5)	Cingulum Ant	Paracentral lobule	(19)
			Precuneus Ant	(17)
	(11)	Temporal Sup (R&L)	Temporal Sup (R&L)	(25)
			Supramarginal (R&L)	(21)

Table 2. Comparison of the regions belonging to the different networks extracted in mouse lemurs and humans.
Regions that were identified with different methods are grouped within a single case. The 3D functional atlas of each species was pasted on different networks obtained by dictionary learning. A region was considered to belong to a network when more than 30% of its volume belonged to this network. The fit between two regions with different names was based on the anatomical proximity. Labels represent the number corresponding to this region in Figure 2 for lemurs and Supplementary Figure 2 for humans.

4. Conclusion

This study provides the first characterisation of functional brain networks in mouse lemur primates. Local functional regions were identified without using any anatomical atlas. Six large scale networks were identified using several complementary data-driven and hypothesis-based methods. Networks identified with each method displayed a strong overlap and we propose a first classification of the most robust mouse lemur networks by selecting only regions identified by two or three methods. We also proposed a second validation method by comparing networks in lemurs and human brains. Indeed, a strong homology was reported between well characterized human cortical networks and lemur cortical networks. This further suggests the accuracy of the identified mouse lemur networks. The mouse lemur brain displayed small-world features leading to optimal information transfer. Finally, critical hubs were detected and involved the posterior and anterior cingulate cortices, the central prefrontal cortex, and the dorsal thalamus.

The mouse lemur is an interesting primate because of its key position in the phylogenetic tree, rodent-like small size and nocturnal and arboreal lifestyle. The 3D functional atlas and resting state network maps are freely available at https://www.nitrc.org/projects/fmri_mouselemur/. The imaging tools used to create and manipulate the template are also available (https://sammba-mri.github.io).

5. Materials and methods

5.1 Animals and breeding

This study was carried out in accordance with the recommendations of the European Communities Council directive (2010/63/EU). The protocol was approved by the local ethics committees CEtEA-CEA DSV IdF (authorization 201506051736524 VI (APAFIS#778)). All mouse lemurs studied were born in the laboratory breeding colony of CNRS/MNHN in Brunoy, France (UMR 7179 CNRS/MNHN) and bred in our laboratory (Molecular Imaging Research Center, CEA, Fontenay-aux-Roses).

Sixteen mouse lemurs (12 males and 4 females) were initially included in this study. Two females that presented brain lesions on anatomical MRI were excluded from the analysis. The 14 analysed animals ranged from 0.9 to 3.1 years old (mean±SD: 1.7±0.7) (Suppl. Table 1). Housing conditions were cages containing one or two lemurs

with jumping and hiding enrichment, temperature 24–26°C, relative humidity 55% and seasonal lighting (summer: 14 hours of light/10 hours of dark; winter: 10 hours of light/14 hours of dark). Food consisted of fresh apples and a homemade mixture of bananas, cereals, eggs and milk. Animals had free access to tap water. None of the animals had previously been involved in pharmacological trials or invasive studies.

5.2 Animal preparation and MRI acquisition

Each animal was scanned twice with an interval of 6 months. All scanning was under isoflurane anaesthesia at 1.25-1.5% in air, with respiratory rate monitored to confirm animal stability until the end of the experiment. Body temperature was maintained by an air heating system at 32°C, inducing a natural torpor in mouse lemurs (Aujard and Vasseur, 2001). This has the advantage of allowing a low anaesthesia level without reawakening.

The MRI system was an 11.7 Tesla Bruker BioSpec (Bruker, Ettlinger, Germany) running ParaVision 6.0.1. Anatomical images were acquired using a T2-weighted multi-slice multi-echo (MSME) sequence: TR = 5000 ms, TE = 17.5 ms, 6 echoes, inter-echo time = 5 ms, FOV = 32 × 32 mm, 75 slices of 0.2 mm thickness, resolution = 200 µm isotropic, acquisition duration 10 min. Resting state time series data were acquired using a gradient-echo EPI sequence: TR = 1000 ms, TE = 10.0 ms, flip angle = 90°, repetitions = 450, FOV = 30 × 20 mm, 23 slices of 0.9 mm thickness and 0.1 mm gap, resolution = 312 × 208 × 1000 µm, acquisition duration 7m30s.

5.3 MRI acquisition in humans

Forty-two healthy participants from the 'Imagerie Multimodale de la Maladie d'Alzheimer à un stade Précoce' (IMAP) study (Caen) were included in the present study (18 males and 24 females ranging from 41 to 60 years old (mean±SD: 50±5.9)). All participants were scanned on a 3.0 T scanner (Philips Achieva, Amsterdam, Netherlands) at the Cyceron Center (Caen, France). Anatomical T1-weighted images were acquired using a 3D fast-field echo sequence (3D-T1-FFE sagittal TR = 20 ms, TE = 4.6 ms, flip angle = 10°, 180 slices of 1 mm with no gap, FOV = 256 × 256 mm^2, in-plane resolution = 1 × 1 mm^2). Resting state time series data were acquired using an interleaved 2D T2* SENSE EPI (2D-T2*-FFE-EPI axial, SENSE = 2; TR = 2382 ms; TE = 30 ms; flip angle = 80°; 42 slices of 2.8 mm with no gap, repetitions = 450, FOV

= 224 × 224 mm^2, in plane resolution = 2.8 × 2.8 mm^2, acquisition duration = 11.5 min). Head motion was minimized with foam pads. Participants were equipped with earplugs and the scanner room's light was turned off. During this acquisition, participants were asked to keep their eyes closed and relax without falling asleep.

5.4 MRI pre-processing

5.4.1 Mouse lemur data

Scanner data were exported as DICOM files then converted into NIfTI-1 format. Then spatial pre-processing was performed using the python module sammba-mri (SmAll MaMmals BrAin MRI; http://sammba-mri.github.io) which, using nipype for pipelining (Gorgolewski et al., 2011), leverages AFNI (Cox, 1996) for most steps and RATS (Oguz et al., 2014) for brain extraction. Anatomical images were mutually registered to create a study template, which was further registered to a high resolution anatomical mouse lemur template (Nadkarni et al., 2018). Resting state images were corrected for slice timing (interleaved), motion, and B0 distortion (per-slice registration to respective anatomicals), then all brought into the same space of the mouse lemur template by successive application of the individual anatomical to study template and study template to mouse lemur atlas transforms. Functional images were further pretreated using Nilearn (Abraham et al., 2014). Nuisance signal regression was applied including a linear trend as well as 24-motion confounds (6 motion parameters, those of the preceding volume, plus each of their squares (Friston et al., 1994)). Images were then spatially smoothed with a 0.9 mm full-width at half-maximum Gaussian filter. The first 10 volumes were excluded from analysis to ensure steady-state magnetization.

5.4.2 Human data

Artefacts were inspected in individual datasets using the TSDiffAna routines (http://imaging.mrc-cbu.cam.ac.uk/imaging/DataDiagnostics). Datasets displaying significant movements (> 1.5° rotation or > 3 mm translation) and abnormal variance distribution and/or artefacted were excluded from the analysis. Data were then preprocessed as defined in Landeau *et al.* (Landeau et al., 2017) with slice timing correction, realignment to the first volume and spatial normalization within native space

to correct for distortion effects. EPI volumes were registered to their own high resolution anatomical image and then registered and normalized to MNI template space. Nuisance signal regression was applied including a linear trend as well as 24-motion confounds (6 motion parameters, those of the preceding volume, plus each of their squares (Friston et al., 1994)). Images were then spatially smoothed with a 2 mm full-width at half-maximum Gaussian filter.

5.5 Identification of functional regions by dictionary learning and creation of a 3D functional atlas

Multi-animal dictionary learning was performed with Nilearn (Mensch et al., 2016) on preprocessed resting state functional MR images. A mask excluding the corpus callosum, hindbrain, ventricles and three systematically artefacted regions (olfactory bulb, ventral entorhinal cortex and prepiriform cortex) was used to restrict functional data to non-noise voxels prior to dictionary learning analysis. During a pilot investigation, several analyses were performed using 20, 30, 35, 40, 45, 50, and 60 sparse components (SCs). The study based on 35 SCs was selected for the final analysis as it highlighted either unilateral local functional regions or bilateral regions. Moreover, the extracted components matched well to anatomy (Nadkarni et al., 2018). The 35 SCs were used to create a 3D functional atlas of the mouse lemur brain. Each bilateral SC was split into two unilateral regions. Regions smaller than 5 mm^3 were excluded leading to 48 local functional regions. Each region was then named using ITK-SNAP to create a 3D functional atlas (Yushkevich et al., 2006). The same procedure than in lemurs was applied to process human fMRI data. We used 35 SCs and a grey matter mask without hindbrain.

5.6 Identification of large scale networks

5.6.1 Connectivity matrix based on functional atlas

Partial correlation matrices were created using fully preprocessed MR images by calculating the partial correlation coefficients between BOLD MR signal timecourses within each region of the 3D functional atlas. Partial correlations were used because they select direct associations between regions and allow the control of indirect correlations (Mechling et al., 2014). Individual partial correlation matrices were

computed from shrunk covariance matrices using the Ledoit and Wolf shrinkage coefficient (Ledoit and Wolf, 2004) as recommended by Varoquaux et al. (Varoquaux et al., 2012) and Brier et al. (Brier et al., 2015). Partial correlation coefficients were then Fisher's z-transformed. Values from different animals were averaged and thresholded based on a one-tailed t-test ($p \leq 0.01$) (Mechling et al., 2014).

5.6.2 Modularity and large scale network identification by graph theory analysis

The modularity of a partition (Q) is the degree to which a network can be subdivided into non-overlapping groups of nodes (D. B. Vincent et al., 2008). The modularity of a partition as well as an optimal segregation of the whole brain network into modules were calculated using Gephi 0.9.2 (Bastian et al., 2009).

5.6.3 Large scale network identification by dictionary learning analysis

A second dictionary analysis was performed in mouse lemurs and humans using a smaller number of SCs in order to highlight large networks and to compare them. Six SCs were used based on the 6 modules found with the graph theory analysis (see Results). In humans, a mask excluding the hindbrain and the white matter was used prior to the analysis to compare the dictionary learning of the two species in a similar space.

5.6.4 Large scale network identification by seed-based analysis

Seeds corresponded to each region of the 3D functional atlas. The BOLD signal was averaged within each seed. The functional connection between the seed's mean BOLD signal and the BOLD signal in any voxel of the brain was estimated using a first-level general linear model (Nistats (Abraham et al., 2014)). The within-animal effect (*i.e.* the two series of MR images from each animal) was entered as a predictor (design matrix) and the mean seed time course as regressor. The model directly returned a fixed effect of the seed across the two sessions, producing 14 z-statistic maps. The functional regions previously identified were used as seeds. For each seed, a visual inspection of the animal mean z-statistic maps allowed the selection of four distinct large scale networks that were spread over the whole brain.

5.7 Identification of functional regions from dictionary-learning and seed-based maps

Dictionary learning and seed-based analysis produced maps showing pixels belonging to different networks. These maps were extracted and pasted into the 3D functional atlas. A brain region was considered to be part of a specific network when the volume of labelled voxels within the map occupied at least 30% of that region.

5.8 Evaluation of functional hubness and small-worldness features of mouse lemur brains by graph theory analysis

We consider in this analysis the absolute value of the correlation coefficient as performed routinely in human fMRI graph theory studies (De Vico Fallani et al., 2014).

5.8.1 Brain hubs in mouse lemurs

Eigenvector centrality, a measure of "hubness", was measured using NetworkX (Hagberg et al., 2008).

5.8.2 Small-worldness of mouse lemur brain networks

Network topology can be characterized using two small-world coefficients (σ and ω) (NetworkX (Hagberg et al., 2008)).

σ is defined as $\sigma = \frac{C/\mathrm{Crand}}{L/\mathrm{Lrand}}$ (Watts and Strogatz, 1998)

ω is defined as $\omega = \frac{L}{\mathrm{Lrand}} - \frac{C}{\mathrm{Crand}}$ (Telesford et al., 2011).

With C and L being, respectively, the average clustering coefficient (a measure of network segregation) and the average shortest path length (a measure of integration) of the network. Crand and Lrand are their equivalent derived random networks. Small-world networks have σ values superior to 1 and ω values close to 0 (Telesford et al., 2011).

6. Acknowledgements

7. Competing interests

The authors do not have financial and non-financial competing interests in relation to the work described.

8. References

Abraham, A., Pedregosa, F., Eickenberg, M., Gervais, P., Mueller, A., Kossaifi, J., Gramfort, A., Thirion, B., & Varoquaux, G. (2014). Machine learning for neuroimaging with scikit-learn. *Front Neuroinform, 8*, 14. doi:10.3389/fninf.2014.00014

Aujard, F., & Vasseur, F. (2001). Effect of ambient temperature on the body temperature rhythm of male gray mouse lemurs (*microcebus murinus*). *Int J Primatol, Vol. 22, No. 1, 2001*. doi:10.1023/A:1026461914534

Barttfeld, P., Uhrig, L., Sitt, J. D., Sigman, M., Jarraya, B., & Dehaene, S. (2015). Signature of consciousness in the dynamics of resting-state brain activity. *Proc Natl Acad Sci U S A, 112*(3), 887-892. doi:10.1073/pnas.1418031112

Bastian, M., Heymann, S., & Jacomy, M. (2009). *Gephi: an open source software for exploring and manipulating networks*. International AAAI Conference on Weblogs and Social Media, San Jose, California, USA. https://www.aaai.org/ocs/index.php/ICWSM/09/paper/view/154. doi:10.13140/2.1.1341.1520

Beckmann, C. F., DeLuca, M., Devlin, J. T., & Smith, S. M. (2005). Investigations into resting-state connectivity using independent component analysis. *Philos Trans R Soc Lond B Biol Sci, 360*(1457), 1001-1013. doi:10.1098/rstb.2005.1634

Belcher, A. M., Yen, C. C., Stepp, H., Gu, H., Lu, H., Yang, Y., Silva, A. C., & Stein, E. A. (2013). Large-scale brain networks in the awake, truly resting marmoset monkey. *J Neurosci, 33*(42), 16796-16804. doi:10.1523/JNEUROSCI.3146-13.2013

Biswal, B., Yetkin, F. Z., Haughton, V. M., & Hyde, J. S. (1995). Functional connectivity in the motor cortex of resting human brain using echo-planar MRI. *Magn Reson Med, 34*(4), 537-541. doi:10.1002/mrm.1910340409

Bons, N., Silhol, S., Barbie, V., Mestre-Frances, N., & Albe-Fessard, D. (1998). A stereotaxic atlas of the grey lesser mouse lemur brain (*microcebus murinus*). *Brain Res Bull, 46*(1-2), 1-173. doi:10.1016/S0361-9230(97)00458-9

Brier, M. R., Mitra, A., McCarthy, J. E., Ances, B. M., & Snyder, A. Z. (2015). Partial covariance based functional connectivity computation using Ledoit-Wolf covariance regularization. *Neuroimage, 121*, 29-38. doi:10.1016/j.neuroimage.2015.07.039

Brodmann, K. (1999 (original in 1909)). Brodmann's localisation in the cerebral cortex [Vergleichende lokalisationslehre der grosshirnrinde in ihren orinzipien dargestellt auf grund des zellenbaus] (Imperial College Press ed.): Garey, Laurence J.

Buckner, R. L., Andrews-Hanna, J. R., & Schacter, D. L. (2008). The brain's default network. *Annals of the New York Academy of Sciences, 1124*(1), 1-38. doi:10.1196/annals.1440.011

Buckner, R. L., Snyder, A. Z., Shannon, B. J., LaRossa, G., Sachs, R., Fotenos, A. F., Sheline, Y. I., Klunk, W. E., Mathis, C. A., Morris, J. C., & Mintun, M. A. (2005). Molecular, structural, and functional characterization of Alzheimer's disease: evidence for a relationship between default activity, amyloid, and memory. *J Neurosci, 25*(34), 7709-7717. doi:10.1523/JNEUROSCI.2177-05.2005

Bullmore, E., & Sporns, O. (2009). Complex brain networks: graph theoretical analysis of structural and functional systems. *Nat Rev Neurosci, 10*(3), 186-198. doi:10.1038/nrn2575

Burkart, J. M., Schubiger, M. N., & van Schaik, C. P. (2016). The evolution of general intelligence. *Behavioral and Brain Sciences, 40*, e195. doi:10.1017/S0140525X16000959

Cox, R. W. (1996). AFNI: software for analysis and visualization of functional magnetic resonance neuroimages. *Comput Biomed Res, 29*(3), 162-173. doi:10.1006/cbmr.1996.0014

Craddock, R. C., James, G. A., Holtzheimer, P. E., 3rd, Hu, X. P., & Mayberg, H. S. (2012). A whole brain fMRI atlas generated via spatially constrained spectral clustering. *Hum Brain Mapp, 33*(8), 1914-1928. doi:10.1002/hbm.21333

D'Souza, D. V., Jonckers, E., Bruns, A., Künnecke, B., von Kienlin, M., Van der Linden, A., Mueggler, T., & Verhoye, M. (2014). Preserved modular network organization in the sedated rat brain. *PLoS One, 9*(9), e106156. doi:10.1371/journal.pone.0106156

Damoiseaux, J. S., Rombouts, S. A., Barkhof, F., Scheltens, P., Stam, C. J., Smith, S. M., & Beckmann, C. F. (2006). Consistent resting-state networks across healthy subjects. *Proc Natl Acad Sci U S A, 103*(37), 13848-13853. doi:10.1073/pnas.0601417103

De Vico Fallani, F., Richiardi, J., Chavez, M., & Achard, S. (2014). Graph analysis of functional brain networks: practical issues in translational neuroscience. *Philos*

Trans R Soc Lond B Biol Sci, 369(1653). doi:10.1098/rstb.2013.0521

Djelti, F., Dhenain, M., Terrien, J., Picq, J. L., Hardy, I., Champeval, D., Perret, M., Schenker, E., Epelbaum, J., & Aujard, F. (2016). Impaired fasting blood glucose is associated to cognitive impairment and cerebral atrophy in middle-aged non-human primates. *Aging (Albany NY), 9*(1), 173-186. doi:10.18632/aging.101148

Friston, K. J., Holmes, A. P., Worsley, K. J., Poline, J. P., Frith, C. D., & Frackowiak, R. S. J. (1994). Statistical parametric maps in functional imaging: a general linear approach. *Hum. Brain Mapp., 2(4):189 - 210*. doi:10.1002/hbm.460020402

Gao, L. L., & Wu, T. (2016). The study of brain functional connectivity in Parkinson's disease. *Transl Neurodegener, 5*, 18. doi:10.1186/s40035-016-0066-0

Gerits, A., Farivar, R., Rosen, B. R., Wald, L. L., Boyden, E. S., & Vanduffel, W. (2012). Optogenetically induced behavioral and functional network changes in primates. *Current Biology, 22*(18), 1722-1726. doi:10.1016/j.cub.2012.07.023

Ghahremani, M., Menon, R. S., Everling, S., & Hutchison, R. M. (2016). Frontoparietal functional connectivity in the common marmoset. *Cereb Cortex, 27*(8), 3890-3905. doi:10.1093/cercor/bhw198

Goense, J. B., Ku, S. P., Merkle, H., Tolias, A. S., & Logothetis, N. K. (2008). fMRI of the temporal lobe of the awake monkey at 7 T. *Neuroimage, 39*(3), 1081-1093. doi:10.1016/j.neuroimage.2007.09.038

Gorgolewski, K., Burns, C. D., Madison, C., Clark, D., Halchenko, Y. O., Waskom, M. L., & Ghosh, S. S. (2011). Nipype: a flexible, lightweight and extensible neuroimaging data processing framework in python. *Front Neuroinform, 5*, 13. doi:10.3389/fninf.2011.00013

Grayson, D. S., Bliss-Moreau, E., Machado, C. J., Bennett, J., Shen, K., Grant, K. A., Fair, D. A., & Amaral, D. G. (2016). The rhesus monkey connectome predicts disrupted functional networks resulting from pharmacogenetic inactivation of the amygdala. *Neuron, 91*(2), 453-466. doi:10.1016/j.neuron.2016.06.005

Hagberg, A. A., Schult, D. A., & Swart, P. J. (2008). *Exploring network structure, dynamics, and function using NetworkX*. Proceedings of the 7th Python in Science Conference, Pasadena, CA.

Hampson, M., Driesen, N. R., Skudlarski, P., Gore, J. C., & Constable, R. T. (2006). Brain connectivity related to working memory performance. *J Neurosci, 26*(51), 13338-13343. doi:10.1523/JNEUROSCI.3408-06.2006

Herrero, M. T., Barcia, C., & Navarro, J. M. (2002). Functional anatomy of thalamus and basal ganglia. *Childs Nerv Syst, 18*(8), 386-404. doi:10.1007/s00381-002-0604-1

Hutchison, R. M., Hutchison, M., Manning, K. Y., Menon, R. S., & Everling, S. (2014). Isoflurane induces dose-dependent alterations in the cortical connectivity profiles and dynamic properties of the brain's functional architecture. *Hum Brain Mapp, 35*(12), 5754-5775. doi:10.1002/hbm.22583

Hutchison, R. M., Mirsattari, S. M., Jones, C. K., Gati, J. S., & Leung, L. S. (2010). Functional networks in the anesthetized rat brain revealed by independent component analysis of resting-state FMRI. *J Neurophysiol, 103*(6), 3398-3406. doi:10.1152/jn.00141.2010

Hutchison, R. M., Womelsdorf, T., Gati, J. S., Leung, L. S., Menon, R. S., & Everling, S. (2012). Resting-state connectivity identifies distinct functional networks in macaque cingulate cortex. *Cereb Cortex, 22*(6), 1294-1308. doi:10.1093/cercor/bhr181

Kraska, A., Dorieux, O., Picq, J. L., Petit, F., Bourrin, E., Chenu, E., Volk, A., Perret, M., Hantraye, P., Mestre-Frances, N., Aujard, F., & Dhenain, M. (2011). Age-associated cerebral atrophy in mouse lemur primates. *Neurobiol Aging, 32*(5), 894-906. doi:10.1016/j.neurobiolaging.2009.05.018

Landeau, B., Mutlu, J., Chételat, G., Desgranges, B., Gaubert, M., & de La Sayette, V. (2017). Distinct influence of specific versus global connectivity on the different Alzheimer's disease biomarkers. *Brain, 140*(12), 3317-3328. doi:10.1093/brain/awx279

Le Gros Clark, W. (1931). The brain of *microcebus murinus*. *Proc Zool Soc London*. doi:1931;101(2):463-86

Ledoit, O., & Wolf, M. (2004). A well-conditioned estimator for large-dimensional covariance matrices. *Journal of Multivariate Analysis, 88*(2), 365-411. doi:10.1016/S0047-259X(03)00096-4

Lee, M. H., Smyser, C. D., & Shimony, J. S. (2013). Resting-state fMRI: a review of methods and clinical applications. *AJNR Am J Neuroradiol, 34*(10), 1866. doi:10.3174/ajnr.A3263

Li, C. X., & Zhang, X. (2018). Evaluation of prolonged administration of isoflurane on cerebral blood flow and default mode network in macaque monkeys anesthetized with different maintenance doses. *Neurosci Lett, 662*, 402-408.

doi:10.1016/j.neulet.2017.10.034

Lu, H., Zou, Q., Gu, H., Raichle, M. E., Stein, E. A., & Yang, Y. (2012). Rat brains also have a default mode network. *Proc Natl Acad Sci U S A, 109*(10), 3979-3984. doi:10.1073/pnas.1200506109

Ma, Z., Perez, P., Ma, Z., Liu, Y., Hamilton, C., Liang, Z., & Zhang, N. (2018). Functional atlas of the awake rat brain: A neuroimaging study of rat brain specialization and integration. *Neuroimage, 170*, 95-112. doi:10.1016/j.neuroimage.2016.07.007

Mechling, A. E., Hubner, N. S., Lee, H. L., Hennig, J., von Elverfeldt, D., & Harsan, L. A. (2014). Fine-grained mapping of mouse brain functional connectivity with resting-state fMRI. *Neuroimage, 96*, 203-215. doi:10.1016/j.neuroimage.2014.03.078

Mensch, A., Varoquaux, G., & Thirion, B. (2016). *Compressed online dictionary learning for fast resting-state fMRI decomposition*. International Symposium on Biomedical Imaging, Prague, Czech Republic. https://hal.archives-ouvertes.fr/hal-01271033. doi:10.1109/isbi.2016.7493501

Mestre-Frances, N., Serratrice, N., Gennetier, A., Devau, G., Cobo, S., Trouche, S. G., Fontes, P., Zussy, C., De Deurwaerdere, P., Salinas, S., Mennechet, F. J., Dusonchet, J., Schneider, B. L., Saggio, I., Kalatzis, V., Luquin-Piudo, M. R., Verdier, J. M., & Kremer, E. J. (2018). Exogenous LRRK2G2019S induces parkinsonian-like pathology in a nonhuman primate. *JCI Insight, 3*(14). doi:10.1172/jci.insight.98202

Mohan, A., Roberto, A. J., Mohan, A., Lorenzo, A., Jones, K., Carney, M. J., Liogier-Weyback, L., Hwang, S., & Lapidus, K. A. (2016). The significance of the default mode network (DMN) in neurological and neuropsychiatric disorders: a review. *Yale J Biol Med, 89*(1), 49-57.

Montgomery, S. H., Capellini, I., Barton, R. A., & Mundy, N. I. (2010). Reconstructing the ups and downs of primate brain evolution: implications for adaptive hypotheses and Homo floresiensis. *BMC Biol, 8*, 9. doi:10.1186/1741-7007-8-9

Nadkarni, N. A., Bougacha, S., Garin, C., Dhenain, M., & Picq, J. L. (2018). A 3D population-based brain atlas of the mouse lemur primate with examples of applications in aging studies and comparative anatomy. *Neuroimage, 185*, 85-95. doi:10.1016/j.neuroimage.2018.10.010

Nelissen, K., & Vanduffel, W. (2011). Grasping-related functional magnetic resonance

imaging brain responses in the macaque monkey. *J Neurosci, 31*(22), 8220-8229. doi:10.1523/jneurosci.0623-11.2011

Oguz, I., Zhang, H., Rumple, A., & Sonka, M. (2014). RATS: Rapid Automatic Tissue Segmentation in rodent brain MRI. *J Neurosci Methods, 221*, 175-182. doi:10.1016/j.jneumeth.2013.09.021

Power, J. D., Schlaggar, B. L., & Petersen, S. E. (2014). Studying brain organization via spontaneous fMRI signal. *Neuron, 84*(4), 681-696. doi:10.1016/j.neuron.2014.09.007

Raichle, M. E. (2011). The restless brain. *Brain Connect, 1*(1), 3-12. doi:10.1089/brain.2011.0019

Sawiak, S. J., Picq, J. L., & Dhenain, M. (2014). Voxel-based morphometry analyses of in vivo MRI in the aging mouse lemur primate. *Front Aging Neurosci, 6*, 82. doi:10.3389/fnagi.2014.00082

Schroeter, A., Schlegel, F., Seuwen, A., Grandjean, J., & Rudin, M. (2014). Specificity of stimulus-evoked fMRI responses in the mouse: the influence of systemic physiological changes associated with innocuous stimulation under four different anesthetics. *Neuroimage, 94*, 372-384. doi:10.1016/j.neuroimage.2014.01.046

Shen, K., Bezgin, G., Hutchison, R. M., Gati, J. S., Menon, R. S., Everling, S., & McIntosh, A. R. (2012). Information processing architecture of functionally defined clusters in the macaque cortex. *J Neurosci, 32*(48), 17465-17476. doi:10.1523/JNEUROSCI.2709-12.2012

Sierakowiak, A., Monnot, C., Aski, S. N., Uppman, M., Li, T. Q., Damberg, P., & Brene, S. (2015). Default mode network, motor network, dorsal and ventral basal ganglia networks in the rat brain: comparison to human networks using resting state-fMRI. *PLoS One, 10*(3), e0120345. doi:10.1371/journal.pone.0120345

Solé-Padullés, C., Castro-Fornieles, J., de la Serna, E., Calvo, R., Baeza, I., Moya, J., Lázaro, L., Rosa, M., Bargalló, N., & Sugranyes, G. (2016). Intrinsic connectivity networks from childhood to late adolescence: Effects of age and sex. *Dev Cogn Neurosci, 17*, 35-44. doi:10.1016/j.dcn.2015.11.004

Telesford, Q. K., Joyce, K. E., Hayasaka, S., Burdette, J. H., & Laurienti, P. J. (2011). The ubiquity of small-world networks. *Brain Connect, 1*(5), 367-375. doi:10.1089/brain.2011.0038

Tzourio-Mazoyer, N., Landeau, B., Papathanassiou, D., Crivello, F., Etard, O.,

Delcroix, N., Mazoyer, B., & Joliot, M. (2002). Anatomical labeling of activations in SPM using a macroscopic anatomical parcellation of the MNI MRI single-subject brain. *Neuroimage, 15*(1), 273-289. doi:10.1006/nimg.2001.0978

Varoquaux, G., Gramfort, A., Pedregosa, F., Michel, V., & Thirion, B. (2011). Multi-subject dictionary learning to segment an atlas of brain spontaneous activity. *Inf Process Med Imaging, 22*, 562-573.

Varoquaux, G., Gramfort, A., Poline, J. B., & Thirion, B. (2012). Markov models for fMRI correlation structure: Is brain functional connectivity small world, or decomposable into networks? *J Physiol Paris, 106*(5-6), 212-221. doi:10.1016/j.jphysparis.2012.01.001

Vincent, D. B., Jean-Loup, G., Renaud, L., & Etienne, L. (2008). Fast unfolding of communities in large networks. *J Stat Mech Theory Exp, 2008*(10), P10008.

Vincent, J. L., Patel, G. H., Fox, M. D., Snyder, A. Z., Baker, J. T., Van Essen, D. C., Zempel, J. M., Snyder, L. H., Corbetta, M., & Raichle, M. E. (2007). Intrinsic functional architecture in the anaesthetized monkey brain. *Nature, 447*(7140), 83-86. doi:10.1038/nature05758

Watts, D. J., & Strogatz, S. H. (1998). Collective dynamics of 'small-world' networks. *Nature, 393*(6684), 440-442. doi:10.1038/30918

Yushkevich, P. A., Piven, J., Hazlett, H. C., Smith, R. G., Ho, S., Gee, J. C., & Gerig, G. (2006). User-guided 3D active contour segmentation of anatomical structures: significantly improved efficiency and reliability. *Neuroimage, 31*(3), 1116-1128. doi:10.1016/j.neuroimage.2006.01.015

Resting state cerebral networks in mouse lemur primates: from multilevel validation to comparison with humans

Clément M. Garin, Nachiket A. Nadkarni, Brigitte Landeau, Gaël Chételat,

Jean-Luc Picq, Salma Bougacha, Marc Dhenain

Supplementary Data

Supplementary Tables

	Sex	Age (months)	Age (years)	Anatomical brain lesion
283EA	M	10.6	0.9	No
365A	M	10.6	0.9	No
285AB	M	10.7	0.9	No
285AAA	M	16.5	1.4	No
283CCA	M	16.6	1.4	No
263BCE	M	17.8	1.5	No
314CA	M	18.0	1.5	No
283CA	M	22.4	1.9	No
285E	M	22.6	1.9	No
276BC	M	28.0	2.3	No
285D	M	28.1	2.3	No
289BB	F	28.8	2.4	No
300BA	M	29.8	2.5	No
288BC	F	37.3	3.1	Yes
208CBF	F	37.5	3.1	No
310C	F	39.9	3.3	Yes

Supplementary Table 1. Cohort of mouse lemurs involved in the study.

	Modules	Dictionary learning	Seed-based
Default mode-like	Cingulum Post		
	Cingulum Ant		
	Frontal Sup Post		
	Parietal (R&L)		
	Supp Motor Area (R&L)		Frontal Mid
	Postcentral (R&L)		Dorsal thalamus
Visual	Occipital Pole (R&L)		
	Cuneus		
	Occipital Mid (R&L)		
	Occipital Inf (L)		
	Temporal Inf (L)	Occipital Inf (R)	
Frontal	Frontal Sup Ant		
	Frontal Mid (R&L)		
	Precentral (R&L)	Frontal Sup Post	
		Cingulum Ant	
Temporal	Temporal Sup (R&L)		
	Temporal Mid (R&L)		
	Temporal Inf (R)		
	Posterior putamen (R)		
Somato-motor		Supp Motor Area (R&L)	
		Postcentral (R&L)	
		Temporal Sup (R&L)	
		Cingulum Ant	
		Parietal (L)	
		Precentral (R&L)	Parietal (R)
			Frontal Mid
			Frontal Sup Post
			Cingulum Post
			Caudate nucleus Post (R)
			Dorsal thalamus
Basal ganglia	Striatum Ant (R&L)		
	Caudate nucleus Post (R&L)		
	Putamen Post (L)		
	Amygdala (R&L)		Frontal Sup Post
	Basal forebrain		Cingulum Ant
	Septal nuclei		
	Hypothalamus	Putamen Post (R)	
	Globus pallidus		
Thalamic	Dorsal thalamus		
	Ventral thalamus (R&L)		
	Hippocampus (R&L)		
	Colliculus (R&L)		
	Pons		
	Midbrain		
	Occipital Inf (R)	Basal forebrain	
		Septal nuclei	
		Globus pallidus	

Supplementary Table 2. Comparison of the regions belonging to the different networks extracted with module, dictionary learning and seed-based analysis. Regions that were identified with different methods are grouped within a single case. The 3D functional atlas was pasted on different networks obtained by dictionary learning or seed-based analysis. A region was considered to belong to a network when more than 30% of its volume belonged to this network.

	Robust functional regions
Default mode-like	Cingulum Post
	Cingulum Ant
	Frontal Sup Post
	Parietal (R&L)
Visual	Occipital Pole (R&L)
	Occipital Mid (R&L)
	Occipital Inf (L)
	Cuneus
Fronto-temporal	Frontal Sup Ant
	Frontal Mid (R&L)
	Frontal Sup Post
	Cingulum Ant
	Temporal Sup (R&L)
	Temporal Mid (R&L)
Somato-motor	Postcentral (R&L)
	Supp Motor Area (R&L)
	Temporal Sup (R&L)
	Cingulum Ant
	Parietal (L)
Basal ganglia	Striatum Ant (R&L)
	Caudate nucleus Post (R&L)
	Putamen Post (L)
	Amygdala (R&L)
	Basal forebrain
	Septal nuclei
Thalamic	Dorsal thalamus
	Ventral thalamus (R&L)
	Hippocampus (R&L)
	Colliculus (R&L)
	Pons
	Midbrain

Supplementary Table 3. Robust functional networks in mouse lemur primates.
This table displays components that could be identified by two or three methods. The different networks are the DMN, visual, fronto-temporal, somato-motor, basal ganglia and thalamic networks.
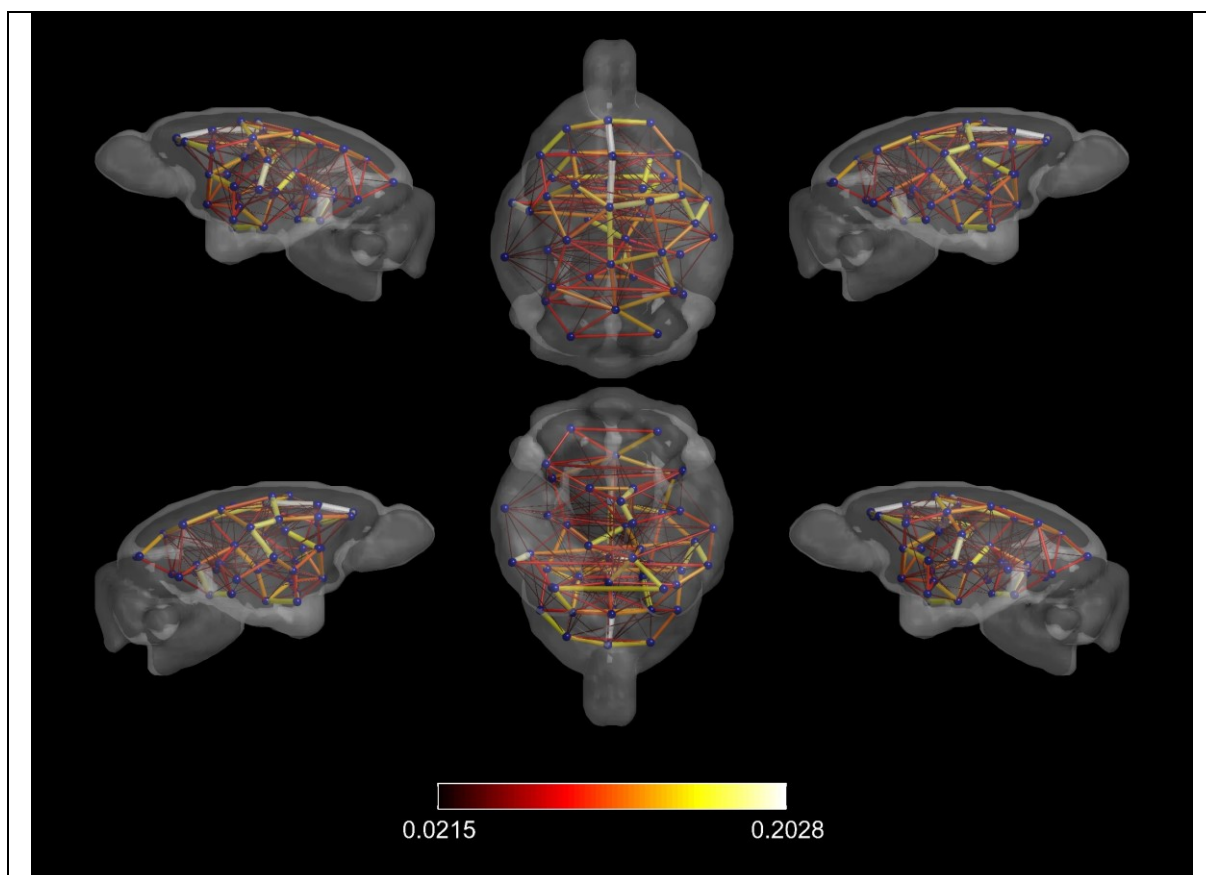
Supplementary Figure 1. Whole brain network in mouse lemurs.
Mean correlation matrix showing the mouse lemur brain network represented on a 3D mouse lemur brain space using BrainNet (Xia et al., 2013). Nodes represent the local functional regions extracted from our 3D functional atlas. They were spatially distributed based on their center of mass. Edges between the nodes represent the mean partial correlation from the 28 mouse lemurs. Color and size of these edges are proportional to this correlation. The color bar represents partial correlation values.
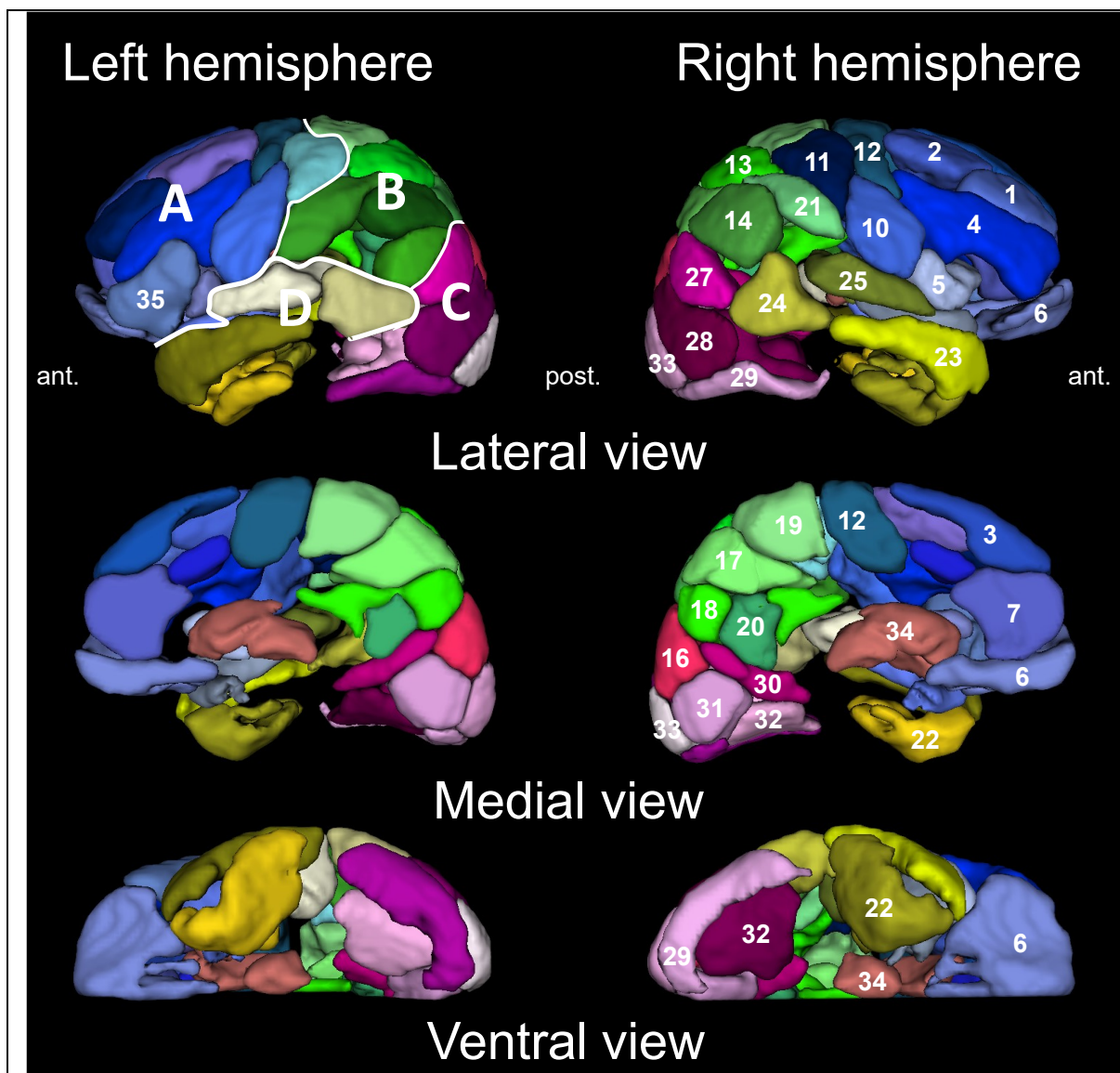
Supplementary Figure 2. Human 3D functional atlas based on dictionary learning.

Functional regions based on dictionary learning. Fifty six local functional regions were identified from the 35 sparse components (region volume ≥ 5000 mm^3). Brain regions were classified based on their locations within the frontal (A), parietal (B), occipital (C), and temporal (D) lobes and on the "AAL for SPM12" atlas (Tzourio-Mazoyer et al., 2002). We display three different views. 1. Frontal Superior Anterior, 2. Frontal Superior Posterior, 3. Frontal Superior Medial, 4. Frontal Middle, 5. Frontal Inferior Opercular, 6. Frontal Orbital, 7. Cingulum Anterior, 8. Cingulum Middle, 9. Insula, 10. Precentral, 11. Postcentral, 12. Supplementary Motor Area, 13. Parietal Superior Anterior, 14. Parietal Inferior, 15. Angular, 16. Parietal Superior Posterior, 17. Precuneus Anterior, 18. Precuneus Posterior, 19. Paracentral Lobule, 20. Cingulum Posterior, 21. Supramarginal, 22. Temporal Inferior, 23. Temporal Middle Anterior, 24. Temporal Middle Posterior, 25. Temporal Superior, 26. Cuneus, 27. Occipital Superior, 28. Occipital Middle, 29. Occipital Inferior, 30. Calcarine, 31. Lingual, 32. Fusiform, 33. Occipital Pole, 34. Striatum-Thalamus, 35. Frontal Inferior.
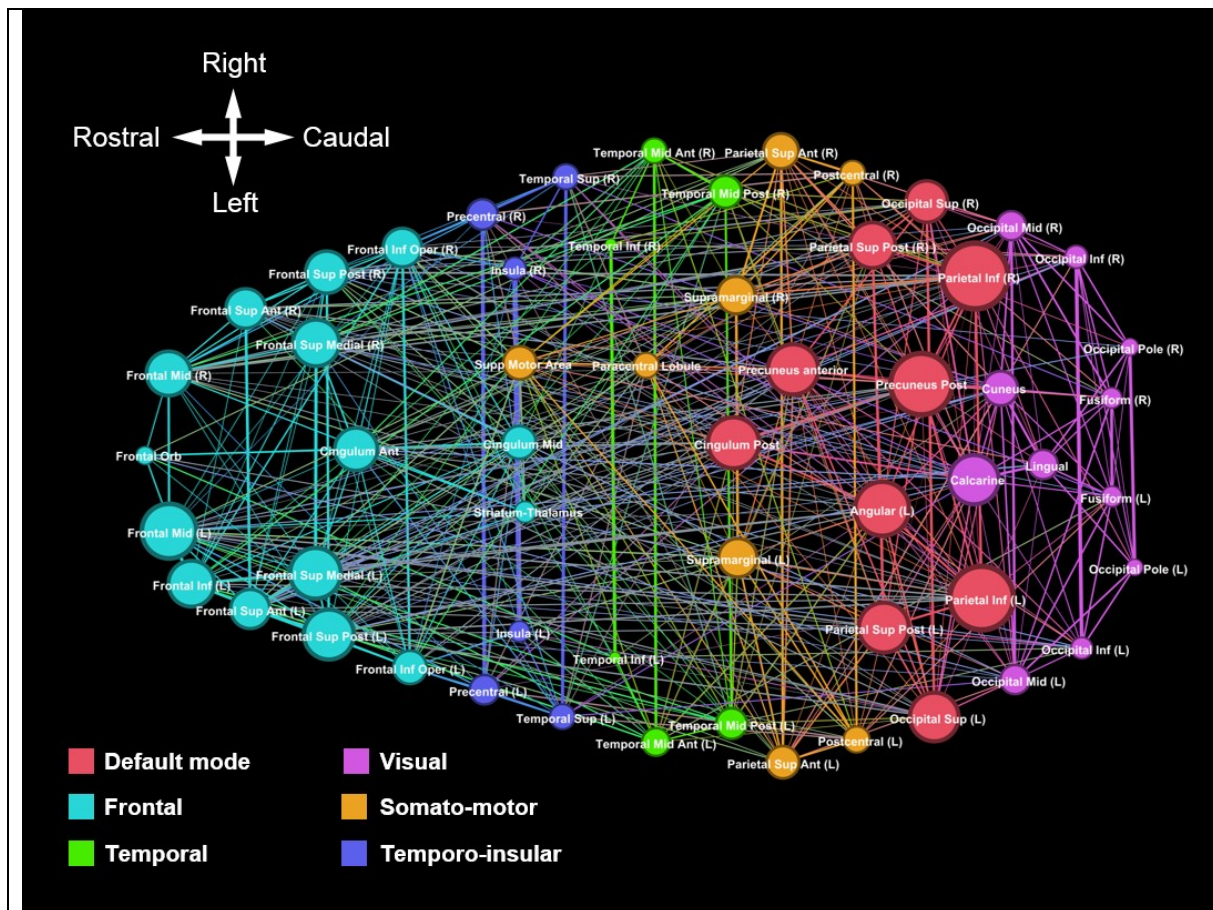
Supplementary Figure 3. Human networks identified using graph analysis based on 56 functional regions.
Using graph analysis, we partitioned the human brain into six cortical and subcortical modules. A color and a name were assigned to each module. Colors highlight interactions between different nodes, *i.e.* they outline large scale networks. Eigenvector centrality, a measure of node influence, is represented by the node size.
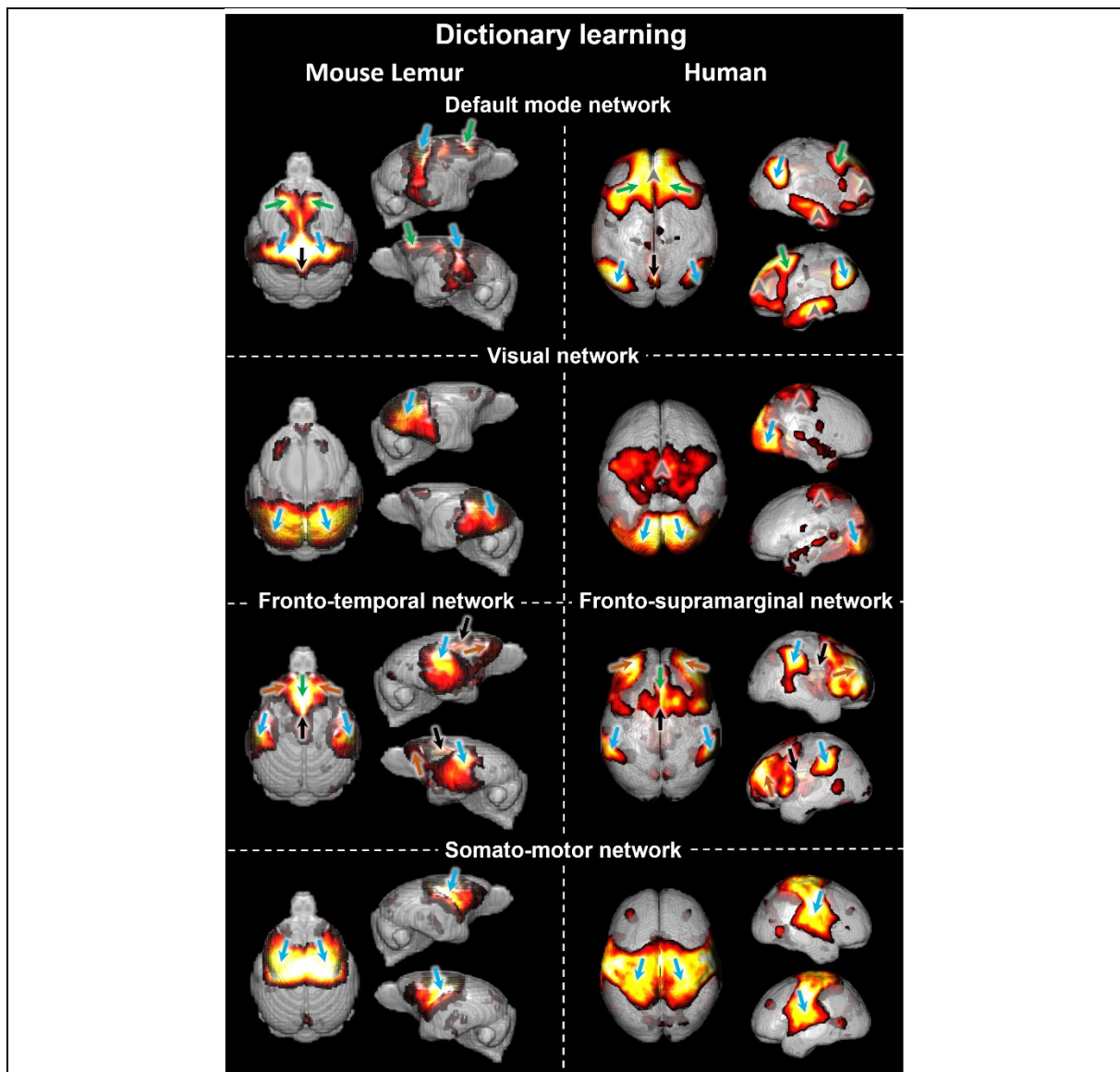
Supplementary Figure 4. Comparison of the resting state network organization in humans and mouse lemurs.

Functional spatial maps extracted with dictionary learning are displayed side by side. Four cortical networks were matched between lemurs and humans. They were classified as default mode network, visual, fronto-temporal/supramarginal, and somato-motor. Regions that are similar across species are pointed out with arrows. In the DMN-like network, frontal cortex (green arrows), posterior cingulum cortex (black arrows), parietal cortex (blue arrows) were detected in both species. The superior medial frontal and temporal cortices (arrow-heads) were detected in humans but not in mouse lemurs. In the visual network, occipital cortex was detected in both species. An additional independent region was detected in the paracentral lobule and postcentral cortices in humans (arrow-head). For the fronto-temporal/supramarginal network the middle frontal (brown arrows), superior frontal (green arrows) and anterior cingulate cortex (black arrow) were detected in both species. Interestingly, in humans the supramarginal cortex seems to fit with the superior temporal cortex, in lemurs (blue arrows). For the somato-motor network, regions were detected on both side of the central sulcus in humans and in a similar region in lemurs (in which there is no central sulcus). In humans, they were in parieto-frontal regions while in lemurs they involved more frontal regions (blue arrows).

References

Tzourio-Mazoyer, N., Landeau, B., Papathanassiou, D., Crivello, F., Etard, O., Delcroix, N., Mazoyer, B., & Joliot, M. (2002). Anatomical labeling of activations in SPM using a macroscopic anatomical parcellation of the MNI MRI single-subject brain. *Neuroimage, 15*(1), 273-289. doi:10.1006/nimg.2001.0978

Xia, M., Wang, J., & He, Y. (2013). BrainNet Viewer: a network visualization tool for human brain connectomics. *PLoS One, 8*(7), e68910. doi:10.1371/journal.pone.0068910

II.3. Study 3: Resting-state fMRI and glutamate measures in the brain of a non-human primate: relationships and age-related alterations

The biological parameters associated to the organization of brain regions into networks are still poorly understood. The ability to detect neuronal networks in mouse lemurs offers the opportunity to further characterize mechanisms responsible for network organization at the level of the whole brain in a primate. In a last part of the study, we characterized the relationships between resting-state fMRI and glutamate levels assessed by Chemical Exchange Saturation Transfer imaging of glutamate (gluCEST). We also evaluated the ability of the functional connectivity matrix to differentiate young and aged lemurs

Contribution: In this article I acquired the fMRI, gluCEST, anatomical images of the lemurs at 11.7T and coregistered them. I performed the functional connectivity analysis (hubs, etc.) and developed a pipeline to extract automatically the gluCEST signal using an atlas. Then, I designed and achieved the comparison between the two sequences as well as the two cohorts (old and middle aged lemurs). GluCEST signal acquisition and pre-treatment protocols were developed by J. Flament and J. Pépin (Pépin, 2018). These developments will not be discussed here.

II.3.1. Combination of fMRI and to other techniques

Many approaches have combined fMRI with other techniques to study neuronal activity. Often generated by physiological stimuli triggers, the neuronal activity induces characteristic responses such as electric currents, vascular reaction or metabolic variations. These responses can be registered thanks to a variety of methods such as electrophysiology to measure the voltage fluctuations; positron emission tomography (PET) and perfusion MRI to measure the cerebral blood flow; PET and NMR spectroscopy to measure glucose consumption/metabolisation and the synthesis of biomolecules such as neurotransmitters. This combination of techniques provides complementary approaches for the exploration of unknown mechanisms such as the characterization of the origin of the BOLD signal, the temporal and spatial characteristics of the neuronal activity in different tasks or pathologies, or as in this

study, the evaluation of an association between highly connected regions, local neuronal activity and glutamate.

II.3.1.1. Electrophysiology and fMRI

Electrophysiology is a technique measuring the voltage fluctuations resulting from ionic current produced by neuronal activity. In comparison to BOLD, electrophysiology provides a direct understanding of the neuronal activity. Therefore, electrophysiology can be used to improve the interpretability of many fMRI studies.

Concerning the neuronal origin of BOLD, Logothetis et al. found that the local field potential is a better theoretical predictor of BOLD signal than single or multiunit recording (Logothetis et al., 2001). This analysis was based on an experiment measuring the BOLD and the electrophysiological response to a stimulus within the visual cortex of anesthetized monkeys. This experiment suggested that BOLD pattern is more likely to represent local synaptic activity (local input) rather than the spiking activity (local output).

Scalp electroencephalography (EEG) or intracranial EEG recordings during sensory, cognitive motor and visual functions (Singh et al., 2003) have revealed positive correlations between electrophysiological signal and BOLD fluctuations. These positive correlations were mainly observed within the gamma ranges (>30 Hz) of the brain regions (network) activated by a given task (Mulert et al., 2010). Negative correlations were mostly reported in the low frequency range (Murta et al., 2015). At rest, Magri et al. found that the spontaneous activity registered with BOLD and local field potential in the visual cortex of macaques display similar relationship profiles than those in activated tasks (Magri et al., 2012). However, the profile of correlations between electrophysiological frequency and BOLD signal reveals a high level of complexity, poorly understood and that can't be reduced to simple and general rules. Indeed, Jann et al. found at rest (eyes closed), strong positive correlations between BOLD and alpha frequencies recorded with EEG, within regions of the DMN (Jann et al., 2009). Moreover, Mantini et al. suggest that each network could be characterized by a specific electrophysiological pattern or combination of frequencies ((D. Mantini et al., 2007); **Figure 25**). Other open questions such as the biological meaning of the BOLD negative response remains highly debated and the EEG profiles suggest that it could reflect a reduced neuronal activity (Moraschi et al., 2012).
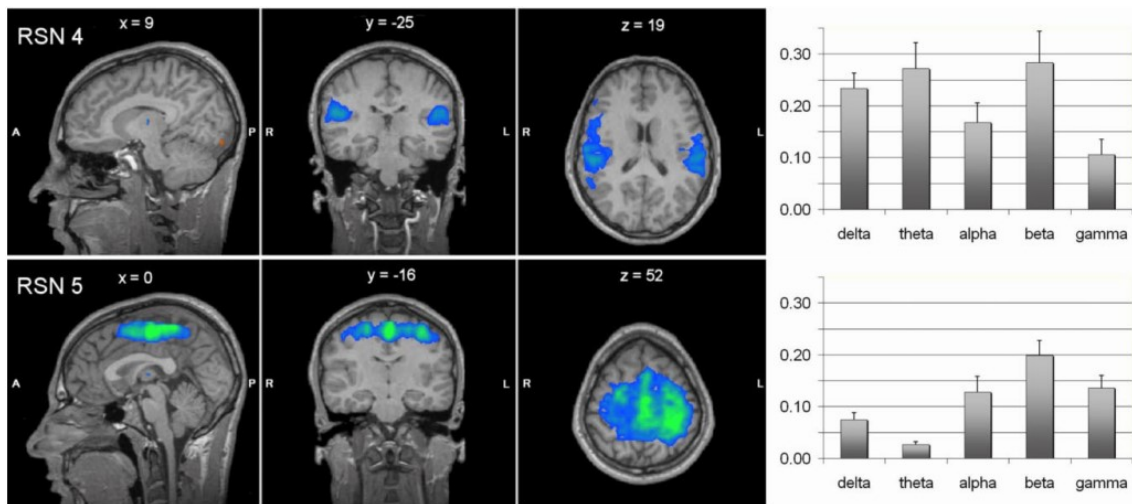
Figure 25 | Association between two rsfMRI networks and their EEG profiles. Auditory network (RSN 4) and motor network (RSN 5) associated with their extracted EEG rhythms. From (D. Mantini et al., 2007).

II.3.1.2. Positron emission tomography and fMRI

PET imaging is a technique used to quantify metabolic processes in the body. It detects the radioactivity emitted by radioactive tracers. A computer analysis will construct 3D images reflecting the concentration or the metabolised tracers within a period of time. As examples, fludeoxyglucose detect regional glucose uptake and $[^{15}O]H_2O$ quantify blood flow. The quantification of the cerebral blood flow with PET imaging allows for the identification of task related activation of several brain regions such as the frontal cortex during verbal working memory (Petrides et al., 1993). The complementarity PET imaging and fMRI has been largely illustrated with the discovery of the default mode network (DMN). Indeed, the DMN was first discovered using $[^{15}O]H_2O$ PET and identified brain regions decreasing their activity during cognitive tasks. ((Shulman et al., 1997) (Raichle et al., 2001); **Figure 26**). In a more recent study and with an interesting multimodal approach Shah et al. found that the glucose uptake measured with fluorodeoxyglucose PET was positively correlated with the activation of the DMN (N. J. Shah et al., 2017). The ability to observe different cerebral networks in rats, with fludeoxyglucose PET has been demonstrated at rest and with unilateral stimulation of the whiskers (Wehrl et al., 2013).
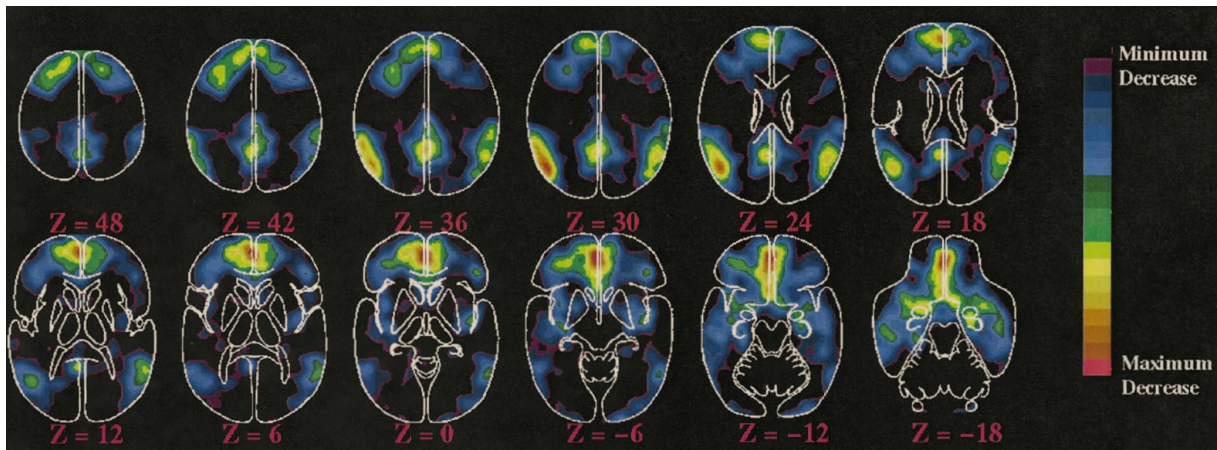
Figure 26 | Brain regions identified as decreasing their activity during cognitive tasks. The color bar represents the cerebral blood flow measured by [^{15}O]H$_2$O PET. From (Raichle et al., 2001).

II.3.1.3. NMR spectroscopy and fMRI

In vivo ^{1}H NMR spectroscopy is a well-established technique for the quantification of the brain metabolites at rest or during activation. However, cerebral metabolic changes during cognitive tasks are poorly understood. Prichard et al. was the first study to describe a metabolite (lactate) increase in the human visual cortex related to stimulation (Prichard et al., 1991). Then other similar studies reported metabolite variations related to stimulation, such as: lactate increase (≈23%), glutamate increase (≈3%) or aspartate decrease (≈15%) (Mangia et al., 2007). Another study observed during pain stimulation, a positive correlation between glutamate and BOLD variations whereas there was a negative correlation found between GABA and BOLD variations (Cleve et al., 2017). Furthermore, the metabolic variations of glutamate were highlighted in a study using a sequence that simultaneously quantifies glutamate and BOLD signals in the human visual cortex (Ip et al., 2017). This technique has recently gained attention due to a high temporal resolution allowing the quantification of glutamate concentration within time scale of under a minute (Stanley et Raz, 2018). Glutamate is one of the most ubiquitous excitatory neurotransmitters involved in the excitatory and inhibitory balance. As for BOLD, observing glutamate variations associated with cognitive processes will probably become possible in future studies. In cerebral networks, GABA was significantly correlated with DMN deactivation during task performance, whereas glutamate concentration was associated with a reduced deactivation (X. Chen et al., 2018) (Hu et al., 2013) (Kapogiannis et al., 2013).

In rodents, similar metabolic responses were found in anesthetized rats (Just et al., 2013). Moreover, Sonnay et al. found that a prolonged stimulation of the rat barrel cortex led to a BOLD signal decrease after an habituation period. Interestingly, they found a prevalence of oxidative metabolism during this prolonged stimulation period (Sonnay et al., 2017).

II.3.1.4.   Other techniques evaluating neuronal activity characteristics

The few techniques previously mentioned which evaluate the biological characteristics of neuronal activity are far to be exhaustive. As an example, the arterial spin labeling MRI or perfusions MRI is a technique measuring the cerebral blood flow. This technique extracted similar cerebral networks when compared to BOLD fMRI in humans (Zhu et al., 2013) and mice (Francesco Sforazzini et al., 2014). These studies attest the major role of cerebral blood flow in the detection of networks with fMRI.

Recently, optical imaging (multi-photon based microscopy) has shown spatial patterns of neuronal activation, traveling through the cerebral cortex and along stereotypical waves. The simultaneous use of neuronal calcium signal (sensitive to neuronal activity) and hemodynamic signal has established their spatial coactivation (Matsui et al., 2016) (Murakami et al., 2018). This result confirms that hemodynamic fluctuations reflect neuronal activity dynamics. In the same study, the delay between the hemodynamic response and the stimulus was also observed. These studies also highlight that the spatiotemporal trajectory of the infra-slow fluctuations of the calcium signal (<0.1 Hz) through the cortex were distinct from other frequencies (Mitra et al., 2018). Interestingly, this spatiotemporal trajectory was modified in anesthetized animals versus those awake.

To our knowledge no studies have evaluated the relationships between highly connected regions, neuronal activity, and regions with elevated glutamate. As for the previous techniques, assumptions were made to identify the biological origin of these associations. This promising combination of non-invasive biomarkers was also used to characterize a large spectrum of the aging process, and has many potential applications for neurodegenerative disease studies.

Resting-state fMRI and glutamate measures in the brain of a non-human primate: relationships and age-related alterations

Clément M. Garin [1,2], Nachiket A. Nadkarni[1,2], Jérémy Pépin J. [1,2], Salma Bougacha[1,2,3,4], Julien Flament [1,2], Marc Dhenain[1,2,*]

[1] Centre National de la Recherche Scientifique (CNRS), Université Paris-Sud, Université Paris-Saclay UMR 9199, Neurodegenerative Diseases Laboratory, 18 Route du Panorama, F-92265 Fontenay-aux-Roses, France

[2] Commissariat à l'Energie Atomique et aux Energies Alternatives (CEA), Direction de la Recherche Fondamentale (DRF), Institut François Jacob, MIRCen, 18 Route du Panorama, F-92265 Fontenay-aux-Roses, France

[3] Inserm, Inserm UMR-S U1237, Normandie Univ, UNICAEN, GIP Cyceron, Caen, France

[4] Normandie University, UNICAEN, EPHE, INSERM, U1077, CHU de Caen, Neuropsychologie et Imagerie de la Mémoire Humaine, 14000 Caen, France

Correspondence

Marc Dhenain
MIRCen, UMR CEA-CNRS 9199
18 Route du Panorama
92 265 Fontenay-aux-Roses CEDEX
France
Tel: +33 1 46 54 81 92; Fax: +33 1 46 54 84 51
email: Marc.Dhenain@cea.fr

1. Introduction

Resting state fMRI (rsfMRI) is a widely used method of functional magnetic resonance imaging (fMRI). It can evaluate brain function in a resting condition, *i.e.* when an explicit task is not being performed and detects blood-oxygen-level dependent (BOLD) signal, a proxy for neuronal activity.

rsfMRI can provide information on functional brain connectivity. This latter can be evaluated by measuring the level of co-activation of BOLD signal between brain regions, defined by the level of correlation between rsfMRI time-series. This allows the characterization of several cerebral networks in the brain (*e.g.* the default mode network (DMN) or sensorimotor networks) (Raichle, 2011). These networks are consistently found in healthy subjects, across species and represent specific patterns of synchronous activity. rsfMRI connectivity also allows the assessment of the level of information transfer through specific brain regions, *i.e.* a measure of hubness.

rsfMRI can also provide information on local neuronal activity by quantifying low-frequency oscillations (LFO) of BOLD signal (Biswal et al., 1995; Zou et al., 2008). For example, the total power of BOLD signal within the frequency range between 0.01 and 0.1 Hz is a LFO index (called amplitude of low-frequency fluctuation (ALFF)) that reflects neuronal activity. Typical patterns of ALFF are displayed in humans in resting state condition, with high values within the DMN (Fransson, 2006). ALFF is correlated with markers of glucose metabolism as well as with functional connectivity (Aiello et al., 2015) or diffusion-based measures of connectivity (Lee et Xue, 2017).

The impacts of multiple neurotransmitters on local cerebral regions are largely evaluated in neuroscience. High level of serotonin innervation from dorsal raphe nucleus to the rest of the brain has been related to the high connectivity of this structure with the rest of the brain (Noori et al., 2017). Also, regional serotonin-1A receptor binding predicts BOLD signal change in three different DMN nodes (retrosplenial, posterior cingulate and dorsomedial prefrontal cortices) (Hahn et al., 2012). Relationships between GABA, the chief inhibitory neurotransmitter in the brain and reduction of network activity have also been reported in the DMN (Kapogiannis et al., 2013). However, the impact of neurotransmitters on functional brain connectivity and neuronal activity is still poorly described at the level of the whole brain.

Glutamate is the principal excitatory neurotransmitter in the brain and is involved in multiple cognitive functions. It is an essential amino acid of the brain metabolism and has the highest amino acid concentration of the brain ($\approx$10 mmol/kg) (Greenamyre,

1986; Niciu et al., 2012). In normal conditions, most of glutamate is located in cells including astrocytes (Cooper et Jeitner, 2016) that surrounds the synapses, neurotransmission being governed by few micromolar of extracellular glutamate. In addition to its major role as an excitatory neurotransmitter, glutamate is central to several metabolic pathways related to energy metabolism and oxidative stress (Y. Zhou et Danbolt, 2014).

Studies combining MR spectroscopy (MRS) and fMRI reported positive correlation between glutamate and BOLD signal (Cleve et al., 2017; Ip et al., 2017). Furthermore, there is evidence suggesting that glutamate/glutamine may modulate functional connectivity (Horn et al., 2010). In cerebral networks glutamate concentration was associated with a reduced deactivation of the DMN in response to task performance (Chen et al., 2018; Y. Hu et al., 2013; Kapogiannis et al., 2013).

Until now, relationships between neurotransmitters and rsfMRI-based indexes of neuronal network connectivity or function were mainly based on the monitoring of neurotransmitters by MRS. One limitation of MRS is that measurements are confined to relatively large voxels, due to limited sensitivity of the method. Recent developments of gluCEST (Chemical Exchange Saturation Transfer of glutamate) imaging allow the quantification of glutamate at the level of the whole brain (Cai et al., 2012; Carrillo-de Sauvage et al., 2015). This opens the possibility to directly compare glutamate activity and rsfMRI-based indexes of neuronal network connectivity or function at the level of the whole brain.

The mouse lemur (*Microcebus murinus*) is a primate attracting increased attention in neuroscience research. This small animal (typical length 12cm, 60-120g weight) has a decade-long lifespan and is a model for studying cerebral aging (Sawiak et al., 2014) or Alzheimer's disease (Kraska et al., 2011). It displays neuronal networks (default-mode like, temporo-prefrontal, somato-motor, visual, thalamic and basal ganglia networks) that are largely similar to those reported in humans (Garin et al., 2019). Because of its small size, it can fit in small bore high field (11.7 T) MRI during resting state conditions. This allows to perform rsfMRI and gluCEST images with optimal conditions.

In this study, we evaluated relationships between rsfMRI indexes of functional connectivity (hubness) or neuronal function (ALFF), and gluCEST signal in two cohorts of middle-aged and old mouse lemurs. Evaluations were performed at the level of individual brain regions or of large scale neuronal networks. Different indexes of

connectivity, ALFF as well as gluCEST signal were strongly correlated. This suggests that connectivity and neuronal function are strongly modulated by glutamate level. Comparison between middle-aged and old lemurs revealed a decrease of the ALFF in the DMN associated to a decrease of the anterior cingulate cortex centrality index of hubness.

2. Results

2.1. ALFF in the mouse lemur brain

Resting-state fMR images were recorded from 29 anaesthetised (isoflurane 1.25-1.5%) mouse lemurs using a gradient-echo echo planar imaging (EPI) sequence at 11.7 Tesla (Suppl. Table 1). Four animals that presented brain lesions or artefacted MRI images were excluded from the analysis. Animals were split in two groups: middle-aged adults (n=14, 1.3 to 3.8 year-old) and old animals (n=15, 8.0 to 10.8 year-old) (Suppl. Table 1). The amplitude of low-frequency fluctuation (ALFF) index was obtained after the time series for each voxel were transformed to the frequency domain with a Fast Fourier Transform (FFT) (Zuo et al., 2010). It was calculated for each voxel of the pre-processed EPI images in the low-frequencies range 0.01 to 0.1 Hz. mALFF index was calculated as ALFF weighted by the average ALFF of the whole brain. The mALFF signal from different brain regions was extracted using a reference functional atlas of the mouse lemur brain (https://www.nitrc.org/projects/fmri_mouselemur/; (Garin et al., 2019), Fig. 1C). High values of mALFF were detected in subcortical regions such as basal forebrain, globus pallidus, putamen and amygdala as well as cortical regions such as the cingulate and parietal cortices (Fig. 1A, B, Suppl. Fig. 1).

mALFF was further quantified within large scale networks previously reported in mouse lemurs (default-mode like, temporo-prefrontal, somato-motor, visual, thalamic and basal ganglia networks) (Garin et al., 2019) (Fig. 2). The basal ganglia network displayed the highest mALFF signal in middle-aged or old animals (Fig. 2A-B). Visual and thalamic networks displayed the lowest mALFF in both groups. The DMN was the cortical network with the highest mALFF in middle-aged animals. Significantly lower mALFF was detected in the DMN of old animals as compared to middle-aged ones (Fig. 1D, *p = 0.002*, Kruskal's test).
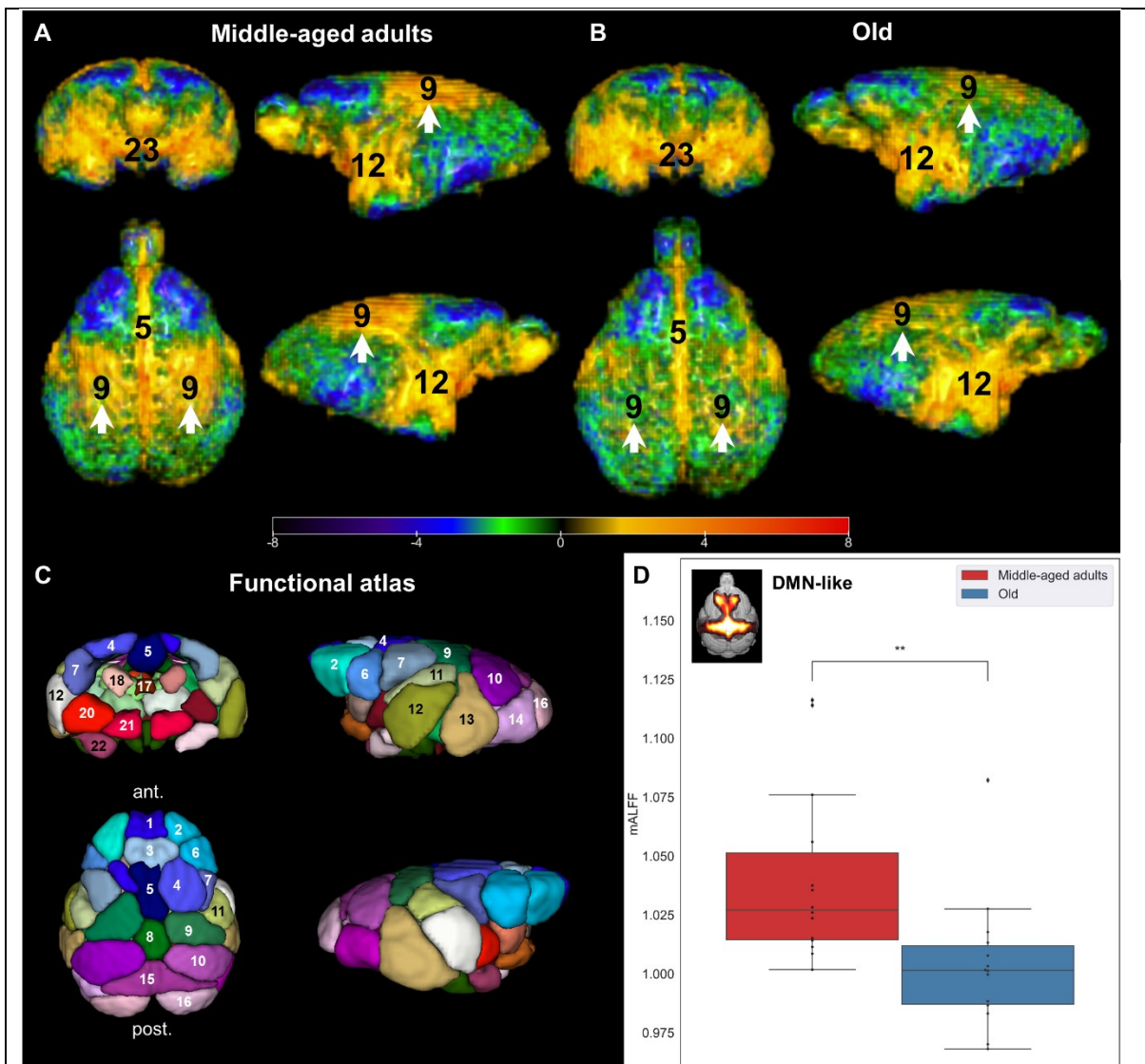
Figure 1. Whole brain mALFF statistical map in middle-aged and old mouse lemurs.

Functional atlas of the mouse lemur brain (C) based on a BOLD signal spatial decomposition. Forty-eight functional regions (27 cortical, 21 subcortical) were extracted following sparse dictionary learning with 35 components. 3D surface t-maps of the mALFF in (A) 14 middle-aged and (B) 15 old mouse lemurs. Elevated mALFF is observed within regions encompassing the basal forebrain, amygdala, putamen and globus pallidus as well as cortical regions such as the middle temporal (12), anterior cingulate (5) and parietal cortices (12). White arrows highlight signal intensity difference in the DMN of old versus middle-aged animals. The color bar represents the t values (one-sample t-test). mALFF contrast lost was observed in the DMN-like of the aged group (D, $p = 0.02$, independent samples t-test). *: $p < 0.05$; **: $p < 0.01$, ***: $p < 0.001$, ****: $p < 0.0001$. 1. Frontal superior anterior, 2. Frontal middle, 3. Frontal superior posterior, 4. Supplementary motor area, 5. Cingulum anterior, 6. Precentral, 7. Postcentral, 8. Cingulum posterior, 9. Parietal, 10. Occipital middle, 11. Temporal superior, 12. Temporal middle, 13. Temporal inferior, 14. Occipital inferior, 15. Cuneus, 16. Occipital pole, 17. Septal nuclei, 18. Caudate nucleus posterior, 20. Putamen posterior, 21. Globus pallidus, 22. Amygdala, 23. Basal forebrain.
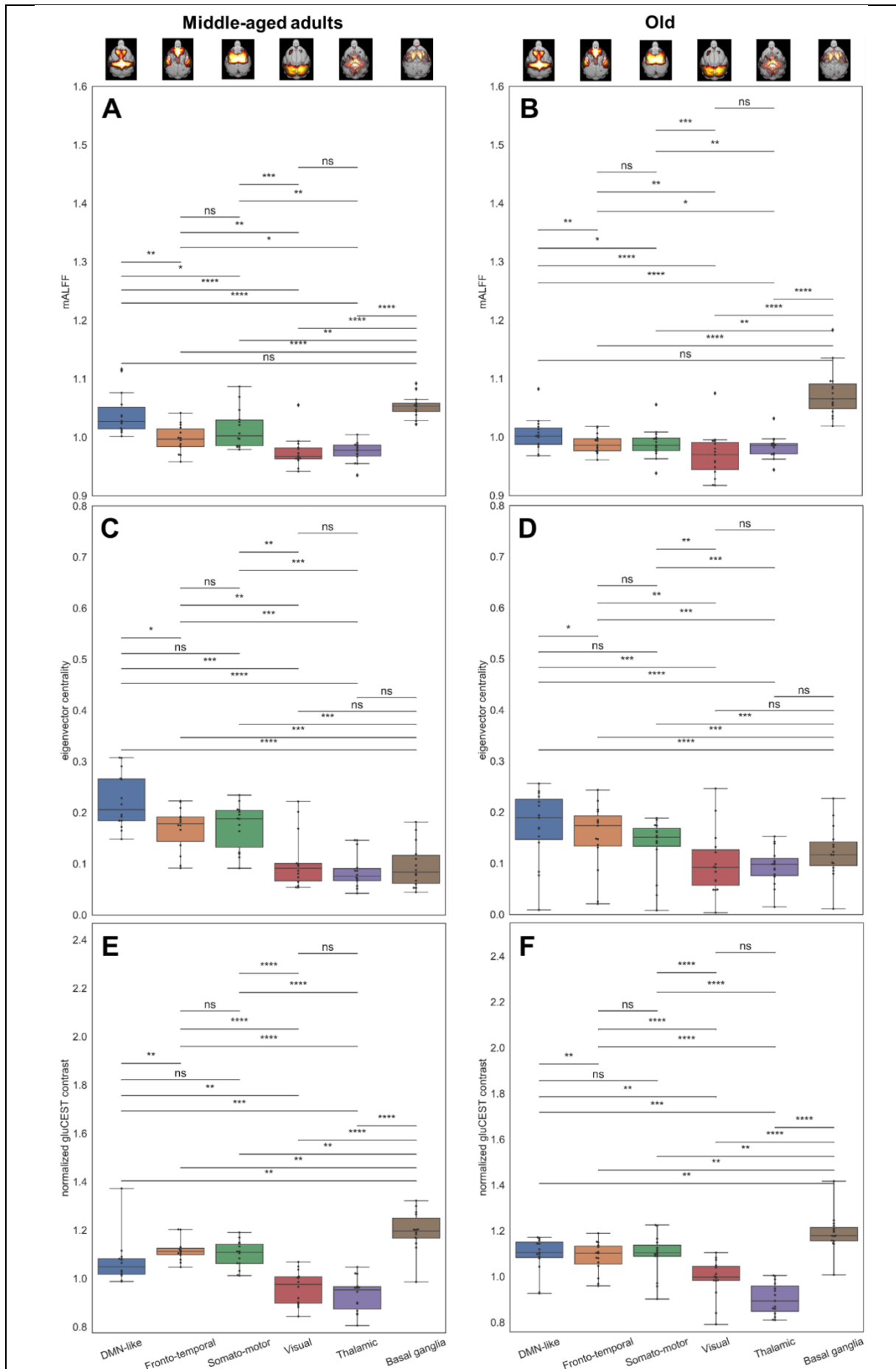
Figure 2. Indexes of functional connectivity (hubness), neuronal function (ALFF), and gluCEST signal in the cerebral networks of the mouse lemurs.
Different neuronal networks can be identified in mouse lemurs. mALFF level was low in the visual and thalamic networks, intermediate in the default-mode like, temporo-prefrontal and somato-motor networks and highest in the basal ganglia networks (A, B). Averaged eigenvector centrality level was low in the visual and thalamic networks and the basal ganglia, intermediate in the temporo-prefrontal and somato-motor networks and highest in the default-mode like (C, D). gluCEST level was highly similar to mALFF with a low signal in the visual and thalamic networks, intermediate in the default-mode like, temporo-prefrontal and somato-motor networks and highest in the basal ganglia networks (E, F).

2.2. Functional hubs in the mouse lemur brain

Resting-state fMR images used for ALFF evaluation were further used to analyse brain hubs. The whole brain network was defined as a set of 48 nodes (basic elements of the system) identified as local functional regions previously described in mouse lemurs (Garin et al., 2019). These nodes were used to build an averaged matrix for middle-aged and old mouse lemur cohorts (Fig. 3A, B).

Influence of each node within the whole brain network (or "hubness") can be characterized using various descriptors. One of them (eigenvector centrality) was calculated for each node, based on node partial correlation values (edges) with all regions of the 3D functional atlas, weighted by the eigenvector scores of its neighbourhood nodes. In other words, nodes which display high eigenvector centrality scores are strongly linked to other nodes and/or to strongly connected nodes. The cingulum anterior and posterior, the frontal superior, posterior, and anterior, the temporal superior cortices and the dorsal thalamus were identified as major hubs in both groups (Suppl. Fig. 2). The gap between the poorly connected regions (low eigenvector centrality) and the mains hubs (high eigenvector centrality) was weaker in the old lemurs. However, the global ranking across functional regions was preserved in both cohorts. Also, eigenvector centrality index was reduced in the anterior cingulate cortex of old animals compared to middle-aged ones (Fig. 3C, *p = 0.02*, independent samples t-test).
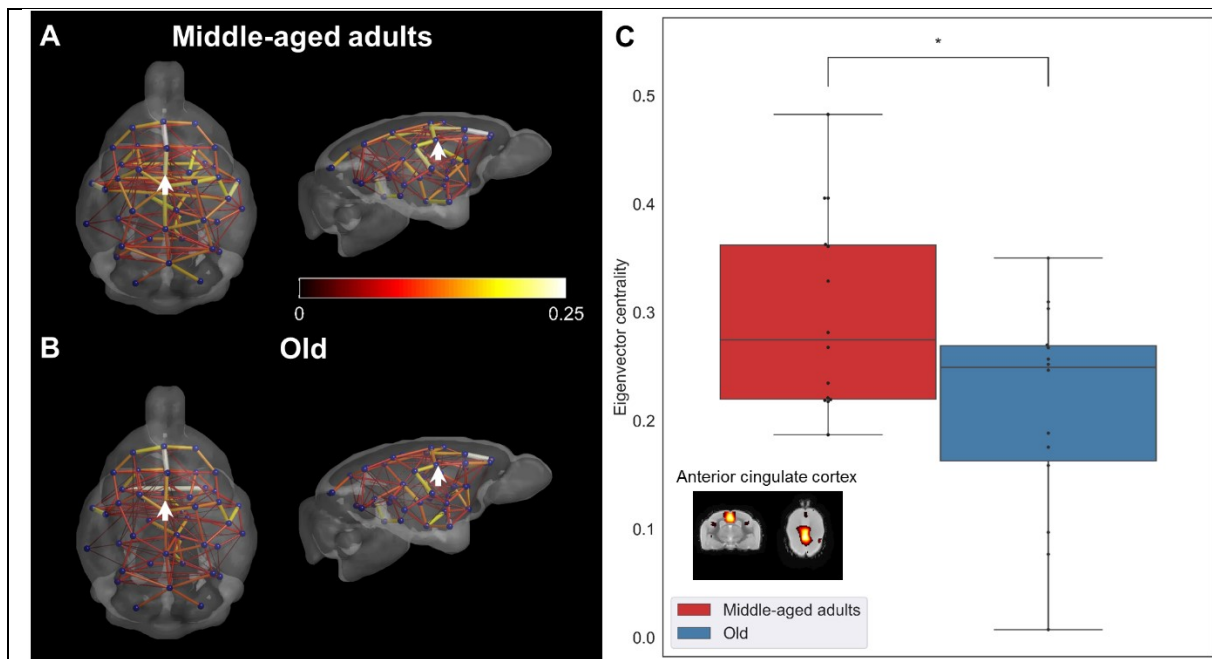
Figure 3. Whole brain networks extracted from middle-aged and old mouse lemurs.

Mean correlation matrix showing the mouse lemur brain network are represented on a 3D mouse lemur brain space (BrainNet (Xia et al., 2013)). Nodes represent the local functional regions extracted from a 3D functional atlas. They were spatially distributed based on their centers of mass. Edges between the nodes represent the mean partial correlation from the (A) 14 middle-aged and (B) 15 old animals. Color and size of these edges are proportional to this correlation. Differences in node centrality were found in the anterior cingulate cortex (white arrows). The color bar represents partial correlation values.

Eigenvector centrality was reduced in the anterior cingulate cortex of the aged animals as compared to middle-aged animals (C, *p = 0.02*, independent samples t-test). *: p < 0.05.

The averaged eigenvector centrality score of each functional network (DMN like, temporo-prefrontal, somato-motor, visual, thalamic and basal ganglia networks) (Garin et al., 2019) could also be calculated (Fig. 2C-D). The DMN-like network displayed the highest eigenvector centrality score. Also, cortical regions (except the visual cortex) had higher eigenvector centrality scores than subcortical regions. No differences were found between large scale networks of middle-aged and old animals.

2.3. GluCEST contrast in mouse lemur brains

GluCEST images were recorded using a 2D fast spin echo sequence in the same animals as those used for the rsfMRI study and during the same imaging session. Individual gluCEST images were brought into the same space as the rsfMR images.

gluCEST maps representative of each cohort were calculated using a one-sample t-test (Fig. 4A, B). GluCEST signal from different brain regions was extracted from a reference functional atlas of the mouse lemur (Suppl. Fig. 3).

Subcortical regions such as caudate nucleus, globus pallidus, and putamen displayed elevate glutamate signal in both cohorts. Cortical regions such as frontal superior posterior as well as supplementary motor area, temporal, cingulum anterior also displayed high GluCEST signal in both groups. In most brain regions, GluCEST signal did not present with major difference between middle-aged and old lemurs except within the globus pallidus (Fig. 3C, $p = 0.0004$, t-test).

The gluCEST signal was also extracted in the six previously defined large scale networks. The ranking of gluCEST signal in the subcortical networks was highly similar to that for the mALFF and was marked by a high gluCEST signal in the basal ganglia and a lower signal in the thalamic network (Fig. 2E-F). The visual network displayed the lowest signal of the cortical networks. No significant differences were found between large scale networks of middle-aged and old animals.
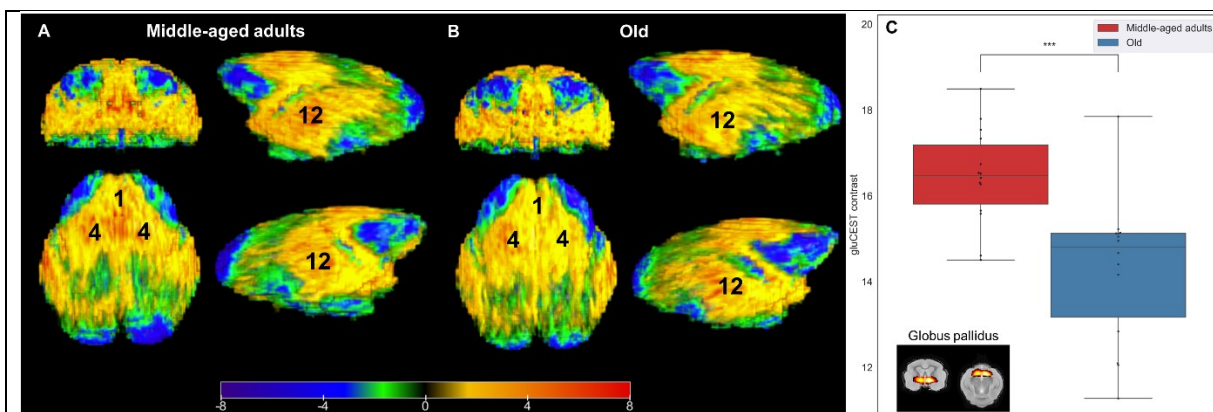
Figure 4. gluCEST signal statistical map in middle-aged and old mouse lemurs. 3D surface t-map of the gluCEST signal in middle-aged (A, n=14) and old (B, n=15) mouse lemurs. Elevated gluCEST signal is observed within regions encompassing the frontal superior anterior cortex (1), supplementary motor area (4), temporal (12) and cingulum anterior cortices as well as subcortical regions such as globus pallidus, caudate nucleus, and putamen. Signal was lower in the globus pallidus of old animals (C, $p = 0.0004$, t-test) of old animals compared to middle-aged animals. ***: $p < 0.0001$. The color bar represents the t values (one-sample t-test).

2.4. Local neuronal activity and functional connectivity are associated to glutamate

We then evaluated the relationships between local neuronal activity or functional connectivity extracted from the various brain regions and glutamate contrast in the same regions. Comparisons of each index were performed systematically in the whole brain, in the cortical and subcortical regions.

2.4.1. mALFF is associated to gluCEST contrast

mALFF and gluCEST signal were positively correlated in both groups when compared in the entire brain (Fig. 5A-B). The correlation detected at the level of the entire brain was mainly driven by a strong correlation at the level of subcortical regions, that was detected in the two cohorts (R = 0.72 and 0.75 in middle-aged and old animals, Fig. 5E-F) rather than in cortical regions, in which a weaker, but significant positive correlation was only found in the middle-aged group (R = 0.53, Fig. 5C) but not in the old group. Interestingly the strong correlation detected in the subcortical regions, reflected two categories of structures: those belonging to the basal ganglia with high mALFF and gluCEST signal and those belonging to the thalamic network with low mALFF and gluCEST signal. These data suggest that high neuronal activity is related to highest glutamate level in particular within the subcortical regions.
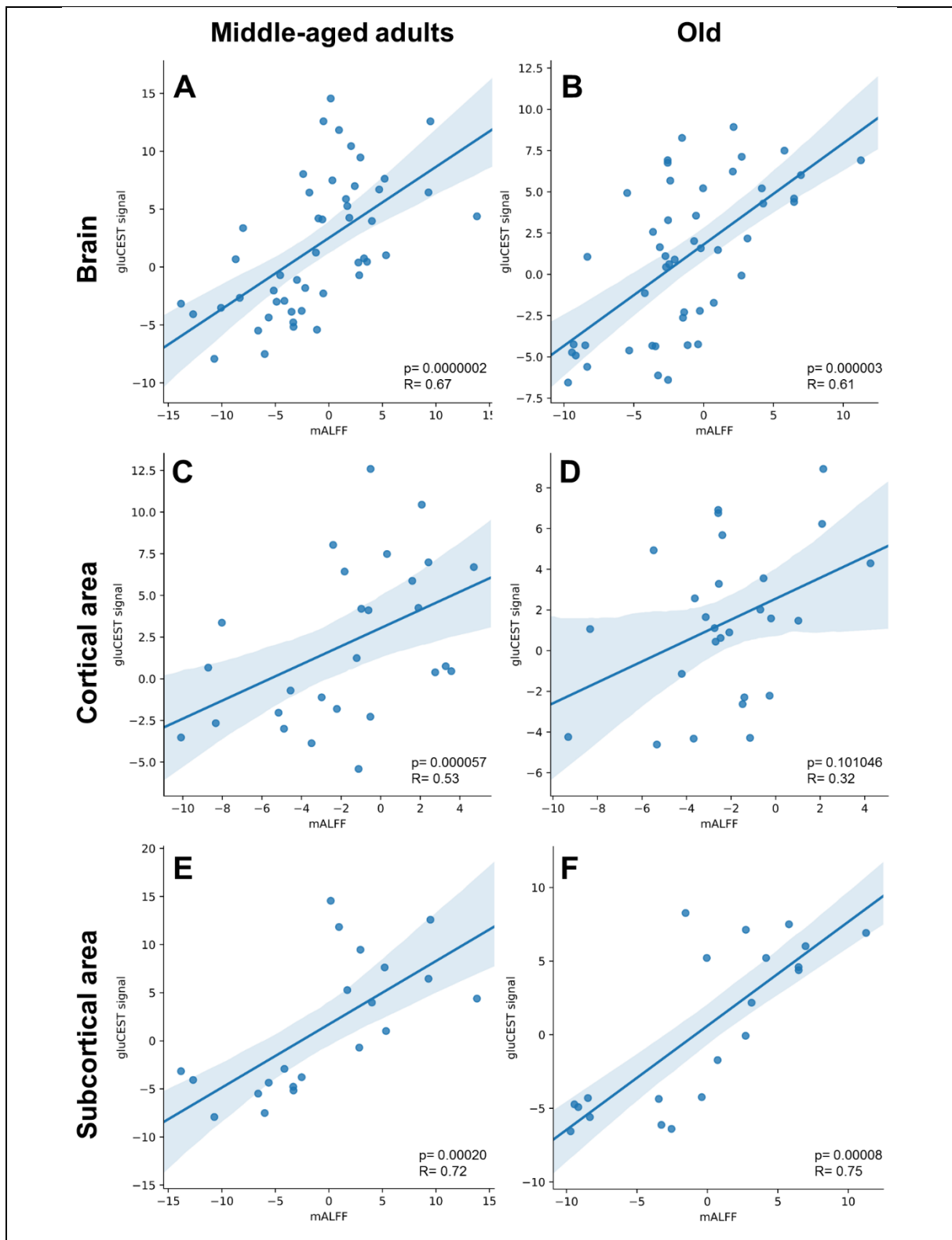
Figure 5. Relationships between mALFF and gluCEST contrast
Positive relationships were observed between mALFF and gluCEST signal in all functional brain regions of the middle-aged (A) and old (B) lemurs as well as in cortical regions of middle-aged animals (C) and subcortical regions of both cohorts (E, F). Spearman correlation indexes are displayed on each graph.

2.4.2. Hubness is associated to gluCEST contrast

Eigenvector centrality was positively correlated with gluCEST signal in the whole brain of middle-aged (Fig. 6A) and old animals (Fig. 6B). Strong correlations between eigenvector centrality and gluCEST signal were also observed in cortical regions (Fig. 6C, D) and subcortical regions (Fig. 6E, F) of both groups.

Eigenvector centrality measures are dependent of the threshold used to remove low correlated and thus non-meaningful edges of the network. Here, we used a threshold based on a one-tailed t-test ($p \leq 0.01$). To assess the impact of this threshold on result outcome, we changed it from 0.0001 to 0.36 with a spacing value of 0.01 leading to 36 new comparisons of the correlations between eigenvector centrality and gluCEST contrast (Suppl. Fig. 4). Different thresholds changed the density of the network from 0.13 to 0.59 but most correlations between eigenvector centrality and gluCEST contrast in the whole brain and in cortical regions were still significant (p<0.05) whatever the mouse lemur cohort. On the contrary correlations were almost never significant in the subcortical regions when thresholds were changed. This suggests that correlations between eigenvector centrality and gluCEST contrast are robust if one considers analyses performed at the whole brain or cortical level but not within subcortical regions.

In this first part of the study, we used eigenvector centrality as an index of hubness. Other indexes of hubness are available. Degree centrality represents the sum of the weighted edges incident upon a node. Current flow betweenness centrality is a betweenness centrality measure that considers the influence from all the paths across nodes. This algorithm gives more weight to the shortest path but also considers the other connections (Newman, 2005). These two indexes were used to further assess relationships between connectivity and gluCEST contrast (Table 1). Degree centrality indexes were positively correlated to gluCEST contrast in the whole brain and in the cortex of both groups. Current flow betweenness centrality indexes were also significantly correlated to gluCEST contrast in the brain and in the cortex of both groups. Overall, these results highlight a strong relationship between glutamate levels and centrality indexes in the whole brain and in the cortical regions, but a weaker relationship in subcortical regions.

Figure 6. Relationships between eigenvector centrality and gluCEST contrast.
A positive relationship was observed between eigenvector centrality and gluCEST signal extracted from all functional brain regions of the middle-aged (A) and old (B) lemurs. Similar correlations were obtained when using only the cortical regions or subcortical regions in middle-aged and old lemurs. Spearman correlation indexes are displayed on each graph.

	gluCEST					mALFF			
	Middle-aged adults		Old			Middle-aged adults		Old	
	R	p	R	p		R	p	R	p
	Eigenvector centrality								
Brain	0.544	0.000065*	0.540	0.000073*		0.390	0.006120*	0.411	0.003701*
Cortical	0.679	0.000007*	0.538	0.003761*		0.730	0.000015*	0.204	0.307650
Subcortical	0.534	0.012698	0.623	0.002535*		0.279	0.220289	0.691	0.000525*
	Degree centrality								
Brain	0.473	0.000693*	0.491	0.000397*		0.471	0.000726*	0.391	0.005952*
Cortical	0.640	0.000326*	0.530	0.004470*		0.618	0.000585*	0.194	0.333441
Subcortical	0.395	0.076527	0.500	0.020992*		0.412	0.063699	0.597	0.004241*
	Current flow betweenness centrality								
Brain	0.430	0.002261*	0.458	0.001066*		0.424	0.002671*	0.335	0.019984*
Cortical	0.628	0.000450*	0.632	0.000401*		0.579	0.001563*	0.275	0.165496
Subcortical	0.319	0.158035	0.358	0.110590		0.358	0.110590	0.448	0.041656*

Table 1. Relationships between different indexes of hubness and gluCEST contrast or mALFF.

Most hubness indexes were correlated to gluCEST contrast in whole brain or cortical regions. Relationships between hubness and gluCEST were less stable in subcortical regions. The correlations between hubness and mALFF display a reproducible pattern amongst the different indexes. The hubness indexes were always positively correlated to mALFF in whole brain of both groups, in the cortical regions of the middle-aged group and in the subcortical regions of the old lemurs.

2.5.   mALFF and hubness are correlated

mALFF and eigenvector centrality evaluated in different brain regions were positively correlated (Fig. 7A, B). Correlation between mALFF and eigenvector centrality was statistically significant in the cortex but not in the subcortical regions of middle-aged animals (Fig. 7C, E). This relationship seemed to be shifted in old animals in which correlation between these two markers was statistically significant in subcortical regions and not in the cortex (Fig. 7D, F). As for the comparison with gluCEST signal, we evaluated the stability to the threshold of this correlation (Suppl. Fig. 5). Cortical correlations were always true for the middle-aged group and surprisingly subcortical correlation were always true in the aged group. Additional indexes of hubness (degree centrality and current flow betweenness centrality indexes) were used to further assess the specificity of the relationships between hubness and mALFF (Table 1). We found positive correlation into the brain with all indexes. Positive correlations between ALFF and all indexes were found in the cortex

of the middle-aged group and in the subcortical regions of aged animals, which further confirmed the age-related shift of cortico/subcortical relationship between ALFF and hubness.
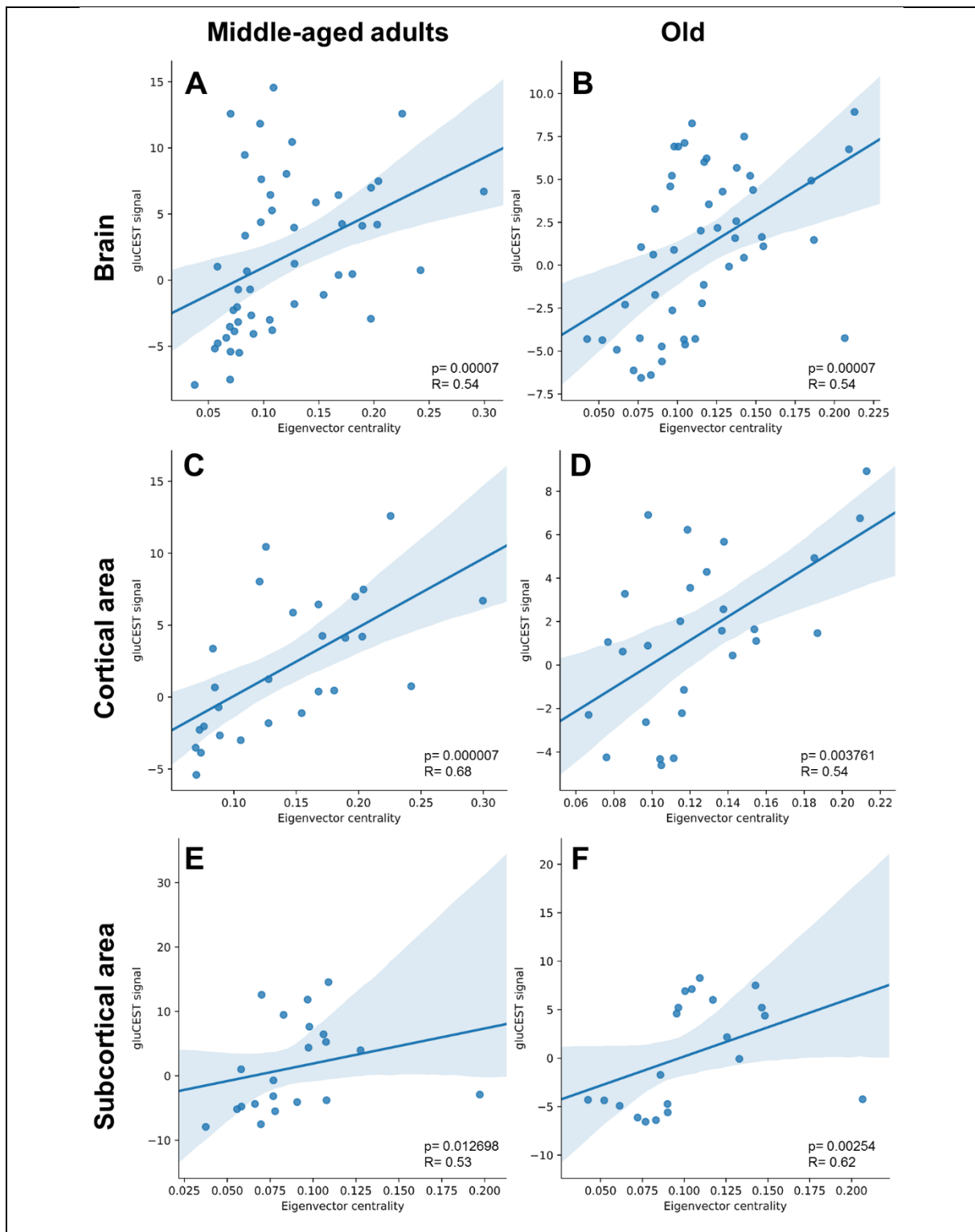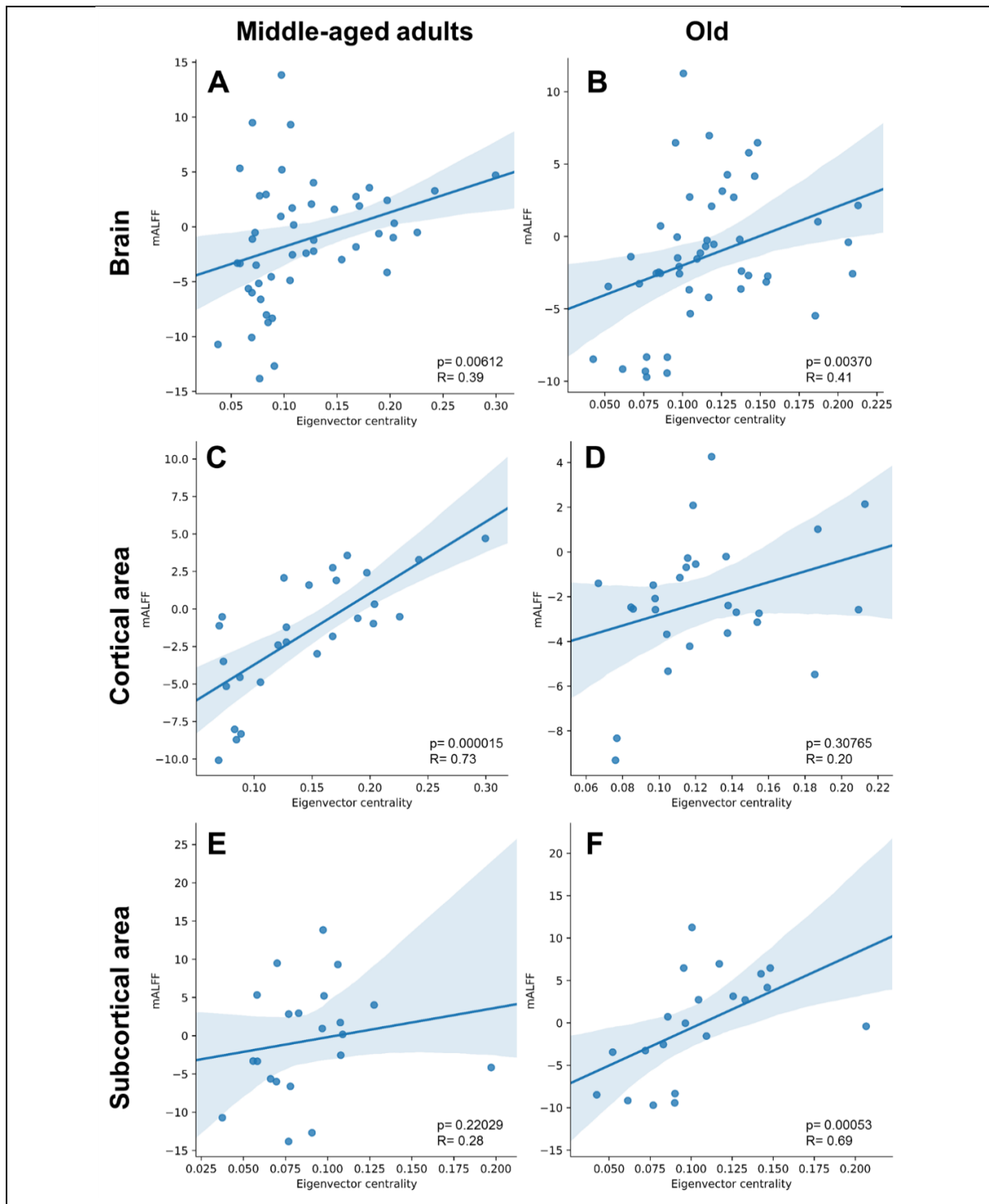

Figure 7. Relationships between eigenvector centrality and mALFF.
A positive relationship was observed between eigenvector centrality and mALFF in all functional brain regions of the middle-aged (A) and old (B) lemurs as well as in cortical regions of middle-aged animals (C) and subcortical regions of old animals (F). Spearman correlation indexes are displayed on each graph.

3. Discussion

This study evaluated mALFF, hubness and glutamate level in mouse lemur primates at high field MRI (11.7T). We focused on two independent cohort of middle-aged and old animals. Several results were consistent between the two cohorts. First, we highlighted different levels of mALFF activity in different brain regions. mALFF is considered as a marker of neuronal activity (Zou et al., 2008). Highest levels of mALFF were detected in structures belonging to the basal ganglia network (putamen, globus pallidus). Moreover, mALFF was well correlated to the gluCEST signal.

Different levels of hubness were also detected in different brain regions and regions with stronger hubness properties were mainly cortical (cingulate, frontal, and temporal cortices). Hubness parameters were well correlated to gluCEST in the cortex but not in subcortical regions.

Together, these results suggest relationships between neuronal activity assessed by mALFF, hubness and glutamate levels. In the cortex, glutamate level is linked to both mALFF and hubness. Glutamate is the major excitatory transmitter in the central nervous system. Relationships between concentration of this neurotransmitter and activation of particular regions (*e.g.* the posterior cingulate cortex/precuneus) or activation of networks (*e.g.* the default mode network) have already been reported (Y. Hu et al., 2013; Kapogiannis et al., 2013). A relationship between glutamate and neuronal activity was thus expected and our results suggest that this relationship is strong and impact most cortical regions. In addition to the role of glutamate for local activity, our study further outlined that in the cortex, glutamate level is linked to hubness, *i.e.* to the ability to have information crossing brain regions. This suggests a relationship between glutamate and long-distance transfer of information in the brain.

In the subcortical regions, high glutamate level was mainly associated to high local activity (and not to hubness properties), in particular in the basal ganglia network. Numerous studies defined the basal ganglia as a main input from the cortical glutamatergic projections (Galvan et al., 2006; Lanciego et al., 2012). Also, according to Greenamyre et al., the striatum is the major region receiving glutamatergic cortical input (Greenamyre, 2001). In consequences, the high gluCEST signal detected in this area may correspond to this pathway and may be responsible for the high activity within the basal ganglia.

The major pools of glutamate are located in cells and neurotransmission is governed by few micromolar of extracellular glutamate. gluCEST is an interesting technique as it is sensitive to the concentration of this intracellular glutamate (Cai et al., 2012). 70% of the gluCEST signal is weighted by intracellular glutamate (Bagga et al., 2018). Glutamate is present within cells close to the synapses and within astrocytes that surround the synapses (Cooper et Jeitner, 2016). High glutamate level may thus reflect high functional synaptic connection in the most active regions. We can however not rule out other explanations for high glutamate level in active brain regions. Indeed, stimulation of brain regions were shown to increase glutamate levels in the activated regions (Just et al., 2013; Sonnay et al., 2017). It is thus also conceivable that the high glutamate level in the most active regions is the result of a prolonged activation of the regions. Even if our study suggests a critical role of glutamate for brain activity in the whole brain and to tune nodal activity in the cortex, they do not exclude possible roles of other neurotransmitters that were not evaluated in the current work. Serotonin for example was shown to be critical to stimulate neuronal networks activity (Noori et al., 2017). GABA was also reported to be critical to reduce activity of neuronal networks (Kapogiannis et al., 2013).

As we evaluated mALFF, hubness and glutamate level in two cohorts of middle-aged and old animals, our study can also provide some clues on aging changes for these markers. First, we highlighted alterations of mALFF index in the DMN-like of the old animals when compared to the middle-aged ones. This result is consistent with data in humans in which ALFF of the DMN is also impaired with aging (S. Hu et al., 2014). We also reported lower eigenvector centrality in the anterior cingulate cortex of old animals. This region is a major hub of the mouse lemur brain and of its DMN-like network (Garin et al., 2019). Thus, this result is consistent with age-related decreases of the functional connectivity reported within regions of the DMN in humans (Sala-Llonch et al., 2015). It further confirms the weakness of DMN during aging.

Interestingly, we also found a shift of the relationship between ALFF and hubness that concerned cortical regions in middle-aged animals and subcortical regions in old animals. This may suggest a reorganization of the brain function in old animals, in relationship to lower capacity to mobilize cortical regions.

Finally, we found an age-related reduction of gluCEST signal in the globus pallidus. The globus pallidus is a key structure of the glutamatergic system strongly involved in glutamatergic transmission (Greenamyre, 2001). Alterations of glutamate in these

structures may have consequences on alterations of cerebral health associated to aging.

4. Conclusion

As a conclusion, using a small primate model that can be studied by high field MRI, we showed that glutamate is strongly associated to mALFF in cortical and subcortical brain regions. In the cortex, glutamate is also associated to functional connectivity and to long-distance transfer of information. We also highlighted age-related changes for these parameters. They concern alterations of mALFF in critical networks and reduction of glutamate in the globus pallidus. We also highlighted an age-related reorganization of the cortical/subcortical relationships between mALFF and functional connectivity.

5. Materials and methods

5.1. Animals and breeding

This study was carried out in accordance with the recommendations of the European Communities Council directive (2010/63/EU). The protocol was approved by the local ethics committees CEtEA-CEA DSV IdF (authorizations 201506051736524 VI (APAFIS#778)). All mouse lemurs studied were born in the laboratory breeding colony of the CNRS/MNHN in Brunoy, France (UMR 7179 CNRS/MNHN) and bred in our laboratory (Molecular Imaging Research Center, CEA, Fontenay-aux-Roses).

Twenty-nine mouse lemurs (21 males and 12 females) were initially included in this study. Four animals that presented brain lesions or artefacted MRI images were excluded from the analysis. Fourteen animals ranged from 1.3 to 3.8 years old (mean±SD: 2.1±0.8 years) were grouped together to form the *"young lemurs cohort"* (Supplementary Table 1). Fifteen animals ranged from 8.0 to 10.8 years old (mean±SD: 8.8±1.1 years) were grouped together to form the *"old lemurs cohort"* (Supplementary Table 1). Housing conditions were cages containing one or two lemurs with jumping and hiding enrichment, temperatures 24–26°C, relative humidity 55% and seasonal lighting (summer: 14 hours of light/10 hours of dark; winter: 10 hours of light/14 hours of dark). Food consisted of fresh apples and a homemade mixture of bananas, cereals, eggs and milk. Animals had free access to tap water. None of the

animals had previously been involved in pharmacological trials or invasive studies.

5.2. Animal preparation and MRI acquisition

Each animal was scanned twice with an interval of 6 months. All scanning was under isoflurane anaesthesia at 1.25-1.5% in air, with respiratory rate monitored to confirm animal stability until the end of the experiment. Body temperature was maintained by an air heating system at 32°C, inducing a natural torpor in mouse lemurs (Aujard et Vasseur, 2001). This has the advantage of allowing a low anaesthesia level without reawakening.

The MRI system was an 11.7 T Bruker BioSpec (Bruker, Ettlingen, Germany) running ParaVision 6.0.1 with a volume coil for radiofrequency transmission and a quadrature surface coil for reception (Bruker, Ettlingen, Germany).

Anatomical images were acquired using a T2-weighted multi-slice multi-echo (MSME) sequence: TR = 5000 ms, TE = 17.5 ms, FOV = 32 × 32 mm, 75 slices of 0.2 mm thickness, 6 echoes, 5 ms IET, resolution = 200 µm isotropic, acquisition duration 10 min.

Resting state time series data were acquired using a gradient-echo echo planar imaging (EPI) sequence: TR = 1000 ms, TE = 10.0 ms, flip angle = 90°, repetitions = 450, FOV = 30 × 20 mm, 23 slices of 0.9 mm thickness and 0.1 mm gap, resolution = 312.5 × 208.33 × 1000 µm, acquisition duration 7m30s.

gluCEST images covering the brain from prefrontal cortex to the occipital cortex were acquired with a 2D fast spin-echo sequence: TR = 20000 ms, TE = 6 ms, FOV = 24 × 24 mm, 12 slices of 1.5 mm thickness, resolution = 0.250 x 0.250 µm^2, acquisition duration 33m00s. The MAPSHIM routine was applied in a voxel encompassing the slices of interest in order to reach a good shim on gluCEST images. gluCEST images were preceded by a frequency-selective continuous wave saturation pulse and acquired with a saturation pulse applied during T_{sat} = 1 s, composed by 10 broad pulse of 100ms, with 20 µs inter-delay and an amplitude B_1 = 5 µT. The frequency of the saturation pulse Δω was applied in a range from −5 ppm to 5 ppm with a step of 1 ppm. In vivo, CEST contrast can be hampered by several competing factors such as direct saturation transfer (DS) of free water and background magnetization transfer (MT). Although we supposed DS symmetrical with respect to water frequency and suppressed by asymmetrical analysis its contribution to CEST contrast (Sun et al.,

2005; van Zijl et Yadav, 2011; J. Zhou et Zijl, 2006).

5.3. MRI pre-processing

CEST images were first processed pixel-by-pixel and analyzed using in-house programs developed on MATLAB software (MathWorks Inc., Natick, MA) used to generate Z-spectra by plotting the longitudinal magnetization as a function of saturation frequency. The specific glutamate contribution was isolated using Asymmetrical Magnetization Transfer Ratio (MTRasym) (Liu et al., 2010) and was calculated as follows: MTRasym($\Delta\omega$) = 100 × (Msat($-\Delta\omega$) − Msat($+\Delta\omega$)) / Msat(-5 ppm), Msat($\pm\Delta\omega$) being the magnetization acquired with saturation pulse applied at '+' or '−' $\Delta\omega$ ppm. GluCEST images were calculated with $\Delta\omega$ centered at ± 3 ppm. GluCEST image was converted into NIfTI-1 format.

The other scanner data were exported as DICOM files then converted into NIfTI-1 format. Then spatial pre-processing was performed using the python module sammba-mri (SmAll MaMmals BrAin MRI; http://sammba-mri.github.io) which, using nipype for pipelining (Gorgolewski et al., 2011), leverages AFNI (Cox, 1996) for most steps and RATS (Oguz et al., 2014) for brain extraction. Anatomical images were mutually registered to create a study template, which was further registered to a high resolution anatomical mouse lemur template of the functional atlas (Garin et al., 2019). Resting state images were corrected for slice timing (interleaved), motion, and B0 distortion (per-slice registration to respective anatomicals). Then all the images (including GluCEST image) were brought into the same space of the mouse lemur template by successive application of the individual anatomical to study template and study template to mouse lemur atlas transforms.

Functional images were further pretreated using Nilearn (Abraham et al., 2014). Nuisance signal regression was applied including a linear trend as well as 24-motion confounds (6 motion parameters, those of the preceding volume, plus each of their squares (Friston et al., 1994)). Images were then spatially smoothed with a 0.9 mm full-width at half-maximum Gaussian filter. The first 10 volumes were excluded from analysis to ensure steady-state magnetization.

5.4. mALFF calculation and extraction

LFO measures were performed using the fast Fourier transform indice: amplitude of low-frequency fluctuation (ALFF) (Zuo et al., 2010). The mALFF correspond to the ALFF index weighted by in the average ALFF of the whole brain and was calculated using AFNI (Cox, 1996). ALFF index was calculated for each voxel of the pre-processed EPI images in the low-frequencies range 0.01 to 0.1 Hz. The mALFF signal of each voxels was extracted within the different regions based on the functional atlas (Garin et al., 2019) using NiftiLabelsMasker from Nilearn (Abraham et al., 2014).

5.5. GluCEST contrast extraction

gluCEST contrast was also extracted in regions based on the functional atlas using NiftiLabelsMasker from Nilearn (Abraham et al., 2014). For each region, the signal was averaged and was divided by its averaged whole brain signal. This normalisation was not performed for the between groups comparison.

5.6. Graph theory analysis

5.6.1. Connectivity matrix based on functional atlas

Partial correlation matrices were created for each animal using fully preprocessed MR images by calculating the partial correlation coefficients between BOLD MR signal timecourses within each region of the 3D functional atlas. Partial correlations were used because they select direct associations between regions and allow the control of indirect correlations (Mechling et al., 2014). Individual partial correlation matrices were computed from shrunk covariance matrices using the Ledoit and Wolf shrinkage coefficient (Ledoit et Wolf, 2004) as recommended by Varoquaux et al. (Varoquaux et al., 2012) and Brier et al. (Brier et al., 2015). Partial correlation coefficients were then Fisher's z-transformed. Values from different animals were averaged and thresholded based on a one-tailed t-test ($p \leq 0.01$) (Mechling et al., 2014).

5.6.2. Hub regions

We consider in this analysis the absolute value of the correlation coefficient as performed routinely in human fMRI graph theory studies (De Vico Fallani et al., 2014).

Hubness is measure of node influence within the whole brain network. For each node, this index is calculated based on its partial correlation values (edges) with all region of the 3D functional atlas. Measure of "hubness" such as eigenvector centrality, degree centrality, betweenness centrality, current flow betweenness centrality were performed using NetworkX (Hagberg et al., 2008). These scores were calculated individually and averaged for the young and the old cohorts.

6. Acknowledgements

7. Competing interests

The authors do not have financial and non-financial competing interests in relation to the work described.

8. References

Abraham, A., Pedregosa, F., Eickenberg, M., Gervais, P., Mueller, A., Kossaifi, J., . . . Varoquaux, G. (2014). Machine learning for neuroimaging with scikit-learn. *Front Neuroinform, 8*, 14. doi:10.3389/fninf.2014.00014

Aiello, M., Salvatore, E., Cachia, A., Pappatà, S., Cavaliere, C., Prinster, A., . . . Quarantelli, M. (2015). Relationship between simultaneously acquired resting-state regional cerebral glucose metabolism and functional MRI: A PET/MR hybrid scanner study. *Neuroimage, 113*, 111-121. doi:10.1016/j.neuroimage.2015.03.017

Aujard, F., & Vasseur, F. (2001). Effect of ambient temperature on the body temperature rhythm of male gray mouse lemurs (Microcebus murinus). *Int J Primatol, Vol. 22, No. 1, 2001*. doi:10.1023/A:1026461914534

Bagga, P., Pickup, S., Crescenzi, R., Martinez, D., Borthakur, A., D'Aquilla, K., . . . Reddy, R. (2018). In vivo GluCEST MRI: Reproducibility, background contribution and source of glutamate changes in the MPTP model of Parkinson's disease. *Sci Rep, 8*(1), 2883. doi:10.1038/s41598-018-21035-3

Biswal, B., Yetkin, F. Z., Haughton, V. M., & Hyde, J. S. (1995). Functional connectivity in the motor cortex of resting human brain using echo-planar MRI. *Magn Reson Med, 34*(4), 537-541. doi:10.1002/mrm.1910340409

Brier, M. R., Mitra, A., McCarthy, J. E., Ances, B. M., & Snyder, A. Z. (2015). Partial covariance based functional connectivity computation using Ledoit-Wolf covariance regularization.

Neuroimage, 121, 29-38. doi:10.1016/j.neuroimage.2015.07.039

Cai, K., Haris, M., Singh, A., Kogan, F., Greenberg, J. H., Hariharan, H., . . . Reddy, R. (2012). Magnetic resonance imaging of glutamate. *Nat Med, 18*, 302. doi:10.1038/nm.2615

Carrillo-de Sauvage, M.-A., Flament, J., Bramoulle, Y., Ben Haim, L., Guillermier, M., Berniard, A., . . . Escartin, C. (2015). The neuroprotective agent CNTF decreases neuronal metabolites in the rat striatum: an in vivo multimodal magnetic resonance imaging study. *J Cereb Blood Flow Metab, 35*(6), 917-921. doi:10.1038/jcbfm.2015.48

Chen, X., Fan, X., Hu, Y., Zuo, C., Whitfield-Gabrieli, S., Holt, D., . . . Ongur, D. (2018). Regional GABA concentrations modulate inter-network resting-state functional connectivity. *Cereb Cortex*. doi:10.1093/cercor/bhy059

Cleve, M., Gussew, A., Wagner, G., Bar, K. J., & Reichenbach, J. R. (2017). Assessment of intra- and inter-regional interrelations between GABA+, Glx and BOLD during pain perception in the human brain - A combined (1)H fMRS and fMRI study. *Neuroscience, 365*, 125-136. doi:10.1016/j.neuroscience.2017.09.037

Cooper, A. J. L., & Jeitner, T. M. (2016). Central role of glutamate metabolism in the maintenance of nitrogen homeostasis in normal and hyperammonemic brain. *Biomolecules, 6*(2), 16. doi:10.3390/biom6020016

Cox, R. W. (1996). AFNI: software for analysis and visualization of functional magnetic resonance neuroimages. *Comput Biomed Res, 29*(3), 162-173. doi:10.1006/cbmr.1996.0014

De Vico Fallani, F., Richiardi, J., Chavez, M., & Achard, S. (2014). Graph analysis of functional brain networks: practical issues in translational neuroscience. *Philos Trans R Soc Lond B Biol Sci, 369*(1653). doi:10.1098/rstb.2013.0521

Fransson, P. (2006). How default is the default mode of brain function?: Further evidence from intrinsic BOLD signal fluctuations. *Neuropsychologia, 44*(14), 2836-2845. doi:10.1016/j.neuropsychologia.2006.06.017

Friston, K. J., Holmes, A. P., Worsley, K. J., Poline, J. P., Frith, C. D., & Frackowiak, R. S. J. (1994). Statistical parametric maps in functional imaging: a general linear approach. *Hum. Brain Mapp., 2(4):189 - 210*. doi:10.1002/hbm.460020402

Galvan, A., Kuwajima, M., & Smith, Y. (2006). Glutamate and GABA receptors and transporters in the basal ganglia: what does their subsynaptic localization reveal about their function? *Neuroscience, 143*(2), 351-375. doi:10.1016/j.neuroscience.2006.09.019

Garin, C. M., Nadkarni, N. A., Landeau, B., Chételat, G., Picq, J.-L., Bougacha, S., & Dhenain, M. (2019). Resting state cerebral networks in mouse lemur primates: from multilevel validation to comparison with humans. *bioRxiv*, 599423. doi:10.1101/599423

Gorgolewski, K., Burns, C. D., Madison, C., Clark, D., Halchenko, Y. O., Waskom, M. L., & Ghosh, S. S. (2011). Nipype: a flexible, lightweight and extensible neuroimaging data

processing framework in python. *Front Neuroinform, 5*, 13. doi:10.3389/fninf.2011.00013

Greenamyre, J. T. (1986). The role of glutamate in neurotransmission and in neurologic disease. *Arch Neurol, 43*(10), 1058-1063. doi:10.1001/archneur.1986.00520100062016

Greenamyre, J. T. (2001). Glutamatergic influences on the basal ganglia. *Clinical Neuropharmacology, 24*(2), 65-70.

Hagberg, A. A., Schult, D. A., & Swart, P. J. (2008). *Exploring network structure, dynamics, and function using NetworkX*. Paper presented at the Proceedings of the 7th Python in Science Conference, Pasadena, CA.

Hahn, A., Wadsak, W., Windischberger, C., Baldinger, P., Höflich, A. S., Losak, J., . . . Lanzenberger, R. (2012). Differential modulation of the default mode network via serotonin-1A receptors. *Proc Natl Acad Sci U S A, 109*(7), 2619-2624. doi:10.1073/pnas.1117104109

Horn, D., Yu, C., Steiner, J., Buchmann, J., Kaufmann, J., Osoba, A., . . . Walter, M. (2010). Glutamatergic and resting-state functional connectivity correlates of severity in major depression – the role of pregenual anterior cingulate cortex and anterior insula. *Front Syst Neurosci, 4*(33). doi:10.3389/fnsys.2010.00033

Hu, S., Chao, H. H. A., Zhang, S., Ide, J. S., & Li, C.-S. R. (2014). Changes in cerebral morphometry and amplitude of low-frequency fluctuations of BOLD signals during healthy aging: correlation with inhibitory control. *Brain Struct Funct, 219*(3), 983-994. doi:10.1007/s00429-013-0548-0

Hu, Y., Chen, X., Gu, H., & Yang, Y. (2013). Resting-state glutamate and GABA concentrations predict task-induced deactivation in the default mode network. *J Neurosci, 33*(47), 18566-18573. doi:10.1523/JNEUROSCI.1973-13.2013

Ip, I. B., Berrington, A., Hess, A. T., Parker, A. J., Emir, U. E., & Bridge, H. (2017). Combined fMRI-MRS acquires simultaneous glutamate and BOLD-fMRI signals in the human brain. *Neuroimage, 155*, 113-119. doi:10.1016/j.neuroimage.2017.04.030

Just, N., Xin, L., Frenkel, H., & Gruetter, R. (2013). Characterization of sustained BOLD activation in the rat barrel cortex and neurochemical consequences. *Neuroimage, 74*, 343-351. doi:10.1016/j.neuroimage.2013.02.042

Kapogiannis, D., Reiter, D. A., Willette, A. A., & Mattson, M. P. (2013). Posteromedial cortex glutamate and GABA predict intrinsic functional connectivity of the default mode network. *Neuroimage, 64*, 112-119. doi:10.1016/j.neuroimage.2012.09.029

Kraska, A., Dorieux, O., Picq, J. L., Petit, F., Bourrin, E., Chenu, E., . . . Dhenain, M. (2011). Age-associated cerebral atrophy in mouse lemur primates. *Neurobiol Aging, 32*(5), 894-906. doi:10.1016/j.neurobiolaging.2009.05.018

Lanciego, J. L., Luquin, N., & Obeso, J. A. (2012). Functional neuroanatomy of the basal ganglia. *Cold Spring Harb Perspect Med, 2*(12), a009621. doi:10.1101/cshperspect.a009621

Ledoit, O., & Wolf, M. (2004). A well-conditioned estimator for large-dimensional covariance matrices. *Journal of Multivariate Analysis, 88*(2), 365-411. doi:10.1016/S0047-259X(03)00096-4

Lee, T.-W., & Xue, S.-W. (2017). Linking graph features of anatomical architecture to regional brain activity: A multi-modal MRI study. *Neurosci Lett, 651*, 123-127. doi:10.1016/j.neulet.2017.05.005

Liu, G., Gilad, A. A., Bulte, J. W. M., van Zijl, P. C. M., & McMahon, M. T. (2010). High-throughput screening of chemical exchange saturation transfer MR contrast agents. *Contrast media & molecular imaging, 5*(3), 162-170. doi:10.1002/cmmi.383

Mechling, A. E., Hubner, N. S., Lee, H. L., Hennig, J., von Elverfeldt, D., & Harsan, L. A. (2014). Fine-grained mapping of mouse brain functional connectivity with resting-state fMRI. *Neuroimage, 96*, 203-215. doi:10.1016/j.neuroimage.2014.03.078

Newman, M. E. J. (2005). A measure of betweenness centrality based on random walks. *Social Networks, 27*(1), 39-54. doi:10.1016/j.socnet.2004.11.009

Niciu, M. J., Kelmendi, B., & Sanacora, G. (2012). Overview of glutamatergic neurotransmission in the nervous system. *Pharmacology, biochemistry, and behavior, 100*(4), 656-664. doi:10.1016/j.pbb.2011.08.008

Noori, H. R., Schöttler, J., Ercsey-Ravasz, M., Cosa-Linan, A., Varga, M., Toroczkai, Z., & Spanagel, R. (2017). A multiscale cerebral neurochemical connectome of the rat brain. *PLoS Biol, 15*(7), e2002612. doi:10.1371/journal.pbio.2002612

Oguz, I., Zhang, H., Rumple, A., & Sonka, M. (2014). RATS: Rapid Automatic Tissue Segmentation in rodent brain MRI. *J Neurosci Methods, 221*, 175-182. doi:10.1016/j.jneumeth.2013.09.021

Raichle, M. E. (2011). The restless brain. *Brain Connect, 1*(1), 3-12. doi:10.1089/brain.2011.0019

Sala-Llonch, R., Bartres-Faz, D., & Junque, C. (2015). Reorganization of brain networks in aging: a review of functional connectivity studies. *Front Psychol, 6*, 663. doi:10.3389/fpsyg.2015.00663

Sawiak, S. J., Picq, J. L., & Dhenain, M. (2014). Voxel-based morphometry analyses of in vivo MRI in the aging mouse lemur primate. *Front Aging Neurosci, 6*, 82. doi:10.3389/fnagi.2014.00082

Sonnay, S., Duarte, J. M. N., & Just, N. (2017). Lactate and glutamate dynamics during prolonged stimulation of the rat barrel cortex suggest adaptation of cerebral glucose and oxygen metabolism. *Neuroscience, 346*, 337-348.

doi:10.1016/j.neuroscience.2017.01.034

Sun, P. Z., van Zijl, P. C. M., & Zhou, J. (2005). Optimization of the irradiation power in chemical exchange dependent saturation transfer experiments. *Journal of Magnetic Resonance, 175*(2), 193-200. doi:10.1016/j.jmr.2005.04.005

van Zijl, P. C. M., & Yadav, N. N. (2011). Chemical exchange saturation transfer (CEST): what is in a name and what isn't? *Magn Reson Med, 65*(4), 927-948. doi:10.1002/mrm.22761

Varoquaux, G., Gramfort, A., Poline, J. B., & Thirion, B. (2012). Markov models for fMRI correlation structure: Is brain functional connectivity small world, or decomposable into networks? *J Physiol Paris, 106*(5-6), 212-221. doi:10.1016/j.jphysparis.2012.01.001

Xia, M., Wang, J., & He, Y. (2013). BrainNet Viewer: a network visualization tool for human brain connectomics. *PLoS One, 8*(7), e68910. doi:10.1371/journal.pone.0068910

Zhou, J., & Zijl, P. C. M. v. (2006). Chemical exchange saturation transfer imaging and spectroscopy. *Progress in Nuclear Magnetic Resonance Spectroscopy, 48*(2), 109-136. doi:10.1016/j.pnmrs.2006.01.001

Zhou, Y., & Danbolt, N. C. (2014). Glutamate as a neurotransmitter in the healthy brain. *Journal of neural transmission (Vienna, Austria : 1996), 121*(8), 799-817. doi:10.1007/s00702-014-1180-8

Zou, Q.-H., Zhu, C.-Z., Yang, Y., Zuo, X.-N., Long, X.-Y., Cao, Q.-J., . . . Zang, Y.-F. (2008). An improved approach to detection of amplitude of low-frequency fluctuation (ALFF) for resting-state fMRI: fractional ALFF. *J Neurosci Methods, 172*(1), 137-141. doi:10.1016/j.jneumeth.2008.04.012

Zuo, X.-N., Di Martino, A., Kelly, C., Shehzad, Z. E., Gee, D. G., Klein, D. F., . . . Milham, M. P. (2010). The oscillating brain: complex and reliable. *Neuroimage, 49*(2), 1432-1445. doi:10.1016/j.neuroimage.2009.09.037

Resting-state fMRI and glutamate measures in the brain of a non-human primate: relationships and age-related alterations

Clément M. Garin, Nachiket A. Nadkarni, Jérémy Pepin, Salma Bougacha,

Julien Flament, Marc Dhenain

Supplementary Data

Supplementary Tables

Subject	Sex	Age (months)	Age (years)	Animal rejected
283EA	M	40.8	1.3	NO
283CCA	M	41.0	1.3	NO
285AAA	M	41.3	1.4	NO
365A	M	41.3	1.4	NO
285AB	M	42.1	1.4	NO
263BCE	M	43.8	1.4	NO
314CA	M	45.0	1.5	NO
285D	M	71.2	2.3	NO
283CA	M	71.8	2.4	NO
276BC	M	72.2	2.4	NO
285E	M	72.4	2.4	NO
300BA	M	75.5	2.5	NO
289BB	F	87.0	2.9	NO
208CBF	F	95.2	3.1	NO
288BC	F	95.8	3.2	cerebral lesion
310C	F	114.8	3.8	cerebral lesion
967HACA	M	243.5	8.0	NO
184CB	F	243.6	8.0	NO
965MBIA	M	243.6	8.0	NO
965MBFA	M	244.3	8.0	NO
965MBFC	F	244.4	8.0	NO
965MBGA	M	244.7	8.0	NO
967HACB	F	244.7	8.0	NO
965MBFB	M	245.4	8.1	NO
169BAB	F	246.0	8.1	NO
965FDBB	M	265.4	8.7	NO
147BCBB	M	265.7	8.7	NO
147BCBA	M	266.3	8.8	artifact
943GKBC	F	266.5	8.8	NO
153FBA	M	311.7	10.3	NO
216B	F	317.3	10.4	NO
965MBG	F	327.7	10.8	artifact
119BBB	F	328.1	10.8	NO

Supplementary Table 1. Cohort of mouse lemurs involved in the study.
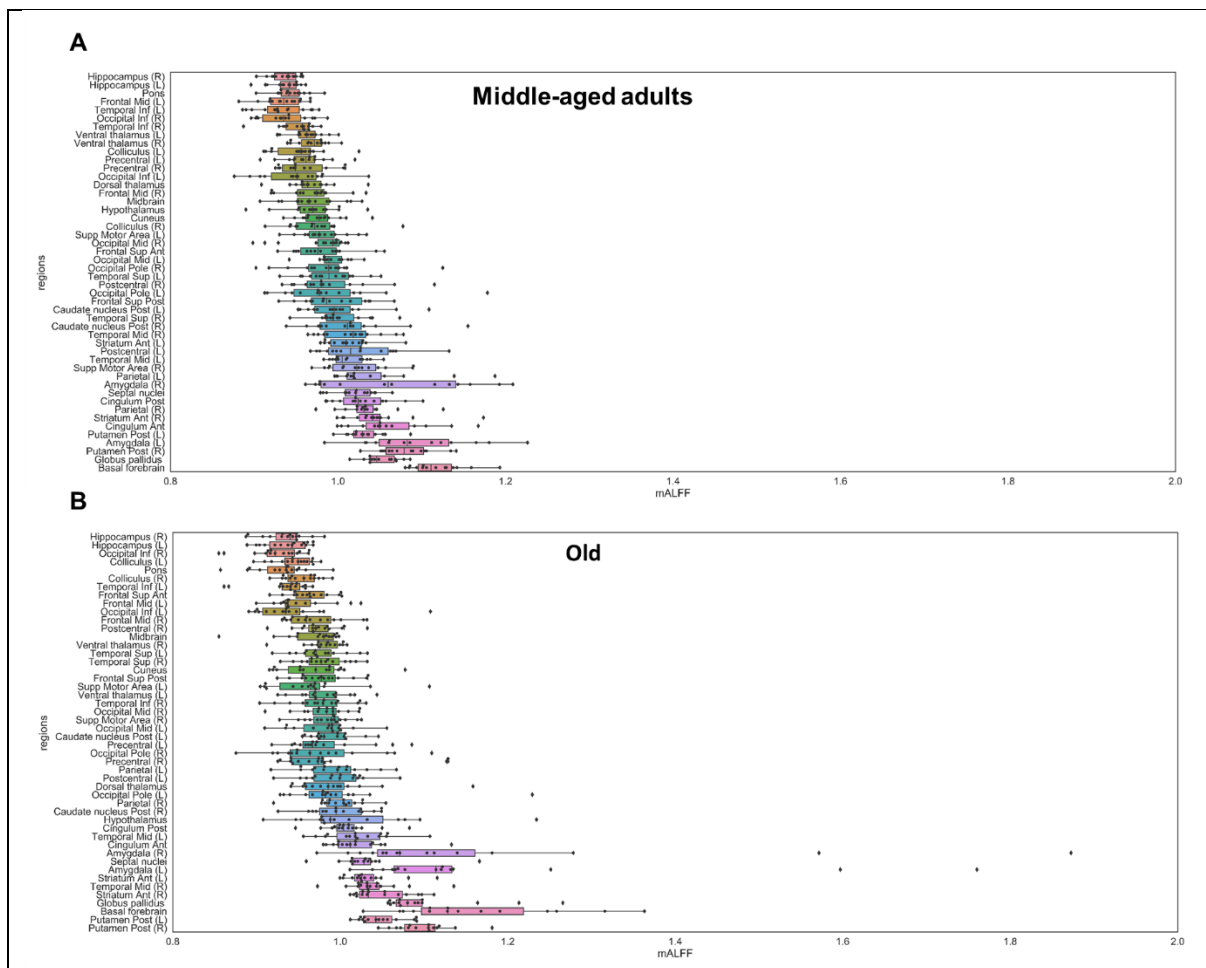
Supplementary figure 1. mALFF scores in middle aged and old mouse lemurs.

Extraction of the averaged mALFF signal in the different regions of the mouse lemur functional atlas. The regions were ranked based on their group t-values (one-sample one-sided t-test to control whether the mALFF signal varied from 1).

Supplementary figure 2. Eigenvector centrality scores, reflecting "hubness" in middle-aged and old mouse lemur brains.

The whole brain network was defined as a set of 48 nodes identified as local functional regions previously described in mouse lemurs. These nodes were used to build an averaged matrix for middle-aged and old mouse lemur cohorts. The measure of node influence was measured by eigenvector centrality. In young animals, the regions displaying the highest scores were the cingulate anterior, cingulate posterior, superior frontal and temporal cortices. The two structures presenting the highest centrality scores in young animals (cingulate cortices) had lower scores in old animals.

Supplementary figure 3. gluCEST signal in middle aged and old mouse lemurs.

Extraction of the averaged gluCEST signal in the different brain regions of the mouse lemur. The regions were ranked based on their group t value (one-sample one-sided t-test to control whether the gluCEST signal varied from 1).
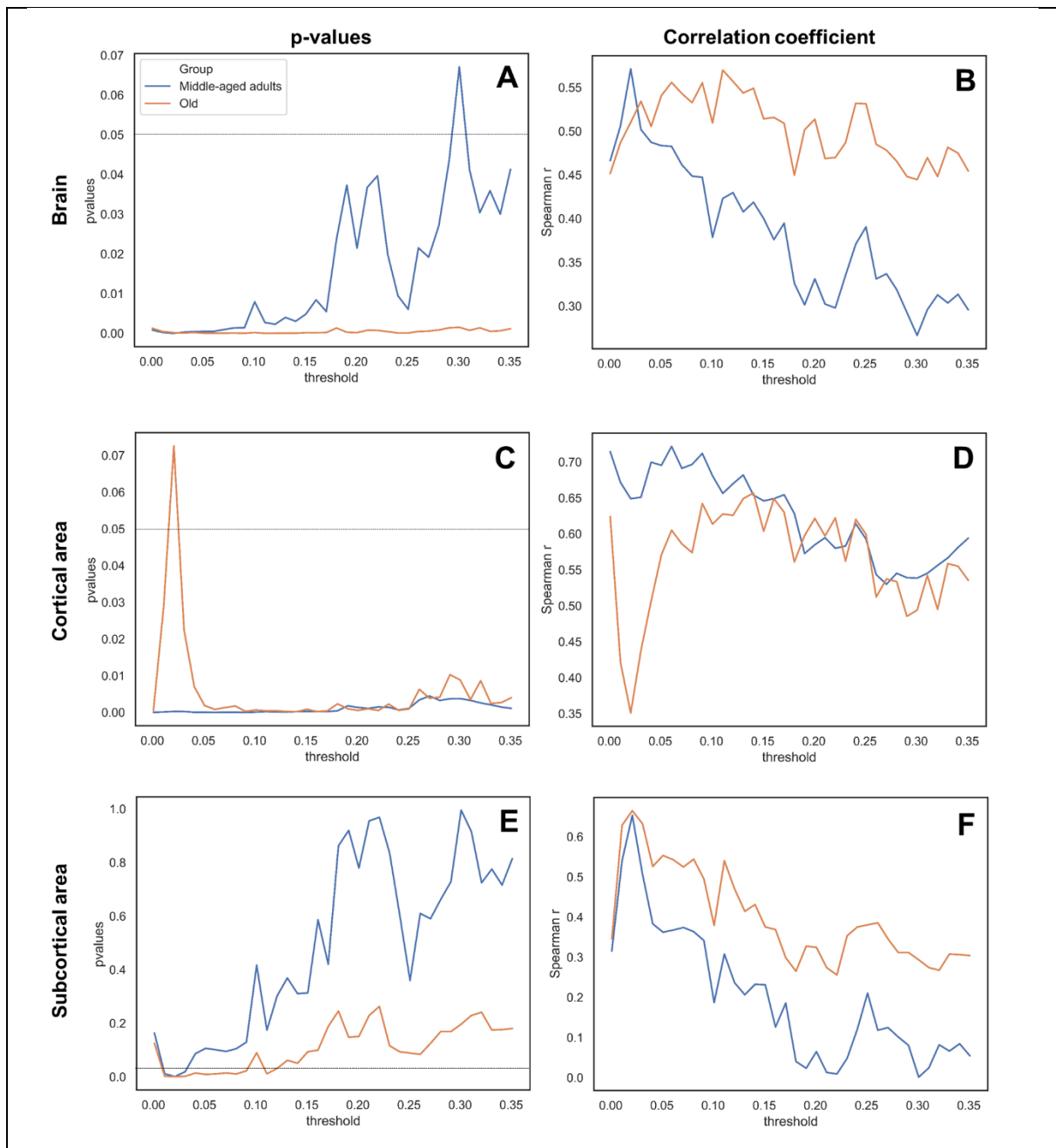
Supplementary figure 4. Stability of the correlations between gluCEST and eigenvector centrality.

The gluCEST signal was extracted and averaged in the different brain regions of mouse lemurs. Hub centrality score was calculated based on the average eigenvector centrality of each brain region. Thresholds used to remove non-significant edges were modulated from 0.0001 to 0.36 with a spacing value of 0.01 on the cortical graph. The correlations were considered statistically significant at $p < 0.05$ (Spearman correlation; black dotted line). This hypothesis was tested all along the 36 points and in the two cohorts.
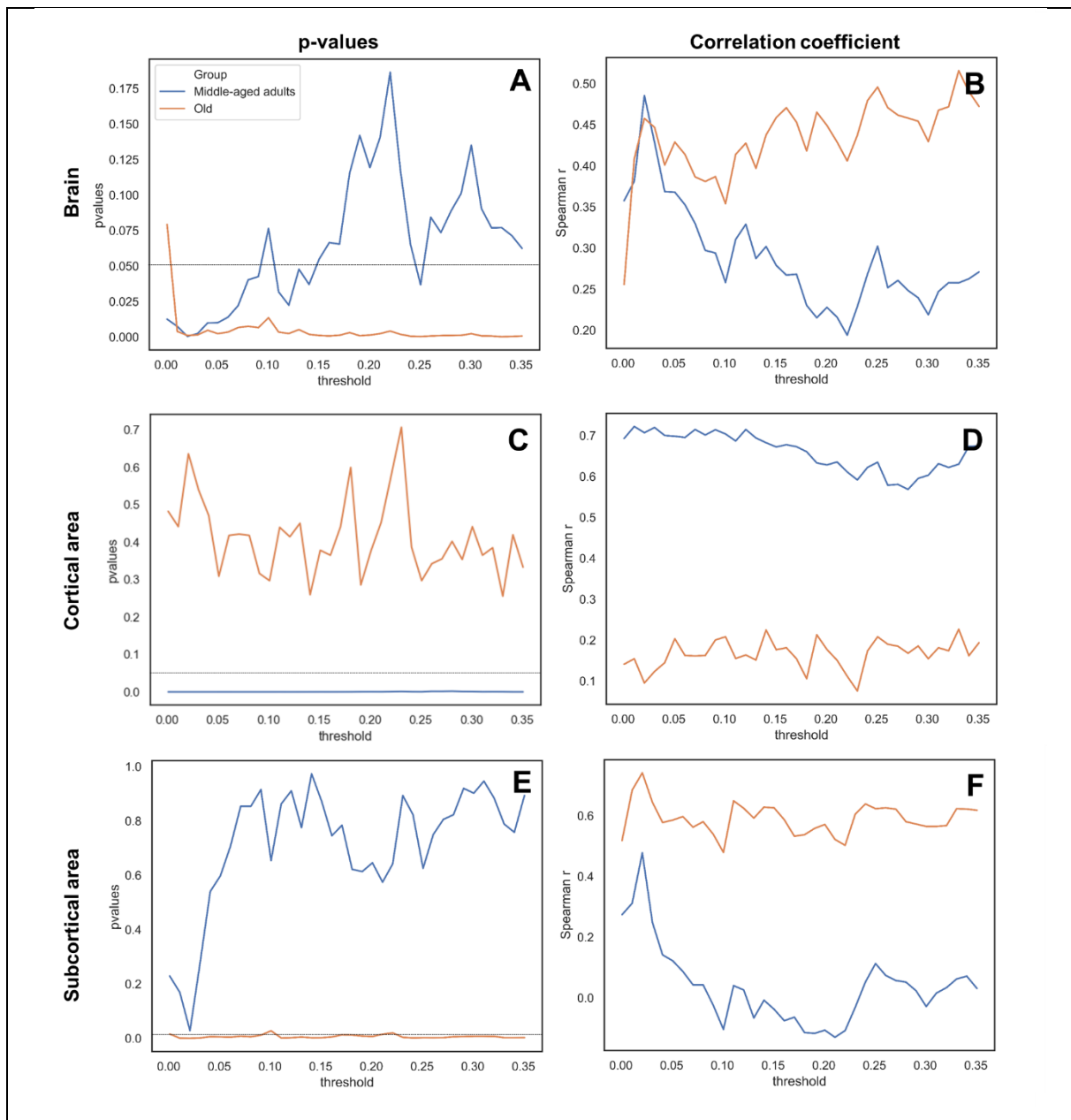
Supplementary figure 5. Stability of the correlations between mALFF and eigenvector centrality.

The mALFF signal was extracted and averaged in the different brain regions of the mouse lemur. Hub centrality score was calculated based on the average eigenvector centrality of each brain region. Thresholds used to remove non-significant edges were modulated from 0.0001 to 0.36 with a spacing value of 0.01 on the cortical graph. The correlations were considered statistically significant at *p* < 0.05 (Spearman correlation; black dotted line). This hypothesis was tested all along the 36 points and in the two cohorts.

III. <u>**Discussion**</u>

Mouse lemurs (*Microcebus murinus*) are the smallest, fastest developing, and among the most prolific and abundant primates in the world. They attract increased attention as potential model organisms for primate biology, behavior, and health (Ezran et al., 2017). In particular, they are used for neuroscience research as model of cerebral aging (Languille et al., 2012) and various neurodegenerative diseases (Mestre-Francés et al., 2018). They also have a key position on the phylogenetic tree of primates and can be used to investigate primate brain evolution. Despite this interest, the tools that are used to characterize mouse lemur brains are based on "old" technologies such as paper atlases. Today 3D atlases are gold standard for atlases. They possess much more visualization and computational power than classical paper atlases. For example, shapes and volumes of brain structures can be visualized directly from a 3D digital atlas. They allow to perform automatic quantification of different information (cerebral atrophy, MRI signal) and make it possible to analyze information from different sources and imaging modalities, such as function, gene and protein expression patterns that can be incorporated into the same framework (Lebenberg et al., 2011) (Ma et al., 2005) (Mazziotta et al., 1997). Here our objective was to develop and use different atlases of mouse lemur brains. First, we developed an anatomical atlas of the brain, then we described resting-state networks and functional maps (based on ALFF) in mouse lemurs. Finally, we created glutamate maps of their brains and used the previously developed atlases to analyse relationships between brain function and glutamate. We also performed a multimodal analysis of age-related changes occurring in mouse lemur brains. The ability to perform such analyses was based on the development of dedicated tools, in particular Sammba-MRI and of image analysis pipelines to analyse rsfMR images.

III.1. From anatomical to functional atlases in mouse lemurs

III.1.1. Comparison of anatomical to functional atlases

Historically, histology-based atlases were used to characterize the brain of most animal species. In addition to the characterization of brain structures, cytoarchitectural analyses allowed to characterize different brain regions including in lemurs (Brodmann, 1999 (original in 1909)) (Le Gros Clark, 1931). Here, first, we proposed a new 3D atlas based on manual segmentation of the brain. 120 regions were identified in this atlas

and the definition of cortical regions was mainly based on the manual transfer of structures found in histological or cytoarchitectural atlases (Le Gros Clark, 1931; Zilles et al., 1979) onto the 3D digital atlas.

In a second approach, we created a functional atlas based on the spatial decomposition of BOLD signal issued from rsfMR images. This atlas was composed of 48 functional regions. **Figure 27** displays a comparison of these two atlases. Prior to perform this comparison, the anatomical atlas was simplified by removing regions smaller than 5 mm^3 and regions that had been excluded for functional analysis (white matter, hindbrain, ventricles, olfactory bulb, entorhinal, and prepiriform cortices). This left 28 cortical and 25 subcortical (*i.e.* 53) regions.

The functional atlas displays a slightly different segmentation of brain regions when compared with the anatomical structures (N. Bons et al., 1998; Nadkarni et al., 2018). However, identification of the functional regions remains coherent with the Brodmann atlas (Brodmann, 1909; Le Gros Clark, 1931). Moreover, the quality of the functional atlas was supported by the robust bilaterality of the extracted regions and localization consistent with resting-state network maps from other primates (Belcher et al., 2013). The quality of the functional atlas is also supported by the property of dictionary learning analysis to decompose the BOLD signal without any anatomical priori.

Precise comparisons between the two atlases remain challenging. The two atlases displayed obvious differences in their cortical limits except in the occipital lobes. The frontal lobe seems to be more scattered in the functional atlas but the subcortical boundaries of the two atlases display strong similarities. Note that in the anatomical atlas, the subcortical areas were described with more details (smaller regions) than with the functional ones. Studying the origins of the discrepancies between these two atlases will be essential to improve the characterization of the mouse lemur brain and to further address an adapted use of each atlas. A combined characterization including histology would be an interesting way to further improve the knowledge of mouse lemur brain.
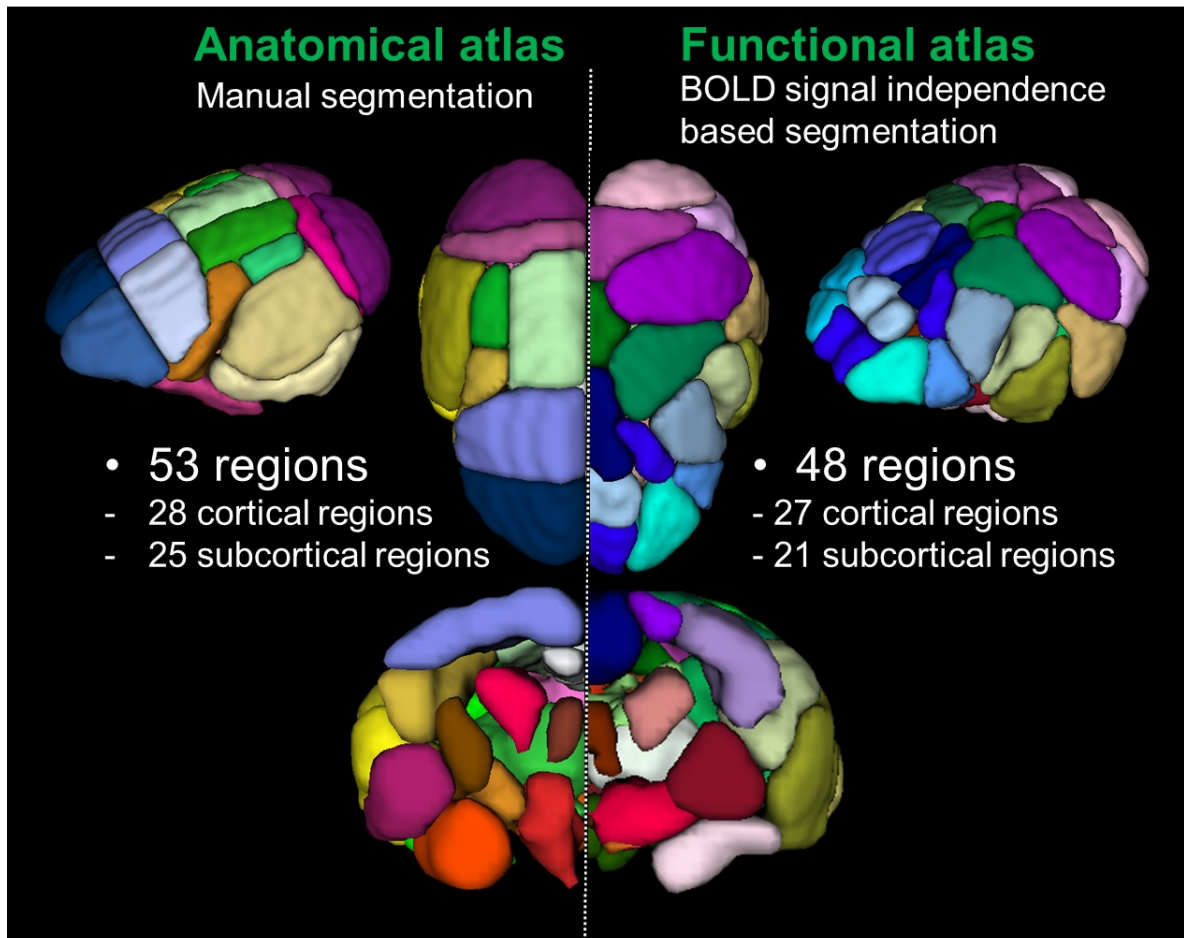
Figure 27 | Mouse lemur 3D functional atlas based on dictionary learning.
Forty-eight local functional regions were identified from the 35 sparse components (regions volume ≥ 5 mm^3). Brain regions were classified based on their locations within the frontal (Blue), parietal (Green), occipital (Purple), temporal (Yellow) lobes. We display three different views and three slices extracted from the functional atlas. This illustration highlights the bilaterality and the distribution of the regions composing our atlas.

It remains difficult to select an adapted atlas for a study, knowing that this choice strongly impacts the quality and the interpretation of the future results. We were confronted with such a choice during our second and third studies. Instead of using an anatomical atlas to identify nodes from mouse lemur cerebral networks, we chose to use the functional atlas. This choice was justified by a homogenous BOLD signal in the functional regions and the quality of the whole brain connectivity graph in the second study.

III.1.2. Graph theory features in mouse lemur brains

Universal properties of the brain topology have emerged recently with graph analysis. One of them is the small-world feature which is an optimal configuration for global information transfer and local processing (Liang et al., 2011; Mechling et al., 2014; Wang et al., 2010). Small-world feature is found in multiple species including humans (Bullmore et Sporns, 2009), non-human primates (Barttfeld et al., 2015), rodents (Mechling et al., 2014) and ferrets (Zhou et al., 2016) and now mouse lemurs. The small world feature of the mouse lemur brain was expected since the brains of most mammals have robust small-world characteristics. It is however interesting to outline that characterization of the brain function in various animals can now be performed using indexes of information processing efficacy.

III.2. Methodological considerations concerning our studies

The characterization of the brain based on resting-state fMRI requires to perform several methodological choices that can modulate the outcome of the studies. We propose to discuss some of the development performed in this context.

III.2.1. Implementation of sammba-MRI

The creation of brain atlases and their manipulations require the use to dedicated tools to register images and compare images issued from different modalities. Optimized workflow for coregistration was already implemented for the human brain since decades. However, an adaptation of the scripts was necessary to resolve the obvious anatomical differences observed between humans and small mammals such as rodents, small primates (differences of grey/white matter volume or brain sizes). Indeed, these anatomical features generate variations in signal intensity that have to be taken into account for each species. Here, we created sammba-MRI to answer to an important need of optimized pipeline for the coregistration of small mammals MR images, especially for fMRI. Using this automated pipeline offers numerous advantages such as the ability to study large cohorts, the possibility to extract unbiased and reproducible information and the ability to save considerable amount of time during image analysis. Recently, using sammba-MRI we tested our coregistration pipeline robustness in four different species (marmoset, mice, rat and mouse lemur). We successfully coregistered their anatomical and fMRI images by just varying the volume

of their brain. Note that an operator quality control is always necessary to assure the quality of the coregistration. However, automated control of the registration quality in mice has recently been proposed (Ioanas et al., 2019). This automated indicator of quality would be interesting to use with sammba-MRI. The different studies presented in my thesis provide examples of sammba-MRI ability to coregister different sources of MR images (anatomical, gluCEST, fMRI) and more recently this capacity has been extended to perfusion MR images. This important flexibility is a significant advantage for the exploration of animal models of pathologies with different MRI approaches.

III.2.2. Anaesthesia and image acquisition protocols

In our studies, rsfMRI were recorded from anaesthetized animals. Anaesthesia remains the major issue for rsfMRI studies in non-compliant species, though it has been published that it preserved the major functional networks (Gozzi et Schwarz, 2016; R. M. Hutchison et al., 2011; J. L. Vincent et al., 2007). However, the reliability of the network under anaesthesia compared to the awake state remains highly discussed (Bukhari et al., 2017; R. M. Hutchison et al., 2010; Paasonen et al., 2018; Uhrig et al., 2018). We used isoflurane which has an effect on the neuronal network depending on the duration and the dose (R. M. Hutchison et al., 2014; Jonckers et al., 2014; C. X. Li et Zhang, 2018). For this reason, we chose the lowest non-awakening isoflurane level possible for mouse lemurs (1.25%). The use of a mix at low doses of medetomine/isoflurane for the anaesthesia might be a way to improve the quality of the images in the future.

Another option might be to record MRI from awake animals. Today, only a few studies have described species scanned whilst awake. However, they have cleaner networks that correspond to a physiological brain state. Working with awake animals is also a great opportunity to further design behavioral experiments associated to BOLD MR acquisitions. Other confounding and practical factors such as stress and the time-consuming training (often leading to a small number of subjects) however need to be taken into account (Belcher et al., 2013).

Further optimization of the rsfMRI dataset can also be obtained by improving the acquisition reproducibility of the EPI images. Several approaches can be proposed to improve the reproducibility of the acquisition: (1) mechanically ventilating the animals

to increase their stability (paCO2) and to avoid movement artefacts due to free breathing (2) the use of a rat cryogenic coil.

III.2.3. fMRI image processing

Image pre-processing is an important key step for data analysis quality during rsfMRI studies in animals. In most resting state fMRI studies, neuronal networks are identified on the basis of a single method and the quality of image processing is left to subjective user judgement (Andronache et al., 2013; Vergara et al., 2017). This subjective intervention can be separated into evaluation of a-priori changes (*i.e.* selection of the best possible dataset) and post-processing analysis (*i.e.* selection of the best (or plausible) neuronal networks within a range of networks obtained). Here, fMRI images were preprocessed with a selective brain mask and by removing movement artefacts. This approach strongly improved the quality of extracted networks and no post-processing analysis or manual removal of irrelevant networks was required.

Then several algorithms can be used to characterize cerebral networks after rsfMRI: seed-based analysis, ICA, dictionary learning… ICA or dictionary learning are strongly dependent on the number of components selected for the study. Classically, this property can be used to test the reproducibility of the component extraction. We found that increasing dictionary learning component numbers provided reproducible but increasingly divided components with similar boundaries. We therefore assumed that, as in humans (Smith et al., 2009), the dictionary analysis could define a functional organization at multiple levels. However, Smith et al. suggested that a tree-structure hierarchy could not be a perfect model covering all levels of details for a highly complex set of interconnected functional areas (Smith et al., 2009).

In our study, we decided to classify whole brain networks into six large scale networks. This choice was based on a user-independent graph analysis algorithm: modularity. This method has the advantage of being user independent although we cannot affirm that it provided the only optimal choices for the brain network partition. Dictionary learning with six components has led to functional maps similar to the resting-state networks observed in other primate fMRI studies (Belcher et al., 2016; Belcher et al., 2013; R. M. Hutchison et al., 2015; R. M. Hutchison et al., 2011).

The similarity between dictionary learning and seed-based analysis concerning the mouse lemur DMN-like had reinforced the assumption that the networks that we identified are accurate (**Figure 28**). However, the thresholds used in seed-based analysis were established visually and by comparison with dictionary learning. We tried to use an automatic threshold (Bonferroni correction) but we found a less accurate organization of brain networks.
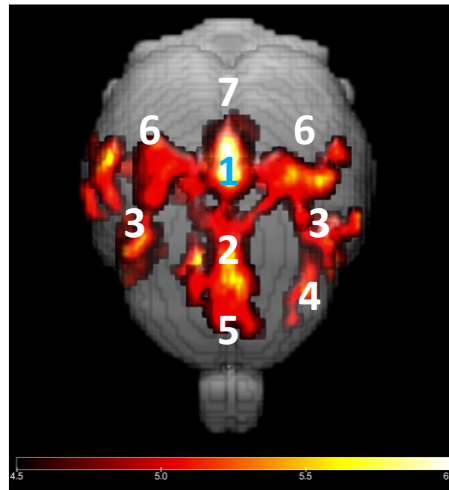
Figure 28 | Mouse lemur DMN-like characterized by seed-based analysis. This figure highlights regions connected to the posterior cingulate cortex (1) used as seed. Correlated activity was observed in the anterior cingulate cortex (2), superior temporal cortex (3), inferior temporal cortex (4), frontal superior posterior cortex (5), parietal cortex (6), and cuneus (7). The color bar represents the one-sample t-test z-score values threshold at p<0.05 (Bonferroni corrected; n=28 animals).

The stability of the whole brain network (connectivity matrices) or the capacity to extract networks individually was not shown in our studies. The use of small animals can cause reproducibility difficulties at the individual scale. It is one of the reasons why resting-state network studies in small mammals require the use of an important number of animals to assure a significant statistical power. In the second study, we used 28 lemurs. This is probably the highest number of non-human primates used to identify neuronal networks. In our studies, the functional hubs identification was reproducible across 2 studies and between two cohorts (middle-aged and old). Also, varying the number of components in the dictionary learning analysis (study 2) allowed the identification of reproducible functional regions across different analysis (not shown). This suggests that the networks that were identified are robust.

III.3.   Perspective of the studies

The description of the mouse lemur network was one of the major results of this thesis. We described these networks with the most detail as possible knowing that they will be reemployed in future studies. The comparison and the detection of the human networks with the same methodology have participated to ensure the accuracy of our results and to propose hypothetic functions for these networks. We also provided multimodal description of mouse lemur brains by focusing on ALFF and gluCEST signal. We showed that glutamate is strongly associated to mALFF in cortical and subcortical brain regions. In the cortex, glutamate is also associated to functional connectivity and to long-distance transfer of information. We also highlighted age-related changes for these parameters. They concern alterations of mALFF in the DMN, a critical network for brain function and reduction of glutamate in the globus pallidus. We also highlighted an age-related reorganization of the cortical/subcortical relationships between mALFF and functional connectivity. Interestingly these analyses were possible because MR images were recorded at high magnetic field (11.7 Tesla). This outline an obvious interest of mouse lemurs that are small primates that fit in such high filed MRI.

In the future, the methodology that was developed in the context of this thesis will allow the characterization of mechanisms behind the various pathological processes that can be induced in this species. It is possible to induce a neurodegenerative process related to Alzheimer pathology in lemurs (Gary et al., 2016). In the future it will be possible to assess relationships between alterations of functional neuronal networks, ALFF or glutamate level and the induction of an "Alzheimer's disease like" pathology.

IV.   Annexe

IV.1.   Résumé

Les modèles animaux sont couramment utilisés pour imiter les maladies afin d'explorer l'impact des processus pathologiques sur les réseaux cérébraux ou pour mesurer l'effet d'une nouvelle thérapie. Le microcèbe murin (Microcebus murinus) est un primate particulièrement intéressant en neuroscience. Ce petit animal est un modèle d'étude du vieillissement cérébral et de diverses maladies comme l'encéphalopathie associée au diabète, la maladie de Parkinson ou la maladie d'Alzheimer. Il occupe une position clé sur l'arbre phylogénétique des primates et est utilisé pour étudier l'évolution du cerveau. Son anatomie cérébrale est encore mal décrite et ses réseaux cérébraux n'ont jamais été étudiés.

L'imagerie fonctionnelle par résonance magnétique fonctionnelle (IRMf) est largement utilisée pour étudier le fonctionnement du cerveau en réponse à des tâches spécifiques. Elle est également utilisée en l'absence de tâches explicites (c'est à dire à l'état de repos). Elle détecte des oscillations du signal BOLD de basse fréquence. Ces oscillations sont similaires dans des structures cérébrales fonctionnellement connectées qui sont appelées réseaux. Les études des réseaux cérébraux ont contribué à de nombreuses percées dans la compréhension des fonctions cérébrales, dans des conditions normales et pathologiques telles que la maladie d'Alzheimer ou la maladie de Parkinson. Cependant, de nombreuses questions subsistent, portant à la fois sur le fonctionnement de la technique d'IRMf et son interprétation. Par exemple, le rôle de ces réseaux dans les fonctions cérébrales et les mécanismes biologiques à l'origine de leurs activités sont encore partiellement inconnus. De plus, l'impact de leurs modulations sur le comportement et la cognition dans des conditions pathologiques fait toujours l'objet de débats.

Une question récurrente concernant l'étude de cohortes d'animaux par IRM anatomique et IRM fonctionnelle est le recalage spatial de grandes séries d'images acquises avec différents protocoles. Certains outils ont été développés au cours de la dernière décennie pour analyser les images obtenues sur des petits animaux. Toutefois, les outils informatiques actuels sont peu avancés en comparaison à ceux l'homme. Nous avons donc développé un logiciel Python appelé sammba-MRI, conçu pour offrir une utilisation efficace des méthodes de recalage spatial existantes chez

l'humain (ANTS, AFNI). Il génère des modèles d'images anatomiques moyennées, spécifiques des cohortes et recale diverses images IRM vers ces modèles. Sur la base d'un modèle généré avec sammba-mri, nous avons construit un atlas anatomique numérique du cerveau du lémurien. Cet atlas, ainsi que plusieurs autres atlas de mammifères disponibles, ont permis de comparer entre espèces les volumes de différentes régions cérébrales. Des mesures issues de ces atlas IRM indiquent que l'indice de volume de la substance blanche par rapport au volume cérébral augmente du rongeur aux petits primates, aux macaques, atteignant leurs valeurs les plus élevées chez les humains.

La deuxième partie de l'étude a été consacrée à l'élaboration de protocoles pour effectuer des études de connectivité chez les microcèbes. Des protocoles IRM dédiés ont été développés et sammba-mri a été utilisé pour recaler les images IRMf. Nous avons créé une méthodologie pour extraire et caractériser, pour la première fois, les réseaux cérébraux chez le microcèbe. Nous avons montré que leur cerveau est organisé en régions fonctionnelles intégrées dans des réseaux fonctionnels à grande échelle. Ils ont été classés comme étant des réseaux de type mode par défaut, fronto-temporaux, moteurs, visuels, ganglions de la base et thalamiques. Ces réseaux ont pu être comparés aux réseaux chez l'humain. Nous avons mis en évidence des règles d'organisation communes, mais aussi des divergences entre ces deux espèces.

Les mécanismes biologiques associés à l'organisation de régions cérébrales en réseaux sont encore mal compris. Dans la dernière partie de cette thèse, nous avons caractérisé une relation entre IRMf à l'état de repos et les niveaux régionaux de glutamate. Ces derniers ont été obtenus à l'aide d'une technique d'imagerie du glutamate appelée transfert de saturation par échange chimique (gluCEST). Nous avons mis en évidence une relation entre une mesure de l'activité cérébrale (ALFF) issue de l'IRMf, le score de hubness et le niveau de glutamate. Ces résultats suggèrent que le glutamate joue un rôle critique dans l'organisation et la régulation de la fonction cérébrale. Une relation entre le hubness, l'activité neuronale locale et un indice du niveau de glutamate dans le cerveau est compatible avec le rôle bien établi du glutamate comme neurotransmetteur excitateur. Nous avons également mis en évidence des changements liés à l'âge pour ces paramètres. Ils concernent les modifications d'ALFF dans le réseau en mode par défaut et la réduction de glutamate dans le globus pallidus. Nous avons également mis en évidence une réorganisation

liée à l'âge des relations corticales / sous-corticales entre ALFF et la connectivité fonctionnelle.

IV.2.1.Oral scientific communications:

<u>Multilevel functional organization of the mouse lemur primate brain</u>

International Society of Magnetic Resonance in Medicine, Montréal, 2019

Clément Garin[1,2], Nachiket Abhay Nadkarni[1,2], Salma Bougacha[1,2], Jean-Luc Picq[1,2], and Marc Dhenain[1,2]

[1]Commissariat à l'Energie Atomique et aux Energies Alternatives (CEA), Direction de la Recherche Fondamentale (DRF), Institut François Jacob, MIRCen, Fontenay-aux-Roses, France, [2]Centre National de la Recherche Scientifique (CNRS), Université Paris-Sud, Université Paris-Saclay UMR 9199, Neurodegenerative Diseases Laboratory, Fontenay-aux-Roses, France

Resting state networks have been characterized in numerous mammals covering human, non-human primates, dogs, rabbits and rodents, though only ever at single semi-arbitrary levels of complexity. In humans, resting state networks analyses have been extended to extracting networks of varying complexity, representing different levels of a possible "functional hierarchy". We performed the first study of "functional hierarchy" in animals. We focused on the gray mouse lemur (Microcebus murinus), a small primate attracting increased attention as a model for cerebral and age-related disorders.

IV.2.2.Invited talk:

<u>Brain network analysis using resting state fMRI, Demonstration studies in small non-human primates</u>
General meeting of NEURATRIS, ICM, Paris, 2019

Resting state, gluCEST and anatomical MRI approaches at 11.7T for brain aging studies in a non-human primate

International Society of Magnetic Resonance in Medicine, Paris, 2018

Clément Garin[1], Nachiket Abhay Nadkarni[1], Salma Bougacha[1,2], Jeremy Pepin[1], Julien Flament[1], Jean-Luc Picq[1,3], and Marc Dhenain[1]

[1]Commissariat à l'Énergie Atomique et aux Énergies Alternatives (CEA), Fontenay-aux-Roses, France, Fontenay aux roses, France, [2]3U1077, INSERM, Caen, France, [3]Laboratoire de psychopathologie et de neuropsychologie, University of Paris 8, Paris, France

The gray mouse lemur (Microcebus murinus) is a small non-human primate with rapid maturity. This study focuses on the development of non-invasive MRI tools applied to neurodegenerative processes. We performed three different types of analysis: anatomical volumetric measures, neuronal network assessment with resting-state fMRI and brain glutamate distribution with gluCEST imaging. We found anatomical atrophy and functional deficiency mostly in cortical regions. To our knowledge, this study is the first to characterize the functional and anatomical brain aging process in a non-human primate. Furthermore, the mouse lemur functional and gluCEST maps have never been described before.

MRI Evaluation of Morphological and Perfusion Changes in Aged APP$_{Swe}$PS1$_{dE9}$

M. Alzheimer's Association International Conference, Londre, 2017

Clément Garin[1,2] , Nachiket Abhay Nadkarni[2,3] , Clemence Dudeffant[1,2] , Marc Dhenain[2,3] ,

[1]Commissariat a l'Energie Atomique et aux Energies Alternatives (CEA), Fontenay-aux-Roses, France; [2] Centre National de la Recherche Scientifique (CNRS), Fontenay-aux-Roses, France; [3] Commissariat a l'Energie Atomique et aux Energies Alternatives (CEA), MIRCen, Fontenay-aux-Roses, France

Animal functional magnetic resonance imaging: Trends and path toward standardization.

Francesca Mandino, Dominic Cerri, Clement M. Garin, Milou Straathof, Geralda van Tilborg, M. Mallar Chakravarty, Marc Dhenain, Rick M. Rijkhuizen, Alessandro Gozzi, Andreas Hess, Shella D. Keilholz, Jason P. Lerch, Yen-Yu Ian Shih, Joanes Grandjean

----

Toward the large scale network evolutionary history: a mammals cross-species comparison using fMRI

IV.2.5.Other contributions

Contrast-enhanced MR microscopy of amyloid plaques in five mouse models of amyloidosis and in human Alzheimer's disease brains

Objective: - Identify the amyloid plaque topologies in different mouse models of amyloidosis and evaluate the impact of various characteristics on their detection by MRI

Contribution: In this article my participation concerned the MRI acquisitions and the breeding of mice.

Common functional networks in the mouse brain revealed by multi-centre resting-state fMRI analysis

Objective: - Identify reproducible and common large scale networks using rsfMRI images produced by different laboratories

- Produce a guideline for the design of rodent rsfMRI investigations

Contribution: In this article my participation mostly concerned the acquisition of fMRI and anatomical images in mice at 11.7T. We also participated in the common reflection for an international standardization of rodent rsfMRI practices.

OPEN

Contrast-enhanced MR microscopy of amyloid plaques in five mouse models of amyloidosis and in human Alzheimer's disease brains

Clémence Dudeffant[1,2], Matthias Vandesquille[1,2], Kelly Herbert[1,2], Clément M. Garin[1,2], Sandro Alves[3], Véronique Blanchard[4], Emmanuel E. Comoy[5], Fanny Petit[1,2] & Marc Dhenain[1,2]

Gadolinium (Gd)-stained MRI is based on Gd contrast agent (CA) administration into the brain parenchyma. The strong signal increase induced by Gd CA can be converted into resolution enhancement to record microscopic MR images. Moreover, inhomogeneous distribution of the Gd CA in the brain improves the contrast between different tissues and provides new contrasts in MR images. Gd-stained MRI detects amyloid plaques, one of the microscopic lesions of Alzheimer's disease (AD), in $APP_{SL}/PS1_{M146L}$ mice or in primates. Numerous transgenic mice with various plaque typologies have been developed to mimic cerebral amyloidosis and comparison of plaque detection between animal models and humans with new imaging methods is a recurrent concern. Here, we investigated detection of amyloid plaques by Gd-stained MRI in five mouse models of amyloidosis ($APP_{SL}/PS1_{M146L}$, APP/$PS1_{dE9}$, APP23, APP_{SwDI}, and 3xTg) presenting with compact, diffuse and intracellular plaques as well as in *post mortem* human-AD brains. The brains were then evaluated by histology to investigate the impact of size, compactness, and iron load of amyloid plaques on their detection by MRI. We show that Gd-stained MRI allows detection of compact amyloid plaques as small as 25 μm, independently of their iron load, in mice as well as in human-AD brains.

Amyloid plaques are one of the earliest hallmarks of Alzheimer's disease (AD), occurring up to 20 years before clinical diagnosis[1]. Even if their role in AD onset is still debated, they appear as an effective biomarker of its preclinical stages. Currently, the clinical detection of amyloid plaques is based on positron emission tomography (PET) imaging with three radioactive agents recently approved by the Food and Drug Administration (FDA)[2]. However, the low spatial resolution of PET does not allow the visualization of individual plaques, and in animals, PET studies have provided controversial results[3, 4]. For example, some studies successfully detected amyloid progression in APP23[5] and 5xFAD[6] mice while others failed to detect signal changes related to amyloidosis[7, 8]. Other imaging modalities, such as optical imaging[9] or two-photon imaging after craniotomy[10], have also been developed to detect amyloid plaques in animals. As with PET, optical imaging is too low-resolution to identify individual plaques. Two-photon imaging, however, can reveal individual amyloid plaques at very high resolution (1 μm)[10] though the field of view of the technique is limited and does not allow recording of images from the whole brain[11].

Continuous efforts are ongoing to implement amyloid plaque detection by high-resolution magnetic resonance imaging (MRI). MRI-based monitoring of amyloid plaques can be divided into three research fields. Some studies are based on the endogenous contrast of the plaques, in both mouse models of amyloidosis[12–15] and in

[1]Centre National de la Recherche Scientifique (CNRS), Université Paris-Sud, Université Paris-Saclay UMR 9199, Neurodegenerative Diseases Laboratory, F-92260, Fontenay-aux-Roses, France. [2]Commissariat à l'Energie Atomique et aux Energies Alternatives (CEA), Direction de la Recherche Fondamentale (DRF), Molecular Imaging Research Center (MIRCen), F-92260, Fontenay-aux-Roses, France. [3]INSERM U986, Université Paris-Sud, 94276, Le Kremlin-Bicêtre, France. [4]Sanofi, Translational Science Unit, Molecular Histopathology and Bioimaging, Chilly-Mazarin, France. [5]Commissariat à l'Energie Atomique et aux Energies Alternatives (CEA), Direction de la Recherche Fondamentale (DRF), Institut des Maladies Emergentes et des Therapies Innovantes (IMETI), SEPIA, 18 Route du Panorama, F-92265, Fontenay-aux-Roses, France. Clémence Dudeffant and Matthias Vandesquille contributed equally to this work. Correspondence and requests for materials should be addressed to M.D. (email: Marc. Dhenain@cea.fr)

humans[16, 17]. This approach is limited by a low sensitivity threshold and is strongly dependent on the iron load of the plaques which locally shortens relaxation times[18, 19]. Also, the possibility to detect plaques by MRI in human tissues on the basis of their endogenous contrast is still disputed[18, 20, 21]. Thus, MR contrast agents seem to be required to facilitate amyloid plaque detection. The first option is to use MR contrast agents specifically targeting amyloid plaques, modulating their MR signal and so increasing their contrast with the brain parenchyma[22–25]. The second option uses non-targeted gadolinium (Gd) contrast agents such as gadoterate meglumine (Dotarem®, Guerbet, France) that is administered in cerebral ventricles after stereotaxic injection[26] or intravenously in association with a non-invasive and safe permeation of the blood-brain barrier using ultrasound[27]. With this method, called Gd-stained MRI, once the contrast agent has reached the brain, amyloid plaques appear as black spots since the hydrophilic Gd-contrast agent increases the signal of tissues surrounding the plaques but do not access their hydrophobic core[28]. As the volume of brain tissue is high compared to the volume of plaques, these agents induce a high signal increase in the brain. This can be converted into resolution enhancement to record high resolution images. Several *in vivo* studies in mice have shown that this method reveals amyloid plaques that otherwise cannot be detected by non-enhanced MRI[26, 27]. Recently, it was used to characterize longitudinally the efficacy of an anti-amyloid immunotherapy[29]. Gd-stained MRI has also been used to detect amyloid plaques in primates[30] and to detect prion plaques in *post mortem* brain samples from Creutzfeldt-Jakob patients[31], but it has never been used to label amyloid plaques in human-AD brains.

Numerous models of amyloidosis with different plaque typologies are used for preclinical investigations. The choice of transgenic mouse model, as well as the stage of Aβ pathology, significantly contributes to the outcome of preclinical studies. Here, we investigated the extent to which Gd-stained MRI allows detection of different types of amyloid lesions including compact, diffuse and intracellular amyloid deposits in five mouse models of amyloidosis (APP$_{SL}$/PS1$_{M146L}$, APP/PS1$_{dE9}$, APP23, APP$_{SwDI}$, 3xTg). Vascular abnormalities often co-exist with amyloid plaques in mouse models of amyloidosis as in AD patients[32]. Aβ peptide may accumulate into the vessel wall of cerebral arteries leading to cerebral amyloid angiopathy (CAA) and microhemorrhages. We also examined the capacity of Gd-stained MRI to detect these lesions. Finally, we explored the capacity of Gd-stained MRI to detect amyloid plaques in *post mortem* human-AD brains. The brain samples were then evaluated by histology to assess the impact of size, compactness, and iron load of amyloid plaques on their detection by MRI. Amyloid plaques from APP$_{SL}$/PS1$_{M146L}$, APP/PS1$_{dE9}$ and human-AD brains had the most similar histological characteristics and could be detected by Gd-stained MRI. Also, we found that the key features associated to amyloid plaque detection by Gd-stained MRI are their size, compactness but not their iron load.

Results

Heterogeneity of amyloid plaque detection in mice. Gd-stained MRI was performed on five mouse models of amyloidosis (APP$_{SL}$/PS1$_{M146L}$, APP/PS1$_{dE9}$, APP23, APP$_{SwDI}$ and 3xTg) and C57Bl/6 amyloid-free control animals. *In vivo* MRI was acquired at a resolution of $29 \times 29 \times 117\,\mu m^3$ after intracerebroventricular injection of gadoterate meglumine. *Ex vivo* MRI was recorded at a resolution of $25 \times 25 \times 100\,\mu m^3$ after incubation of the brains in a Gd solution. *In vivo* and *ex vivo* MRI without Gd-staining were also performed in APP$_{SL}$/PS1$_{M146L}$ mice. Following *ex vivo* MRI acquisitions, brains were processed by histology to label amyloid plaques or iron (Figs 1, 2).

As already reported[26], Gd-staining increased the signal-to-noise ratio in MR images (Suppl. Fig. S1). This protocol revealed several hypointense spots that could not be detected without contrast agent (Suppl. Fig. S1). These spots were mainly found in the cerebral cortex, hippocampus, thalamus and amygdala (Figs 1–3) on *in vivo* or *ex vivo* images of APP$_{SL}$/PS1$_{M146L}$ (Fig. 1A,B, Suppl. Fig. S1), APP/PS1$_{dE9}$ (Fig. 1E,F) and APP23 (Fig. 1I,J) mice. Figure 3 focuses on images of 35 and 80-week-old animals and shows the increased spot density with age. In the youngest animals, hypointense spots were mainly visible in APP$_{SL}$/PS1$_{M146L}$ mice (Fig. 3A) although discrete spots could be detected in the two other strains (Fig. 3B,C). In the oldest animals, the density of hypointense spots was highest in APP$_{SL}$/PS1$_{M146L}$ mice (Fig. 3D) although APP23 mice displayed the largest spots (Fig. 3F). Hypointense spots observed by MRI were identified as amyloid deposits by co-registering MR images with Aβ-stained histological sections (Figs 1, 2). APP$_{SL}$/PS1$_{M146L}$, APP/PS1$_{dE9}$ and APP23 exhibited mainly compact plaques with a dense β-amyloid core (Fig. 1, inserts in C, G, and K). Plaques from APP23 mice were the largest but were less numerous than those of the other two strains. The smallest plaques that could be detected by *in vivo* MRI measured 36 µm, 37 µm and 46 µm for the APP$_{SL}$/PS1$_{M146L}$, APP/PS1$_{dE9}$ and APP23 mice, respectively. On *ex vivo* images, the detection thresholds were 36 µm, 30 µm and 49 µm for the APP$_{SL}$/PS1$_{M146L}$, APP/PS1$_{dE9}$ and APP23 mice, respectively. Iron deposition was also evaluated for each mouse strain either by using Perls-DAB staining alone (Figs 1, 2) or a double staining based on Perls-DAB and Congo red (Fig. 4). APP$_{SL}$/PS1$_{M146L}$ and APP/PS1$_{dE9}$ mice displayed high focal iron accumulations while in APP23 mice iron staining was weak (Figs 1, 4). Registration between MR images and histological sections showed that, some amyloid plaques seen by MRI corresponded with iron deposits (Figs 1, 4, black arrows and circles), while some others could not easily be matched with iron-positive elements (Figs 1, 4, red arrows and circles). This suggests that iron is not mandatory for amyloid plaque detection after Gd-staining.

Correlative studies were performed to further evaluate relationships between the loads of hypointense spots detected by *in vivo* MRI, amyloid plaques and iron deposits in animals in which amyloid plaques could be detected *in vivo* (APP$_{SL}$/PS1$_{M146L}$, APP/PS1$_{dE9}$ and APP23). We found a significant correlation between the hypointense spots load and the amyloid load ($R^2 = 0.82$; $p < 0.01$, Fig. 5A), but no correlation between the hypointense spots load and the iron deposits load ($R^2 = 0.35$, $p > 0.05$, Fig. 5B). We then further evaluated the proportion of iron-positive plaques detected by Gd-stained MRI. Amyloid plaques bigger than the detection threshold ($\geq 36\,\mu m$) were categorized into one of the following four categories: iron-positive plaques detected by MRI, iron-negative plaques detected by MRI, iron-positive plaques not detected by MRI and iron-negative plaques not detected by MRI (Fig. 6). Seventy-six percent of cortical amyloid plaques seen on histological sections
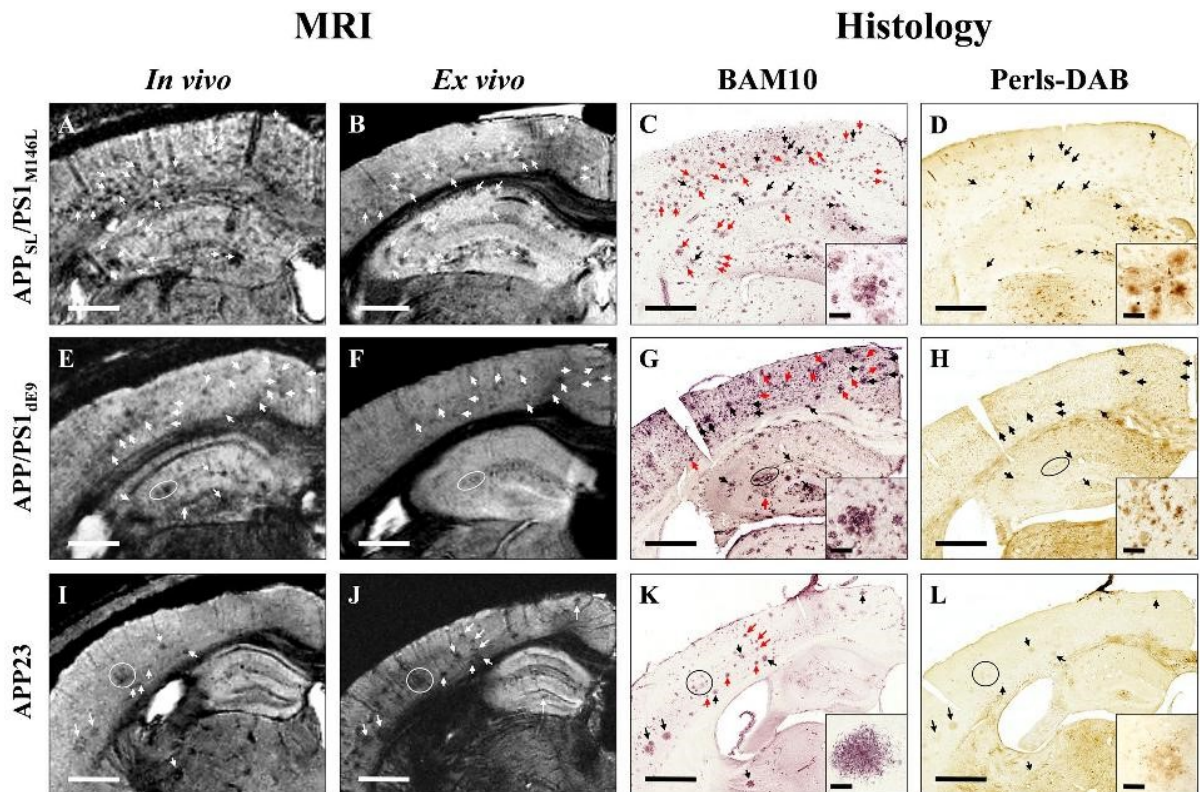
Figure 1. Comparison between detection of amyloid plaques by Gd-stained MRI and immunohistochemistry in $APP_{SL}/PS1_{M146L}$, $APP/PS1_{dE9}$, and APP23 mice. Gd-stained *in vivo* (column 1) *or ex vivo* (column 2) MR images were registered with β-amyloid (BAM10, column 3) and iron-stained (Perls-DAB, column 4) histological sections in $APP_{SL}/PS1_{M146L}$ (**A–D**), $APP/PS1_{dE9}$ (**E–H**) and APP23 (**I–L**) mice. Inserts in columns 3 and 4 display typical plaques for each strain. Hypointense spots (white arrows and circles) are visible in the *in vivo* and/or *ex vivo* MR images of $APP_{SL}/PS1_{M146L}$ (**A,B**), $APP/PS1_{dE9}$ (**E,F**) and APP23 (**I,J**) mice. They can be registered with amyloid plaques (black and red arrows and circles) on BAM10-stained sections (**C,G,K**). Iron staining reveals iron deposits that can be registered with hypointense spots and amyloid plaques in $APP_{SL}/PS1_{M146L}$ (**D**), $APP/PS1_{dE9}$ (**H**) and APP23 (**L**) mice. Some amyloid plaques containing iron (black arrows and circles) are visible on MR images. Some others are iron-free (red arrows) and are also detected by MRI indicating that iron is not necessary for MR detection. Scale bars: 500 μm for main images and 50 μm for inserts.

were detected by Gd-stained MRI (Fig. 6A). Among these, 67% were iron-positive and 33% were iron-negative (Fig. 6B). Few differences were observed between the $APP_{SL}/PS1_{M146L}$, $APP/PS1_{dE9}$ and APP23 mice (Fig. 6). 24% of amyloid plaques seen on histological sections were not detected by Gd-stained MRI (Fig. 6A). We cannot exclude that this lack of detection was related to an imperfect registration between MR images and histological sections because of their different thicknesses (117 and 40 μm, respectively) and because of partial volume effects. Among these 24% of amyloid plaques not detected by Gd-stained MRI, 58% were iron-positive and 42% were iron-negative (Fig. 6C).

In APP_{SwDI} mice, hypointense spots were never detected either on *in vivo* or *ex vivo* images (Fig. 2A,B). On histological sections, these mice displayed large, diffuse and poorly circumscribed plaques (Fig. 2C, red shape, Fig. 4H) and did not display any obvious iron deposits at the level of the plaques (Figs 2D, 4H).

In 3xTg mice, hypointense spots were not detected in most brain regions (Fig. 2E,F). In 3xTg mice younger than 70 weeks, amyloid deposits were mainly intracellular and measured less than 20 μm (Fig. 2G, red arrows). These intracellular deposits were not detected by Gd-stained MRI. Perls-DAB staining did not show iron accumulation within these deposits (Figs 2H, 4J). In older animals, a strong extracellular amyloidosis was observed by histology in most of the brain areas, but only plaques of the subiculum were detected by Gd-stained MRI. These subicular plaques were congophilic and iron-positive while plaques from other brain regions, not detected by MRI, were diffuse and iron-negative (Suppl. Fig. S2).

Control animals did not display any hypointense spots on MR sections (Fig. 2I,J), amyloid plaques (Fig. 2K) or focal accumulations of iron (Fig. 2L) on histological sections.

Visualization of CAA and cerebral microhemorrhages by Gd-stained MRI. CAA and microhemorrhages are often detected in mouse models of amyloidosis. We thus evaluated whether they could be visualized by Gd-stained MRI. Blood vessels were associated with linear or punctuate hypointensities on *in vivo* and *ex vivo* Gd-stained MR images of the five studied models (Fig. 7A–C) but also of amyloid-free control animals
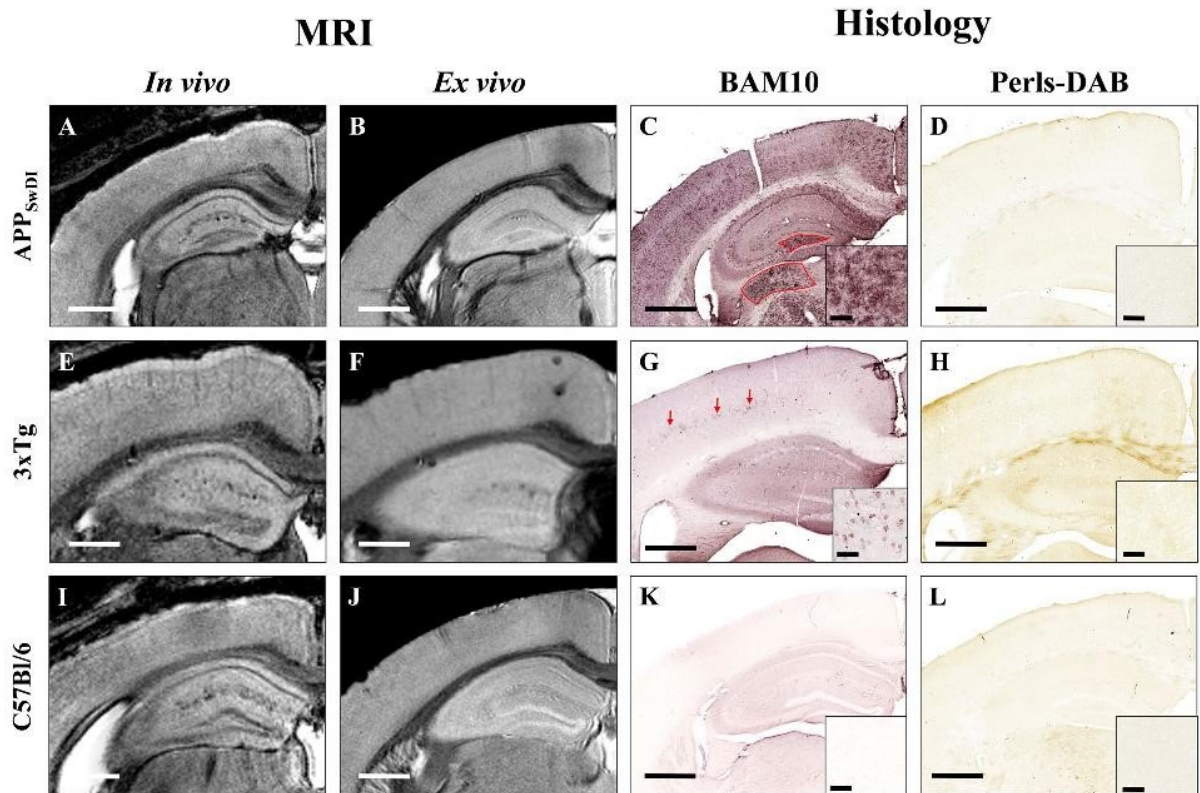
MRI

Histology

| *In vivo* | *Ex vivo* | BAM10 | Perls-DAB |

Figure 2. Comparison between detection of amyloid plaques by Gd-stained MRI and immunohistochemistry in APP_{SwDI}, 3xTg, and C57Bl/6 amyloid-free mice. Gd-stained *in vivo* (column 1) or *ex vivo* (column 2) MR images were registered with β-amyloid (BAM10, column 3) and iron-stained (Perls-DAB, column 4) histological sections in APP_{SwDI} (**A–D**), 3xTg (**E–H**) and C57Bl/6 amyloid-free (**I–L**) mice. Inserts in columns 3 and 4 display typical plaques for each strain. MR images of APP_{SwDI} mice do not present with hypointense spots (**A,B**). BAM10 and iron staining show large diffuse Aβ-positive lesions (**C**, red shape) devoid of iron deposits (**D**). 3xTg mice do not present with hypointense spots on MR images (**E,F**). BAM10 and iron staining show intracellular Aβ deposits (**G**, red arrows) devoid of iron (**H**). In C57Bl/6 amyloid-free mice, no hypointense spots on MR images (**I,J**) or amyloid plaques on BAM10 sections (**K**) are detected. Scale bars: 500 μm for main images and 50 μm for inserts.

(Fig. 7D,E). Registration between MR images and histological sections showed that the hypointense nature of blood vessels was not related to the presence of amyloid angiopathy (Fig. 7B,C).

To evaluate the appearance of microhemorrhages on Gd-stained MR images, we compared MRI recorded before and after Gd-staining. As previously reported[33–35], on non-stained MRI, microhemorrhages were visible as rare hypointense spots (Fig. 7F,G). After Gd-staining, microhemorrhages identified in pre-contrast images remained detected in addition to amyloid plaques. Differentiation between these two lesions could be made on the basis of their size and large microbleeds were the only ones that could easily be differentiated from plaques (Fig. 7H,I). Signal from smaller microbleeds was close to that of plaques (Fig. 7H,I).

Amyloid plaque detection in human-AD brains. Brain samples from three AD patients were imaged by *ex vivo* Gd-stained MRI. Hypointense spots were detected in the cortex but not in the white matter of these patients (Fig. 8A,B,E,F). Registration between MRI and histological sections showed that most of the hypointense spots seen on MR images corresponded to amyloid plaques (Fig. 8B,C,F,G, black and red arrows) or blood vessels (Fig. 8B,C,F,G, blue circles). Hypointense spots within blood vessels can be explained by the presence of blood within the vessels in non-perfused *post mortem* samples. On histological sections, amyloid plaques measured 10 to 200 μm with most plaques smaller than 25 μm. The smallest plaques that could be detected by MRI measured 25 μm.

Finally, Perls-DAB staining revealed iron deposition in most of the human plaques detected by MRI (Fig. 8B–D,F,G, black arrows). However, as in mice, some iron-free plaques were detected by MRI (Fig. 8B–D, red arrows). Double labelling of histological sections with Perls-DAB staining and Congo red revealed two types of iron deposits associated with plaques, *i.e.* some punctate accumulations in the entire plaques (Fig. 8H) and ramified intracellular accumulations surrounding the plaques (Fig. 8I).
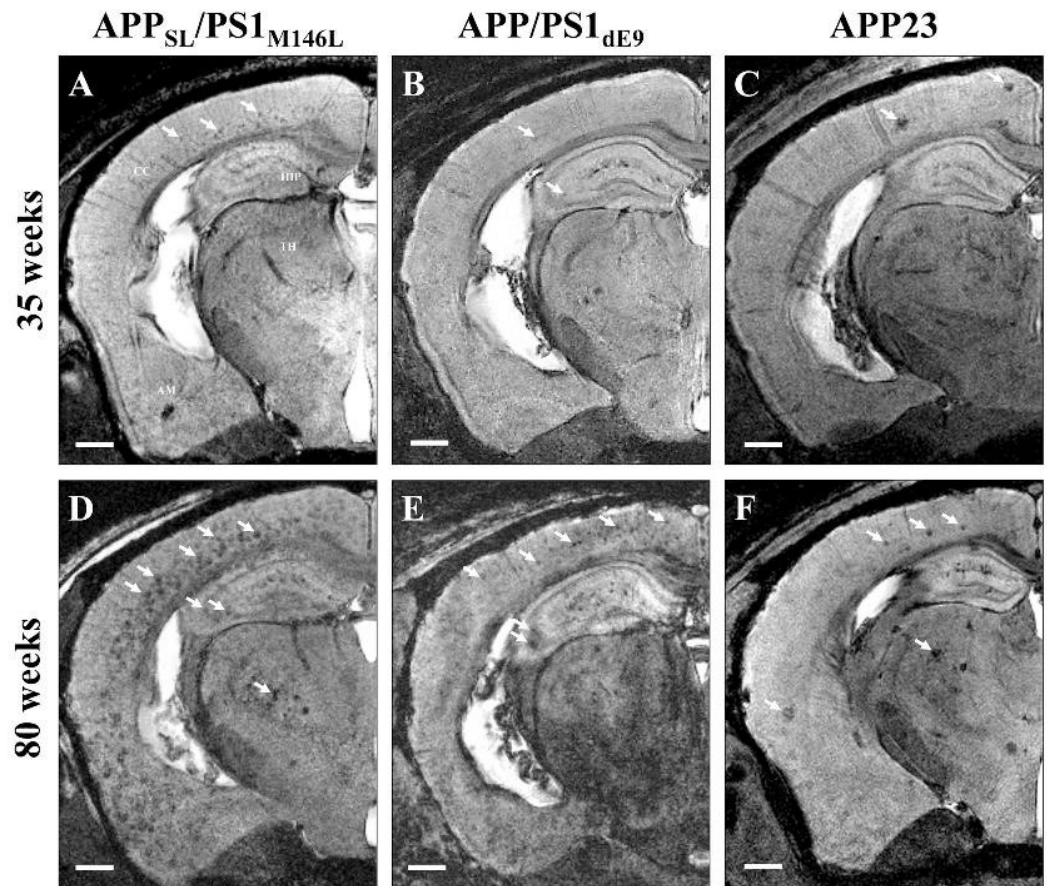
Figure 3. Hypointense spots on MRI sections of 35-week-old (**A–C**) and ~80-week-old (**D–F**) $APP_{SL}/PS1_{M146L}$, $APP/PS1_{dE9}$ and APP23 mice. Hypointense spots (white arrows) are detected in the brain of 35-week-old $APP_{SL}/PS1_{M146L}$ (**A**), $APPPS1_{dE9}$ (**B**), and APP23 (**C**) in the cerebral cortex (CC), hippocampus (HIP), thalamus (TH) and amygdala (AM). These spots increase in number and size in older animals (**D–F**). Scale bars: 500 μm.

Discussion

We compared amyloid lesions in five transgenic mouse models of amyloidosis as well as in human-AD brain samples and explored the ability of Gd-stained MRI to detect amyloid plaques in these brains. Detection of amyloid plaques by Gd-stained MRI was strikingly different among the various models used in this study and in humans. Amyloid plaques were detected *in vivo* and *ex vivo* in $APP_{SL}/PS1_{M146L}$, $APP/PS1_{dE9}$, APP23 and to a lesser extent in 3xTg mice but never in APP_{SwDI} mice. In human-AD brains, amyloid plaques could be detected by *post mortem* Gd-stained MRI.

Our histological evaluation showed that $APP_{SL}/PS1_{M146L}$, $APP/PS1_{dE9}$ and APP23 mice displayed mainly compact plaques. Similar lesions were the most frequently found in the human-AD brain samples studied. Striking differences were observed in the two other strains. Diffuse plaques were detected in APP_{SwDI} mice, whereas intracellular amyloid deposits were found in the 3xTg mice. Intracellular amyloid plaques have been observed in humans[36, 37], but are not the most widely reported as they might occur in early stages of AD[38]. Regarding iron, we detected iron deposits in association with the amyloid plaques of $APP_{SL}/PS1_{M146L}$, $APP/PS1_{dE9}$, APP23, 3xTg mice and of humans. Different iron loads were found in the different models, which is consistent with data from other studies. Jack *et al.* reported strong iron deposits in the plaques of $APP_{S(i.e. Tg2576)}/PS1_{M146L}$ mice[39] while Meadowcroft *et al.* reported a very reduced iron load in the plaques of $APP_{S(i.e. Tg2576)}/PS1_{A246E}$ mice[18]. In humans, some studies reported a close relationship between amyloid plaques and iron depositions[18] while some others suggested high or low iron levels in amyloid plaques even within the same subject[40]. In fact, the relationship between amyloid plaques and iron depositions in humans is still not consensual[41]. Our study supports the presence of iron in some but not all amyloid plaques. Moreover, the shape of the iron deposits is highly variable with focal deposits in mice, while in humans we detected punctate iron accumulations in the entire plaques as well as ramified accumulations surrounding the plaques.

One of the main purposes of our study was to compare MRI and histological characteristics of amyloid plaques in different mouse strains to investigate the critical parameters required for Gd-stained detection of amyloid plaques. The size of amyloid plaques is an important factor that influences their MR detection. Amyloid plaque detection was more efficient in the strains having the largest plaques as observed in $APP_{SL}/PS1_{M146L}$, $APP/PS1_{dE9}$ or APP23 with detection thresholds of 36 and 30 μm for *in vivo* and *ex vivo* images, respectively, which corresponds approximately to 1.2 times the voxel size. This threshold can explain the poor detection achieved in the
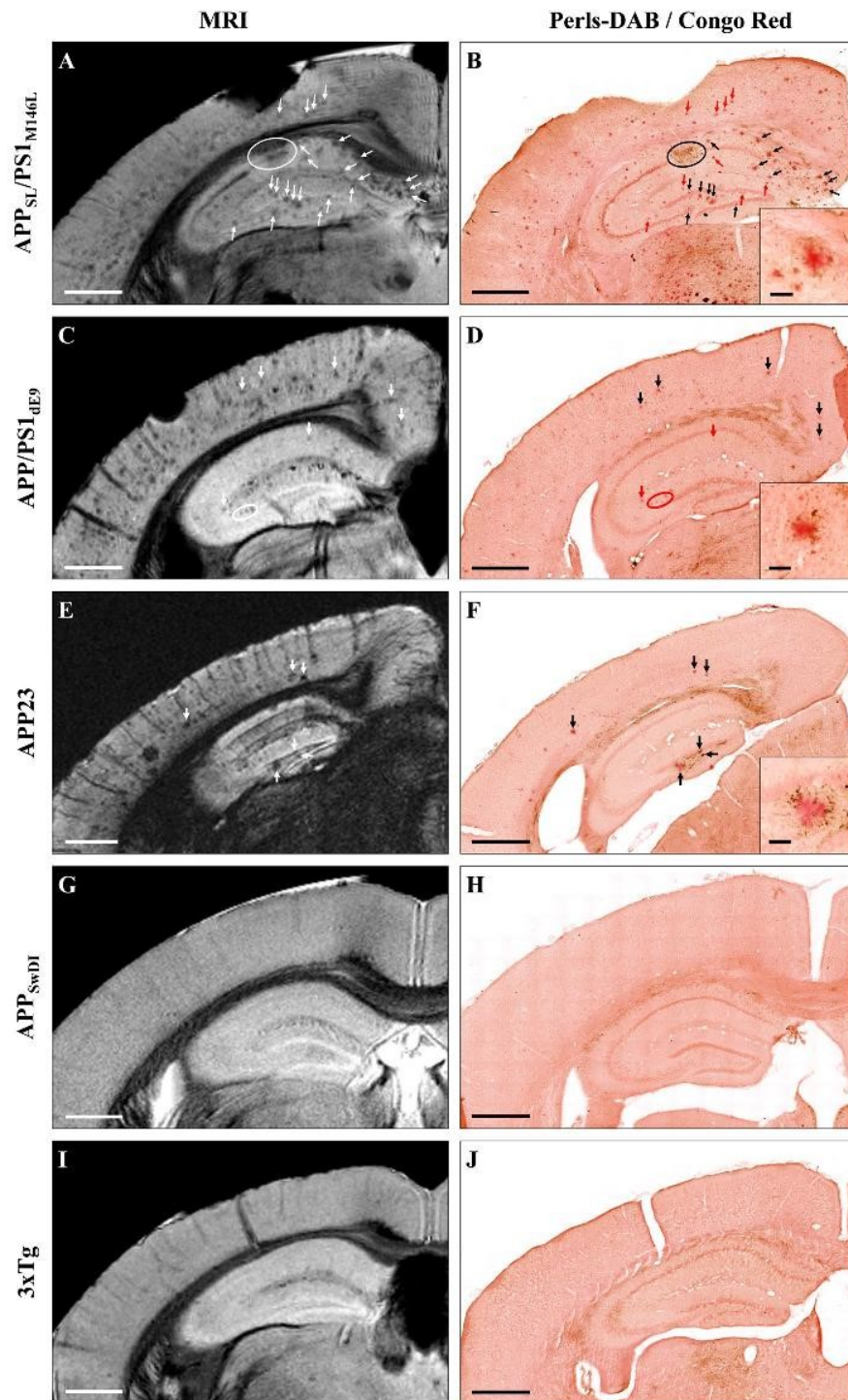
Figure 4. Comparison between detection of amyloid plaques by Gd-stained MRI and histological sections double-stained for amyloid and iron in five mouse strains. Gd-stained MR images (left) were registered with histological sections double-stained for β-amyloid (Congo red) and iron (Perls-DAB) (right) in $APP_{SL}/PS1_{M146L}$ (**A,B**), APP/PS1$_{dE9}$ (**C,D**), APP23 (**E,F**), APP_{SwDI} (**G,H**) and 3xTg (**I,J**) mice. Hypointense spots (white arrows and circles) were visible in the MR images of $APP_{SL}/PS1_{M146L}$ (**A**), APP/PS1$_{dE9}$ (**C**) and APP23 (**E**) mice. They could be registered with congophilic amyloid plaques on histological sections (**B,D,F**, black and red arrows and circles). No congophilic plaques were detected in APP_{SwDI} (**H**) and 3xTg (**J**) mice. Iron staining revealed iron deposits that co-localize with amyloid plaques (black arrows and circles) in $APP_{SL}/PS1_{M146L}$ (**B**), APP/PS1$_{dE9}$ (**D**) and APP23 (**F**) mice. Some other plaques were iron-free (red arrows and circles) and were also detectable by MRI indicating that iron is not necessary for their detection. No iron accumulation was observed in APP_{SwDI} (**H**) and 3xTg (**J**) mice. Scale bars: 500 μm for main images and 50 μm for inserts.
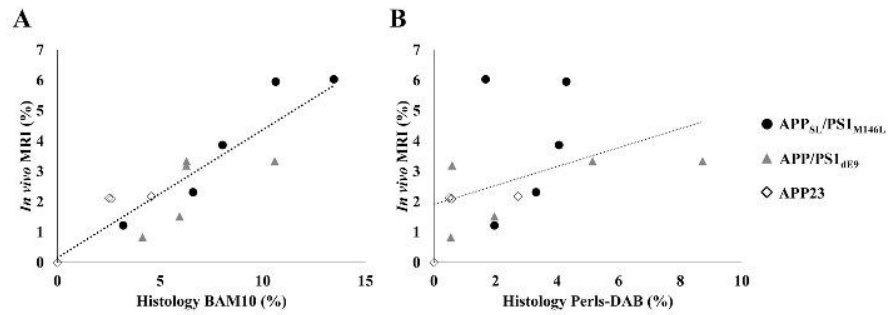
211

Figure 5. Relationships between amyloid load quantified from *in vivo* Gd-stained MR images, and from amyloid-stained histological sections (BAM10) (**A**) or from iron-stained histological sections (Perls-DAB) (**B**). Amyloid load measured from Gd-stained MRI showed a correlation with BAM10 staining ($R^2 = 0.82$; $p < 0.01$) but was not correlated with Perls-DAB staining ($R^2 = 0.35$; $p > 0.05$).
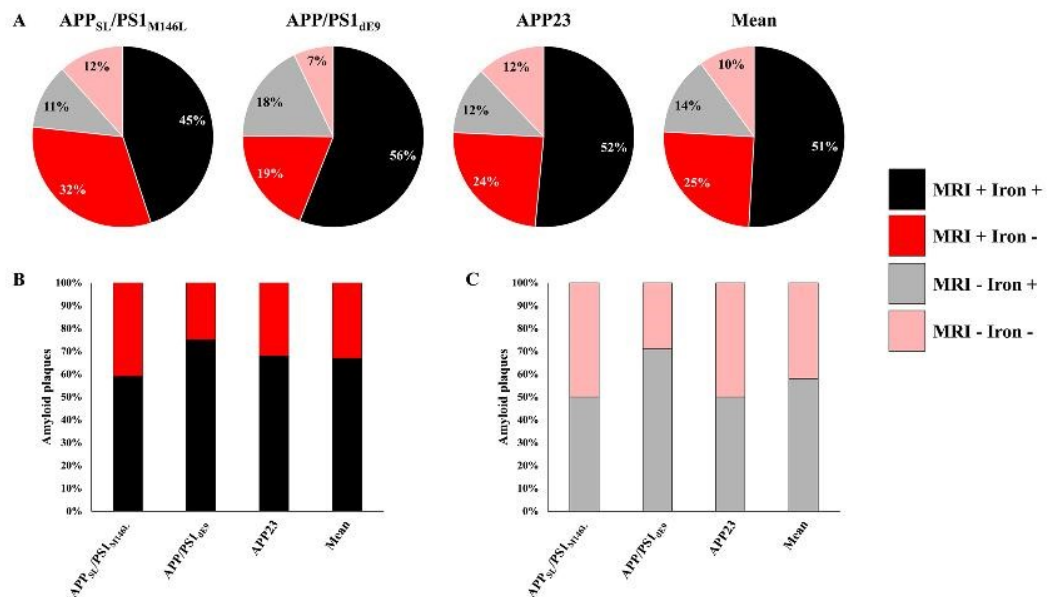

Figure 6. Detectability of amyloid plaques by Gd-stained MRI according to their iron content. Cortical amyloid plaques with a diameter $\geq 36\,\mu m$ were categorized into one of the following four categories: iron-positive plaques detected by MRI (MRI + Iron +, black), iron-negative plaques detected by MRI (MRI + Iron −, red), iron-positive plaques not detected by MRI (MRI − Iron+, grey) and iron-negative plaques not detected by MRI (MRI − Iron −, pink) in $APP_{SL}/PS1_{M146L}$, $APP/PS1_{dE9}$ and APP23 mice (**A**). Among amyloid plaques detected by Gd-stained MRI, 59%, 75% and 68% contained iron in $APP_{SL}/PS1_{M146L}$, $APP/PS1_{dE9}$ and APP23 mice, respectively (**B**). Among amyloid plaques not detected by Gd-stained MRI, 50%, 71% and 50% contained iron in $APP_{SL}/PS1_{M146L}$, $APP/PS1_{dE9}$ and APP23 mice, respectively (**C**).

3xTg mice. In this strain, only the largest plaques could be detected, while most of the amyloid deposits that were intracellular and smaller than $20\,\mu m$ were not seen by MRI. In human-AD brains, the minimum visible plaque size was similar to that in mice (*i.e.* $25\,\mu m$ for human-AD and $30\,\mu m$ for mice).

Our study also showed that the compactness of amyloid plaques seemingly impacts their detection by the Gd-staining procedure. Amyloid plaques were detected in models with compact plaques, but not in models with large diffuse Aβ deposits (*i.e.* APP_{SwDI} or 3xTg mice). The mechanism of contrast enhancement is assumed to be due to the hydrophobic property of amyloid plaques that limits the penetration of the contrast agent within them. Because this hydrophobicity is related to the concentration of the amyloid peptide, diffuse deposits are probably less prone to be revealed by Gd-stained MRI than compact plaques. Interestingly, previous studies have shown that diffuse deposits are not detected by MRI without contrast agents in mice[42] or in human brains[43]. Thus, it seems that Gd-stained MRI does not improve the ability to detect diffuse plaques as compared to contrast-agent free MRI.

Finally, our study showed that iron accumulation is not necessary for plaque detection after Gd-staining. Indeed, in mice, 33% of the amyloid plaques detected with Gd-stained MRI contained little or no iron. Also, in human-AD brain samples, although most of the plaques detected by Gd-stained MRI contained iron deposits,
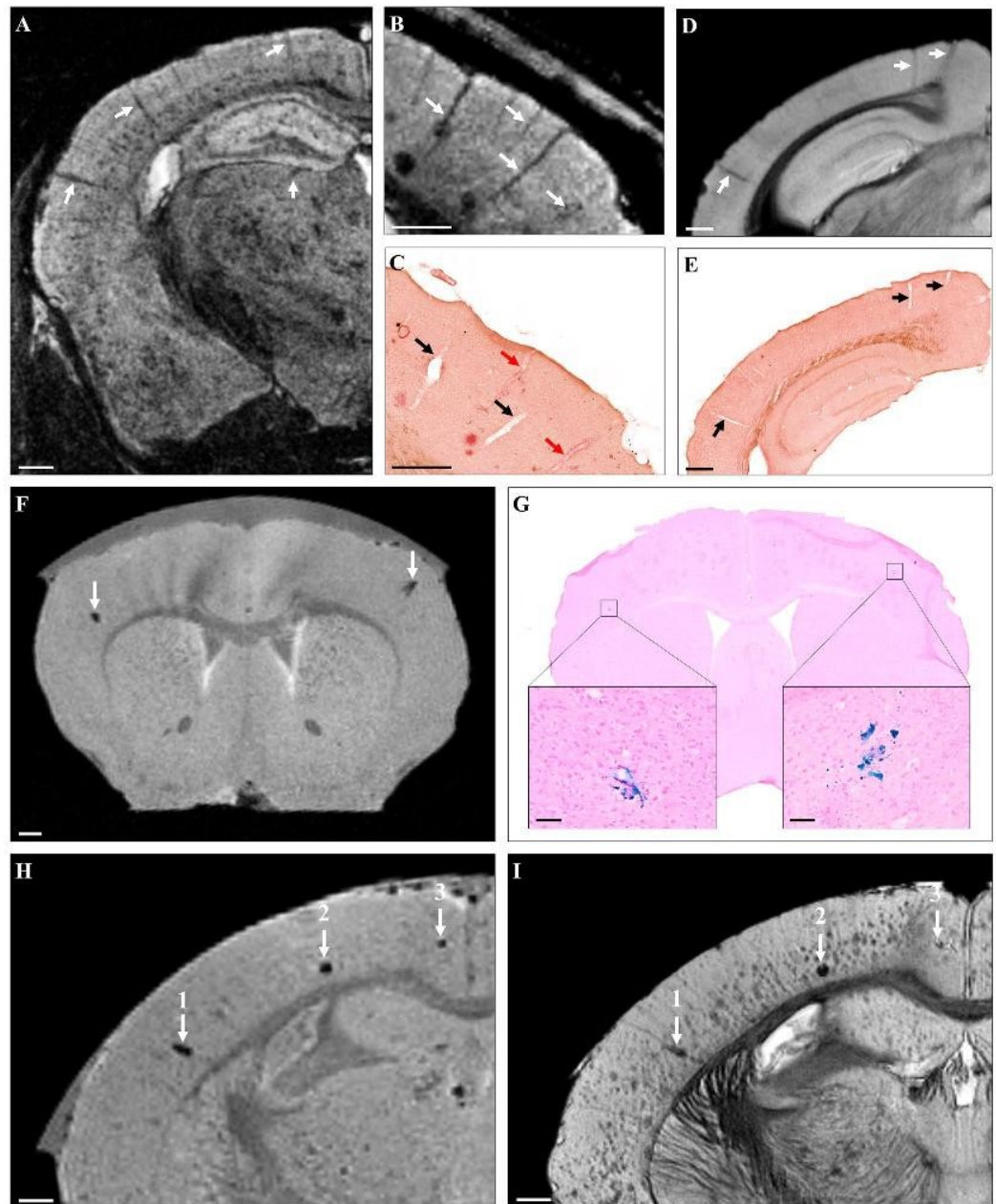
Figure 7. Visualization of CAA and cerebral microhemorrhages by Gd-stained MRI. Linear hypointense elements corresponding to blood vessels were detected on MR images of mouse models of amyloidosis (**A–C**, arrows). Registration between MR images (**B**) and histological sections (**C**) showed that some blood vessels seen on MRI were matched with CAA-positive vessels (red arrows) while some others were matched with CAA-negative vessels (black arrows). MR images of C57Bl/6 amyloid-free mice showed similar hypointensities (**D**, arrows) that were matched with blood vessels (**E**, arrows) confirming that CAA was not responsible of the hypointense nature of blood vessels by Gd-stained MRI. Sparse focal signal attenuations were observed on MR images before Gd-staining (**F**). They could be registered with microhemorrhages on Perls' stained histological sections (**G**, boxes). Microhemorrhages easily seen on MRI before Gd-staining (**H**, arrows) could be matched with some hypointense spots on Gd-stained MRI (**I**, arrows). Large microhemorrhages (1, 2) were easily distinguished from amyloid plaques on MR images but small microbleeds (3) and amyloid plaques were similar in appearance. Scale bars: 500 μm (**A–F,H,I**) and 100 μm (**G**).

some plaques devoid of iron were detected. In *ex vivo* experiments without contrast agents, previous studies reported that in some transgenic mice (*i.e.* APP$_{S(i.e. Tg2576)}$/PS1$_{A246E}$ mice and APP$_{S(i.e. Tg2576)}$/PS1$_{M146L}$), plaques that do not contain iron can be detected[18, 42]. However, in most *in vivo* studies without contrast agent, iron is considered as critical for plaque detection[14, 15, 39]. Since iron accumulation in plaques is age-dependent and variable
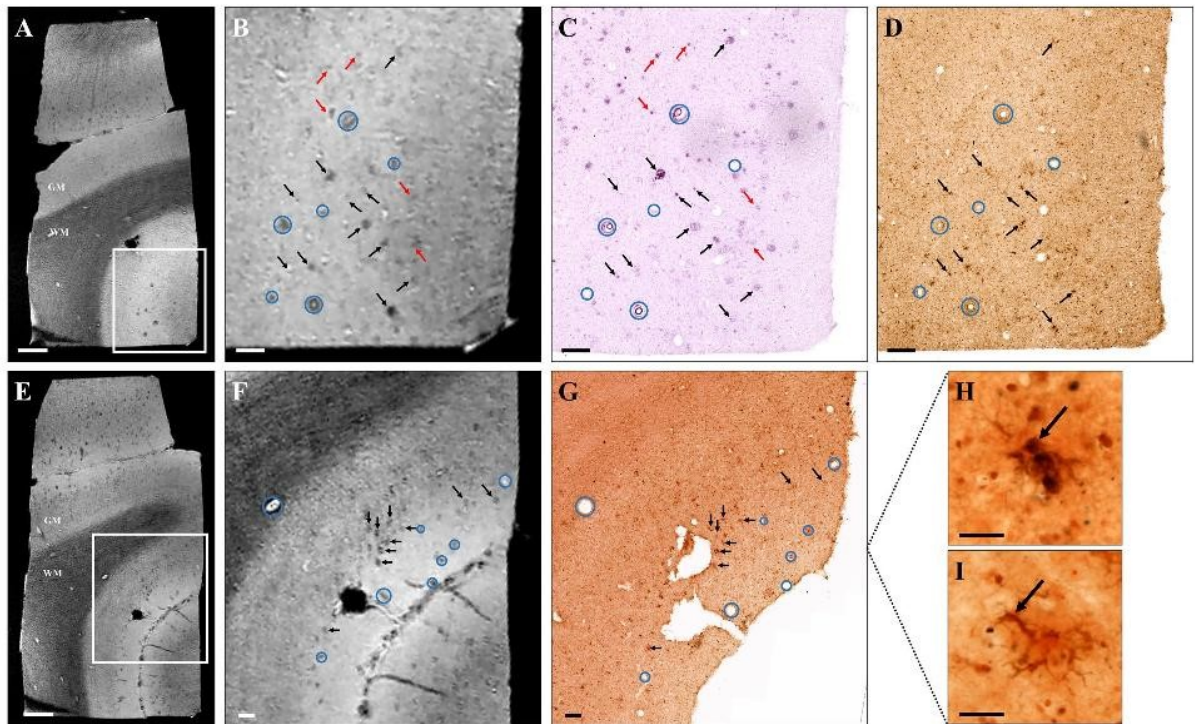
213

Figure 8. Amyloid plaque detection by Gd-stained MRI in human Alzheimer's disease brains. Gd-stained *post mortem* MR images (**A,B,E,F**) were registered with histological sections stained for β-amyloid (BAM10, **C**), iron (Perls-DAB, **D**) or double-stained for β-amyloid and iron (Congo red/Perls-DAB, **G**). Grey and white matter (GM and WM respectively) could easily be identified in Gd-stained MRI (**A,B,E,F**). Numerous hypointense spots were visible in the grey matter of AD patients (**A,B,E,F**). Slices were registered according to orientation and landmarks such as blood vessels (blue circles). Most of the hypointense spots (black and red arrows) seen on MR images (**A,B,E,F**) can be registered with β-amyloid lesions (black and red arrows) on BAM10 (**C**) and Congo-red/Perls-DAB (**G**) stained histological sections. Iron staining (Perls-DAB) revealed iron deposits that co-localize with amyloid plaques (**D,G**, black arrows) in most of the human plaques. Some other plaques were iron-free (**C,D**, red arrows) and were also detected by MRI indicating that iron is not necessary for detection. Perls-DAB-stained sections demonstrate two types of iron accumulation near amyloid plaques (**H,I**): punctate (**H**) or intracellular deposits (**I**). Scale bars: 1000 μm (**A,E**), 200 μm (**B–D,F,G**) and 50 μm (**H,I**).

according to brain region, one of the advantages of Gd-stained MRI is to allow plaque detection without depending on iron accumulation which is a covariate related to aging and not to plaque load.

We then examined the capacity of Gd-stained MRI to detect microhemorrhages and CAA. Microhemorrhages are often associated with aging and amyloid pathology in mice and in humans[32]. These lesions are hypointense on MR images[33–35], and could thus be misinterpreted as amyloid plaques on Gd-stained MR images. We showed that large microbleeds are distinguishable from amyloid plaques based on their superior size. Small microbleeds are the only lesions that could be confounded with amyloid plaques. Their number is however low compared to that of plaques, and exclusion of these lesions is always possible by recording T2* or susceptibility-weighted MR images before Gd-staining. Regarding CAA, we observed that blood vessels appeared as hypointense structures by *in vivo* MRI owing to the paramagnetic properties of blood, independently of the presence of CAA. On *post mortem* MR images, the hypointense nature of blood vessels could reflect the presence of Aβ peptide in the vessel wall but also a small amount of blood trapped in the vessels. Gd-stained MRI is thus not appropriate to detect amyloid angiopathy.

In this article, we also showed for the first time that Gd-stained MRI is able to detect amyloid plaques in human-AD brain tissues. Several significant technical barriers must be solved for this method to become suitable for use in living human subjects, including the ability to administer the contrast agent in the brain as well as resolution and imaging time considerations. The aim of this article is not to propose immediate solutions for these issues and we acknowledge that today the application of Gd-stained MRI as a routine method can be envisioned only in animal models. Gd-stained MRI can be repeated over the lifetime of animals and individual plaques can be followed-up longitudinally[26]. This method can thus be used to study amyloid biology or anti-amyloid therapies[29]. Here, we showed that among the models used in our study, APP$_{SL}$/PS1$_{M146L}$, APP/PS1$_{dE9}$ and APP23 are the models of choice to apply Gd-stained MRI and amyloid plaque detection in these models provides similar results to those obtained with human brain samples.

In conclusion, this study clearly highlights differences among amyloid plaques found in different mouse models of amyloidosis, and provides a better understanding of the origin of contrast induced by amyloid plaques in Gd-stained MRI. We also showed that Gd-stained MRI can be used to detect amyloid lesions in models with large

214

compact amyloid plaques such as $APP_{SL}/PS1_{M146L}$, $APP/PS1_{dE9}$ or APP23 mice independently of their iron load, and suggest that detection of amyloid plaques by Gd-stained MRI in $APP_{SL}/PS1_{M146L}$ and $APP/PS1_{dE9}$ is the most similar to that in human-AD brains.

Material and Methods

Animals. We selected male mice from five transgenic strains presenting with compact amyloid plaques ($APP_{SL}/PS1_{M146L}$ (n = 6), $APP/PS1_{dE9}$ (n = 6) and APP23 (n = 4)), diffuse amyloid plaques (APP_{SwDI} (n = 6)) and intracellular amyloid deposits (3xTg (n = 7)). C57Bl/6 amyloid-free mice (n = 2) were used as controls. *In vivo* and *ex vivo* Gd-stained MR images from brains of these animals were recorded to detect amyloid plaques. Two $APP_{SL}/PS1_{M146L}$ were also imaged *in vivo* and *ex vivo* before Gd-staining. Ages of the animals were selected to image the youngest animals with already well-established lesions (based on preliminary histological studies and on published pathophysiological characteristics of each strain) and the oldest animals available in our colony (approximately 100-week-old animals). A cohort of 75 week-old $APP_{SL}/PS1M_{146L}$ mice (n = 5) was further evaluated to study microhemorrhage detection. Their brains were studied before and after Gd-staining. An overview of the selected strains is presented below.

$APP_{SL}/PS1_{M146L}$ mice co-express human APP with Swedish double mutation (KM670/671NL) and London mutation (V717I) and human presenilin 1 (PS1) with M146L mutation under the control of a neuron-specific Thy1 promoter. This leads to a 3-fold higher expression of the human APP transgene than endogenous murine APP. These mice develop dense-cored amyloid plaques that reach a significant level in the neocortex and in the hippocampus at ~26 weeks[44]. These plaques have already been widely evaluated with Gd-stained MRI[26, 27, 29] and they can be detected in ~26-week-old animals[26]. These mice were imaged from 24 to 78 weeks (n = 6 and 5 for amyloid plaque and microhemorrhage detection, respectively).

$APP/PS1_{dE9}$ mice co-express human APP with the Swedish double mutation (KM670/671NL) and human PS1 deleted in exon 9 under the control of the mouse prion protein promoter. Significant amyloid plaque burden is seen in the hippocampus and cortex by 36 weeks[45] and increases with age[46]. These mice develop amyloid plaques with a dense core, surrounded by dystrophic neurites[45]. These mice were imaged from 35 to 126 weeks (n = 6).

APP23 mice express human APP with the Swedish double mutation (KM670/671NL) driven by the mouse Thy1.2 promoter allowing a neuron-specific expression of the transgene. This leads to a 7-fold higher expression of the human mutated APP than the endogenous murine APP[47]. APP23 mice develop a significant amyloidosis between 24 and 56 weeks[47, 48]. Then, dense-cored amyloid plaques increase in size and number with age, mainly in the neocortex and the hippocampus[47]. These mice were imaged from 39 to 77 weeks (n = 4).

APP_{SwDI} mice express human APP containing three mutations: Swedish (KM670/671NL), Dutch (E693Q) and Iowa (D694N), under the control of the mouse Thy1 promoter. These mice display mainly diffuse amyloid plaques and a significant number of plaques is reached at 52 weeks[49]. These mice were imaged from 52 to 114 weeks (n = 6).

3xTg mice express three mutated transgenes ($APP_{KM670/671NL}$, $MAPT_{P301L}$, and $PSEN1_{M146V}$) to comparable levels in the same brain regions. Consequently, they display both amyloid and neurofibrillary tangle pathologies. Amyloidosis starts at 12 weeks in the neocortex and at 24 weeks in the hippocampus, before neurofibrillary tangle formation. At this age, amyloid is mainly intraneuronal. Extracellular amyloid deposits become readily evident at 52 weeks[50]. These mice were imaged from 44 to 112 weeks (n = 7).

C57Bl/6 are amyloid-free mice used as controls. These mice were imaged at 48 and 79 weeks (n = 2).

All animal experiments were conducted in accordance with the European Communities Council Directive (2010/63/UE). Animal care was in accordance with institutional guidelines and experimental procedures were approved by local ethics committees (authorization 12-062; ethics committee CETEA-CEA DSV IdF).

Human-AD brain samples. Human *post mortem* brain samples from the cerebral cortex and adjacent white matter of three AD patients were obtained from the Gie-Neuro-CEB brain bank. This brain bank is run by a consortium of patients associations including France Alzheimer, with the support of Fondation Plan Alzheimer and IHU A-ICM. All methods using human brains were carried out in accordance with French guidelines and regulations. The informed consent forms were signed by either the patients themselves or their next of kin in their name, in accordance with French bioethical laws. The Brain Bank GIE NeuroCEB has been declared at the Ministry of Higher Education and Research and has received approval to distribute samples (agreement AC-2013-1887).

Surgical procedure. Animals were anesthetized with a mixture of isoflurane (1–2%) and air (1 L/min). After their heads were shaved, the mice were placed on a stereotaxic frame using ear bars and a tooth bar to secure them. A heating pad maintained physiological temperature throughout the procedure. After a midline incision of the skin, the coordinates of the bregma were recorded for anterior-posterior (A/P) and lateral (L) references. The skull was bilaterally perforated with a Dremel at coordinates A/P −0.2 mm and L ± 1 mm, according to a stereotaxic atlas[51]. Blunt Hamilton syringes were used to inject gadoterate meglumine (DOTAREM®, Guerbet, Aulnay-sous-Bois, France) into the lateral ventricles at coordinate −1.75 mm relative to the surface of the dura mater. A total volume of 1 μL (0.5 mmol/mL) was injected into each side at a rate of 0.1 μL/minute. Upon completion of the injections, needles were not moved for 10 minutes to allow the diffusion of the contrast agent. Then, needles were slowly withdrawn to minimize any outflow from pressure release and the skin was then sutured back.

***In vivo* MRI experiments.** *In vivo* MRI was performed with a 7T spectrometer (Agilent, USA) interfaced with a console running VnmrJ 3.2. The spectrometer was equipped with a rodent gradient insert of 700 mT/m. A birdcage coil (RapidBiomed, GmbH, Germany) and a mouse brain surface coil (RapidBiomed, GmbH, Germany) were used for emission and reception, respectively. A high-resolution 3D-Gradient Echo sequence was

used to achieve a resolution of $29 \times 29 \times 117$ μm^3 (matrix $= 512 \times 512 \times 128$, repetition time (TR) $= 50$ ms, echo time (TE) $= 13$ ms, flip angle $= 20°$, number of averages (Nex) $= 2$, bandwidth $= 25$ kHz, acquisition time $= 1$ h 49 min)[26]. All the MR images were recorded starting at 60 minutes after administration of the Gd contrast agent. During MRI experiments, animals were anesthetized with a mixture of isoflurane (0.75–1.5%) and carbogen (95% O_2–5% CO_2). Their breathing rate and their body temperature was monitored. Carbogen was used to reduce the signal coming from circulating blood[52].

All animals were sacrificed after *in vivo* MRI experiments using a high dose of sodium pentobarbital (100 mg/kg) and then fixed with a transcardiac perfusion of 4% paraformaldehyde (PFA). The brains were then removed, immersed in 4% PFA overnight at 4 °C, and preserved in PBS 0.1 M at 4 °C until *ex vivo* MRI experiments.

Ex vivo MRI experiments.

Brains were incubated in a Gd solution (DOTAREM® diluted to 2.5 mM in PBS) for 48 hours before MR experiments. Then, they were placed in a tight plastic tube filled with an aprotonic perfluorocarbon-based fluid (Fluorinert®, 3 M™) that provides a black background. A high-resolution 3D-Gradient Echo sequence was used to achieve a resolution of $25 \times 25 \times 100$ μm^3 (matrix $= 512 \times 512 \times 128$, TR $= 40$ ms, TE $= 15$ ms, flip angle $= 20°$, Nex $= 2$, bandwidth $= 25$ kHz, acquisition time $= 11$ h 39 min).

To detect microhemorrhages, *ex vivo* MR images were recorded to achieve a resolution of $50.8 \times 50.8 \times 50.8$ μm^3 (matrix $= 256 \times 256 \times 512$, TR $= 40$ ms, TE $= 15$ ms, flip angle $= 20°$, Nex $= 8$, acquisition time $= 11$ h 39 min).

Histology.

Brains were cryoprotected in 30% PBS-sucrose solution for 72 hours, cut into 40 µm thick coronal sections on a freezing microtome and mounted on slides (Ultrafrost, Thermo-Fisher®). Sections were stained for β-amyloid deposits (BAM10 immunohistochemistry and Congo red staining) and for iron deposits (Perls-DAB staining).

For BAM10 immunohistochemistry, sections were first rinsed in PBS 0.1 M and then in 30% hydrogen peroxide (H_2O_2). Then, they were pretreated with 0.2% octylphenol ethylene oxide condensate (Triton X-100™, Sigma-Aldrich®). After this pretreatment, they were incubated with an anti-amyloid primary antibody (monoclonal BAM10, dilution 1:1000, Sigma®) for 48 hours and then with a secondary antibody (biotinylated IgG anti-mouse, BA-9200, dilution 1:1000, Vector® Laboratories, Burlingame, USA) for 1 hour. Before revelation (VIP substrate kit for peroxidase, Vector® Labs), the reaction was amplified for 1 hour with a biotin-avidin complex (ABC Vectastain kit, Vector® Labs)[53]. For Congo red staining, sections were pretreated with 1% NaOH in 80% EthOH saturated with NaCl for 30 min. Then, they were again immersed in the same solution saturated with Congo red for 30 min. For Perls' staining, endogenous peroxidases were first inactivated by immersion in a methanol/H_2O_2 solution. Then, sections were stained with 2% potassium ferrocyanide (P9387, Sigma-Aldrich®) and 2% hydrogen chloride for 20 min. Iron staining was finally intensified using DAB (1 g/l), Tris (0.2 M) and 30% H_2O_2 for 20 min[54].

Microhemorrhage detection was evaluated on 20 µm thick-sections. The sections were stained by incubation, for 30 minutes at 40 °C, in a freshly prepared Perl's reagent: potassium ferrocyanide (10%) in hydrochloric acid (20%). After 3 washings in distilled water, they were counterstained for 5 minutes in a filtered nuclear fast red solution (Vector, H-3403, Burlingame, USA).

Correlation between in vivo MRI, ex vivo MRI and histology.

MR images were manually registered to histological sections using the "3D/Volume viewer" plugin from ImageJ[55]. This plugin enables manual rotation of the 3D MR volume in any direction. We identified typical landmarks such as layers of the hippocampus, blood vessels or amyloid plaques on histological sections. The 3D MR images were then manually rotated until we could identify these landmarks in the MR images. The minimum plaque size resolvable by *in vivo* or *ex vivo* MRI was established by measuring plaque diameters on the registered BAM10 stained sections employing ZEN lite 2012 analysis software (Zeiss, Oberkochen, Germany). Freehand boundaries were drawn around the plaques and their diameter estimated from the average length of the major and minor axes from the resulting ellipsoid[18].

The properties of the plaques detected by MRI were determined after registration between MRI and histological sections double-stained for Aβ and iron in APP$_{SL}$/PS1$_{M146L}$, APP/PS1$_{dE9}$, and APP23 mice. Only cortical amyloid plaques with a diameter ≥ 36 µm (which corresponds to the minimum plaque size resolvable *in vivo*) were considered. A total number of 369 amyloid plaques detected on histological sections were classified into four categories. 1. Iron-positive plaques detected by MRI, 2. Iron-negative plaques detected by MRI, 3. Iron-positive plaques not detected by MRI, 4. Iron-negative plaques not detected by MRI.

Amyloid load quantification from MR and histological sections.

Amyloid load was quantified from *in vivo* MR images and histological sections of APP$_{SL}$/PS1$_{M146L}$ (n $= 5$), APP/PS1$_{dE9}$ (n $= 5$), and APP23 (n $= 4$) mice. For MR images, cortical amyloid load was calculated by using a method similar to that reported by Jack et al.[39]. A total of 32 regions of interest (ROIs) per animal were analyzed for *in vivo* and *ex vivo* samples: 8 slices equally spaced along the rostro-caudal axis with 4 circular ROIs (diameter ~900 µm) drawn in the cortex on each of these slices (2 in each hemisphere). Hypointense spots were manually counted in each ROI, excluding hypointense elements that could be tracked over more than 2 adjacent slices, or that had a tube-like shape, suggesting that they were blood vessels. The area of each hypointense spot was measured in each ROI. Plaque load was determined as the ratio of the total area of hypointense spots over the area of the ROI.

For histological sections, amyloid and iron load were quantified by the same method used for quantification of amyloid load on MR images after digitization of amyloid and iron-stained sections with a Zeiss Axio Scan.Z1 (Oberkochen, Germany) whole slide imaging microscope at a lateral resolution of 0.5 µm.

References

1. Jack, C. R. *et al.* Tracking pathophysiological processes in Alzheimer's disease: an updated hypothetical model of dynamic biomarkers. *Lancet Neurol.* **12**, 207–216 (2013).
2. Morris, E. *et al.* Diagnostic accuracy of (18)F amyloid PET tracers for the diagnosis of Alzheimer's disease: a systematic review and meta-analysis. *Eur. J. Nucl. Med. Mol. Imaging* **43**, 374–385 (2016).
3. Maeda, J. *et al.* Longitudinal, quantitative assessment of amyloid, neuroinflammation, and anti-amyloid treatment in a living mouse model of Alzheimer's disease enabled by positron emission tomography. *J. Neurosci. Off. J. Soc. Neurosci.* **27**, 10957–10968 (2007).
4. Klunk, W. E. *et al.* Binding of the positron emission tomography tracer Pittsburgh compound-B reflects the amount of amyloid-beta in Alzheimer's disease brain but not in transgenic mouse brain. *J. Neurosci. Off. J. Soc. Neurosci.* **25**, 10598–10606 (2005).
5. Snellman, A. *et al.* Longitudinal amyloid imaging in mouse brain with 11C-PIB: comparison of APP23, Tg2576, and APPswe-PS1dE9 mouse models of Alzheimer disease. *J. Nucl. Med. Off. Publ. Soc. Nucl. Med.* **54**, 1434–1441 (2013).
6. Rojas, S. *et al. In vivo* evaluation of amyloid deposition and brain glucose metabolism of 5XFAD mice using positron emission tomography. *Neurobiol. Aging* **34**, 1790–1798 (2013).
7. Kuntner, C. *et al.* Limitations of small animal PET imaging with [18F]FDDNP and FDG for quantitative studies in a transgenic mouse model of Alzheimer's disease. *Mol. Imaging Biol. MIB Off. Publ. Acad. Mol. Imaging* **11**, 236–240 (2009).
8. Poisnel, G. *et al.* PET imaging with [18F]AV-45 in an APP/PS1-21 murine model of amyloid plaque deposition. *Neurobiol. Aging* **33**, 2561–2571 (2012).
9. Hintersteiner, M. *et al. In vivo* detection of amyloid-beta deposits by near-infrared imaging using an oxazine-derivative probe. *Nat. Biotechnol.* **23**, 577–583 (2005).
10. Dong, J., Revilla-Sanchez, R., Moss, S. & Haydon, P. G. Multiphoton *in vivo* imaging of amyloid in animal models of Alzheimer's disease. *Neuropharmacology* **59**, 268–275 (2010).
11. Delatour, B., Epelbaum, S., Petiet, A. & Dhenain, M. *In vivo* imaging biomarkers in mouse models of Alzheimer's disease: are we lost in translation or breaking through? *Int. J. Alzheimers Dis.* **2010** (2010).
12. Jack, C. R. *et al. In vivo* visualization of Alzheimer's amyloid plaques by magnetic resonance imaging in transgenic mice without a contrast agent. *Magn. Reson. Med.* **52**, 1263–1271 (2004).
13. Borthakur, A. *et al. In vivo* measurement of plaque burden in a mouse model of Alzheimer's disease. *J. Magn. Reson. Imaging JMRI* **24**, 1011–1017 (2006).
14. Chamberlain, R. *et al.* Comparison of amyloid plaque contrast generated by T2-weighted, T2*-weighted, and susceptibility-weighted imaging methods in transgenic mouse models of Alzheimer's disease. *Magn. Reson. Med.* **61**, 1158–1164 (2009).
15. Dhenain, M. *et al.* Characterization of *in vivo* MRI detectable thalamic amyloid plaques from APP/PS1 mice. *Neurobiol. Aging* **30**, 41–53 (2009).
16. Benveniste, H., Einstein, G., Kim, K. R., Hulette, C. & Johnson, G. A. Detection of neuritic plaques in Alzheimer's disease by magnetic resonance microscopy. *Proc. Natl. Acad. Sci. USA* **96**, 14079–14084 (1999).
17. Nakada, T., Matsuzawa, H., Igarashi, H., Fujii, Y. & Kwee, I. L. *In vivo* visualization of senile-plaque-like pathology in Alzheimer's disease patients by MR microscopy on a 7T system. *J. Neuroimaging Off. J. Am. Soc. Neuroimaging* **18**, 125–129 (2008).
18. Meadowcroft, M. D., Connor, J. R., Smith, M. B. & Yang, Q. X. MRI and histological analysis of beta-amyloid plaques in both human Alzheimer's disease and APP/PS1 transgenic mice. *J. Magn. Reson. Imaging JMRI* **29**, 997–1007 (2009).
19. Falangola, M. F., Lee, S.-P., Nixon, R. A., Duff, K. & Helpern, J. A. Histological co-localization of iron in Abeta plaques of PS/APP transgenic mice. *Neurochem. Res.* **30**, 201–205 (2005).
20. Dhenain, M., Privat, N., Duyckaerts, C. & Jacobs, R. E. Senile plaques do not induce susceptibility effects in T2*-weighted MR microscopic images. *NMR Biomed.* **15**, 197–203 (2002).
21. Zeineh, M. M. *et al.* Activated iron-containing microglia in the human hippocampus identified by magnetic resonance imaging in Alzheimer disease. *Neurobiol. Aging* **36**, 2483–2500 (2015).
22. Poduslo, J. F. *et al.* Molecular targeting of Alzheimer's amyloid plaques for contrast-enhanced magnetic resonance imaging. *Neurobiol. Dis.* **11**, 315–329 (2002).
23. Higuchi, M. *et al.* 19F and 1H MRI detection of amyloid beta plaques *in vivo*. *Nat. Neurosci.* **8**, 527–533 (2005).
24. Sigurdsson, E. M. *et al.* A non-toxic ligand for voxel-based MRI analysis of plaques in AD transgenic mice. *Neurobiol. Aging* **29**, 836–847 (2008).
25. Wadghiri, Y. Z. *et al.* Detection of amyloid plaques targeted by bifunctional USPIO in Alzheimer's disease transgenic mice using magnetic resonance microimaging. *PloS One* **8**, e57097 (2013).
26. Petiet, A. *et al.* Gadolinium-staining reveals amyloid plaques in the brain of Alzheimer's transgenic mice. *Neurobiol. Aging* **33**, 1533–1544 (2012).
27. Santin, M. D., Debeir, T., Bridal, S. L., Rooney, T. & Dhenain, M. Fast *in vivo* imaging of amyloid plaques using μ-MRI Gd-staining combined with ultrasound-induced blood-brain barrier opening. *NeuroImage* **79**, 288–294 (2013).
28. Dhenain, M., Delatour, B., Walczak, C. & Volk, A. Passive staining: a novel *ex vivo* MRI protocol to detect amyloid deposits in mouse models of Alzheimer's disease. *Magn. Reson. Med.* **55**, 687–693 (2006).
29. Santin, M. D. *et al. In vivo* detection of amyloid plaques by Gadolinium-stained MRI can be used to demonstrate the efficacy of an anti-amyloid immunotherapy. *Front. Aging Neurosci.* **8**, 55 (2016).
30. Bertrand, A. *et al.* Micro-MRI study of cerebral aging: *ex vivo* detection of hippocampal subfield reorganization, microhemorrhages and amyloid plaques in mouse lemur primates. *PloS One* **8**, e56593 (2013).
31. Hyare, H., So, P.-W., Brandner, S., Collinge, J. & Parkes, H. G. MRI detection of prion protein plaques in variant Creutzfeldt-Jakob disease. *Neurology* **84**, 1498–1499 (2015).
32. Love, S. & Miners, J. S. Cerebrovascular disease in ageing and Alzheimer's disease. *Acta Neuropathol. (Berl.)* **131**, 645–658 (2016).
33. Barakos, J. *et al.* MR Imaging Features of Amyloid-Related Imaging Abnormalities. *Am. J. Neuroradiol* **34**, 1958–1965 (2013).
34. Beckmann, N., Gerard, C., Abramowski, D., Cannet, C. & Staufenbiel, M. Noninvasive magnetic resonance imaging detection of cerebral amyloid angiopathy-related microvascular alterations using superparamagnetic iron oxide particles in APP transgenic mouse models of Alzheimer's disease: application to passive Abeta immunotherapy. *J. Neurosci.* **31**, 1023–1031 (2011).
35. Luo, F. *et al.* Magnetic resonance imaging detection and time course of cerebral microhemorrhages during passive immunotherapy in living amyloid precursor protein transgenic mice. *J. Pharmacol. Exp. Ther.* **335**, 580–588 (2010).
36. Gyure, K. A., Durham, R., Stewart, W. F., Smialek, J. E. & Troncoso, J. C. Intraneuronal abeta-amyloid precedes development of amyloid plaques in Down syndrome. *Arch. Pathol. Lab. Med.* **125**, 489–492 (2001).
37. Gouras, G. K. *et al.* Intraneuronal Abeta42 accumulation in human brain. *Am. J. Pathol.* **156**, 15–20 (2000).
38. LaFerla, F. M., Green, K. N. & Oddo, S. Intracellular amyloid-beta in Alzheimer's disease. *Nat. Rev. Neurosci.* **8**, 499–509 (2007).
39. Jack, C. R. *et al. In vivo* magnetic resonance microimaging of individual amyloid plaques in Alzheimer's transgenic mice. *J. Neurosci. Off. J. Soc. Neurosci.* **25**, 10041–10048 (2005).
40. Nabuurs, R. J. A. *et al.* High-field MRI of single histological slices using an inductively coupled, self-resonant microcoil: application to *ex vivo* samples of patients with Alzheimer's disease. *NMR Biomed.* **24**, 351–357 (2011).
41. Schrag, M., Mueller, C., Oyoyo, U., Smith, M. A. & Kirsch, W. M. Iron, zinc and copper in the Alzheimer's disease brain: a quantitative meta-analysis. Some insight on the influence of citation bias on scientific opinion. *Prog. Neurobiol.* **94**, 296–306 (2011).
42. Wengenack, T. M. *et al.* Regional differences in MRI detection of amyloid plaques in AD transgenic mouse brain. *NeuroImage* **54**, 113–122 (2011).

43. Nabuurs, R. J. A. *et al.* MR microscopy of human amyloid-β deposits: characterization of parenchymal amyloid, diffuse plaques, and vascular amyloid. *J. Alzheimers Dis. JAD* **34**, 1037–1049 (2013).
44. Blanchard, V. *et al.* Time sequence of maturation of dystrophic neurites associated with Abeta deposits in APP/PS1 transgenic mice. *Exp. Neurol.* **184**, 247–263 (2003).
45. Jankowsky, J. L. *et al.* Mutant presenilins specifically elevate the levels of the 42 residue beta-amyloid peptide *in vivo*: evidence for augmentation of a 42-specific gamma secretase. *Hum. Mol. Genet* **13**, 159–170 (2004).
46. Garcia-Alloza, M. *et al.* Characterization of amyloid deposition in the APPswe/PS1dE9 mouse model of Alzheimer disease. *Neurobiol. Dis.* **24**, 516–524 (2006).
47. Sturchler-Pierrat, C. *et al.* Two amyloid precursor protein transgenic mouse models with Alzheimer disease-like pathology. *Proc. Natl. Acad. Sci. USA* **94**, 13287–13292 (1997).
48. Calhoun, M. E. *et al.* Neuron loss in APP transgenic mice. *Nature* **395**, 755–756 (1998).
49. Davis, J. *et al.* Early-onset and robust cerebral microvascular accumulation of amyloid beta-protein in transgenic mice expressing low levels of a vasculotropic Dutch/Iowa mutant form of amyloid beta-protein precursor. *J. Biol. Chem.* **279**, 20296–20306 (2004).
50. Oddo, S. *et al.* Triple-transgenic model of Alzheimer's disease with plaques and tangles: intracellular Abeta and synaptic dysfunction. *Neuron* **39**, 409–421 (2003).
51. Paxinos, G. & Franklin, K. B. G. *The mouse brain in stereotaxic coordinates*. (Academic Press, 2001).
52. Thomas, C. D. *et al.* Morphological and carbogen-based functional MRI of a chemically induced liver tumor model in mice. *Magn. Reson. Med.* **50**, 522–530 (2003).
53. Berghorn, K. A., Bonnett, J. H. & Hoffman, G. E. cFos immunoreactivity is enhanced with biotin amplification. *J. Histochem. Cytochem. Off. J. Histochem. Soc* **42**, 1635–1642 (1994).
54. El Tannir El Tayara, N. *et al.* Age-related evolution of amyloid burden, iron load, and MR relaxation times in a transgenic mouse model of Alzheimer's disease. *Neurobiol. Dis.* **22**, 199–208 (2006).
55. Schneider, C. A., Rasband, W. S. & Eliceiri, K. W. NIH Image to ImageJ: 25 years of image analysis. *Nat. Methods* **9**, 671–675 (2012).

Acknowledgements

Author Contributions

C.D., M.V., M.D. designed the study. M.D. coordinated the study. C.D., M.V., K.H., S.A., C.G., V.B., F.P. performed the MRI and histological studies. C.D., M.V., and M.D. wrote the manuscript. C.D., M.V., E.C., and M.D. revised the manuscript.

Additional Information

Supplementary information accompanies this paper at doi:10.1038/s41598-017-05285-1

Competing Interests: The authors declare that they have no competing interests.

Publisher's note: Springer Nature remains neutral with regard to jurisdictional claims in published maps and institutional affiliations.

Common functional networks in the mouse brain revealed by multi-centre resting-state fMRI analysis

47 authors, including:

Joanes Grandjean
Agency for Science, Technology and Research (A*STAR)
28 PUBLICATIONS   341 CITATIONS

SEE PROFILE

Salma Bougacha
Atomic Energy and Alternative Energies Commission
6 PUBLICATIONS   33 CITATIONS

SEE PROFILE

Thomas Bienert
University Medical Center Freiburg
16 PUBLICATIONS   63 CITATIONS

SEE PROFILE

Natalia Gass
Central Institute of Mental Health
35 PUBLICATIONS   341 CITATIONS

SEE PROFILE

Some of the authors of this publication are also working on these related projects:

Expert neural mechanisms of rhythmic timing and their age-related changes   View project

Identifying structural and functional biomarkers of the brain indicating SensoriMotor Recovery in Cerebral Palsy   View project

219

Common functional networks in the mouse brain revealed by multi-centre resting-state fMRI analysis

Joanes Grandjean[a], Carola Canella[b,c], Cynthia Anckaerts[d], Gülebru Ayrancı[e], Salma Bougacha[f,g], Thomas Bienert[j], David Buehlmann[h], Ludovico Coletta[b,c], Daniel Gallino[e], Natalia Gass[i], Clément M. Garin[f,g], Nachiket Abhay Nadkarni[f,g], Neele Hübner[j], Meltem Karatas[k], Yuji Komaki[l,m], Silke Kreitz[n], Francesca Mandino[a,o], Anna E. Mechling[j], Chika Sato[p], Katja Sauer[n], Disha Shah[d,q], Sandra Strobelt[n], Norio Takata[l,r], Isabel Wank[n], Tong Wu[s,t], Noriaki Yahata[p], Ling Yun Yeow[a], Yohan Yee[u], Ichio Aoki[p], M. Mallar Chakravarty[e], Wei-Tang Chang[a], Marc Dhenain[f,g], Dominik von Elverfeldt[j], Laura-Adela Harsan[k], Andreas Hess[n], Tianzi Jiang[s,v], Georgios A. Keliris[d], Jason P. Lerch[u], Hideyuki Okano[m,w], Markus Rudin[h], Alexander Sartorius[i], Annemie Van der Linden[d], Marleen Verhoye[d], Wolfgang Weber-Fahr[i], Nicole Wenderoth[x], Valerio Zerbi[x], Alessandro Gozzi[b]

a Singapore Bioimaging Consortium, Agency for Science, Technology and Research, 11 Biopolis Way, Singapore 138667, Singapore
b Functional Neuroimaging Laboratory, Istituto Italiano di Tecnologia, Centre for Neuroscience and Cognitive Systems @ UNITN, 38068 Rovereto, Italy
c CIMeC, centre for Mind/Brain Sciences, University of Trento, 38068 Rovereto, Italy
d Bio-Imaging Lab, University of Antwerp, CDE, Universiteitsplein 1, 2610 Antwerp, Belgium
e Douglas Mental Health University Institute & Departments of Psychiatry and Biological and Biomedical Engineering, McGill University, Montreal, Quebec, Canada.
f Commissariat à l'Énergie Atomique et aux Énergies Alternatives (CEA), Direction de la Recherche Fondamentale (DRF), Institut François Jacob, MIRCen, Fontenay aux roses, France
g Centre National de la Recherche Scientifique (CNRS), Université Paris-Sud, Université Paris-Saclay UMR 9199, Neurodegenerative Diseases Laboratory, Fontenay-aux-Roses, France
h Institute for Biomedical Engineering, University and ETH Zürich, Wolfgang-Pauli-Str. 27, 8093 Zürich, Switzerland, & Institute of Pharmacology and Toxicology, University of Zürich, Winterthurerstrasse 190, 8057 Zürich, Switzerland
i Department of Neuroimaging, Central Institute of Mental Health, Medical Faculty Mannheim, University of Heidelberg, Mannheim, Germany
j Department of Radiology, Medical Physics, Medical Center – University of Freiburg, Faculty of Medicine, University of Freiburg, Killianstr. 5a, 79106 Freiburg, Germany; BrainLinks-BrainTools Cluster of Excellence, University of Freiburg, Georges-Köhler-Allee 80, 79110 Freiburg, Germany
k Department of Biophysics and Nuclear Medicine, University Hospital Strasbourg, 67000 Strasbourg, France
l Central Institute for Experimental Animals (CIEA), 3-25-12, Tonomachi, Kawasaki, Kanagawa 210-0821, Japan
m Department of Physiology, Keio University School of Medicine, 35 Shinanomachi, Shinjuku, Tokyo 160-8582, Japan
n Institute of Experimental and Clinical Pharmacology and Toxicology, Friedrich-Alexander University Erlangen-Nürnberg (FAU), Fahrstraße 17, 91054, Erlangen, Germany
o Faculty of Life Sciences, University of Manchester, Manchester, United Kingdom
p Functional and Molecular Imaging Team, Department of Molecular Imaging and Theranostics, National Institute of Radiological Sciences, National Institutes for Quantum and Radiological Science and Technology, Anagawa 4-9-1, Inage, Chiba-city, Chiba 263-8555, Japan
q Laboratory for the Research of Neurodegenerative Diseases, VIB center for Brain and Disease Research, KU Leuven, O&N4 Herestraat 49 box 602, 3000 Leuven, Belgium
r Department of Neuropsychiatry, Keio University School of Medicine, 35 Shinanomachi, Shinjuku, Tokyo 160-8582, Japan
s Queensland Brain Institute, The University of Queensland, Brisbane, Queensland, Australia
t Centre for Medical Image Computing, Department of Computer Science, & Max Planck University College London Centre for Computational Psychiatry and Ageing Research, University College London, London, UK
u Hospital for Sick Children and Department of Medical Biophysics, The University of Toronto, Toronto, Ontario, Canada
v Brainnetome Centre, Institute of Automation, Chinese Academy of Sciences, Beijing & Key Laboratory for NeuroInformation of the Ministry of Education, School of Life Science and Technology, University of Electronic Science and Technology of China, Chengdu 625014, China
w Laboratory for Marmoset Neural Architecture, RIKEN Brain Science Institute, Wako, Saitama 351-0198, Japan
x Neural Control of Movement Lab, Department of Health Sciences and Technology, ETH Zürich, Winterthurerstrasse 190, 8057 Zurich, Switzerland

Corresponding author
Joanes Grandjean, PhD
Singapore Bioimaging Consortium (SBIC)
11 Biopolis Way
#01-02 Helios Building
Singapore 138667
Tel: +65 91434319
Fax: +65 6478 9957
Joanes_Grandjean@sbic.a-star.edu.sg

Abstract

Preclinical applications of resting-state functional magnetic resonance imaging (rsfMRI) offer the possibility to non-invasively probe whole-brain network dynamics and to investigate the determinants of altered network signatures observed in human studies. Mouse rsfMRI has been increasingly adopted by numerous laboratories world-wide. Here we describe a multi-centre comparison of 17 mouse rsfMRI datasets via a common image processing and analysis pipeline. Despite prominent cross-laboratory differences in equipment and imaging procedures, we report the reproducible identification of several large-scale resting-state networks (RSN), including a murine default-mode network, in the majority of datasets. A combination of factors was associated with enhanced reproducibility in functional connectivity parameter estimation, including animal handling procedures and equipment performance. Our work describes a set of representative RSNs in the mouse brain and highlights key experimental parameters that can critically guide the design and analysis of future rodent rsfMRI investigations.

Introduction

The brain is the most complex organ, consisting of 86 billion neurons (Azevedo et al., 2009), each forming on average 7000 synapses. Approaching the complexity of the brain is rendered difficult due to the limited access to the tissue and the imperative for minimally invasive procedures in human subjects. Resting-state functional magnetic resonance imaging (rsfMRI) has gained attention within the human neuroimaging community due to the possibility to interrogate multiple resting-state networks (RSNs) in parallel with a relatively high spatial and temporal resolution (Biswal et al., 1995, 2010; Fox and Raichle, 2007). Functional connectivity (FC), i.e. the statistical dependence of two or more time series extracted from spatially defined regions in the brain (Friston, 2011), is the principal parameter estimated from rsfMRI studies. The importance of FC to neuroscience research can be understood through its widespread use to describe functional alterations in psychiatric and neurological disorders, e.g. for review (Buckner et al., 2008; Greicius, 2008). However, despite an extensive characterization of the functional endophenotype associated with diseased states, limitations with respect to invasiveness and terminal experiments generally preclude the establishment of detailed mechanisms in humans, as can be achieved with animal models.

Since its onset in 2011 (Jonckers et al., 2011), mouse rsfMRI has developed in a number of centres and has grown to become a routine method with a number of applications, reviewed in (Chuang and Nasrallah, 2017; Gozzi and Schwarz, 2016; Hoyer et al., 2014; Jonckers et al., 2015, 2013; Pan et al., 2015). Prominently, mouse rsfMRI has been used to investigate an extensive list of models, including Alzheimer's disease (Grandjean et al., 2014b, 2016b, Shah et al., 2013, 2016c; Wiesmann et al., 2016; Zerbi et al., 2014), motor (DeSimone et al., 2016; Li et al., 2017), affective (Grandjean et al., 2016a), autism spectrum (Bertero et al., 2018; Haberl et al., 2015; Liska et al., 2018; Liska and Gozzi, 2016; Michetti et al., 2017; Sforazzini et al., 2016; Zerbi et al., 2018; Zhan et al., 2014), schizophrenia (Errico et al., 2015; Gass et al., 2016), pain (Buehlmann et al., 2018; Komaki et al., 2016), reward (Charbogne et al., 2017; Mechling et al., 2016), and demyelinating disorders (Hübner et al., 2017). Another application of mouse rsfMRI is the elucidation of large-scale functional alterations exerted by pharmacological agents (Razoux et al., 2013; Shah et al., 2016a, 2015). Finally, the method has been used to address fundamental questions. These include the investigation of the structural basis underlying FC (Bergmann et al., 2016; Grandjean et al., 2017b; Hübner et al., 2017; Schroeter et al., 2017; Sforazzini et al., 2016; Stafford et al., 2014), the nature of the dynamical event encoded in the resting-state signal (Belloy et al., 2018a, 2018b; Bukhari et al., 2018; Grandjean et al., 2017a;

222

Sethi et al., 2017), as well as strain (Jonckers et al., 2011; Schroeter et al., 2017; Shah et al., 2016b), and the impact of sedation or awake conditions on the underlying signal and connectivity patterns (Bukhari et al., 2017; Grandjean et al., 2014a; Jonckers et al., 2014; Wu et al., 2017; Yoshida et al., 2016). This body of work obtained mainly over the past 5 years reflects the growth and interest into this modality as a translational tool to understand mechanisms underlying RSNs organisation in the healthy and diseased states, with the promise to highlight relevant targets in the drug development process and to advance fundamental knowledge in neuroscience.

Despite a growing interest in the field, rsfMRI studies in animals have been inherently difficult to compare. On top of centre-related contributions analogous to those observed in human studies (Jovicich et al., 2016), comparisons in rodents are further confounded by greater variability in preclinical equipment (e.g. field strength, hardware design), animal handling protocols and sedation regimens employed to control for motion and stress. Discrepancies between reports, such as the anatomical and spatial extent of a rodent homologue of the human default-mode network (DMN) (Becerra et al., 2011; Gozzi and Schwarz, 2016; Guilfoyle et al., 2013; Hübner et al., 2017; Liska et al., 2015; Lu et al., 2012; Sforazzini et al., 2014; Stafford et al., 2014; Upadhyay et al., 2011), or the organisation of murine RSNs (Jonckers et al., 2011), have stark consequences for the interpretations of the results. To meet a growing need to establish standards and points of comparison in rodent fMRI, we carried out a multi-centre comparison of mouse rsfMRI datasets. Multiple datasets representative of the local centre acquisitions were analysed with a common preprocessing pipeline and examined with seed-based analysis (SBA) and independent component analysis (ICA), two common brain mapping methods used to investigate RSNs. The aims of our work were to identify representative mouse RSNs, to establish a set of reference pre-processing and analytical steps and good-practices, and to highlight protocol requirements enabling more sensitive and specific FC detection in the mouse brain.

Results

Dataset description and preprocessing validation

A total of 17 datasets were included in this study. Dataset selection was restricted to 15 gradient-echo echo planar imaging acquired on C57Bl/6J mice, any gender, any age, any sedation protocol (**Supplementary table 1**). Cortical signal-to-noise ratio (SNR) ranged from 17.04 to 448.56, while temporal SNR (tSNR) ranged from 8.11 to 112.68 (**Supplementary figure 1ab**). A comparison between SNR and tSNR indicated a positive association between the two measures (pearson's r = 0.75, t = 18.30, df = 253, p = 2.2e-16). Due to the lack of orthogonality between the two factors, only SNR was considered in the remaining of the analysis. Mean framewise displacement (FWD) ranged 0.0025 mm to 0.15 mm (**Supplementary figure 1c**). A summary of representative estimated motion parameters is shown in the supplementary material (**Supplementary figure 2**). Each preprocessing output was visually inspected. Automatic brain extraction generated plausible brain masks. Normalisation was carried out to the Allen Institute for Brain Science (AIBS) template (**Supplementary figure 3**). Spatial coverage along the anterior-posterior axis varied across datasets. The following analysis is thus restricted to areas fully covered by all scans, corresponding to approximately 2.96 and -2.92 mm relative to Bregma. Moreover, distortions made it impossible to cover the amygdala region in full. No marked differences in the performance of each preprocessing steps were identified between datasets. The brain masked, spatially smoothed, temporally filtered, and normalized scans were further processed as follows.

Vascular and ventricle signal regression enhances functional connectivity specificity

Denoising procedures are an integral step in all FC analyses relying on rsfMRI acquisitions. Nuisance signal originates from multiple sources, including physiological and equipment related noise (Murphy et al., 2013). No consensus exists both in human and rodent fMRI fields regarding optimal noise removal procedures. In this study the following six nuisance regression models were designed and compared with the aim to select one model based on objective criteria for the remaining of the analysis. The first nuisance model includes only motion correction and parameter regression (MC). Global signal regression (GSR) was added to the motion parameter in a second model. Signal from either white-matter (WM), ventricle (VEN), or vascular (VASC) masks (**Supplementary figure 4bcd**) were combined with motion parameters in additional regression models. Finally, based on results obtained with these approaches, a combination (VV) model including VEN and VASC signal regression was included for the comparison. The effectiveness of nuisance regression models and the specificity of the resulting

224

networks at the subject level were assessed based on the outcome of a SBA using the anterior cingulate area (ACA, **Supplementary figure 4a**) as seed region. This seed was selected as a central node of the putative rodent DMN (Gozzi and Schwarz, 2016).
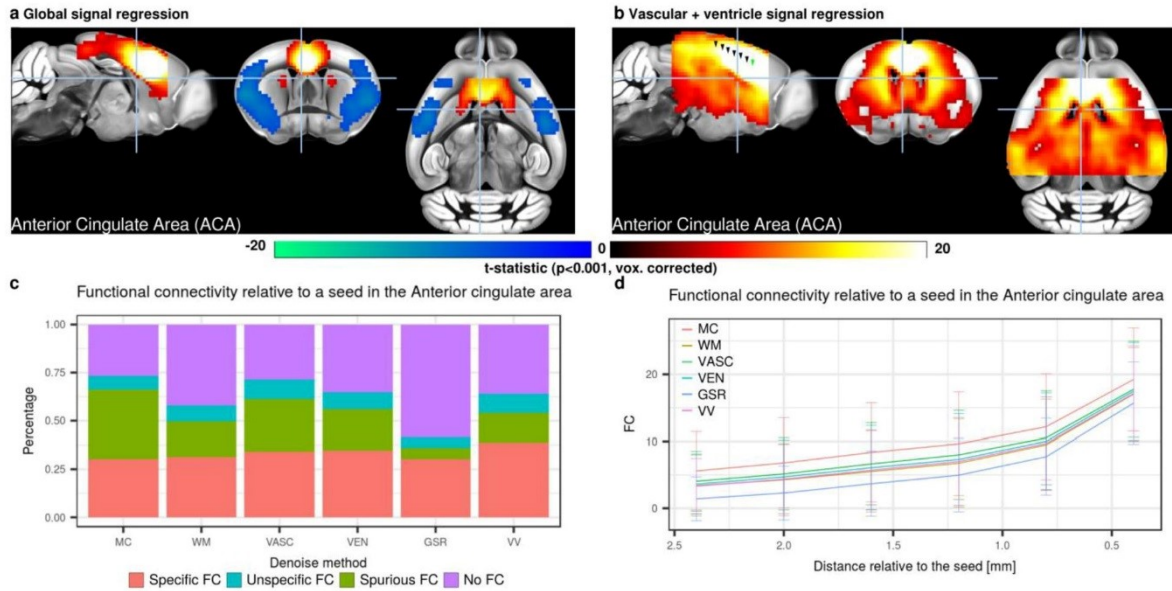

Figure 1 | *Denoising strategies and their impact on functional connectivity (FC) specificity.* ***a-b,*** *Seed-based analysis for a seed in the anterior cingulate area (ACA) following either global signal regression (GSR, **a**) or vascular+ventricle signal regression (VV, **b**). The spatial maps obtained lead to a set of regions for which the BOLD signals were positively associated to the BOLD signal of the ACA. These included the prefrontal cortex, retrosplenial area (RSP), dorsal striatum. Under VV, the connectivity profile extended to peri-hippocampal areas. Significant anti-correlation (negative t-statistic, blue) are also present in the primary somatosensory areas (SSp) under GSR but not VV condition. Individual scans were classified as presenting "Specific", "Unspecific", "Spurious", or "No" FC relative to the ACA seed (**c**, see **Supplementary figure 5** for details). Comparison of each FC category depending on the denoising strategies revealed that motion correction and GSR lead to lowest percentage of "specific FC" at 30%, while that percentage was highest under VV condition (38%). FC as a function of distance to the ACA seed indicates comparable rate of decline between denoising strategies (**d**). Green arrowhead indicates the position of the ACA seed, black arrowheads indicate ROIs spaced 0.4 mm apart. Voxelwise corrected t-statistic for one-sample t-tests (p<0.001, corrected) are shown as a colour-coded overlay on the AIBS reference template. Descriptive statistics are shown as mean ± 1 standard deviation.*

The statistical maps of the one-sample t-test across all individual maps following GSR (**Figure 1a**) indicated positive FC along rostro-caudal axis, through the ACA and extending to the retrosplenial area (RSP), with anti-correlations in adjacent primary somatosensory areas (SSp). Comparatively, in the VV nuisance model, a more extended network was revealed to include posterior parietal cortical areas (**Figure 1b**), while anti-correlations in the SSp did not reach statistical significance. To assess the specificity of the obtained functional networks, subject-level FC parameter (z-statistic) were extracted from ROIs located in the RSP and left SSp. The former was defined as a specific ROI, i.e. a ROI where positive FC is expected, while the latter was defined as a non-specific ROI, i.e. a ROI where low or negative FC is expected. The decision to consider these two areas as belonging to separable network systems reflects several lines of converging evidence: a) these regions are not linked by major white matter bundles or direct axonal projections in the mouse brain (Oh et al., 2014), b) they reflect separable electrophysiological signatures in mammals (Popa et al., 2009) c) they belong to separable functional communities (Liska et al., 2015) and are similarly characterized by the absence of significant positive correlation in corresponding human RSN (Fox et al., 2005).

Detailed FC within the specific ROI for the GSR and VV nuisance model are shown as a function of FC within the corresponding non-specific ROI at the single-subject level (**Supplementary figure 5**). In the VV condition, 98/255 (i.e. 38%) of individual scans fell into the "specific FC" category while both MC and GSR reach lowest percentage (30%) of scans exhibiting "specific FC" relative to the ACA seed (**Figure 1c**). Out of the 98/255 scans categorised as presenting "specific FC" relative to the ACA seed, up to 14/15 scans originated from the same dataset (median = 6/15). Two datasets did not contain scans that met the definition. Correspondingly, the 98 scans were also unevenly distributed according to the different acquisition parameters, including field strength (4.7T N = 1/15, 7T N = 41/120, 9.4T N = 38/90, 11.7T = 18/30, X^2 = 13.76, df = 3, p-value = 0.0032), coil type (room-temperature N = 26/105, cryoprobe N = 72/150, X^2 = 13.13, df = 1, p-value = 0.00029), breathing condition (free-breathing N = 58/180, ventilated N = 40/75, X^2 = 9.10, df = 1, p-value = 0.0026), and sedation condition (awake N = 7/15, isoflurane/halothane N = 18/90, medetomidine N = 26/75, medetomidine+isoflurane N = 47/75, X^2 = 32.42, df = 3, p-value = 4.28e-07). Hence, scans presenting "specific FC" patterns were more often found in datasets acquired at higher field strengths, with cryoprobes, in ventilated animals, and under medetomidine+isoflurane combination sedation.

To test how FC is affected as a function of distance to the seed and nuisance model, FC in the ACA and RSP along the anterior - posterior axis was extracted (**Figure 1d**). Comparable rate of decrease was observed in all conditions, with GSR displaying an overall decrease of FC throughout. This is consistent with the overall decrease in FC induced by GSR relative to VV in the specificity analysis (**Supplementary figure 5**). In summary, the VV nuisance model enhanced specificity of SBA-derived DMN, as indicated by higher incidence of scans in the "specific FC" category. Based on this criterion, this nuisance model was used in all the subsequent analyses.

Seed-based analysis identifies common and reproducible murine resting-state networks

We sought to identify common murine RSNs by means of SBA and to compare reproducibility across datasets. Seeds positioned in representative anatomical regions of the left hemisphere (**Supplementary figure 4a**) were used to reveal the spatial extent of previously described mouse resting-state networks. The seeds were selected to represent different cortical (somatosensory, motor, high order processing), as well as subcortical systems (striatum, hippocampal formation, thalamus). To obtain high-specificity and high-confidence group-level SBA maps, we first probed only the 98/255 scans listed as containing "specific FC" in the previous analysis. We next extended these analyses to include all the 255/255 scans (**Supplementary figure 7**). For datasets comparisons, all 15 scans from each dataset were included to reflect inter-dataset variability in the incidence maps.

All group-level SBA maps exhibited a strong bilateral and homotopic extension (**Figure 2a, Supplementary figure 6**). A seed in the ACA revealed a network involving the prefrontal cortex, RSP, dorsal striatum, dorsal thalamus and peri-hippocampal areas. This recapitulates anatomical features reminiscent of the human, primate and rat DMN (Gozzi and Schwarz, 2016; Hutchison and Everling, 2012; Sforazzini et al., 2014; Stafford et al., 2014). Comparable regions were observed with a seed in the RSP, a region evolutionarily related to the posterior cingulate cortex found in the human DMN (**Supplementary figure 6**). The anterior insular seed was found to co-activate with the dorsal cingulate and the amygdalar areas, corresponding to the putative rodent salience network (Gozzi and Schwarz, 2016), while the primary somatomotor region (MO) defined a previously described latero-cortical network that appears to be antagonistic to midline DMN regions, and that has been for this reason postulated to serve as a possible rodent homologous of the primate task-positive network (**Figure 2a**)(Liska et al., 2015;

Sforazzini et al., 2014). Corresponding network across all scans (255/255) recapitulated features identified in the 98/255 scans listed as containing "specific FC", but appeared to be characterized by much lower spatial specificity (**Supplementary figure 7**). Maps derived from individual datasets revealed that 70% (12/17) of the datasets presented the features listed above (**Figure 2b**, **Supplementary figure 8**). Incidence maps indicate, on a voxel basis, the percentage of the dataset presenting a significant FC. They confirmed the different extent of network detection in the different dataset. In summary, this analysis revealed the commonly shared spatial extent of mouse RSNs derived from SBA but also indicates that a small subset of the datasets failed to present these features with sufficient sensitivity or specificity.
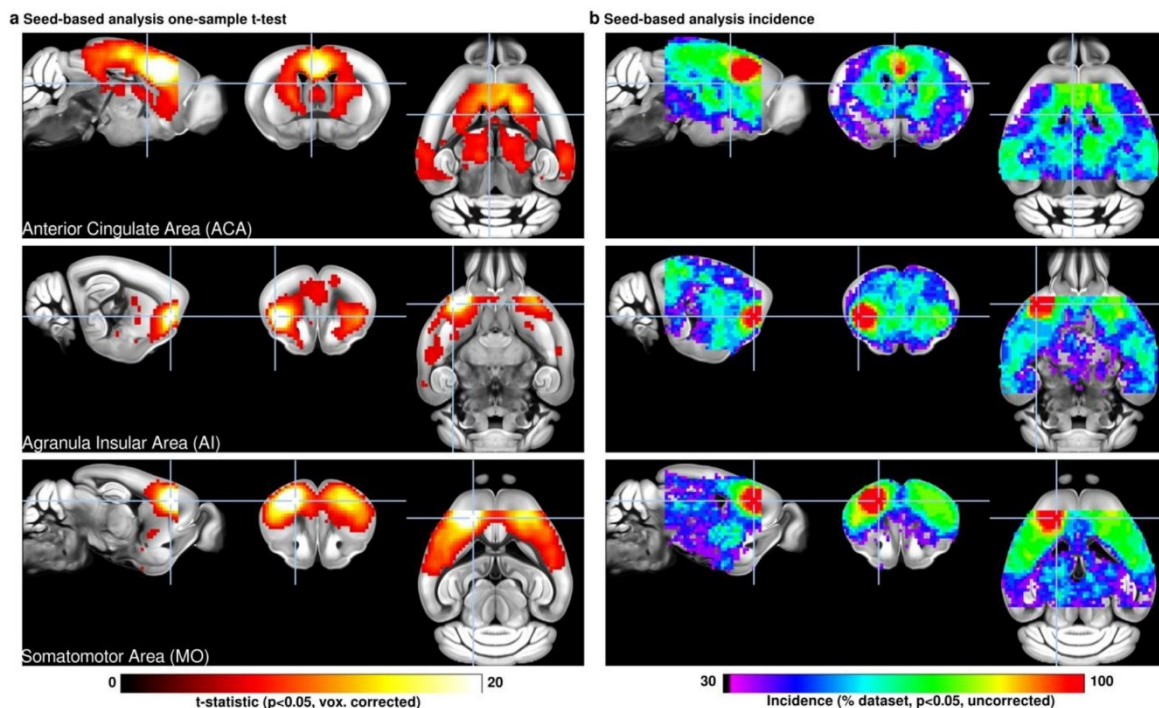
Figure 2 | *Seed-based analysis (SBA) for 3 selected seeds positioned on the left hemisphere. One-sample t-test maps of individual maps reveal the full extent of SBA-derived resting-state networks in the mouse brain across 98/255 scans that presented "specific FC" following vascular+ventricle signal regression. Functional connectivity (FC) relative to a seed located in the anterior cingulate area reveals the extent of the murine default-mode network, including the dorsal caudoputamen, dorsal thalamus, and peri-hippocampal areas. The seed in the insular area reveals significant FC in dorsal cingulate and amygdalar areas, corresponding to areas previously associated with the human salience network. Inter-hemispheric homotopic FC is found relative to the MO seed, together with lateral striatal FC. Incidence maps, indicating the*

*percentage of dataset presenting significant FC in one-sample t-test (p<0.05, uncorrected), reveal that 12/17 of datasets recapitulated the features stated above. Out of these, 5 were not considered to overlap specifically (**Supplementary figure 6**). Voxelwise corrected t-statistic for one-sample t-tests and incidence maps are shown as a colour-coded overlay on the AIBS reference template.*

Sedation protocol and SNR affect connectivity strength

The datasets analysed here were acquired at varying field strengths, coil designs, EPI sequence parameters, animal handling, and with different anesthesia protocols, i.e. either awake or sedated states. Hence the acquisitions were not purposefully balanced to test for specific effects. To identify factors associated with FC strength, a simplified linear model was designed including the following explanatory factors: sedation and breathing conditions, SNR, and motion (mean framewise displacement). Limitations in orthogonality and representation of specific acquisition factors such as field strength, coil design, EPI sequence parameters, number of volumes, gender and age precluded a more extensive model.

Individual-level FC values (z-statistic) were extracted from SBA maps estimated from the ACA seed using a ROI located in the RSP and shown as a function of different acquisition parameters (**Figure 3**). Sedation protocol ($F_{(247, 251)}$ = 18.29, p = 3.5e-13) and SNR ($F_{(247, 248)}$ = 12.39, p = 5.1e-4) were significantly associated with FC, while the remaining factors, breathing condition ($F_{(247, 248)}$ = 3.48, p = 0.063) and motion ($F_{(247, 248)}$ = 0.082, p = 0.77) were not. The awake and medetomidine+isoflurane combination led to higher FC compared to the other two sedation categories. With respect to SNR, high FC values started to be observed at SNR > 50, suggesting that lower SNR may not be sufficient to detect relevant fluctuations. Interestingly, these effects were found consistently across the different ROI pairs considered (**Supplementary table 2**), thus confirming the importance of sedation conditions and SNR, and suggesting that breathing conditions impact mildly FC sensitivity.

These animal handling conditions and sedation protocols highlighted here may not be applicable to all studies or laboratories due to local legislation, equipment availability, or technical knowledge. Distributions of FC values may hence provide useful reference points. Connectivity strength between the ACA and RSP, representing a central feature of the rodent DMN, reached z = 2.77, 5.71, and 10.46 at the 50th, 75th, and 95th percentile respectively (Pearson's r = 0.15, 0.26, 0.43, when SBA is carried out with a correlation analysis instead of a

general linear model). Additional SBA parameter distributions are provided for other ROI pairs in **Supplementary table 2**. The parameters of the acquisitions featured in this analysis offer an objective criterion to evaluate and compare sensitivity to FC in a new dataset or in previous publications, insofar comparable metrics are available.
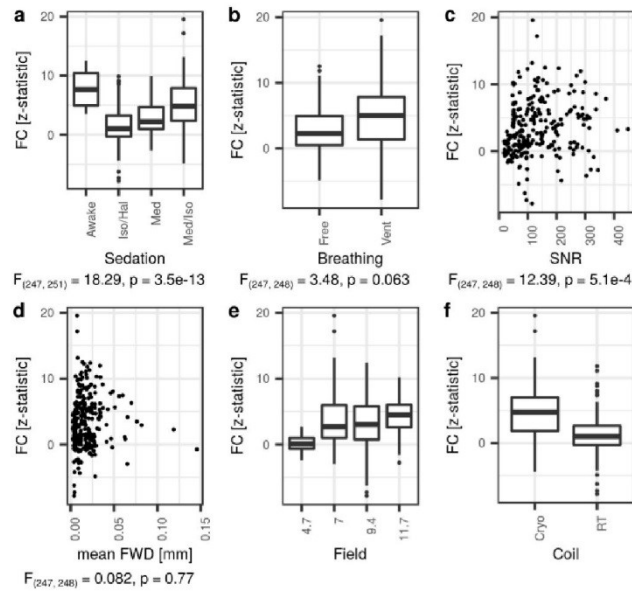
Figure 3 | Functional connectivity (FC) in the retrosplenial cortex relative to a seed located in the anterior cingulate area, as a function of acquisition parameters. A statistically significant association was determined between sedation effect and FC (a, $F_{(247, 251)}$ = 18.29, p = 3.5e-13) and between SNR and FC (c, $F_{(247,248)}$ = 12.39, p = 5.1e-4). Neither breathing condition nor motion effects were significant with FC (b, d). Due to limitations in the representation of each level within a factor, coil design (e) and magnetic field (f) were omitted from the final statistical model. Free = Free-breathing, Vent = Mechanically ventilated, Cryo = cryoprobe, RT = room-temperature.

Network-specific functional connectivity is found in all datasets

Evidence for robust distal FC could not be established in all datasets with SBA. To investigate the presence of network-specific FC also in datasets characterized by weaker long range connectivity, a dual regression combined with group-level ICA (drICA) approach was undertaken (Filippini et al., 2009). To obtain an enriched data-driven reference atlas, a group ICA atlas was generated out of the 98 "specific FC" scans selected in the SBA above, using 20

dimensions. The atlas revealed 9 cortical components (**Figure 4a, Supplementary figure 9, Supplementary table 3**), 5 overlapping with the latero-cortical network (somatomotor area (MO) and 4 SSp areas), 3 overlapping with elements of the DMN (prefrontal, cingulate/RSP, and temporal associative areas) and 1 overlapping with the insular area (AI). Additionally, 5 sub-cortical components were revealed, overlapping with the nucleus accumbens (ACB), caudoputamen (CP), pallidum (PAL), hippocampal region (HIP), and thalamus (TH) (**Supplementary figure 10**). The components recapitulate many of the features identified with SBA (**Figure 4b**), namely a strong emphasis on homotopic bilateral organization. The components identified here also presented strong similarities to a previous analysis (Zerbi et al., 2015). Due to uneven brain coverages across datasets, rostral and caudal RSNs could not be examined, including olfactory, auditory, and visual networks. To obtain individual-level representation of these components, a dual regression approach was implemented using the reference ICA identified above. These group-level ICA were used as masks to extract time series which were then regressed into individual scans using a general linear model. To investigate specificity relative to a DMN-related component, FC relative to the cingulate/RSP component was extracted from the ACA ROI (Specific ROI, z = 8.33, 14.41, and 22.32, 50th, 75th, and 95th percentiles) and SSp ROI (Unspecific ROI). "Specific FC" was determined in 79% (201/255) of the scans, "Unspecific FC" in 16%, "Spurious FC" in 1.5%, and "No FC" in 3.1% (**Figure 4c**). "Specific FC" in 15/15 scans was determined in 2 datasets (Median = 12/15). The "Specific FC" category was also more evenly distributed relative to acquisition protocols and equipments: Field strength (4.7T N = 14/15, 7T N = 89/120, 9.4T N = 73/90, 11.7T N = 25/30, X^2 = 4.01, df = 3, p-value = 0.25), coil type (room-temperature N = 88/105, cryoprobe N = 113/150, X^2 = 2.17, df = 1, p-value = 0.14), breathing condition (free-breathing N = 138/180, ventilated N = 63/75, X^2 = 1.29, df = 1, p-value = 0.25), and sedation condition (awake N = 13/15, isoflurane/halothane N = 65/90, medetomidine N = 55/75, medetomidine+isoflurane N = 68/75, X^2 = 10.56, df = 3, p-value = 0.014). Importantly, statistical inference revealed that significant within-component FC could be established in 17/17 datasets for all 14 components (**Figure 4d, Supplementary figure 11, Supplementary figure 12**). This suggests that network-specific inferences can be probed in all rsfMRI datasets, and that drICA is a powerful approach enabling robust FC detection in all datasets, including those that may not robustly exhibit distal connectivity patterns.
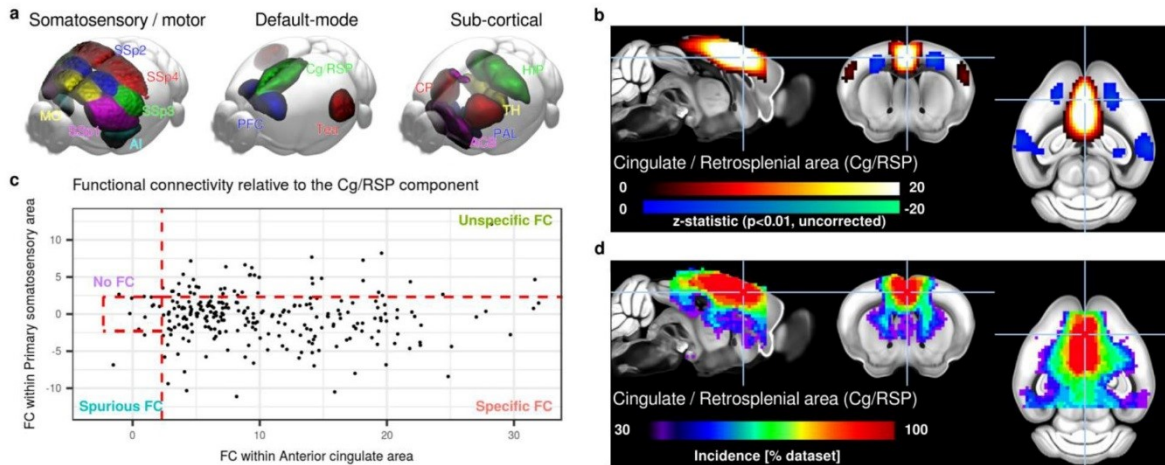
Figure 4 | *Group-level independent component analysis (ICA) estimated across 98/255 "specific FC" scans reveals canonical murine components (**a**). All components presented a marked bilateral organisation. Nine components were found to overlap principally with the isocortex including regions attributed to latero-cortical, salience and DMN networks by SBA, 3 components overlapped with the striatum, one with the hippocampal areas, and one with the thalamus. Detailed representations of the Cingulate / Retrosplenial area component (Cg/RSP* **b**). *Remaining components are presented in* **Supplementary figure 9, 10**. *FC relative to Cg/RSP is found specifically in the anterior cingulate area but not in the primary somatosensory in 79% of the individual scans following dual-regression (**c**). One-sample t-test within datasets indicates 100% of datasets presented significant FC (p < 0.05, uncorrected) within the Cg/RSP component. Incidence for the remaining components are presented in* **Supplementary figure 11, 12**. *AI = insular area, MO = somatomotor area, SSp = primary somatosensory area, PFC = prefrontal cortex, Cg/RSP = cingulate + retrosplenial area, Tea = temporal associative area, CP = caudoputamen, ACB = nucleus accumbens, PAL = pallidum, HIP = hippocampal region, TH = thalamus.*

Discussion

Rodent rsfMRI has been a growing research field in neuroscience over the past 10 years (Chuang and Nasrallah, 2017; Gozzi and Schwarz, 2016; Hoyer et al., 2014; Jonckers et al., 2015, 2013; Pan et al., 2015). The fast-paced development of the field has yielded a number of exciting results, yet the comparability of these findings remains unclear. The results presented here indicate that, despite major differences in cross-site equipment, scan conditions, sedation protocols and experience in the implementation of these procedures, mouse rsfMRI networks converge toward spatially defined motifs encompassing previously described neuroanatomical

systems of the mouse brain. Importantly, we also highlight the possibility to use rsfMRI to probe distributed network systems of high translational relevance, including a rodent DMN, salience network, and latero-cortical network. While not reliably identified in all datasets and scan conditions, these large-scale networks were found to colocalize into well delineated boundaries in the majority of scans and datasets respectively, recapitulating previous descriptions in rodents (Gozzi and Schwarz, 2016; Lu et al., 2012; Sforazzini et al., 2014; Stafford et al., 2014), monkeys (Hutchison and Everling, 2012) and humans (Buckner et al., 2008).

Interestingly, most (70%) of the datasets converged toward spatially defined common RSN when long-range FC relative to a seed was assessed. When the analysis was restricted to local connectivity, all datasets converged. These results indicate that group-level, or second-level inferences, may be assessed irrespective of acquisition protocol or animal handling procedures in all datasets using robust analysis strategies. At the subject level, "specific FC" relative to the DMN was found in 38% of the scans, indicating that first-level inference on long-range FC is within reaches in some, but not all datasets. Sedation and equipment performance leading to increased SNR were the major factors associated with both FC sensitivity and specificity, together with breathing conditions. Awake animals presented higher FC overall, however datasets acquired with medetomidine+isoflurane combination together with mechanical ventilation were associated with greater specificity within elements of the DMN. Importantly, the results converged irrespective of sedation or awake protocols. This underlines that all datasets should be examined with the same expectations and criteria to further enhance results comparability. Hence, the set of standards provided here (e.g. spatial maps and FC parameter distributions), will allow the calibration of future multi-centre projects and assist in designing meta-analysis and replication studies, the gold standards in evidence-based research.

In addition to acquisition procedures, the adoption of analysis standards must be encouraged. A MRI template (Dorr et al., 2008) transformed into the AIBS standard space provides a common space that extends beyond animal MRI studies, including the seamless implementation of AIBS resources (Bergmann et al., 2016; Grandjean et al., 2017b; Oh et al., 2014; Richiardi et al., 2015; Stafford et al., 2014). Moreover, analysis based on robust methods (Zuo and Xing, 2014), such as drICA (Filippini et al., 2009), together with considerations for statistical analysis (Eklund et al., 2016), and sharing datasets on online repositories (Nichols et al., 2017) provide a comprehensive evidence-based roadmap to improve the comparability of acquisitions carried out between centres and enhance the robustness and reproducibility of future results. In

particular, all the dataset analyzed in the context of this study will be shared and therefore provide references for scientists developing customized rsfMRI protocols.

Several major limitations within this study should be acknowledged. First and foremost, the lack of consensus quality assurance parameters for the estimation of FC led us to devise a strategy to examine FC specificity. Because this study grouped together a set of existing scans, factors were not entirely orthogonal and it was not possible to model a number of potentially relevant effects impacting FC metrics, such as specific sequence parameters (e.g. number of volumes), as well as biologically relevant factors including sex, age, and mouse strain. Finally, lack of distal FC in some datasets could not be attributed to specific animal handling protocols or equipment performance. This indicates that additional experimental factors not considered here may be better predictors estimating this particular kind of FC. For example, the implementation of procedures to control the arterial level of carbon dioxide may be critical to prevent hypercapnic conditions, a feature that is associated with reduced FC connectivity (Biswal et al., 1997) and that is often observed in freely breathing anesthetized rodents. Despite these limitations, the work presented here is likely to enhance the true scientific value of mouse rsfMRI by establishing standards and how to attain them. With these, the field is set to meet its goals toward the establishments and understanding of the cellular and molecular mechanisms of large-scale brain functional reorganisation in the healthy and diseased brain.

234

Material and methods

Comparison dataset acquisition

All animal experiments were carried out with explicit permits from local regulatory bodies. Seventeen datasets, consisting of 15 individual pre-acquired rsfMRI scans each, were acquired with parameters reflecting each centre standards. A summary of equipment, acquisition parameters, and animal handling procedures is listed in **Supplementary table 1**. Scans were acquired on dedicated Bruker magnets operating at 4.7T (N = 1 dataset), 7T (N = 8), 9.4T (N = 6), 11.7T (N = 2), with either room-temperature coils (N = 7) or cryoprobes (N = 10). Gradient-echo echo planar imaging (EPI) sequences were used to acquire all datasets, with repetition time (TR) ranging 1000 - 2000 ms, echo time (TE) 10 - 25 ms, and number of volume 150 - 1000. Acquisitions were performed on awake (N = 1) or anesthetized C57Bl/6J mice (both male and female) with either isoflurane 1-1.25% (N = 5), halothane 0.75% (N = 1), medetomidine 0.1-0.4 mg/kg bolus and 0.2-0.8 mg/kg/h infusion (N = 5), or a combination of isoflurane 0.2-0.5% and medetomidine 0.05-0.3 mg/kg bolus and 0-0.1 mg/kg/h infusion (N = 5). Awake mice were fitted with a non-magnetic head implant to fix the heads to a compatible cradle (Yoshida et al., 2016). Animals were either freely-breathing (N = 12) or mechanically ventilated (N = 5). Datasets are publicly available in BIDS format on openneuro.org (project ID : Mouse_rest_multicentre, https://openneuro.org/datasets/ds001720).

Data preprocessing

Volumes were analysed in their native resolution. Firstly, image axes were reoriented into LPI orientation (*3dresample*, Analysis of Functional NeuroImages, AFNI_16.1.26, https://afni.nimh.nih.gov) (Cox, 1996). Temporal spikes were removed (*3dDespike*), followed by motion correction (*3dvolreg*). Brain masks (*RATS_MM*, https://www.iibi.uiowa.edu) (Oguz et al., 2014) were estimated on temporally averaged EPI volume (*fslmaths*). Motion outliers were detected based on relative framewise displacement estimated during motion correction. Volumes with spikes or framewise displacement greater than 0.100 mm, corresponding to approximately 0.5 voxel of the average in-plane resolution, were labelled in a confound file to be excluded from later seed-based analysis and dual-regression. Linear affine parameters and nonlinear deformations with greedy SyN diffeomorphic transformation (*antsIntroduction.sh*) were estimated relative to a reference T2 MRI template (Dorr et al., 2008) registered into the AIBS Common Coordinate Framework (CCF v3, http://www.brain-map.org/) resampled to 0.200 mm³. Normalisation to AIBS space was carried out on brain masked EPI directly using ANTS (Advanced Normalization Tools, http://picsl.upenn.edu/software/ants/) (Avants et al., 2014,

2011). Anatomical scans corresponding to each EPI acquisition were not available in all cases. Despite this limitation, plausible registrations of murine EPI directly onto a T2 MRI template were rendered possible due to the relatively simple structure of the lissencephalic cerebrum and high EPI quality. Individual registered brain mask were multiplied (*fslmaths*) to obtain a study mask. The analysis was bounded within this study mask, i..e the brain areas covered by all individual scans. References to anatomical areas are made with respect to the AIBS atlas. All brain masks and registrations were visually inspected and considered plausible.

Six different denoising approaches were applied: i) 6 motion parameters regression (MC), or the following together with motion parameters, ii) white matter (WM), iii) ventricle (VEN), iv) vascular (VASC), v) vascular + ventricle (VV), or vi) global (GSR) signal regression. White matter and ventricle masks were adapted from the AIBS atlas (**Supplementary figure 4cd**), a vascular mask was obtained by averaging and thresholding hand-selected individual-level independent components registered to AIBS space (**Supplementary figure 4b**). Inverse transformations were applied to each mask. Average time series within masks were extracted (*fslmeants*) and regressed out (*fsl_regfilt*). Finally, spatial smoothing was applied with a isotropic 0.45 mm kernel (*3dBlurInMask*), and bandpass filtering was applied between 0.01 - 0.1 Hz (*3dBandpass*). The smoothing kernel was selected to correspond approximately to 1.5 x voxel dimension of the lowest in-plane resolution. The bandpass filter was applied to all datasets to enhance comparability between datasets, despite indications that medetomidine leads to a shift in resting fluctuation frequencies (Grandjean et al., 2014a; Kalthoff et al., 2013; Paasonen et al., 2018). The denoised and filtered individual scans were normalised to AIBS reference space (*WarpTimeSeriesImageMultiTransform*).

Noise was estimated by extracting the signal standard deviation from manually defined regions-of-interest (ROIs) in the upper corners of at least 3 slices, carefully avoiding ghosting artefacts or tissues (brain or otherwise). Mean signal was extracted from the 20th acquisition volume using a cortical mask spanning over the whole isocortex (defined by AIBS atlas) and registered in individual spaces to estimate signal-to-noise ratio (SNR). The same cortical mask was used to extract standard deviation of temporal signals to estimate temporal SNR (tSNR).

Seed-based analysis and independent component analysis
Seeds on the left hemisphere were defined in AIBS space based on the AIBS atlas using 0.300 mm^3 spheres, corresponding to 27 voxels (**Figure S1a**). Mean BOLD signal time series within a

seed were extracted (*fslmeants*) and regressed into individual scans to obtain z-statistic maps (*fsl_glm*). Multi-session temporal concatenation ICA was carried out using MELODIC (Multivariate Exploratory Linear Optimized Decomposition into Independent Components, v3.14) using 20 components. Group-level component classification was adapted on a set of rules defined in (Zerbi et al., 2015). The following were considered plausible resting-state networks: (i) components with either bilateral organisation or (ii) unilateral components with a corresponding separate contralateral component, (iii) minimal crossing of relevant brain boundaries such as white matter tracts, (iv) spatial extent covering more than one slice. The following were considered as implausible resting-state networks: (i) components overlapping mainly with either white matter, ventricle, or vascular masks (**Supplementary figure 4bcd**), (ii) components mainly localised on brain edges. Dual-regression was carried out using the eponymous FSL function to obtain individual-level representations of 14 selected plausible group-level components (Filippini et al., 2009).

Statistical analysis and data representation

Voxelwise statistics were carried out in FSL using either non-parametric permutation tests (*randomise*) for across datasets one-sample t-tests using 5000 permutations and voxelwise correction, or uncorrected parametric one-sample t-tests for within-dataset comparisons (*fsl_glm*). Voxelwise statistical maps are shown as colour-coded t-statistics overlays on the ABI template resampled at $25\mu m^3$ isotropic using MRIcron (Rorden et al., 2007). Statistical analysis carried out on parameters extracted from ROIs was performed in R (v3.4.4, "Someone to Lean on", R Foundation for Statistical Computing, Vienna, Austria, https://R-project.org) using a linear model (*lm*). A simplified model was designed including the following fixed effects: breathing conditions (2 levels: ventilated or free-breathing), sedation conditions (4 levels: awake, isoflurane/halothane, medetomidine, medetomidine + isoflurane combination), SNR (continuous variable), mean FWD (continuous variable). Interactions effects between these factors were not modeled. Fixed effects significance was tested using likelihood ratio test. Scan parameter occurrence rates were assessed with Chi-square test (*chisq.test*). Residual analysis was performed with QQ-plots to inspect normal distribution, Tukey–Anscombe plots for the homogeneity of the variance and skewness, and scale location plots for homoscedasticity (i.e., the homogeneity of residual variance). The assumption of normality of the residuals was considered plausible in all statistical tests. Plots were generated using ggplot2 (v2.1.0) package for R. Significance level was set at $p<=0.05$ one-tailed with family-wise error correction at a

voxelwise level, unless specified otherwise. Descriptive statistics are given as mean ± 1 standard deviation.

Acknowledgements

Author Contributions

JG designed the study. Every author contributed to data acquisition. JG, CC and AG carried out the analysis. Every author participated in the preparation of the manuscript.

Competing interests statement

The authors have no conflicts of interest to declare.

References

Bergmann, E., Zur, G., Bershadsky, G., Kahn, I., 2016. The Organization of Mouse and Human Cortico-Hippocampal Networks Estimated by Intrinsic Functional Connectivity. Cereb. Cortex 26, 4497–4512. doi:10.1093/cercor/bhw327resting state

Avants, B.B., Tustison, N.J., Song, G., Cook, P.A., Klein, A., Gee, J.C., 2011. A reproducible evaluation of ANTs similarity metric performance in brain image registration. Neuroimage 54, 2033–2044. doi:10.1016/j.neuroimage.2010.09.025

Avants, B.B., Tustison, N.J., Stauffer, M., Song, G., Wu, B., Gee, J.C., 2014. The Insight ToolKit image registration framework. Front. Neuroinformatics 8, 44. doi:10.3389/fninf.2014.00044

Azevedo, F.A.C., Carvalho, L.R.B., Grinberg, L.T., Farfel, J.M., Ferretti, R.E.L., Leite, R.E.P., Jacob Filho, W., Lent, R., Herculano-Houzel, S., 2009. Equal numbers of neuronal and nonneuronal cells make the human brain an isometrically scaled-up primate brain. J. Comp. Neurol. 513, 532–541. doi:10.1002/cne.21974

Becerra, L., Pendse, G., Chang, P.-C., Bishop, J., Borsook, D., 2011. Robust reproducible resting state networks in the awake rodent brain. PLoS ONE 6, e25701. doi:10.1371/journal.pone.0025701

Belloy, M.E., Naeyaert, M., Abbas, A., Shah, D., Vanreusel, V., van Audekerke, J., Keilholz, S.D., Keliris, G.A., Van der Linden, A., Verhoye, M., 2018a. Dynamic resting state fMRI analysis in mice reveals a set of Quasi-Periodic Patterns and illustrates their relationship with the global signal. Neuroimage 180, 463–484. doi:10.1016/j.neuroimage.2018.01.075

Belloy, M.E., Shah, D., Abbas, A., Kashyap, A., Roßner, S., Van der Linden, A., Keilholz, S.D., Keliris, G.A., Verhoye, M., 2018b. Quasi-Periodic Patterns of Neural Activity improve Classification of Alzheimer's Disease in Mice. Sci. Rep. 8, 10024. doi:10.1038/s41598-018-28237-9

Bergmann, E., Zur, G., Bershadsky, G., Kahn, I., 2016. The Organization of Mouse and Human Cortico-Hippocampal Networks Estimated by Intrinsic Functional Connectivity. Cereb. Cortex 26, 4497–4512. doi:10.1093/cercor/bhw327

Bertero, A., Liska, A., Pagani, M., Parolisi, R., Masferrer, M.E., Gritti, M., Pedrazzoli, M., Galbusera, A., Sarica, A., Cerasa, A., Buffelli, M., Tonini, R., Buffo, A., Gross, C., Pasqualetti, M., Gozzi, A., 2018. Autism-associated 16p11.2 microdeletion impairs prefrontal functional connectivity in mouse and human. Brain 141, 2055–2065. doi:10.1093/brain/awy111

Biswal, B., Hudetz, A.G., Yetkin, F.Z., Haughton, V.M., Hyde, J.S., 1997. Hypercapnia reversibly suppresses low-frequency fluctuations in the human motor cortex during rest using echo-

planar MRI. J. Cereb. Blood Flow Metab. 17, 301–308. doi:10.1097/00004647-199703000-00007

Biswal, B., Yetkin, F.Z., Haughton, V.M., Hyde, J.S., 1995. Functional connectivity in the motor cortex of resting human brain using echo-planar MRI. Magn. Reson. Med. 34, 537–541. doi:10.1002/mrm.1910340409

Biswal, B.B., Mennes, M., Zuo, X.-N., Gohel, S., Kelly, C., Smith, S.M., Beckmann, C.F., Adelstein, J.S., Buckner, R.L., Colcombe, S., Dogonowski, A.-M., Ernst, M., Fair, D., Hampson, M., Hoptman, M.J., Hyde, J.S., Kiviniemi, V.J., Kötter, R., Li, S.-J., Lin, C.-P., Milham, M.P., 2010. Toward discovery science of human brain function. Proc Natl Acad Sci USA 107, 4734–4739. doi:10.1073/pnas.0911855107

Buckner, R.L., Andrews-Hanna, J.R., Schacter, D.L., 2008. The brain's default network: anatomy, function, and relevance to disease. Ann. N. Y. Acad. Sci. 1124, 1–38. doi:10.1196/annals.1440.011

Buehlmann, D., Grandjean, J., Xandry, J., Rudin, M., 2018. Longitudinal resting-state functional magnetic resonance imaging in a mouse model of metastatic bone cancer reveals distinct functional reorganizations along a developing chronic pain state. Pain 159, 719–727. doi:10.1097/j.pain.0000000000001148

Bukhari, Q., Schroeter, A., Cole, D.M., Rudin, M., 2017. Resting State fMRI in Mice Reveals Anesthesia Specific Signatures of Brain Functional Networks and Their Interactions. Front. Neural Circuits 11, 5. doi:10.3389/fncir.2017.00005

Bukhari, Q., Schroeter, A., Rudin, M., 2018. Increasing isoflurane dose reduces homotopic correlation and functional segregation of brain networks in mice as revealed by resting-state fMRI. Sci. Rep. 8, 10591. doi:10.1038/s41598-018-28766-3

Charbogne, P., Gardon, O., Martín-García, E., Keyworth, H.L., Matsui, A., Mechling, A.E., Bienert, T., Nasseef, T., Robé, A., Moquin, L., Darcq, E., Ben Hamida, S., Robledo, P., Matifas, A., Befort, K., Gavériaux-Ruff, C., Harsan, L.-A., von Elverfeldt, D., Hennig, J., Gratton, A., Kieffer, B.L., 2017. Mu Opioid Receptors in Gamma-Aminobutyric Acidergic Forebrain Neurons Moderate Motivation for Heroin and Palatable Food. Biol. Psychiatry 81, 778–788. doi:10.1016/j.biopsych.2016.12.022

Chuang, K.-H., Nasrallah, F.A., 2017. Functional networks and network perturbations in rodents. Neuroimage 163, 419–436. doi:10.1016/j.neuroimage.2017.09.038

Cox, R.W., 1996. AFNI: software for analysis and visualization of functional magnetic resonance neuroimages. Comput. Biomed. Res. 29, 162–173. doi:10.1006/cbmr.1996.0014

DeSimone, J.C., Febo, M., Shukla, P., Ofori, E., Colon-Perez, L.M., Li, Y., Vaillancourt, D.E.,

2016. In vivo imaging reveals impaired connectivity across cortical and subcortical networks in a mouse model of DYT1 dystonia. Neurobiol. Dis. 95, 35–45. doi:10.1016/j.nbd.2016.07.005

Dorr, A.E., Lerch, J.P., Spring, S., Kabani, N., Henkelman, R.M., 2008. High resolution three-dimensional brain atlas using an average magnetic resonance image of 40 adult C57Bl/6J mice. Neuroimage 42, 60–69. doi:10.1016/j.neuroimage.2008.03.037

Eklund, A., Nichols, T.E., Knutsson, H., 2016. Cluster failure: Why fMRI inferences for spatial extent have inflated false-positive rates. Proc Natl Acad Sci USA 113, 7900–7905. doi:10.1073/pnas.1602413113

Errico, F., D'Argenio, V., Sforazzini, F., Iasevoli, F., Squillace, M., Guerri, G., Napolitano, F., Angrisano, T., Di Maio, A., Keller, S., Vitucci, D., Galbusera, A., Chiariotti, L., Bertolino, A., de Bartolomeis, A., Salvatore, F., Gozzi, A., Usiello, A., 2015. A role for D-aspartate oxidase in schizophrenia and in schizophrenia-related symptoms induced by phencyclidine in mice. Transl. Psychiatry 5, e512. doi:10.1038/tp.2015.2

Filippini, N., MacIntosh, B.J., Hough, M.G., Goodwin, G.M., Frisoni, G.B., Smith, S.M., Matthews, P.M., Beckmann, C.F., Mackay, C.E., 2009. Distinct patterns of brain activity in young carriers of the APOE-epsilon4 allele. Proc Natl Acad Sci USA 106, 7209–7214. doi:10.1073/pnas.0811879106

Fox, M.D., Raichle, M.E., 2007. Spontaneous fluctuations in brain activity observed with functional magnetic resonance imaging. Nat. Rev. Neurosci. 8, 700–711. doi:10.1038/nrn2201

Fox, M.D., Snyder, A.Z., Vincent, J.L., Corbetta, M., Van Essen, D.C., Raichle, M.E., 2005. The human brain is intrinsically organized into dynamic, anticorrelated functional networks. Proc Natl Acad Sci USA 102, 9673–9678. doi:10.1073/pnas.0504136102

Friston, K.J., 2011. Functional and effective connectivity: a review. Brain Connect. 1, 13–36. doi:10.1089/brain.2011.0008

Gass, N., Weber-Fahr, W., Sartorius, A., Becker, R., Didriksen, M., Stensbøl, T.B., Bastlund, J.F., Meyer-Lindenberg, A., Schwarz, A.J., 2016. An acetylcholine alpha7 positive allosteric modulator rescues a schizophrenia-associated brain endophenotype in the 15q13.3 microdeletion, encompassing CHRNA7. Eur. Neuropsychopharmacol. 26, 1150–1160. doi:10.1016/j.euroneuro.2016.03.013

Gozzi, A., Schwarz, A.J., 2016. Large-scale functional connectivity networks in the rodent brain. Neuroimage 127, 496–509. doi:10.1016/j.neuroimage.2015.12.017

Grandjean, J., Azzinnari, D., Seuwen, A., Sigrist, H., Seifritz, E., Pryce, C.R., Rudin, M., 2016a.

Chronic psychosocial stress in mice leads to changes in brain functional connectivity and metabolite levels comparable to human depression. Neuroimage 142, 544–552. doi:10.1016/j.neuroimage.2016.08.013

Grandjean, J., Derungs, R., Kulic, L., Welt, T., Henkelman, M., Nitsch, R.M., Rudin, M., 2016b. Complex interplay between brain function and structure during cerebral amyloidosis in APP transgenic mouse strains revealed by multi-parametric MRI comparison. Neuroimage 134, 1–11. doi:10.1016/j.neuroimage.2016.03.042

Grandjean, J., Preti, M.G., Bolton, T.A.W., Buerge, M., Seifritz, E., Pryce, C.R., Van De Ville, D., Rudin, M., 2017a. Dynamic reorganization of intrinsic functional networks in the mouse brain. Neuroimage 152, 497–508. doi:10.1016/j.neuroimage.2017.03.026

Grandjean, J., Schroeter, A., Batata, I., Rudin, M., 2014a. Optimization of anesthesia protocol for resting-state fMRI in mice based on differential effects of anesthetics on functional connectivity patterns. Neuroimage 102 Pt 2, 838–847. doi:10.1016/j.neuroimage.2014.08.043

Grandjean, J., Schroeter, A., He, P., Tanadini, M., Keist, R., Krstic, D., Konietzko, U., Klohs, J., Nitsch, R.M., Rudin, M., 2014b. Early alterations in functional connectivity and white matter structure in a transgenic mouse model of cerebral amyloidosis. J. Neurosci. 34, 13780–13789. doi:10.1523/JNEUROSCI.4762-13.2014

Grandjean, J., Zerbi, V., Balsters, J.H., Wenderoth, N., Rudin, M., 2017b. Structural Basis of Large-Scale Functional Connectivity in the Mouse. J. Neurosci. 37, 8092–8101. doi:10.1523/JNEUROSCI.0438-17.2017

Greicius, M., 2008. Resting-state functional connectivity in neuropsychiatric disorders. Curr. Opin. Neurol. 21, 424–430. doi:10.1097/WCO.0b013e328306f2c5

Guilfoyle, D.N., Gerum, S.V., Sanchez, J.L., Balla, A., Sershen, H., Javitt, D.C., Hoptman, M.J., 2013. Functional connectivity fMRI in mouse brain at 7T using isoflurane. J. Neurosci. Methods 214, 144–148. doi:10.1016/j.jneumeth.2013.01.019

Haberl, M.G., Zerbi, V., Veltien, A., Ginger, M., Heerschap, A., Frick, A., 2015. Structural-functional connectivity deficits of neocortical circuits in the Fmr1 (-/y) mouse model of autism. Sci. Adv. 1, e1500775. doi:10.1126/sciadv.1500775

Hoyer, C., Gass, N., Weber-Fahr, W., Sartorius, A., 2014. Advantages and challenges of small animal magnetic resonance imaging as a translational tool. Neuropsychobiology 69, 187–201. doi:10.1159/000360859

Hübner, N.S., Mechling, A.E., Lee, H.-L., Reisert, M., Bienert, T., Hennig, J., von Elverfeldt, D., Harsan, L.-A., 2017. The connectomics of brain demyelination: Functional and structural

patterns in the cuprizone mouse model. Neuroimage 146, 1–18.
doi:10.1016/j.neuroimage.2016.11.008

Hutchison, R.M., Everling, S., 2012. Monkey in the middle: why non-human primates are needed to bridge the gap in resting-state investigations. Front. Neuroanat. 6, 29. doi:10.3389/fnana.2012.00029

Jonckers, E., Delgado y Palacios, R., Shah, D., Guglielmetti, C., Verhoye, M., Van der Linden, A., 2014. Different anesthesia regimes modulate the functional connectivity outcome in mice. Magn. Reson. Med. 72, 1103–1112. doi:10.1002/mrm.24990

Jonckers, E., Shah, D., Hamaide, J., Verhoye, M., Van der Linden, A., 2015. The power of using functional fMRI on small rodents to study brain pharmacology and disease. Front. Pharmacol. 6, 231. doi:10.3389/fphar.2015.00231

Jonckers, E., Van Audekerke, J., De Visscher, G., Van der Linden, A., Verhoye, M., 2011. Functional connectivity fMRI of the rodent brain: comparison of functional connectivity networks in rat and mouse. PLoS ONE 6, e18876. doi:10.1371/journal.pone.0018876

Jonckers, E., Van der Linden, A., Verhoye, M., 2013. Functional magnetic resonance imaging in rodents: an unique tool to study in vivo pharmacologic neuromodulation. Curr. Opin. Pharmacol. 13, 813–820. doi:10.1016/j.coph.2013.06.008

Jovicich, J., Minati, L., Marizzoni, M., Marchitelli, R., Sala-Llonch, R., Bartrés-Faz, D., Arnold, J., Benninghoff, J., Fiedler, U., Roccatagliata, L., Picco, A., Nobili, F., Blin, O., Bombois, S., Lopes, R., Bordet, R., Sein, J., Ranjeva, J.-P., Didic, M., Gros-Dagnac, H., PharmaCog Consortium, 2016. Longitudinal reproducibility of default-mode network connectivity in healthy elderly participants: A multicentric resting-state fMRI study. Neuroimage 124, 442–454. doi:10.1016/j.neuroimage.2015.07.010

Kalthoff, D., Po, C., Wiedermann, D., Hoehn, M., 2013. Reliability and spatial specificity of rat brain sensorimotor functional connectivity networks are superior under sedation compared with general anesthesia. NMR Biomed. 26, 638–650. doi:10.1002/nbm.2908

Komaki, Y., Hikishima, K., Shibata, S., Konomi, T., Seki, F., Yamada, M., Miyasaka, N., Fujiyoshi, K., Okano, H.J., Nakamura, M., Okano, H., 2016. Functional brain mapping using specific sensory-circuit stimulation and a theoretical graph network analysis in mice with neuropathic allodynia. Sci. Rep. 6, 37802. doi:10.1038/srep37802

Li, Q., Li, G., Wu, D., Lu, H., Hou, Z., Ross, C.A., Yang, Y., Zhang, J., Duan, W., 2017. Resting-state functional MRI reveals altered brain connectivity and its correlation with motor dysfunction in a mouse model of Huntington's disease. Sci. Rep. 7, 16742. doi:10.1038/s41598-017-17026-5

Liska, A., Bertero, A., Gomolka, R., Sabbioni, M., Galbusera, A., Barsotti, N., Panzeri, S., Scattoni, M.L., Pasqualetti, M., Gozzi, A., 2018. Homozygous Loss of Autism-Risk Gene CNTNAP2 Results in Reduced Local and Long-Range Prefrontal Functional Connectivity. Cereb. Cortex 28, 1141–1153. doi:10.1093/cercor/bhx022

Liska, A., Galbusera, A., Schwarz, A.J., Gozzi, A., 2015. Functional connectivity hubs of the mouse brain. Neuroimage 115, 281–291. doi:10.1016/j.neuroimage.2015.04.033

Liska, A., Gozzi, A., 2016. Can mouse imaging studies bring order to autism connectivity chaos? Front. Neurosci. 10, 484. doi:10.3389/fnins.2016.00484

Lu, H., Zou, Q., Gu, H., Raichle, M.E., Stein, E.A., Yang, Y., 2012. Rat brains also have a default mode network. Proc Natl Acad Sci USA 109, 3979–3984. doi:10.1073/pnas.1200506109

Mechling, A.E., Arefin, T., Lee, H.-L., Bienert, T., Reisert, M., Ben Hamida, S., Darcq, E., Ehrlich, A., Gaveriaux-Ruff, C., Parent, M.J., Rosa-Neto, P., Hennig, J., von Elverfeldt, D., Kieffer, B.L., Harsan, L.-A., 2016. Deletion of the mu opioid receptor gene in mice reshapes the reward-aversion connectome. Proc Natl Acad Sci USA 113, 11603–11608. doi:10.1073/pnas.1601640113

Michetti, C., Caruso, A., Pagani, M., Sabbioni, M., Medrihan, L., David, G., Galbusera, A., Morini, M., Gozzi, A., Benfenati, F., Scattoni, M.L., 2017. The Knockout of Synapsin II in Mice Impairs Social Behavior and Functional Connectivity Generating an ASD-like Phenotype. Cereb. Cortex 27, 5014–5023. doi:10.1093/cercor/bhx207

Murphy, K., Birn, R.M., Bandettini, P.A., 2013. Resting-state fMRI confounds and cleanup. Neuroimage 80, 349–359. doi:10.1016/j.neuroimage.2013.04.001

Nichols, T.E., Das, S., Eickhoff, S.B., Evans, A.C., Glatard, T., Hanke, M., Kriegeskorte, N., Milham, M.P., Poldrack, R.A., Poline, J.-B., Proal, E., Thirion, B., Van Essen, D.C., White, T., Yeo, B.T.T., 2017. Best practices in data analysis and sharing in neuroimaging using MRI. Nat. Neurosci. 20, 299–303. doi:10.1038/nn.4500

Oguz, I., Zhang, H., Rumple, A., Sonka, M., 2014. RATS: Rapid Automatic Tissue Segmentation in rodent brain MRI. J. Neurosci. Methods 221, 175–182. doi:10.1016/j.jneumeth.2013.09.021

Oh, S.W., Harris, J.A., Ng, L., Winslow, B., Cain, N., Mihalas, S., Wang, Q., Lau, C., Kuan, L., Henry, A.M., Mortrud, M.T., Ouellette, B., Nguyen, T.N., Sorensen, S.A., Slaughterbeck, C.R., Wakeman, W., Li, Y., Feng, D., Ho, A., Nicholas, E., Zeng, H., 2014. A mesoscale connectome of the mouse brain. Nature 508, 207–214. doi:10.1038/nature13186

Paasonen, J., Stenroos, P., Salo, R.A., Kiviniemi, V., Gröhn, O., 2018. Functional connectivity

under six anesthesia protocols and the awake condition in rat brain. Neuroimage 172, 9–20. doi:10.1016/j.neuroimage.2018.01.014

Pan, W.-J., Billings, J.C.W., Grooms, J.K., Shakil, S., Keilholz, S.D., 2015. Considerations for resting state functional MRI and functional connectivity studies in rodents. Front. Neurosci. 9, 269. doi:10.3389/fnins.2015.00269

Popa, D., Popescu, A.T., Paré, D., 2009. Contrasting activity profile of two distributed cortical networks as a function of attentional demands. J. Neurosci. 29, 1191–1201. doi:10.1523/JNEUROSCI.4867-08.2009

Razoux, F., Baltes, C., Mueggler, T., Seuwen, A., Russig, H., Mansuy, I., Rudin, M., 2013. Functional MRI to assess alterations of functional networks in response to pharmacological or genetic manipulations of the serotonergic system in mice. Neuroimage 74, 326–336. doi:10.1016/j.neuroimage.2013.02.031

Richiardi, J., Altmann, A., Milazzo, A.-C., Chang, C., Chakravarty, M.M., Banaschewski, T., Barker, G.J., Bokde, A.L.W., Bromberg, U., Büchel, C., Conrod, P., Fauth-Bühler, M., Flor, H., Frouin, V., Gallinat, J., Garavan, H., Gowland, P., Heinz, A., Lemaître, H., Mann, K.F., IMAGEN consortium, 2015. BRAIN NETWORKS. Correlated gene expression supports synchronous activity in brain networks. Science 348, 1241–1244. doi:10.1126/science.1255905

Rorden, C., Karnath, H.-O., Bonilha, L., 2007. Improving lesion-symptom mapping. J. Cogn. Neurosci. 19, 1081–1088. doi:10.1162/jocn.2007.19.7.1081

Schroeter, A., Grandjean, J., Schlegel, F., Saab, B.J., Rudin, M., 2017. Contributions of structural connectivity and cerebrovascular parameters to functional magnetic resonance imaging signals in mice at rest and during sensory paw stimulation. J. Cereb. Blood Flow Metab. 37, 2368–2382. doi:10.1177/0271678X16666292

Sethi, S.S., Zerbi, V., Wenderoth, N., Fornito, A., Fulcher, B.D., 2017. Structural connectome topology relates to regional BOLD signal dynamics in the mouse brain. Chaos 27, 047405. doi:10.1063/1.4979281

Sforazzini, F., Bertero, A., Dodero, L., David, G., Galbusera, A., Scattoni, M.L., Pasqualetti, M., Gozzi, A., 2016. Altered functional connectivity networks in acallosal and socially impaired BTBR mice. Brain Struct. Funct. 221, 941–954. doi:10.1007/s00429-014-0948-9

Sforazzini, F., Schwarz, A.J., Galbusera, A., Bifone, A., Gozzi, A., 2014. Distributed BOLD and CBV-weighted resting-state networks in the mouse brain. Neuroimage 87, 403–415. doi:10.1016/j.neuroimage.2013.09.050

Shah, D., Blockx, I., Guns, P.-J., De Deyn, P.P., Van Dam, D., Jonckers, E., Delgado Y

Palacios, R., Verhoye, M., Van der Linden, A., 2015. Acute modulation of the cholinergic system in the mouse brain detected by pharmacological resting-state functional MRI. Neuroimage 109, 151–159. doi:10.1016/j.neuroimage.2015.01.009

Shah, D., Blockx, I., Keliris, G.A., Kara, F., Jonckers, E., Verhoye, M., Van der Linden, A., 2016a. Cholinergic and serotonergic modulations differentially affect large-scale functional networks in the mouse brain. Brain Struct. Funct. 221, 3067–3079. doi:10.1007/s00429-015-1087-7

Shah, D., Deleye, S., Verhoye, M., Staelens, S., Van der Linden, A., 2016b. Resting-state functional MRI and [18F]-FDG PET demonstrate differences in neuronal activity between commonly used mouse strains. Neuroimage 125, 571–577. doi:10.1016/j.neuroimage.2015.10.073

Shah, D., Jonckers, E., Praet, J., Vanhoutte, G., Delgado Y Palacios, R., Bigot, C., D'Souza, D.V., Verhoye, M., Van der Linden, A., 2013. Resting state FMRI reveals diminished functional connectivity in a mouse model of amyloidosis. PLoS ONE 8, e84241. doi:10.1371/journal.pone.0084241

Shah, D., Praet, J., Latif Hernandez, A., Höfling, C., Anckaerts, C., Bard, F., Morawski, M., Detrez, J.R., Prinsen, E., Villa, A., De Vos, W.H., Maggi, A., D'Hooge, R., Balschun, D., Rossner, S., Verhoye, M., Van der Linden, A., 2016c. Early pathologic amyloid induces hypersynchrony of BOLD resting-state networks in transgenic mice and provides an early therapeutic window before amyloid plaque deposition. Alzheimers Dement 12, 964–976. doi:10.1016/j.jalz.2016.03.010

Stafford, J.M., Jarrett, B.R., Miranda-Dominguez, O., Mills, B.D., Cain, N., Mihalas, S., Lahvis, G.P., Lattal, K.M., Mitchell, S.H., David, S.V., Fryer, J.D., Nigg, J.T., Fair, D.A., 2014. Large-scale topology and the default mode network in the mouse connectome. Proc Natl Acad Sci USA 111, 18745–18750. doi:10.1073/pnas.1404346111

Upadhyay, J., Baker, S.J., Chandran, P., Miller, L., Lee, Y., Marek, G.J., Sakoglu, U., Chin, C.-L., Luo, F., Fox, G.B., Day, M., 2011. Default-mode-like network activation in awake rodents. PLoS ONE 6, e27839. doi:10.1371/journal.pone.0027839

Wiesmann, M., Zerbi, V., Jansen, D., Haast, R., Lütjohann, D., Broersen, L.M., Heerschap, A., Kiliaan, A.J., 2016. A Dietary Treatment Improves Cerebral Blood Flow and Brain Connectivity in Aging apoE4 Mice. Neural Plast. 2016, 6846721. doi:10.1155/2016/6846721

Wu, T., Grandjean, J., Bosshard, S.C., Rudin, M., Reutens, D., Jiang, T., 2017. Altered regional connectivity reflecting effects of different anaesthesia protocols in the mouse brain.

Neuroimage 149, 190–199. doi:10.1016/j.neuroimage.2017.01.074

Yoshida, K., Mimura, Y., Ishihara, R., Nishida, H., Komaki, Y., Minakuchi, T., Tsurugizawa, T., Mimura, M., Okano, H., Tanaka, K.F., Takata, N., 2016. Physiological effects of a habituation procedure for functional MRI in awake mice using a cryogenic radiofrequency probe. J. Neurosci. Methods 274, 38–48. doi:10.1016/j.jneumeth.2016.09.013

Zerbi, V., Grandjean, J., Rudin, M., Wenderoth, N., 2015. Mapping the mouse brain with rs-fMRI: An optimized pipeline for functional network identification. Neuroimage 123, 11–21. doi:10.1016/j.neuroimage.2015.07.090

Zerbi, V., Ielacqua, G.D., Markicevic, M., Haberl, M.G., Ellisman, M.H., A-Bhaskaran, A., Frick, A., Rudin, M., Wenderoth, N., 2018. Dysfunctional Autism Risk Genes Cause Circuit-Specific Connectivity Deficits With Distinct Developmental Trajectories. Cereb. Cortex 28, 2495–2506. doi:10.1093/cercor/bhy046

Zerbi, V., Wiesmann, M., Emmerzaal, T.L., Jansen, D., Van Beek, M., Mutsaers, M.P.C., Beckmann, C.F., Heerschap, A., Kiliaan, A.J., 2014. Resting-state functional connectivity changes in aging apoE4 and apoE-KO mice. J. Neurosci. 34, 13963–13975. doi:10.1523/JNEUROSCI.0684-14.2014

Zhan, Y., Paolicelli, R.C., Sforazzini, F., Weinhard, L., Bolasco, G., Pagani, F., Vyssotski, A.L., Bifone, A., Gozzi, A., Ragozzino, D., Gross, C.T., 2014. Deficient neuron-microglia signaling results in impaired functional brain connectivity and social behavior. Nat. Neurosci. 17, 400–406. doi:10.1038/nn.3641

Zuo, X.-N., Xing, X.-X., 2014. Test-retest reliabilities of resting-state FMRI measurements in human brain functional connectomics: a systems neuroscience perspective. Neurosci. Biobehav. Rev. 45, 100–118. doi:10.1016/j.neubiorev.2014.05.009

V. Bibliography

Afifi, A. K. (2003). The basal ganglia: A neural network with more than motor function. *Seminars in Pediatric Neurology, 10*(1), 3-10. doi:10.1016/S1071-9091(02)00003-7

Alakorkko, T., Saarimaki, H., Glerean, E., Saramaki, J., & Korhonen, O. (2017). Effects of spatial smoothing on functional brain networks. *Eur J Neurosci, 46*(9), 2471-2480. doi:10.1111/ejn.13717

Anderson, A., & Cohen, M. S. (2013). Decreased small-world functional network connectivity and clustering across resting state networks in schizophrenia: an fMRI classification tutorial. *Front Hum Neurosci, 7*, 520-520. doi:10.3389/fnhum.2013.00520

Andoh, J., Matsushita, R., & Zatorre, R. J. (2015). Asymmetric Interhemispheric Transfer in the Auditory Network: Evidence from TMS, Resting-State fMRI, and Diffusion Imaging. *The Journal of Neuroscience, 35*(43), 14602-14611. doi:10.1523/jneurosci.2333-15.2015

Andronache, A., Rosazza, C., Sattin, D., Leonardi, M., D'Incerti, L., Minati, L., & Coma Research Centre – Besta, I. (2013). Impact of functional MRI data preprocessing pipeline on default-mode network detectability in patients with disorders of consciousness. *Front Neuroinform, 7*, 16-16. doi:10.3389/fninf.2013.00016

Ash, J. A., Lu, H., Taxier, L. R., Long, J. M., Yang, Y., Stein, E. A., & Rapp, P. R. (2016). Functional connectivity with the retrosplenial cortex predicts cognitive aging in rats. *Proc Natl Acad Sci U S A, 113*(43), 12286-12291. doi:10.1073/pnas.1525309113

Balbastre, Y., Rivière, D., Souedet, N., Fischer, C., Hérard, A.-S., Williams, S., . . . Delzescaux, T. (2017). Primatologist: A modular segmentation pipeline for macaque brain morphometry. *Neuroimage, 162*, 306-321. doi:10.1016/j.neuroimage.2017.09.007

Bandettini, P. A., Wong, E. C., Jesmanowicz, A., Hinks, R. S., & Hyde, J. S. (1994). Spin-echo and gradient-echo epi of human brain activation using bold contrast: A comparative study at 1.5 T. *NMR in Biomedicine, 7*(1-2), 12-20. doi:10.1002/nbm.1940070104

Barks, S. K., Parr, L. A., & Rilling, J. K. (2015). The default mode network in chimpanzees (Pan troglodytes) is similar to that of humans. *Cereb Cortex, 25*(2), 538-544. doi:10.1093/cercor/bht253

Barth, M., & Poser, B. A. (2011). Advances in High-Field BOLD fMRI. *Materials (Basel, Switzerland), 4*(11), 1941-1955. doi:10.3390/ma4111941

Barttfeld, P., Uhrig, L., Sitt, J. D., Sigman, M., Jarraya, B., & Dehaene, S. (2015). Signature of consciousness in the dynamics of resting-state brain activity. *Proc Natl Acad Sci U S A, 112*(3), 887-892. doi:10.1073/pnas.1418031112

Becerra, L., Bishop, J., Barmettler, G., Kainz, V., Burstein, R., & Borsook, D. (2017). Brain network alterations in the inflammatory soup animal model of migraine. *Brain Res, 1660*, 36-46. doi:10.1016/j.brainres.2017.02.001

Becerra, L., Pendse, G., Chang, P. C., Bishop, J., & Borsook, D. (2011). Robust reproducible resting state networks in the awake rodent brain. *PLoS One, 6*(10), e25701. doi:10.1371/journal.pone.0025701

Beckmann, C. F., DeLuca, M., Devlin, J. T., & Smith, S. M. (2005). Investigations into resting-state connectivity using independent component analysis. *Philos Trans R Soc Lond B Biol Sci, 360*(1457), 1001-1013. doi:10.1098/rstb.2005.1634

Beckmann, C. F., DeLuca, M., Devlin, J. T., & Smith, S. M. (2005). Investigations into resting-state connectivity using independent component analysis. *Philos Trans R Soc Lond B Biol Sci, 360*(1457), 1001-1013. doi:10.1098/rstb.2005.1634

Bednark, J. G., Campbell, M. E. J., & Cunnington, R. (2015). Basal ganglia and cortical networks for sequential ordering and rhythm of complex movements. *Front Hum Neurosci, 9*, 421-421. doi:10.3389/fnhum.2015.00421

Belcher, A. M., Yen, C. C., Notardonato, L., Ross, T. J., Volkow, N. D., Yang, Y., . . . Tomasi, D. (2016). Functional Connectivity Hubs and Networks in the Awake Marmoset Brain. *Front Integr Neurosci, 10*, 9. doi:10.3389/fnint.2016.00009

Belcher, A. M., Yen, C. C., Stepp, H., Gu, H., Lu, H., Yang, Y., . . . Stein, E. A. (2013). Large-scale brain networks in the awake, truly resting marmoset monkey. *J Neurosci, 33*(42), 16796-16804. doi:10.1523/JNEUROSCI.3146-13.2013

Beltran, W. A., Vanore, M., Ollivet, F., Nemoz-Bertholet, F., Aujard, F., Clerc, B., & Chahory, S. (2007). Ocular findings in two colonies of gray mouse lemurs (Microcebus murinus). *Vet Ophthalmol, 10*(1), 43-49. doi:10.1111/j.1463-5224.2007.00491.x

Bergmann, E., Zur, G., Bershadsky, G., & Kahn, I. (2016). The Organization of Mouse and Human Cortico-Hippocampal Networks Estimated by Intrinsic Functional Connectivity. *Cereb Cortex, 26*(12), 4497-4512. doi:10.1093/cercor/bhw327

Biswal, B., Hudetz, A. G., Yetkin, F. Z., Haughton, V. M., & Hyde, J. S. (1997). Hypercapnia Reversibly Suppresses Low-Frequency Fluctuations in the Human Motor Cortex during Rest Using Echo–Planar MRI. *Journal of Cerebral Blood Flow & Metabolism, 17*(3), 301-308. doi:10.1097/00004647-199703000-00007

Biswal, B., Yetkin, F. Z., Haughton, V. M., & Hyde, J. S. (1995). Functional connectivity in the motor cortex of resting human brain using echo-planar MRI. *Magn Reson Med, 34*(4), 537-541. doi:10.1002/mrm.1910340409

Biswal, B. B. (2012). Resting state fMRI: A personal history. *Neuroimage, 62*(2), 938-944. doi:10.1016/j.neuroimage.2012.01.090

Biswal, B. B., Kylen, J. V., & Hyde, J. S. (1997). Simultaneous assessment of flow and BOLD signals in resting-state functional connectivity maps. *NMR in Biomedicine, 10*(4-5), 165-170. doi:10.1002/(sici)1099-1492(199706/08)10:4/5<165::aid-nbm454>3.0.co;2-7

Biswal, B. B., Mennes, M., Zuo, X. N., Gohel, S., Kelly, C., Smith, S. M., . . . Milham, M. P. (2010). Toward discovery science of human brain function. *Proc Natl Acad Sci U S A, 107*(10), 4734-4739. doi:10.1073/pnas.0911855107

Blamire, A. M., Ogawa, S., Ugurbil, K., Rothman, D., McCarthy, G., Ellermann, J. M., . . . Shulman, R. G. (1992). Dynamic mapping of the human visual cortex by high-speed magnetic resonance imaging. *Proc Natl Acad Sci U S A, 89*(22), 11069-11073.

Bloch, F. (1946). Nuclear Induction. *Physical Review, 70*(7-8), 460-474. doi:10.1103/PhysRev.70.460

Bonhomme, V., Boveroux, P., Brichant, J. F., Laureys, S., & Boly, M. (2012). Neural correlates of consciousness during general anesthesia using functional magnetic resonance imaging (fMRI). *Arch Ital Biol, 150*(2-3), 155-163. doi:10.4449/aib.v150i2.1242

Boniface, O. J. A. a. S. (2002). How well do we understand the neural origins of the fMRI BOLD signal? *TRENDS in Neurosciences*.

Bons, N., Mestre, N., & Petter, A. (1992). Senile plaques and neurofibrillary changes in the brain of an aged lemurian primate, Microcebus murinus. *Neurobiol Aging, 13*(1), 99-105. doi:10.1016/0197-4580(92)90016-Q

Bons, N., Rieger, F., Prudhomme, D., Fisher, A., & Krause, K. H. (2006). Microcebus murinus: a useful primate model for human cerebral aging and Alzheimer's disease? *Genes Brain Behav, 5*(2), 120-130. doi:10.1111/j.1601-183X.2005.00149.x

Bons, N., Silhol, S., Barbie, V., Mestre-Frances, N., & Albe-Fessard, D. (1998). A stereotaxic atlas of the grey lesser mouse lemur brain (microcebus murinus). *Brain Res Bull, 46*(1-2), 1-173. doi:10.1016/S0361-9230(97)00458-9

Brett, M., Johnsrude, I. S., & Owen, A. M. (2002). The problem of functional localization in the human brain. *Nature Reviews Neuroscience, 3*, 243. doi:10.1038/nrn756

Brodmann, K. (1909). Vergleichende Lokalisationslehre der Grosshirnrinde in ihren Prinzipien dargestellt auf Grund des Zellenbaues.

Brodmann, K. (1999 (original in 1909)). Brodmann's localisation in the cerebral cortex [Vergleichende lokalisationslehre der grosshirnrinde in ihren orinzipien dargestellt auf grund des zellenbaus] (Imperial College Press ed.): Garey, Laurence J.

Buckner, R. L., Bandettini, P. A., O'Craven, K. M., Savoy, R. L., Petersen, S. E., Raichle, M. E., & Rosen, B. R. (1996). Detection of cortical activation during averaged single trials of a cognitive task using functional magnetic resonance imaging. *Proc Natl Acad Sci U S A, 93*(25), 14878-14883.

Buckner, R. L., Snyder, A. Z., Shannon, B. J., LaRossa, G., Sachs, R., Fotenos, A. F., . . . Mintun, M. A. (2005). Molecular, structural, and functional characterization of Alzheimer's disease: evidence for a relationship between default activity, amyloid, and memory. *J Neurosci, 25*(34), 7709-7717. doi:10.1523/JNEUROSCI.2177-05.2005

Bukhari, Q., Schroeter, A., Cole, D. M., & Rudin, M. (2017). Resting State fMRI in Mice Reveals Anesthesia Specific Signatures of Brain Functional Networks and Their Interactions. *Front Neural Circuits, 11*, 5. doi:10.3389/fncir.2017.00005

Bukhari, Q., Schroeter, A., & Rudin, M. (2018). Increasing isoflurane dose reduces homotopic correlation and functional segregation of brain networks in mice as revealed by resting-state fMRI. *Sci Rep, 8*(1), 10591. doi:10.1038/s41598-018-28766-3

Bullmore, E., & Sporns, O. (2009). Complex brain networks: graph theoretical analysis of structural and functional systems. *Nat Rev Neurosci, 10*(3), 186-198. doi:10.1038/nrn2575

Chen, X., Fan, X., Hu, Y., Zuo, C., Whitfield-Gabrieli, S., Holt, D., . . . Ongur, D. (2018). Regional GABA concentrations modulate inter-network resting-state functional connectivity. *Cereb Cortex*. doi:10.1093/cercor/bhy059

Chen, Z., & Calhoun, V. (2018). Effect of Spatial Smoothing on Task fMRI ICA and Functional Connectivity. *Front Neurosci, 12*(15). doi:10.3389/fnins.2018.00015

Chiong, W., Wilson, S. M., D'Esposito, M., Kayser, A. S., Grossman, S. N., Poorzand, P., . . . Rankin, K. P. (2013). The salience network causally influences default mode network activity during moral reasoning. *Brain, 136*(Pt 6), 1929-1941. doi:10.1093/brain/awt066

Ciobanu, L., Reynaud, O., Uhrig, L., Jarraya, B., & Le Bihan, D. (2012). Effects of Anesthetic Agents on Brain Blood Oxygenation Level Revealed with Ultra-High Field MRI. *PLoS One, 7*(3), e32645. doi:10.1371/journal.pone.0032645

Ciric, R., Wolf, D. H., Power, J. D., Roalf, D. R., Baum, G. L., Ruparel, K., . . . Satterthwaite, T. D. (2017). Benchmarking of participant-level confound regression strategies for the control of motion artifact in studies of functional connectivity. *Neuroimage, 154*, 174-187. doi:10.1016/j.neuroimage.2017.03.020

Cleve, M., Gussew, A., Wagner, G., Bar, K. J., & Reichenbach, J. R. (2017). Assessment of intra- and inter-regional interrelations between GABA+, Glx and BOLD during pain perception in the human brain - A combined (1)H fMRS and fMRI study. *Neuroscience, 365*, 125-136. doi:10.1016/j.neuroscience.2017.09.037

Cohen, M. S., & Weisskoff, R. M. (1991). Ultra-fast imaging. *Magn Reson Imaging, 9*(1), 1-37. doi:10.1016/0730-725X(91)90094-3

Cox, R. W. (1996). AFNI: software for analysis and visualization of functional magnetic resonance neuroimages. *Comput Biomed Res, 29*(3), 162-173. doi:10.1006/cbmr.1996.0014

D'Souza, D. V., Jonckers, E., Bruns, A., Künnecke, B., von Kienlin, M., Van der Linden, A., . . . Verhoye, M. (2014). Preserved modular network organization in the sedated rat brain. *PLoS One, 9*(9), e106156. doi:10.1371/journal.pone.0106156

Damoiseaux, J. S., & Greicius, M. D. (2009). Greater than the sum of its parts: a review of studies combining structural connectivity and resting-state functional connectivity. *Brain Structure and Function, 213*(6), 525-533. doi:10.1007/s00429-009-0208-6

Damoiseaux, J. S., Rombouts, S. A., Barkhof, F., Scheltens, P., Stam, C. J., Smith, S. M., & Beckmann, C. F. (2006). Consistent resting-state networks across healthy subjects. *Proc Natl Acad Sci U S A, 103*(37), 13848-13853. doi:10.1073/pnas.0601417103

Davey, C. E., Grayden, D. B., Egan, G. F., & Johnston, L. A. (2013). Filtering induces correlation in fMRI resting state data. *Neuroimage, 64*, 728-740. doi:10.1016/j.neuroimage.2012.08.022

Davey, C. G., & Harrison, B. J. (2018). The brain's center of gravity: how the default mode network helps us to understand the self. *World Psychiatry, 17*(3), 278-279. doi:10.1002/wps.20553

Davey, C. G., Pujol, J., & Harrison, B. J. (2016). Mapping the self in the brain's default mode network. *Neuroimage, 132*, 390-397. doi:10.1016/j.neuroimage.2016.02.022

DeSimone, J. C., Pappas, S. S., Febo, M., Burciu, R. G., Shukla, P., Colon-Perez, L. M., . . . Vaillancourt, D. E. (2017). Forebrain knock-out of torsinA reduces striatal free-water and impairs whole-brain functional connectivity in a symptomatic mouse model of DYT1 dystonia. *Neurobiol Dis, 106*, 124-132. doi:10.1016/j.nbd.2017.06.015

Dhenain, M., Michot, J. L., Privat, N., Picq, J. L., Boller, F., Duyckaerts, C., & Volk, A. (2000). MRI description of cerebral atrophy in mouse lemur primates. *Neurobiol Aging, 21*(1), 81-88. doi:10.1016/S0197-4580(00)00098-1

Doll, A., Holzel, B. K., Boucard, C. C., Wohlschlager, A. M., & Sorg, C. (2015). Mindfulness is associated with intrinsic functional connectivity between default mode and salience networks. *Front Hum Neurosci, 9*, 461. doi:10.3389/fnhum.2015.00461

Dorr, A. E., Lerch, J. P., Spring, S., Kabani, N., & Henkelman, R. M. (2008). High resolution three-dimensional brain atlas using an average magnetic resonance image of 40 adult C57Bl/6J mice. *Neuroimage, 42*(1), 60-69. doi:10.1016/j.neuroimage.2008.03.037

Ezran, C., Karanewsky, C. J., Pendleton, J. L., Sholtz, A., Krasnow, M. R., Willick, J., . . . Krasnow, M. A. (2017). The Mouse Lemur, a Genetic Model Organism for Primate Biology, Behavior, and Health. *Genetics, 206*(2), 651-664. doi:10.1534/genetics.116.199448

Fan, L., Chu, C., Li, H., Chen, L., Xie, S., Zhang, Y., . . . Eickhoff, S. B. (2016). The Human Brainnetome Atlas: A New Brain Atlas Based on Connectional Architecture. *Cereb Cortex, 26*(8), 3508-3526. doi:10.1093/cercor/bhw157

Ferrari, L., Turrini, G., Crestan, V., Bertani, S., Cristofori, P., Bifone, A., & Gozzi, A. (2012). A robust experimental protocol for pharmacological fMRI in rats and mice. *J Neurosci Methods, 204*(1), 9-18. doi:10.1016/j.jneumeth.2011.10.020

Fox, M. D., & Raichle, M. E. (2007). Spontaneous fluctuations in brain activity observed with functional magnetic resonance imaging. *Nat Rev Neurosci, 8*(9), 700-711. doi:10.1038/nrn2201

Francx, W., Oldehinkel, M., Oosterlaan, J., Heslenfeld, D., Hartman, C. A., Hoekstra, P. J., . . . Mennes, M. (2015). The executive control network and symptomatic improvement in attention-deficit/hyperactivity disorder. *Cortex, 73*, 62-72. doi:10.1016/j.cortex.2015.08.012

Franks, N. P. (2008). General anaesthesia: from molecular targets to neuronal pathways of sleep and arousal. *Nature Reviews Neuroscience, 9*, 370. doi:10.1038/nrn2372

Friston, K. J., Ashburner, J., Kiebel, S. J., Nichols, T. E., & Penny, W. D. (2007). *Statistical parametric mapping: the analysis of functional brain images*: Academic Press.

Friston, K. J., Holmes, A. P., Worsley, K. J., Poline, J. P., Frith, C. D., & Frackowiak, R. S. J. (1994). Statistical parametric maps in functional imaging: a general linear approach. *Hum. Brain Mapp., 2(4):189 - 210*. doi:10.1002/hbm.460020402

Gao, L. L., & Wu, T. (2016). The study of brain functional connectivity in Parkinson's disease. *Transl Neurodegener, 5*, 18. doi:10.1186/s40035-016-0066-0

Garcia, P. S., Kolesky, S. E., & Jenkins, A. (2010). General anesthetic actions on GABA(A) receptors. *Current neuropharmacology, 8*(1), 2-9. doi:10.2174/157015910790909502

Garrett, K. M., & Gan, J. (1998). Enhancement of γ-Aminobutyric Acid<sub>A</sub> Receptor Activity by α-Chloralose. *Journal of Pharmacology and Experimental Therapeutics, 285*(2), 680.

Gary, C., Koch, J., Petit, F., Hanss, Z., Palash, A. R., Eddarkaoui, S., . . . Dhenain, M. (2016). First demonstration of functional and morphological alterations in primates after alzheimer brain homogenates inoculation *Alzheimer's & Dementia: The Journal of the Alzheimer's Association, 12*(7), P360-P361. doi:10.1016/j.jalz.2016.06.668

Gary, C., Pifferi, F., Koch, J., Petit, F., Comoy, E., Picq, J.-L., & Dhenain, M. (2015). *Experimental transmissibility of Alzheimer pathology in a non-human primate*. Paper presented at the 12th International conference on Alzheimer's and Parkinson's diseases and related neurological disorders, Nice, France.

Gass, N., Weber-Fahr, W., Sartorius, A., Becker, R., Didriksen, M., Stensbol, T. B., . . . Schwarz, A. J. (2016). An acetylcholine alpha7 positive allosteric modulator rescues a schizophrenia-associated brain endophenotype in the 15q13.3 microdeletion, encompassing CHRNA7. *Eur Neuropsychopharmacol, 26*(7), 1150-1160. doi:10.1016/j.euroneuro.2016.03.013

Ghahremani, M., Menon, R. S., Everling, S., & Hutchison, R. M. (2016). Frontoparietal functional connectivity in the common marmoset. *Cereb Cortex, 27*(8), 3890-3905. doi:10.1093/cercor/bhw198

Giannakopoulos, P., Silhol, S., Arnal, V., Mallet, J., Bons, N., Bouras, C., & Delaère, P. (1997). *Quantitative analysis of tau protein-immunoreactive accumulations and ?? amyloid protein deposits in the cerebral cortex of the mouse lemur, Microcebus murinus* (Vol. 94).

Gore, J. C. (2003). Principles and practice of functional MRI of the human brain. *J Clin Invest, 112*(1), 4-9. doi:10.1172/JCI19010

Gozzi, A., & Schwarz, A. J. (2016). Large-scale functional connectivity networks in the rodent brain. *Neuroimage, 127*, 496-509. doi:10.1016/j.neuroimage.2015.12.017

Grandjean, J., Canella, C., Anckaerts, C., Ayrancı, G., Bougacha, S., Bienert, T., . . . Gozzi, A. (2019). Common functional networks in the mouse brain revealed by multi-centre resting-state fMRI analysis. *bioRxiv*, 541060. doi:10.1101/541060

Grandjean, J., Derungs, R., Kulic, L., Welt, T., Henkelman, M., Nitsch, R. M., & Rudin, M. (2016). Complex interplay between brain function and structure during cerebral amyloidosis in APP transgenic mouse strains revealed by multi-parametric MRI comparison. *Neuroimage, 134*, 1-11. doi:10.1016/j.neuroimage.2016.03.042

Grandjean, J., Preti, M. G., Bolton, T. A. W., Buerge, M., Seifritz, E., Pryce, C. R., . . . Rudin, M. (2017). Dynamic reorganization of intrinsic functional networks in the mouse brain. *Neuroimage, 152*, 497-508. doi:10.1016/j.neuroimage.2017.03.026

Grandjean, J., Schroeter, A., Batata, I., & Rudin, M. (2014). Optimization of anesthesia protocol for resting-state fMRI in mice based on differential effects of anesthetics on functional connectivity patterns. *Neuroimage, 102 Pt 2*, 838-847. doi:10.1016/j.neuroimage.2014.08.043

Grandjean, J., Schroeter, A., He, P., Tanadini, M., Keist, R., Krstic, D., . . . Rudin, M. (2014). Early alterations in functional connectivity and white matter structure in a transgenic mouse model of cerebral amyloidosis. *J Neurosci, 34*(41), 13780-13789. doi:10.1523/JNEUROSCI.4762-13.2014

Grandjean, J., Zerbi, V., Balsters, J. H., Wenderoth, N., & Rudin, M. (2017). Structural basis of large-scale functional connectivity in the mouse. *J Neurosci, 37*(34), 8092-8101. doi:10.1523/JNEUROSCI.0438-17.2017

Grayson, D. S., Bliss-Moreau, E., Machado, C. J., Bennett, J., Shen, K., Grant, K. A., . . . Amaral, D. G. (2016). The rhesus monkey connectome predicts disrupted functional networks resulting from pharmacogenetic inactivation of the amygdala. *Neuron, 91*(2), 453-466. doi:10.1016/j.neuron.2016.06.005

Greicius, M. D., Krasnow, B., Reiss, A. L., & Menon, V. (2003). Functional connectivity in the resting brain: a network analysis of the default mode hypothesis. *Proc Natl Acad Sci U S A, 100*(1), 253-258. doi:10.1073/pnas.0135058100

Grodd, W., Hülsmann, E., Lotze, M., Wildgruber, D., & Erb, M. (2001). *Sensorimotor mapping of the human Cerebellum: fMRI evidence of somatotopic organization* (Vol. 13).

Grover, V. P. B., Tognarelli, J. M., Crossey, M. M. E., Cox, I. J., Taylor-Robinson, S. D., & McPhail, M. J. W. (2015). Magnetic Resonance Imaging: Principles and Techniques: Lessons for Clinicians. *Journal of clinical and experimental hepatology, 5*(3), 246-255. doi:10.1016/j.jceh.2015.08.001

Guye, M., Bartolomei, F., & Ranjeva, J. P. (2008). Imaging structural and functional connectivity: towards a unified definition of human brain organization? *Curr Opin Neurol, 21*(4), 393-403. doi:10.1097/WCO.0b013e3283065cfb

Hagberg, A. A., Schult, D. A., & Swart, P. J. (2008). *Exploring network structure, dynamics, and function using NetworkX*. Paper presented at the Proceedings of the 7th Python in Science Conference, Pasadena, CA.

Hampson, M., Driesen, N. R., Skudlarski, P., Gore, J. C., & Constable, R. T. (2006). Brain connectivity related to working memory performance. *J Neurosci, 26*(51), 13338-13343. doi:10.1523/JNEUROSCI.3408-06.2006

Hayden, B. Y., Smith, D. V., & Platt, M. L. (2009). Electrophysiological correlates of default-mode processing in macaque posterior cingulate cortex. *Proc Natl Acad Sci U S A, 106*(14), 5948-5953. doi:10.1073/pnas.0812035106

Henckens, M. J., van der Marel, K., van der Toorn, A., Pillai, A. G., Fernandez, G., Dijkhuizen, R. M., & Joels, M. (2015). Stress-induced alterations in large-scale functional networks of the rodent brain. *Neuroimage, 105*, 312-322. doi:10.1016/j.neuroimage.2014.10.037

Hinke, R. M., Hu, X. T., Stillman, A. E., Kim, S., Merkle, H., Salmi, R., & Ugurbil, K. (1993). Functional magnetic resonance imaging of Broca's area during internal speech. *Neuroreport, 4*(6), 675-678.

Hong, K.-S., & Zafar, A. (2018). Existence of Initial Dip for BCI: An Illusion or Reality. *Frontiers in Neurorobotics, 12*(69). doi:10.3389/fnbot.2018.00069

Hong, X., To, X. V., Teh, I., Soh, J. R., & Chuang, K.-H. (2015). Evaluation of EPI distortion correction methods for quantitative MRI of the brain at high magnetic field. *Magn Reson Imaging, 33*(9), 1098-1105. doi:10.1016/j.mri.2015.06.010

Hopfinger, J., H Buonocore, M., & Mangun, G. (2000). *Hopfinger JB, Buonocore MH, Mangun GR. The neural mechanisms of top-down attentional control. Nat Neurosci 3: 284-291* (Vol. 3).

Hsu, L. M., Liang, X., Gu, H., Brynildsen, J. K., Stark, J. A., Ash, J. A., . . . Yang, Y. (2016). Constituents and functional implications of the rat default mode network. *Proc Natl Acad Sci U S A, 113*(31), E4541-4547. doi:10.1073/pnas.1601485113

Hu, Y., Chen, X., Gu, H., & Yang, Y. (2013). Resting-state glutamate and GABA concentrations predict task-induced deactivation in the default mode network. *J Neurosci, 33*(47), 18566-18573. doi:10.1523/JNEUROSCI.1973-13.2013

Huang, S. M., Wu, Y. L., Peng, S. L., Peng, H. H., Huang, T. Y., Ho, K. C., & Wang, F. N. (2016). Inter-Strain Differences in Default Mode Network: A Resting State fMRI Study on Spontaneously Hypertensive Rat and Wistar Kyoto Rat. *Sci Rep, 6*, 21697. doi:10.1038/srep21697

Hubner, N. S., Mechling, A. E., Lee, H. L., Reisert, M., Bienert, T., Hennig, J., . . . Harsan, L. A. (2017). The connectomics of brain demyelination: Functional and structural patterns in the cuprizone mouse model. *Neuroimage, 146*, 1-18. doi:10.1016/j.neuroimage.2016.11.008

Hudetz, A. G. (2012). General anesthesia and human brain connectivity. *Brain Connect, 2*(6), 291-302. doi:10.1089/brain.2012.0107

Huo, L., Li, R., Wang, P., Zheng, Z., & Li, J. (2018). The Default Mode Network Supports Episodic Memory in Cognitively Unimpaired Elderly Individuals: Different Contributions to Immediate Recall and Delayed Recall. *Front Aging Neurosci, 10*, 6-6. doi:10.3389/fnagi.2018.00006

Hutchison, R. M., Culham, J. C., Flanagan, J. R., Everling, S., & Gallivan, J. P. (2015). Functional subdivisions of medial parieto-occipital cortex in humans and nonhuman primates using resting-state fMRI. *Neuroimage, 116*, 10-29. doi:10.1016/j.neuroimage.2015.04.068

Hutchison, R. M., & Everling, S. (2012). Monkey in the middle: why non-human primates are needed to bridge the gap in resting-state investigations. *Front Neuroanat, 6*, 29. doi:10.3389/fnana.2012.00029

Hutchison, R. M., Gallivan, J. P., Culham, J. C., Gati, J. S., Menon, R. S., & Everling, S. (2012). Functional connectivity of the frontal eye fields in humans and macaque monkeys investigated with resting-state fMRI. *J Neurophysiol, 107*(9), 2463-2474. doi:10.1152/jn.00891.2011

Hutchison, R. M., Hutchison, M., Manning, K. Y., Menon, R. S., & Everling, S. (2014). Isoflurane induces dose-dependent alterations in the cortical connectivity profiles and dynamic properties of the brain's functional architecture. *Hum Brain Mapp, 35*(12), 5754-5775. doi:10.1002/hbm.22583

Hutchison, R. M., Leung, L. S., Mirsattari, S. M., Gati, J. S., Menon, R. S., & Everling, S. (2011). Resting-state networks in the macaque at 7 T. *Neuroimage, 56*(3), 1546-1555. doi:10.1016/j.neuroimage.2011.02.063

Hutchison, R. M., Mirsattari, S. M., Jones, C. K., Gati, J. S., & Leung, L. S. (2010). Functional networks in the anesthetized rat brain revealed by independent component analysis of resting-state FMRI. *J Neurophysiol, 103*(6), 3398-3406. doi:10.1152/jn.00141.2010

Hutchison, R. M., Womelsdorf, T., Gati, J. S., Everling, S., & Menon, R. S. (2013). Resting-state networks show dynamic functional connectivity in awake humans and anesthetized macaques. *Hum Brain Mapp, 34*(9), 2154-2177. doi:10.1002/hbm.22058

Hutchison, R. M., Womelsdorf, T., Gati, J. S., Leung, L. S., Menon, R. S., & Everling, S. (2012). Resting-state connectivity identifies distinct functional networks in macaque cingulate cortex. *Cereb Cortex, 22*(6), 1294-1308. doi:10.1093/cercor/bhr181

Ioanas, H.-I., Marks, M., Yanik, M. F., & Rudin, M. (2019). An Optimized Registration Workflow and Standard Geometric Space for Small Animal Brain Imaging. *bioRxiv*, 619650. doi:10.1101/619650

Ip, I. B., Berrington, A., Hess, A. T., Parker, A. J., Emir, U. E., & Bridge, H. (2017). Combined fMRI-MRS acquires simultaneous glutamate and BOLD-fMRI signals in the human brain. *Neuroimage, 155*, 113-119. doi:10.1016/j.neuroimage.2017.04.030

Jann, K., Dierks, T., Boesch, C., Kottlow, M., Strik, W., & Koenig, T. (2009). BOLD correlates of EEG alpha phase-locking and the fMRI default mode network. *Neuroimage, 45*(3), 903-916. doi:10.1016/j.neuroimage.2009.01.001

Jenkinson, M., Beckmann, C. F., Behrens, T. E. J., Woolrich, M. W., & Smith, S. M. (2012). FSL. *Neuroimage, 62*(2), 782-790. doi:10.1016/j.neuroimage.2011.09.015

Jo, H. J., Saad, Z. S., Simmons, W. K., Milbury, L. A., & Cox, R. W. (2010). Mapping sources of correlation in resting state FMRI, with artifact detection and removal. *Neuroimage, 52*(2), 571-582. doi:10.1016/j.neuroimage.2010.04.246

Jonckers, E., Delgado y Palacios, R., Shah, D., Guglielmetti, C., Verhoye, M., & Van der Linden, A. (2014). Different anesthesia regimes modulate the functional connectivity outcome in mice. *Magn Reson Med, 72*(4), 1103-1112. doi:10.1002/mrm.24990

Jonckers, E., Van Audekerke, J., De Visscher, G., Van der Linden, A., & Verhoye, M. (2011). Functional connectivity fMRI of the rodent brain: comparison of functional connectivity networks in rat and mouse. *PLoS One, 6*(4), e18876. doi:10.1371/journal.pone.0018876

Just, N., Xin, L., Frenkel, H., & Gruetter, R. (2013). Characterization of sustained BOLD activation in the rat barrel cortex and neurochemical consequences. *Neuroimage, 74*, 343-351. doi:10.1016/j.neuroimage.2013.02.042

Kagan, I., Iyer, A., Lindner, A., & Andersen, R. A. (2010). Space representation for eye movements is more contralateral in monkeys than in humans. *Proceedings of the National Academy of Sciences, 107*(17), 7933-7938. doi:10.1073/pnas.1002825107

Kalthoff, D., Seehafer, J. U., Po, C., Wiedermann, D., & Hoehn, M. (2011). Functional connectivity in the rat at 11.7T: Impact of physiological noise in resting state fMRI. *Neuroimage, 54*(4), 2828-2839. doi:10.1016/j.neuroimage.2010.10.053

Kapogiannis, D., Reiter, D. A., Willette, A. A., & Mattson, M. P. (2013). Posteromedial cortex glutamate and GABA predict intrinsic functional connectivity of the default mode network. *Neuroimage, 64*, 112-119. doi:10.1016/j.neuroimage.2012.09.029

Kobbe, S., Nowack, J., & Dausmann, K. H. (2014). Torpor is not the only option: seasonal variations of the thermoneutral zone in a small primate. *J Comp Physiol B, 184*(6), 789-797. doi:10.1007/s00360-014-0834-z

Kojima, T., Onoe, H., Hikosaka, K., Tsutsui, K., Tsukada, H., & Watanabe, M. (2009). Default mode of brain activity demonstrated by positron emission tomography imaging in awake monkeys: higher rest-related than working memory-related activity in medial cortical areas. *J Neurosci, 29*(46), 14463-14471. doi:10.1523/JNEUROSCI.1786-09.2009

Kraska, A., Dorieux, O., Picq, J. L., Petit, F., Bourrin, E., Chenu, E., . . . Dhenain, M. (2011). Age-associated cerebral atrophy in mouse lemur primates. *Neurobiol Aging, 32*(5), 894-906. doi:10.1016/j.neurobiolaging.2009.05.018

Kundu, P., Santin, M. D., Bandettini, P. A., Bullmore, E. T., & Petiet, A. (2014). Differentiating BOLD and non-BOLD signals in fMRI time series from anesthetized rats using multi-echo EPI at 11.7 T. *Neuroimage, 102 Pt 2*, 861-874. doi:10.1016/j.neuroimage.2014.07.025

Kyathanahally, S. P., Jia, H., Pustovyy, O. M., Waggoner, P., Beyers, R., Schumacher, J., . . . Deshpande, G. (2015). Anterior-posterior dissociation of the default mode network in dogs. *Brain Struct Funct, 220*(2), 1063-1076. doi:10.1007/s00429-013-0700-x

Långsjö, Jaakko W. M. D., Kaisti, Kaike K. M. D., Aalto, S. M. S., Hinkka, S. P. L., Aantaa, R. M. D., Oikonen, V. M. S., . . . Scheinin, H. M. D. (2003). Effects of Subanesthetic Doses of Ketamine on Regional Cerebral Blood Flow, Oxygen Consumption, and Blood Volume in Humans. *Anesthesiology: The Journal of the American Society of Anesthesiologists, 99*(3), 614-623.

Languille, S., Blanc, S., Blin, O., Canale, C. I., Dal-Pan, A., Devau, G., . . . Aujard, F. (2012). The grey mouse lemur: a non-human primate model for ageing studies. *Ageing Res Rev, 11*(1), 150-162. doi:10.1016/j.arr.2011.07.001

Latif-Hernandez, A., Shah, D., Ahmed, T., Lo, A. C., Callaerts-Vegh, Z., Van der Linden, A., . . . D'Hooge, R. (2016). Quinolinic acid injection in mouse medial prefrontal cortex

affects reversal learning abilities, cortical connectivity and hippocampal synaptic plasticity. *Sci Rep, 6*, 36489. doi:10.1038/srep36489

Le Gros Clark, W. (1931). The brain of microcebus murinus. *Proc Zool Soc London*. doi:1931;101(2):463-86

Lebenberg, J., Hérard, A. S., Dubois, A., Dhenain, M., Hantraye, P., & Delzescaux, T. (2011). A combination of atlas-based and voxel-wise approaches to analyze metabolic changes in autoradiographic data from Alzheimer's mice. *Neuroimage, 57*(4), 1447-1457. doi:10.1016/j.neuroimage.2011.04.059

Lenz, C., Rebel, A., van Ackern, K., Kuschinsky, W., & Waschke, K. F. (1998). Local cerebral blood flow, local cerebral glucose utilization, and flow-metabolism coupling during sevoflurane versus isoflurane anesthesia in rats. *Anesthesiology, 89*(6), 1480-1488.

Li, C., Li, Z., Ward, B. D., Dwinell, M. R., Lombard, J. H., Hudetz, A. G., & Pawela, C. P. (2014). Enhancement of resting-state fcMRI networks by prior sensory stimulation. *Brain Connect, 4*(9), 760-768. doi:10.1089/brain.2014.0326

Li, C. X., & Zhang, X. (2018). Evaluation of prolonged administration of isoflurane on cerebral blood flow and default mode network in macaque monkeys anesthetized with different maintenance doses. *Neurosci Lett, 662*, 402-408. doi:10.1016/j.neulet.2017.10.034

Li, Q., Li, G., Wu, D., Lu, H., Hou, Z., Ross, C. A., . . . Duan, W. (2017). Resting-state functional MRI reveals altered brain connectivity and its correlation with motor dysfunction in a mouse model of Huntington's disease. *Sci Rep, 7*(1), 16742. doi:10.1038/s41598-017-17026-5

Liang, Z., King, J., & Zhang, N. (2011). Uncovering intrinsic connectional architecture of functional networks in awake rat brain. *J Neurosci, 31*(10), 3776-3783. doi:10.1523/JNEUROSCI.4557-10.2011

Liang, Z., King, J., & Zhang, N. (2014). Neuroplasticity to a single-episode traumatic stress revealed by resting-state fMRI in awake rats. *Neuroimage, 103*, 485-491. doi:10.1016/j.neuroimage.2014.08.050

Liska, A., Galbusera, A., Schwarz, A. J., & Gozzi, A. (2015). Functional connectivity hubs of the mouse brain. *Neuroimage, 115*, 281-291. doi:10.1016/j.neuroimage.2015.04.033

Liu, P., Calhoun, V., & Chen, Z. (2017). Functional overestimation due to spatial smoothing of fMRI data. *J Neurosci Methods, 291*, 1-12. doi:10.1016/j.jneumeth.2017.08.003

Logothetis, N. K. (2003). The Underpinnings of the BOLD Functional Magnetic Resonance Imaging Signal. *The Journal of Neuroscience, 23*(10), 3963. doi:10.1523/JNEUROSCI.23-10-03963.2003

Logothetis, N. K., Pauls, J., Augath, M., Trinath, T., & Oeltermann, A. (2001). Neurophysiological investigation of the basis of the fMRI signal. *Nature, 412*, 150. doi:10.1038/35084005

Lohmann, G., Margulies, D. S., Horstmann, A., Pleger, B., Lepsien, J., Goldhahn, D., . . . Turner, R. (2010). Eigenvector centrality mapping for analyzing connectivity patterns in fMRI data of the human brain. *PLoS One, 5*(4), e10232. doi:10.1371/journal.pone.0010232

Lu, H., Zou, Q., Gu, H., Raichle, M. E., Stein, E. A., & Yang, Y. (2012). Rat brains also have a default mode network. *Proc Natl Acad Sci U S A, 109*(10), 3979-3984. doi:10.1073/pnas.1200506109

Lydon-Staley, D. M., Ciric, R., Satterthwaite, T. D., & Bassett, D. S. (2019). Evaluation of confound regression strategies for the mitigation of micromovement artifact in studies of dynamic resting-state functional connectivity and multilayer network modularity. *Netw Neurosci, 3*(2), 427-454. doi:10.1162/netn_a_00071

Ma, Y., Hof, P. R., Grant, S. C., Blackband, S. J., Bennett, R., Slatest, L., . . . Benveniste, H. (2005). A three-dimensional digital atlas database of the adult C57BL/6J mouse brain by magnetic resonance microscopy. *Neuroscience, 135*(4), 1203-1215. doi:10.1016/j.neuroscience.2005.07.014

Magri, C., Schridde, U., Murayama, Y., Panzeri, S., & Logothetis, N. K. (2012). The Amplitude and Timing of the BOLD Signal Reflects the Relationship between Local Field Potential Power at Different Frequencies. *The Journal of Neuroscience, 32*(4), 1395. doi:10.1523/JNEUROSCI.3985-11.2012

Mangia, S., Tkac, I., Gruetter, R., Van de Moortele, P. F., Maraviglia, B., & Ugurbil, K. (2007). Sustained neuronal activation raises oxidative metabolism to a new steady-state level: evidence from 1H NMR spectroscopy in the human visual cortex. *J Cereb Blood Flow Metab, 27*(5), 1055-1063. doi:10.1038/sj.jcbfm.9600401

Mantini, D., Corbetta, M., Romani, G. L., Orban, G. A., & Vanduffel, W. (2013). Evolutionarily Novel Functional Networks in the Human Brain? *The Journal of Neuroscience, 33*(8), 3259-3275. doi:10.1523/jneurosci.4392-12.2013

Mantini, D., Gerits, A., Nelissen, K., Durand, J. B., Joly, O., Simone, L., . . . Vanduffel, W. (2011). Default mode of brain function in monkeys. *J Neurosci, 31*(36), 12954-12962. doi:10.1523/JNEUROSCI.2318-11.2011

Mantini, D., Perrucci, M. G., Del Gratta, C., Romani, G. L., & Corbetta, M. (2007). Electrophysiological signatures of resting state networks in the human brain. *Proc Natl Acad Sci U S A, 104*(32), 13170-13175. doi:10.1073/pnas.0700668104

Margulies, D. S., Vincent, J. L., Kelly, C., Lohmann, G., Uddin, L. Q., Biswal, B. B., . . . Petrides, M. (2009). Precuneus shares intrinsic functional architecture in humans and monkeys. *Proc Natl Acad Sci U S A, 106*(47), 20069-20074. doi:10.1073/pnas.0905314106

Mather, M., Cacioppo, J. T., & Kanwisher, N. (2013). How fMRI Can Inform Cognitive Theories. *Perspect Psychol Sci, 8*(1), 108-113. doi:10.1177/1745691612469037

Matsui, T., Murakami, T., & Ohki, K. (2016). Transient neuronal coactivations embedded in globally propagating waves underlie resting-state functional connectivity. *Proceedings of the National Academy of Sciences, 113*(23), 6556. doi:10.1073/pnas.1521299113

Mazoyer, B., Zago, L., Mellet, E., Bricogne, S., Etard, O., Houdé, O., . . . Tzourio-Mazoyer, N. (2001). Cortical networks for working memory and executive functions sustain the conscious resting state in man. *Brain Res Bull, 54*(3), 287-298. doi:10.1016/S0361-9230(00)00437-8

Mazziotta, J. C., Toga, A., Evans, A. C., Fox, P., & Lancaster, J. (1997). *Brain maps: Linking the present to the future.* (R. S. J. F. (Ed.) Ed.). San Diego: Human brain function: Academic Press.

Mechling, A. E., Arefin, T., Lee, H. L., Bienert, T., Reisert, M., Ben Hamida, S., . . . Harsan, L. A. (2016). Deletion of the mu opioid receptor gene in mice reshapes the reward-aversion connectome. *Proc Natl Acad Sci U S A, 113*(41), 11603-11608. doi:10.1073/pnas.1601640113

Mechling, A. E., Hubner, N. S., Lee, H. L., Hennig, J., von Elverfeldt, D., & Harsan, L. A. (2014). Fine-grained mapping of mouse brain functional connectivity with resting-state fMRI. *Neuroimage, 96*, 203-215. doi:10.1016/j.neuroimage.2014.03.078

Menon, V., & Uddin, L. Q. (2010). Saliency, switching, attention and control: a network model of insula function. *Brain Struct Funct, 214*(5-6), 655-667. doi:10.1007/s00429-010-0262-0

Mestre-Frances, N., Serratrice, N., Gennetier, A., Devau, G., Cobo, S., Trouche, S. G., . . . Kremer, E. J. (2018). Exogenous LRRK2G2019S induces parkinsonian-like pathology in a nonhuman primate. *JCI Insight, 3*(14). doi:10.1172/jci.insight.98202

Mestre-Francés, N., Trouche, S., Fontes, P., Lautier, C., Devau, G., Lasbleiz, C., . . . Verdier, J.-M. (2018). Old Gray Mouse Lemur Behavior, Cognition, and Neuropathology. In L. R. Jeffrey & P. M. Conn (Eds.), *Conn's Handbook of Models for Human Aging (Second Edition)* (pp. 287-300): Elsevier.

Miranda-Dominguez, O., Mills, B. D., Grayson, D., Woodall, A., Grant, K. A., Kroenke, C. D., & Fair, D. A. (2014). Bridging the gap between the human and macaque connectome: a quantitative comparison of global interspecies structure-function relationships and network topology. *J Neurosci, 34*(16), 5552-5563. doi:10.1523/JNEUROSCI.4229-13.2014

Mitra, A., Kraft, A., Wright, P., Acland, B., Snyder, A. Z., Rosenthal, Z., . . . Raichle, M. E. (2018). Spontaneous Infra-slow Brain Activity Has Unique Spatiotemporal Dynamics and Laminar Structure. *Neuron, 98*(2), 297-305 e296. doi:10.1016/j.neuron.2018.03.015

Mittermeier, R. A., Ganzhorn, J. U., Konstant, W. R., Glander, K., Tattersall, I., Groves, C. P., . . . Rasoloarison, R. M. (2008). Lemur Diversity in Madagascar. *International Journal of Primatology, 29*(6), 1607-1656. doi:10.1007/s10764-008-9317-y

Montgomery, S. H., Capellini, I., Barton, R. A., & Mundy, N. I. (2010). Reconstructing the ups and downs of primate brain evolution: implications for adaptive hypotheses and Homo floresiensis. *BMC Biol, 8*, 9. doi:10.1186/1741-7007-8-9

Moraschi, M., DiNuzzo, M., & Giove, F. (2012). On the origin of sustained negative BOLD response. *J Neurophysiol, 108*(9), 2339-2342. doi:10.1152/jn.01199.2011

Moussa, M. N., Steen, M. R., Laurienti, P. J., & Hayasaka, S. (2012). Consistency of network modules in resting-state FMRI connectome data. *PLoS One, 7*(8), e44428. doi:10.1371/journal.pone.0044428

Mulert, C., Leicht, G., Hepp, P., Kirsch, V., Karch, S., Pogarell, O., . . . McCarley, R. W. (2010). Single-trial coupling of the gamma-band response and the corresponding BOLD signal. *Neuroimage, 49*(3), 2238-2247. doi:10.1016/j.neuroimage.2009.10.058

Murakami, T., Matsui, T., & Ohki, K. (2018). Neuronal Origin of the Temporal Dynamics of Spontaneous BOLD Activity Correlation. doi:10.1093/cercor/bhy045

Murphy, K., Birn, R. M., & Bandettini, P. A. (2013). Resting-state fMRI confounds and cleanup. *Neuroimage, 80*, 349-359. doi:10.1016/j.neuroimage.2013.04.001

Murphy, K., & Fox, M. D. (2017). Towards a consensus regarding global signal regression for resting state functional connectivity MRI. *Neuroimage, 154*, 169-173. doi:10.1016/j.neuroimage.2016.11.052

Murta, T., Leite, M., Carmichael, D. W., Figueiredo, P., & Lemieux, L. (2015). Electrophysiological correlates of the BOLD signal for EEG-informed fMRI. *Hum Brain Mapp, 36*(1), 391-414. doi:10.1002/hbm.22623

Muschelli, J., Nebel, M. B., Caffo, B. S., Barber, A. D., Pekar, J. J., & Mostofsky, S. H. (2014). Reduction of motion-related artifacts in resting state fMRI using aCompCor. *Neuroimage, 96*, 22-35. doi:10.1016/j.neuroimage.2014.03.028

Nachev, P., & Husain, M. (2006). Disorders of Visual Attention and the Posterior Parietal Cortex. *Cortex, 42*(5), 766-773. doi:10.1016/S0010-9452(08)70415-5

Nadkarni, N. A., Bougacha, S., Garin, C., Dhenain, M., & Picq, J. L. (2018). A 3D population-based brain atlas of the mouse lemur primate with examples of applications in aging studies and comparative anatomy. *Neuroimage, 185*, 85-95. doi:10.1016/j.neuroimage.2018.10.010

Nasrallah, F. A., Lew, S. K., Low, A. S., & Chuang, K. H. (2014). Neural correlate of resting-state functional connectivity under alpha2 adrenergic receptor agonist, medetomidine. *Neuroimage, 84*, 27-34. doi:10.1016/j.neuroimage.2013.08.004

Nasrallah, F. A., Yeow, L. Y., Biswal, B., & Chuang, K.-H. (2015). Dependence of BOLD signal fluctuation on arterial blood CO2 and O2: Implication for resting-state functional connectivity. *Neuroimage, 117*, 29-39. doi:10.1016/j.neuroimage.2015.05.035

Nemoz-Bertholet, F., & Aujard, F. (2003). Physical activity and balance performance as a function of age in a prosimian primate (Microcebus murinus). *Exp Gerontol, 38*(4), 407-414.

Newman, M. E. (2006). Modularity and community structure in networks. *Proc Natl Acad Sci U S A, 103*(23), 8577-8582. doi:10.1073/pnas.0601602103

Newman, M. E. J. (2005). A measure of betweenness centrality based on random walks. *Social Networks, 27*(1), 39-54. doi:10.1016/j.socnet.2004.11.009

Ogawa, S., Lee, T.-M., Nayak, A. S., & Glynn, P. (1990). Oxygenation-sensitive contrast in magnetic resonance image of rodent brain at high magnetic fields. *Magn Reson Med, 14*(1), 68-78. doi:10.1002/mrm.1910140108

Ogawa, S., Lee, T. M., Kay, A. R., & Tank, D. W. (1990). Brain magnetic resonance imaging with contrast dependent on blood oxygenation. *Proc Natl Acad Sci U S A, 87*(24), 9868-9872.

Oguz, I., Zhang, H., Rumple, A., & Sonka, M. (2014). RATS: Rapid Automatic Tissue Segmentation in rodent brain MRI. *J Neurosci Methods, 221*, 175-182. doi:10.1016/j.jneumeth.2013.09.021

Okano, K. (2016). Functional brain mapping using specific sensory-circuit stimulation and a theoretical graph network analysis in mice with neuropathic allodynia.

Op de Beeck, H. P. (2010). Against hyperacuity in brain reading: Spatial smoothing does not hurt multivariate fMRI analyses? *Neuroimage, 49*(3), 1943-1948. doi:10.1016/j.neuroimage.2009.02.047

Ortiz, J. J., Portillo, W., Paredes, R. G., Young, L. J., & Alcauter, S. (2018). Resting state brain networks in the prairie vole. *Sci Rep, 8*(1), 1231. doi:10.1038/s41598-017-17610-9

Paasonen, J., Stenroos, P., Salo, R. A., Kiviniemi, V., & Grohn, O. (2018). Functional connectivity under six anesthesia protocols and the awake condition in rat brain. *Neuroimage, 172*, 9-20. doi:10.1016/j.neuroimage.2018.01.014

Patel, A. J., Honoré, E., Lesage, F., Fink, M., Romey, G., & Lazdunski, M. (1999). Inhalational anesthetics activate two-pore-domain background K + channels. *Nat Neurosci, 2*, 422. doi:10.1038/8084

Pawela, C. P., Biswal, B. B., Cho, Y. R., Kao, D. S., Li, R., Jones, S. R., . . . Hyde, J. S. (2008). Resting-state functional connectivity of the rat brain. *Magn Reson Med, 59*(5), 1021-1029. doi:10.1002/mrm.21524

Pépin, J. r. m. (2018). *Development of metabolic imaging using CEST-MRI : application to Huntington's disease.* Université Paris-Saclay. Retrieved from https://tel.archives-ouvertes.fr/tel-01740330 (2018SACLS032)

Perret, M. (1997). Change in Photoperiodic Cycle Affects Life Span in a Prosimian Primate (Microcebus murinus. *Journal of Biological Rhythms, 12*(2), 136-145. doi:10.1177/074873049701200205

Petrides, M., Alivisatos, B., Meyer, E., & Evans, A. C. (1993). Functional activation of the human frontal cortex during the performance of verbal working memory tasks. *Proc Natl Acad Sci U S A, 90*(3), 878-882.

Picq, J. L., Aujard, F., Volk, A., & Dhenain, M. (2012). Age-related cerebral atrophy in nonhuman primates predicts cognitive impairments. *Neurobiol Aging, 33*(6), 1096-1109. doi:10.1016/j.neurobiolaging.2010.09.009

Pifferi, F., Dorieux, O., Castellano, C. A., Croteau, E., Masson, M., Guillermier, M., . . . Aujard, F. (2015). Long-chain n-3 PUFAs from fish oil enhance resting state brain glucose utilization and reduce anxiety in an adult nonhuman primate, the grey mouse lemur. *J Lipid Res, 56*(8), 1511-1518. doi:10.1194/jlr.M058933

Pifferi, F., Terrien, J., Marchal, J., Dal-Pan, A., Djelti, F., Hardy, I., . . . Aujard, F. (2018). Caloric restriction increases lifespan but affects brain integrity in grey mouse lemur primates. *Commun Biol, 1*, 30. doi:10.1038/s42003-018-0024-8

Power, J. D., Mitra, A., Laumann, T. O., Snyder, A. Z., Schlaggar, B. L., & Petersen, S. E. (2014). Methods to detect, characterize, and remove motion artifact in resting state fMRI. *Neuroimage, 84*, 320-341. doi:10.1016/j.neuroimage.2013.08.048

Power, J. D., Schlaggar, B. L., & Petersen, S. E. (2014). Studying brain organization via spontaneous fMRI signal. *Neuron, 84*(4), 681-696. doi:10.1016/j.neuron.2014.09.007

Prichard, J., Rothman, D., Novotny, E., Petroff, O., Kuwabara, T., Avison, M., . . . Shulman, R. (1991). Lactate rise detected by 1H NMR in human visual cortex during physiologic stimulation. *Proc Natl Acad Sci U S A, 88*(13), 5829-5831.

Purcell, E. M., Torrey, H. C., & Pound, R. V. (1946). Resonance Absorption by Nuclear Magnetic Moments in a Solid. *Physical Review, 69*(1-2), 37-38. doi:10.1103/PhysRev.69.37

Raichle, M. E. (2011). The restless brain. *Brain Connect, 1*(1), 3-12. doi:10.1089/brain.2011.0019

Raichle, M. E., MacLeod, A. M., Snyder, A. Z., Powers, W. J., Gusnard, D. A., & Shulman, G. L. (2001). A default mode of brain function. *Proc Natl Acad Sci U S A, 98*(2), 676-682. doi:10.1073/pnas.98.2.676

Ramos-Cabrer, P., Weber, R., Wiedermann, D., & Hoehn, M. (2005). Continuous noninvasive monitoring of transcutaneous blood gases for a stable and persistent BOLD contrast in fMRI studies in the rat. *NMR Biomed, 18*(7), 440-446. doi:10.1002/nbm.978

Rilling, J. K., Barks, S. K., Parr, L. A., Preuss, T. M., Faber, T. L., Pagnoni, G., . . . Votaw, J. R. (2007). A comparison of resting-state brain activity in humans and chimpanzees. *Proc Natl Acad Sci U S A, 104*(43), 17146-17151. doi:10.1073/pnas.0705132104

Rolinski, M., Griffanti, L., Szewczyk-Krolikowski, K., Menke, R. A. L., Wilcock, G. K., Filippini, N., . . . Mackay, C. E. (2015). Aberrant functional connectivity within the basal ganglia of patients with Parkinson's disease. *NeuroImage: Clinical, 8*, 126-132. doi:10.1016/j.nicl.2015.04.003

Sanganahalli, B. G., Herman, P., Behar, K. L., Blumenfeld, H., Rothman, D. L., & Hyder, F. (2013). Functional MRI and neural responses in a rat model of Alzheimer's disease. *Neuroimage, 79*, 404-411. doi:10.1016/j.neuroimage.2013.04.099

Schroeder, M. P., Weiss, C., Procissi, D., Disterhoft, J. F., & Wang, L. (2016). Intrinsic connectivity of neural networks in the awake rabbit. *Neuroimage, 129*, 260-267. doi:10.1016/j.neuroimage.2016.01.010

Seeley, W. W., Menon, V., Schatzberg, A. F., Keller, J., Glover, G. H., Kenna, H., . . . Greicius, M. D. (2007a). Dissociable intrinsic connectivity networks for salience processing and executive control. *J Neurosci, 27*(9), 2349-2356. doi:10.1523/JNEUROSCI.5587-06.2007

Seeley, W. W., Menon, V., Schatzberg, A. F., Keller, J., Glover, G. H., Kenna, H., . . . Greicius, M. D. (2007b). Dissociable Intrinsic Connectivity Networks for Salience Processing and Executive Control. *The Journal of Neuroscience, 27*(9), 2349-2356. doi:10.1523/jneurosci.5587-06.2007

Sforazzini, F., Schwarz, A. J., Galbusera, A., Bifone, A., & Gozzi, A. (2014). Distributed BOLD and CBV-weighted resting-state networks in the mouse brain. *Neuroimage, 87*, 403-415. doi:10.1016/j.neuroimage.2013.09.050

Sforazzini, F., Schwarz, A. J., Galbusera, A., Bifone, A., & Gozzi, A. (2014). Distributed BOLD and CBV-weighted resting-state networks in the mouse brain. *Neuroimage, 87*, 403-415. doi:10.1016/j.neuroimage.2013.09.050

Shah, D., Blockx, I., Guns, P. J., De Deyn, P. P., Van Dam, D., Jonckers, E., . . . Van der Linden, A. (2015). Acute modulation of the cholinergic system in the mouse brain detected by pharmacological resting-state functional MRI. *Neuroimage, 109*, 151-159. doi:10.1016/j.neuroimage.2015.01.009

Shah, D., Deleye, S., Verhoye, M., Staelens, S., & Van der Linden, A. (2016). Resting-state functional MRI and [18F]-FDG PET demonstrate differences in neuronal activity

between commonly used mouse strains. *Neuroimage, 125*, 571-577. doi:10.1016/j.neuroimage.2015.10.073

Shah, D., Latif-Hernandez, A., De Strooper, B., Saito, T., Saido, T., Verhoye, M., . . . Van der Linden, A. (2018). Spatial reversal learning defect coincides with hypersynchronous telencephalic BOLD functional connectivity in APP(NL-F/NL-F) knock-in mice. *Sci Rep, 8*(1), 6264. doi:10.1038/s41598-018-24657-9

Shah, D., Praet, J., Latif Hernandez, A., Hofling, C., Anckaerts, C., Bard, F., . . . Van der Linden, A. (2016). Early pathologic amyloid induces hypersynchrony of BOLD resting-state networks in transgenic mice and provides an early therapeutic window before amyloid plaque deposition. *Alzheimers Dement*. doi:10.1016/j.jalz.2016.03.010

Shah, N. J., Arrubla, J., Rajkumar, R., Farrher, E., Mauler, J., Kops, E. R., . . . Neuner, I. (2017). Multimodal Fingerprints of Resting State Networks as assessed by Simultaneous Trimodal MR-PET-EEG Imaging. *Sci Rep, 7*(1), 6452. doi:10.1038/s41598-017-05484-w

Shim, W. H., Baek, K., Kim, J. K., Chae, Y., Suh, J. Y., Rosen, B. R., . . . Kim, Y. R. (2013). Frequency distribution of causal connectivity in rat sensorimotor network: resting-state fMRI analyses. *J Neurophysiol, 109*(1), 238-248. doi:10.1152/jn.00332.2012

Shulman, G. L., Corbetta, M., Fiez, J. A., Buckner, R. L., Miezin, F. M., Raichle, M. E., & Petersen, S. E. (1997). Searching for activations that generalize over tasks. *Hum Brain Mapp, 5*(4), 317-322. doi:10.1002/(SICI)1097-0193(1997)5:4<317::AID-HBM19>3.0.CO;2-A

Sicard, K. M., & Duong, T. Q. (2005). Effects of hypoxia, hyperoxia, and hypercapnia on baseline and stimulus-evoked BOLD, CBF, and CMRO2 in spontaneously breathing animals. *Neuroimage, 25*(3), 850-858. doi:10.1016/j.neuroimage.2004.12.010

Sierakowiak, A., Monnot, C., Aski, S. N., Uppman, M., Li, T. Q., Damberg, P., & Brene, S. (2015). Default mode network, motor network, dorsal and ventral basal ganglia networks in the rat brain: comparison to human networks using resting state-fMRI. *PLoS One, 10*(3), e0120345. doi:10.1371/journal.pone.0120345

Sinclair, M. D. (2003). A review of the physiological effects of alpha2-agonists related to the clinical use of medetomidine in small animal practice. *The Canadian veterinary journal = La revue veterinaire canadienne, 44*(11), 885-897.

Singh, M., Kim, S., & Kim, T.-S. (2003). Correlation between BOLD-fMRI and EEG signal changes in response to visual stimulus frequency in humans. *Magn Reson Med, 49*(1), 108-114. doi:10.1002/mrm.10335

Smith, S. M., Fox, P. T., Miller, K. L., Glahn, D. C., Fox, P. M., Mackay, C. E., . . . Beckmann, C. F. (2009). Correspondence of the brain's functional architecture during activation

and rest. *Proc Natl Acad Sci U S A, 106*(31), 13040-13045. doi:10.1073/pnas.0905267106

Song, Y., Sanganahalli, B. G., Hyder, F., Lin, W. C., & Riera, J. J. (2015). Distributions of Irritative Zones Are Related to Individual Alterations of Resting-State Networks in Focal Epilepsy. *PLoS One, 10*(7), e0134352. doi:10.1371/journal.pone.0134352

Sonnay, S., Duarte, J. M. N., & Just, N. (2017). Lactate and glutamate dynamics during prolonged stimulation of the rat barrel cortex suggest adaptation of cerebral glucose and oxygen metabolism. *Neuroscience, 346*, 337-348. doi:10.1016/j.neuroscience.2017.01.034

Stafford, J. M., Jarrett, B. R., Miranda-Dominguez, O., Mills, B. D., Cain, N., Mihalas, S., . . . Fair, D. A. (2014). Large-scale topology and the default mode network in the mouse connectome. *Proc Natl Acad Sci U S A, 111*(52), 18745-18750. doi:10.1073/pnas.1404346111

Stanley, J. A., & Raz, N. (2018). Functional Magnetic Resonance Spectroscopy: The "New" MRS for Cognitive Neuroscience and Psychiatry Research. *Front Psychiatry, 9*, 76-76. doi:10.3389/fpsyt.2018.00076

Steimke, R., Nomi, J. S., Calhoun, V. D., Stelzel, C., Paschke, L. M., Gaschler, R., . . . Uddin, L. Q. (2017). Salience network dynamics underlying successful resistance of temptation. *Social cognitive and affective neuroscience, 12*(12), 1928-1939. doi:10.1093/scan/nsx123

Stevens, M. C., Calhoun, V. D., & Kiehl, K. A. (2005). fMRI in an oddball task: Effects of target-to-target interval. *Psychophysiology, 42*(6), 636-642. doi:10.1111/j.1469-8986.2005.00368.x

Takata, Y. (2016). Physiological effects of a habituation procedure for functional MRI in awake mice using a cryogenic radiofrequency probe.

Tambini, A., Ketz, N., & Davachi, L. (2010). Enhanced brain correlations during rest are related to memory for recent experiences. *Neuron, 65*(2), 280-290. doi:10.1016/j.neuron.2010.01.001

Teichert, T., Grinband, J., Hirsch, J., & Ferrera, V. P. (2010). Effects of heartbeat and respiration on macaque fMRI: implications for functional connectivity. *Neuropsychologia, 48*(7), 1886-1894. doi:10.1016/j.neuropsychologia.2009.11.026

Telesford, Q. K., Joyce, K. E., Hayasaka, S., Burdette, J. H., & Laurienti, P. J. (2011). The ubiquity of small-world networks. *Brain Connect, 1*(5), 367-375. doi:10.1089/brain.2011.0038

Tian, L., Kong, Y., Ren, J., Varoquaux, G., Zang, Y., & Smith, S. M. (2013). Spatial vs. Temporal Features in ICA of Resting-State fMRI – A Quantitative and Qualitative

Investigation in the Context of Response Inhibition. *PLoS One, 8*(6), e66572. doi:10.1371/journal.pone.0066572

Touroutoglou, A., Bliss-Moreau, E., Zhang, J., Mantini, D., Vanduffel, W., Dickerson, B. C., & Barrett, L. F. (2016). A ventral salience network in the macaque brain. *Neuroimage, 132*, 190-197. doi:10.1016/j.neuroimage.2016.02.029

Tustison, N. J., Cook, P. A., Klein, A., Song, G., Das, S. R., Duda, J. T., . . . Avants, B. B. (2014). Large-scale evaluation of ANTs and FreeSurfer cortical thickness measurements. *Neuroimage, 99*, 166-179. doi:10.1016/j.neuroimage.2014.05.044

Uddin, L. Q. (2014). Salience processing and insular cortical function and dysfunction. *Nature Reviews Neuroscience, 16*, 55. doi:10.1038/nrn3857

Uhrig, L., Ciobanu, L., Djemai, B., Le Bihan, D., & Jarraya, B. (2014). Sedation Agents Differentially Modulate Cortical and Subcortical Blood Oxygenation: Evidence from Ultra-High Field MRI at 17.2 T. *PLoS One, 9*(7), e100323. doi:10.1371/journal.pone.0100323

Uhrig, L., Dehaene, S., & Jarraya, B. (2014). Cerebral mechanisms of general anesthesia. *Ann Fr Anesth Reanim, 33*(2), 72-82. doi:10.1016/j.annfar.2013.11.005

Uhrig, L., Sitt, J. D., Jacob, A., Tasserie, J., Barttfeld, P., Dupont, M., . . . Jarraya, B. (2018). Resting-state Dynamics as a Cortical Signature of Anesthesia in Monkeys. *Anesthesiology*. doi:10.1097/ALN.0000000000002336

Upadhyay, J., Baker, S. J., Chandran, P., Miller, L., Lee, Y., Marek, G. J., . . . Day, M. (2011). Default-mode-like network activation in awake rodents. *PLoS One, 6*(11), e27839. doi:10.1371/journal.pone.0027839

van den Heuvel, M. P., Mandl, R. C. W., Stam, C. J., Kahn, R. S., & Hulshoff Pol, H. E. (2010). Aberrant Frontal and Temporal Complex Network Structure in Schizophrenia: A Graph Theoretical Analysis. *The Journal of Neuroscience, 30*(47), 15915. doi:10.1523/JNEUROSCI.2874-10.2010

Vandenberghe, M. E., Herard, A. S., Souedet, N., Sadouni, E., Santin, M. D., Briet, D., . . . Delzescaux, T. (2016). High-throughput 3D whole-brain quantitative histopathology in rodents. *Sci Rep, 6*, 20958. doi:10.1038/srep20958

Vergara, V. M., Mayer, A. R., Damaraju, E., Hutchison, K., & Calhoun, V. D. (2017). The effect of preprocessing pipelines in subject classification and detection of abnormal resting state functional network connectivity using group ICA. *Neuroimage, 145*(Pt B), 365-376. doi:10.1016/j.neuroimage.2016.03.038

Vincent, D. B., Jean-Loup, G., Renaud, L., & Etienne, L. (2008). Fast unfolding of communities in large networks. *J Stat Mech Theory Exp, 2008*(10), P10008.

Vincent, J. L., Kahn, I., Van Essen, D. C., & Buckner, R. L. (2010). Functional connectivity of the macaque posterior parahippocampal cortex. *J Neurophysiol, 103*(2), 793-800. doi:10.1152/jn.00546.2009

Vincent, J. L., Patel, G. H., Fox, M. D., Snyder, A. Z., Baker, J. T., Van Essen, D. C., . . . Raichle, M. E. (2007). Intrinsic functional architecture in the anaesthetized monkey brain. *Nature, 447*(7140), 83-86. doi:10.1038/nature05758

Vogt, K. M., Ibinson, J. W., Schmalbrock, P., & Small, R. H. (2011). The impact of physiologic noise correction applied to functional MRI of pain at 1.5 and 3.0 T. *Magn Reson Imaging, 29*(6), 819-826. doi:10.1016/j.mri.2011.02.017

Vossel, S., Geng, J. J., & Fink, G. R. (2014). Dorsal and ventral attention systems: distinct neural circuits but collaborative roles. *Neuroscientist, 20*(2), 150-159. doi:10.1177/1073858413494269

Vossel, S., Thiel, C. M., & Fink, G. R. (2006). Cue validity modulates the neural correlates of covert endogenous orienting of attention in parietal and frontal cortex. *Neuroimage, 32*(3), 1257-1264. doi:10.1016/j.neuroimage.2006.05.019

Wang, J., Zuo, X., & He, Y. (2010). Graph-based network analysis of resting-state functional MRI. *Front Syst Neurosci, 4*, 16-16. doi:10.3389/fnsys.2010.00016

Watts, D. J., & Strogatz, S. H. (1998). Collective dynamics of 'small-world' networks. *Nature, 393*(6684), 440-442. doi:10.1038/30918

Wehrl, H. F., Hossain, M., Lankes, K., Liu, C.-C., Bezrukov, I., Martirosian, P., . . . Pichler, B. J. (2013). Simultaneous PET-MRI reveals brain function in activated and resting state on metabolic, hemodynamic and multiple temporal scales. *Nat Med, 19*, 1184. doi:10.1038/nm.3290

Wen, X., Yao, L., Fan, T., Wu, X., & Liu, J. (2012, 1-4 July 2012). *The spatial pattern of basal ganglia network: A resting state fMRI study.* Paper presented at the 2012 ICME International Conference on Complex Medical Engineering (CME).

Westphal, R., Simmons, C., Mesquita, M. B., Wood, T. C., Williams, S. C., Vernon, A. C., & Cash, D. (2017). Characterization of the resting-state brain network topology in the 6-hydroxydopamine rat model of Parkinson's disease. *PLoS One, 12*(3), e0172394. doi:10.1371/journal.pone.0172394

Wey, H.-Y., Phillips, K. A., McKay, D. R., Laird, A. R., Kochunov, P., Davis, M. D., . . . Fox, P. T. (2014). Multi-region hemispheric specialization differentiates human from nonhuman primate brain function. *Brain Structure and Function, 219*(6), 2187-2194. doi:10.1007/s00429-013-0620-9

Wren-Dail, M. A., Dauchy, R. T., Blask, D. E., Hill, S. M., Ooms, T. G., Dupepe, L. M., & Bohm, R. P., Jr. (2017). Effect of Isoflurane Anesthesia on Circadian Metabolism and Physiology in Rats. *Comp Med, 67*(2), 138-146.

Xu, F., Uh, J., Brier, M. R., Hart, J., Jr., Yezhuvath, U. S., Gu, H., . . . Lu, H. (2011). The influence of carbon dioxide on brain activity and metabolism in conscious humans. *J Cereb Blood Flow Metab, 31*(1), 58-67. doi:10.1038/jcbfm.2010.153

Zerbi, V., Grandjean, J., Rudin, M., & Wenderoth, N. (2015). Mapping the mouse brain with rs-fMRI: An optimized pipeline for functional network identification. *Neuroimage, 123*, 11-21. doi:10.1016/j.neuroimage.2015.07.090

Zhang, N., Rane, P., Huang, W., Liang, Z., Kennedy, D., Frazier, J. A., & King, J. (2010). Mapping resting-state brain networks in conscious animals. *J Neurosci Methods, 189*(2), 186-196. doi:10.1016/j.jneumeth.2010.04.001

Zhang, W., Lv, J., Li, X., Zhu, D., Jiang, X., Zhang, S., . . . Liu, T. (2019). Experimental Comparisons of Sparse Dictionary Learning and Independent Component Analysis for Brain Network Inference From fMRI Data. *IEEE Trans Biomed Eng, 66*(1), 289-299. doi:10.1109/TBME.2018.2831186

Zhao, F., Zhao, T., Zhou, L., Wu, Q., & Hu, X. (2008). BOLD study of stimulation-induced neural activity and resting-state connectivity in medetomidine-sedated rat. *Neuroimage, 39*(1), 248-260. doi:10.1016/j.neuroimage.2007.07.063

Zhao, X., Liu, Y., Wang, X., Liu, B., Xi, Q., Guo, Q., . . . Wang, P. (2012). Disrupted small-world brain networks in moderate Alzheimer's disease: a resting-state FMRI study. *PLoS One, 7*(3), e33540-e33540. doi:10.1371/journal.pone.0033540

Zhou, Z. C., Salzwedel, A. P., Radtke-Schuller, S., Li, Y., Sellers, K. K., Gilmore, J. H., . . . Gao, W. (2016). Resting state network topology of the ferret brain. *Neuroimage, 143*, 70-81. doi:10.1016/j.neuroimage.2016.09.003

Zhu, S., Fang, Z., Hu, S., Wang, Z., & Rao, H. (2013). Resting State Brain Function Analysis Using Concurrent BOLD in ASL Perfusion fMRI. *PLoS One, 8*(6), e65884. doi:10.1371/journal.pone.0065884

Zilles, K., Rehkämper, G., & Schleicher, A. (1979). *A quantitative approach to cytoarchitectonics - V. The areal pattern of the cortex of microcebus murinus (E. Geoffroy 1828), (Lemuridae, Primates)* (Vol. 157).

Titre : Caractérisation du cerveau des microcèbes murins par IRM anatomique, fonctionnelle et du glutamate

Mots clés : Réseaux, Microcèbe murin, Etat de repos, Fonctionelle, IRM, gluCEST.

Résumé : Le microcèbe murin (Microcebus murinus) est un primate attirant l'attention de la recherche neuroscientifique. Son anatomie cérébrale est encore mal décrite et ses réseaux cérébraux n'ont jamais été étudiés. Le premier objectif de cette thèse était de développer de nouveaux outils menant à la création d'un atlas numérique 3D du cerveau du microcèbe. Cet atlas est un outil fondamental car pouvant être utilisé pour extraire automatiquement des biomarqueurs cérébraux de diverses neuropathologies. Par la suite, nous avons mis en place des protocoles IRM et informatiques pour analyser la connectivité neuronale du microcèbe murin. Nous avons évalué pour la première fois les réseaux cérébraux de cet animal et révélé que son cerveau est organisé en régions fonctionnelles intégrées dans des réseaux fonctionnels à plus grande échelle.

Ces réseaux ont été classés et comparés à des réseaux similaires chez l'homme. Cette comparaison multi-espèces a mis en évidence des règles d'organisation communes mais aussi des divergences. L'imagerie du glutamate par transfert de saturation et par échange chimique (gluCEST) est une méthode permettant de créer des cartes 3D de la distribution du glutamate. Dans une troisième étude, nous avons comparé l'activité neuronale locale, la connectivité fonctionnelle et le contraste gluCEST dans diverses régions du cerveau. Nous avons ainsi mis en évidence différentes associations entre ces trois biomarqueurs. Enfin, l'impact du vieillissement sur la connectivité fonctionnelle, l'activité neuronale locale et le contraste gluCEST a été évalué en comparant deux cohortes de microcèbes murins.

Title : Characterization of mouse lemur brain by anatomical, functional and glutamate MRI

Keywords : Networks, Mouse lemur, Resting state, Functional, MRI, gluCEST.

Abstract : The mouse lemur (Microcebus murinus) is a primate that has attracted attention within neuroscience research. Its cerebral anatomy is still poorly described and its cerebral networks have never been investigated. The first objective of this study was to develop new tools to create a 3D digital atlas of the brain of this model and to use this atlas to automatically follow-up brain characteristics in cohorts of animals. We then implemented protocols to analyze connectivity in mouse lemurs so we could evaluate for the first time the cerebral networks in this species. We revealed that the mouse lemur brain is organised in local functional regions integrated within large scale functional networks.

These latter networks were classified and compared to large scale networks in humans. This multispecies comparison highlighted common organization rules but also discrepancies. Additionally, Chemical Exchange Saturation Transfer imaging of glutamate (gluCEST) is a method that allows the creation of 3D maps weighted by the glutamate distribution. In a third study, we compared local neuronal activity, functional connectivity and gluCEST contrast in various brain regions. We highlighted various associations between these three biomarkers. Lastly, the impact of aging on local neuronal activity, functional connectivity and gluCEST has been analyzed by comparing two cohorts of lemurs.